THÈSE

Pour l'obtention du grade de
DOCTEUR DE L'UNIVERSITÉ DE POITIERS
UFR des sciences fondamentales et appliquées
Institut de chimie des milieux et matériaux de Poitiers - IC2MP
(Diplôme National - Arrêté du 7 août 2006)

École doctorale : Sciences pour l'environnement - Gay Lussac (La Rochelle)
Secteur de recherche : Chimie organique, minérale, industrielle

Cotutelle : Université de Wuhan (Chine)

Présentée par :
Liwei Hou

Metal oxide synthesis and its application in the heterogeneous catalytic oxidation processes, using H2O2 or peroxydisulfate as oxidant

Directeur(s) de Thèse :
Sébastien Royer, Hui Zhang

Soutenue le 13 septembre 2013 devant le jury

Jury :

Président	**Jean-François Lamonier**	Professeur des Universités, Université de Lille 1
Rapporteur	**Jean-François Lamonier**	Professeur des Universités, Université de Lille 1
Rapporteur	**Lihua Zhu**	Professor, Huazhong University of Science and Technology, China
Membre	**Sébastien Royer**	Maître de conférences, Université de Poitiers
Membre	**Hui Zhang**	Professor, University of Wuhan, China

Pour citer cette thèse :
Liwei Hou. *Metal oxide synthesis and its application in the heterogeneous catalytic oxidation processes, using H2O2 or peroxydisulfate as oxidant* [En ligne]. Thèse Chimie organique, minérale, industrielle. Poitiers : Université de Poitiers, 2013. Disponible sur Internet <http://theses.univ-poitiers.fr>

THESE

Pour l'obtention du Grade de

DOCTEUR DE L'UNIVERSITE DE POITIERS

(Diplôme National - Arrêté du 7 août 2006)

Ecole Doctorale : Sciences pour l'Environnement Gay Lussac

Secteur de Recherche : Chimie organique, minérale, industrielle

Présentée par :

Liwei HOU

****

METAL OXIDE SYNTHESIS AND ITS APPLICATION IN THE HETEROGENEOUS CATALYTIC OXIDATION PROCESSES, USING H_2O_2 OR PEROXYDISULFATE AS OXIDANT

****

Directeur de Thèse : Hui ZHANG
Co-directeur de these: Sébastien ROYER

****

Soutenue le 13 Septembre 2013 devant la Commission d'Examen

****

JURY

Rapporteurs:

Lihua ZHU, Professor – Huzhang University of Science and Technology
Jean-François LAMONIER, Professor – University of Lille 1

Examinateurs:

Sébastien ROYER, Maitre de Conférences – HDR, Université de Poitiers
Hui ZHANG, Professor – University of Wuhan

THESE

Pour l'obtention du Grade de

DOCTEUR DE L'UNIVERSITE DE POITIERS

(Diplôme National - Arrêté du 7 août 2006)

Ecole Doctorale : Sciences pour l'Environnement Gay Lussac

Secteur de Recherche : Chimie organique, minérale, industrielle

Présentée par :

Liwei HOU

****

METAL OXIDE SYNTHESIS AND ITS APPLICATION IN THE HETEROGENEOUS CATALYTIC OXIDATION PROCESSES, USING H_2O_2 OR PEROXYDISULFATE AS OXIDANT

****

Directeur de Thèse : Hui ZHANG
Co-directeur de these: Sébastien ROYER

****

Soutenue le 13 Septembre 2013 devant la Commission d'Examen

****

JURY

Rapporteurs:

Lihua ZHU, Professor – Huzhang University of Science and Technology
Jean-François LAMONIER, Professor – University of Lille 1

Examinateurs:

Sébastien ROYER, Maitre de Conférences – HDR, Université de Poitiers
Hui ZHANG, Professor – University of Wuhan

Acknowledgements

I would like to thank very much to my supervisor Dr. Sebastien Royer. During my two years in France, he not only helped me with my work, but also gave many helps for my living. It is my pleasure and I am very lucky to work with him, I learned many things from him. He helped me about the experiment, he helped me about the papers, and also he helped me with my thesis. Without his help I cannot finish all my works in two years. Without his support I cannot made the interuniversity program between Poitiers University and Wuhan University.

I would also like to thanks very much to my supervisor Prof. Hui Zhang. Thanks for his guidance during the three years study in Wuhan University, thanks for his support of the interuniversity program between Poitiers University and Wuhan University.

I would like to thanks Prof. Nansheng Deng, and Prof. Feng Wu, for their kindly help and guide about my experiments during my study in Wuhan University.

Thanks for my friends Wei Yang and Qinghua Zhang, during the years I study in Poitiers University. They had given many help to me about my experiments. And he also gave many help to my living in France. I am always very happy to work together with them. And also thanks for the kindly help from my colleagues Mrs. Alejadana, Mr. François Jérôme, Stephane Pronier…

Thanks for Dr. Changbo Zhang, he gave a lots of help to me when I was in Wuhan university. I am to have the opportunity to work with Dr Xin Zhong, Dr Heng Lin, Dr Chun Cai, Dr. Haigang Li, Dr. Xu Zhang, Ms. Huiyuan Li, Ms. Pan Yi, Ms. Xue Wang and also thanks for their help.

Thanks for the fund support of China Scholarship Council (CSC) affiliated with the Ministry of Education of the P.R. China. Thanks for choosing me and giving me this chance. Thanks for Ms. Jingmei Zhao who is working in the Education Service of China Embassy in Paris France.

Finally, I would especially like to thank my family, my parents and my boyfriend for always being there with encouragement; I would like to thank my boyfriend Jian Wu, for his love, understanding and support, I can overcome any difficulties. We have been together since France, we work hard together to pursue the happiness of life for years, I cannot image my life without him.

ACKNOWLEDGEMENTS

Résumé

Parmi les procédés avancés d'oxydation (AOPs), les procédés de type Fenton (réactif de Fenton: Fe^{2+}/H_2O_2) et les procédés d'oxydation par le persulfate, sont décrits comme des procédés très performants. Le procédé Fenton est une voie prometteuse et attractive pour le traitement d'une large variété de composés organiques polluants, difficiles à traiter par les voies classiques de dépollution. Au cours du procédé Fenton, des radicaux hydroxyls, molécules à fort pouvoir oxydant capable de réagir avec pratiquement tous types de composés organiques et inorganiques, sont générés. De même, du fait de la structure similaire entre H_2O_2 et les ions peroxydisulfate, ces derniers peuvent se décomposer en radicaux sulfates ($SO_4^{-\bullet}$), un autre type d'oxydant hautement réactif pouvant réagir avec les composés organiques. Cependant, les procédés Fenton et d'activation du peroxydisulfate classiques présentent plusieurs inconvénients. En effet, la solution doit être acidifiée avant la réaction, et des procédés complexes de purification / séparation sont nécessaires après réaction. Afin de contourner ces inconvénients, le développement de procédés de traitement hétérogènes est proposé pour le traitement de l'eau. Dans cette optique de développement de procédés économes, les oxydes de fer comme la magnétite sont proposés comme remplaçants des sels solubles de fer. Une utilisation de tels matériaux, à l'état solide, présente des avantages indéniables, dont la séparation aisée de l'espèce active après réaction par sédimentation ou filtration.

Dans le cadre de ce travail de doctorat, différents types d'oxydes de fer, hématite ou magnétite, ont été synthétisés en milieu liquide ionique. La morphologie, les propriétés structurales, les rapports de surface Fe^{II}/Fe^{III}, les surfaces spécifiques, les tailles de domaine cristallin, *etc.* ont été évaluées. Deux molécules différentes, la tétracycline (TC) et le phénol, couramment utilisées dans l'industrie chimique, ont été sélectionnées comme polluants modèles afin d'évaluer les performances des matériaux préparés pour leur élimination. Une partie importante du travail de doctorat a donc été l'étude des propriétés des matériaux pour l'élimination de polluants organiques par le procédé Fenton hétérogène. Les résultats montrent clairement que differents facteurs affectent les performances du procédé. Certains de ces facteurs sont reliés aux propriétés de la phase active, du fait du caractère surfacique des réactions, tandis que d'autres dépendent des conditions de fonctionnement du procédé (nature de

l'oxydant, nature de l'énergie fournie au procédé). La stabilité des systèmes catalytiques préparés est néanmoins une propriété cruciale également étudiée. Le manuscrit de doctorat met donc l'accent sur la conception de matériaux originaux destinés à une utilisation dans les procédés avancés d'oxydation dans l'eau.

Le manuscrit est constitué de 6 études expérimentales :

Etude 1: Des matériaux de structure hématite (α-Fe_2O_3) ont été synthétisés en utilisant une voie en milieu liquide ionique. Il a ainsi été possible de préparer différentes morphologies, parmi lesquelles des cubes, des sphères et des nanotiges poreuses. Du fait de morphologies radicalement différentes, ces solides présentent des aires spécifiques variant de quelques $m^2\ g^{-1}$ à plus de 50 $m^2\ g^{-1}$. Ces différences entraînent d'importantes modifications au niveau de la mobilité des oxygènes du réseau du solide, les nanotiges poreuses présentant les mobilités d'oxygène les plus élevées. Cette étude était un pré requis à l'étude de la synthèse de matériaux de type magnétite, destinés aux réactions de dépollution dans l'eau. Ces matériaux, de type hématite, ont néanmoins été testés pour des réactions en phase gazeuse afin d'évaluer leur réactivité de surface. Ces solides de morphologies bien définies présentent des activités catalytiques remarquables. Ainsi, un catalyseur à base d'or supporté sur nanotige poreuse permet la conversion de CO à basse température (< 100°C).

Etude 2: Du fait de l'importance de la tétracycline (TC) dans l'industrie chimique, l'oxydation de la TC a été étudiée sur un catalyseur commercial Fe_3O_4, par un procédé couplé ultrason/Fenton hétérogène, décrit dans la littérature comme un procédé hautement performant pour l'élimination de polluants réfractaires. L'effet des conditions opératoires, l'évolution de la toxicité de l'effluent, et le mécanisme réactionnel ont été étudiés. Les résultats obtenus montrent que l'activité du catalyseur est fortement améliorée sous irradiation ultrason. Dans des conditions optimisées, la TC peut être convertie à 93.7% en 60 min de traitement. Le carbone organique total (COT) atteint 14.9% d'abattement, mais augmente jusqu'à 31.8% après seulement 180 min de réaction. Un système membranaire original a été utilisé pour étudier le mécanisme réactionnel et l'impact des différents radicaux générés lors de la réaction. Il a été démontré que les radicaux hydroxyls étaient les principales espèces réactives responsables de la dégradation de la TC.

Etude 3: Cette étude traite de l'élimination de la tétracycline par procédé catalytique hétérogène en présence d'ions peroxydisulfate ($Na_2S_2O_8$) sous ultrasons (procédé d'oxydation $Na_2S_2O_8/Fe_3O_4$/ultrason). L'étude de l'effet des conditions réactionnelles est présentée (concentration en $Na_2S_2O_8$, chargement en Fe_3O_4, concentration initiale en TC, pH de réaction…). Les résultats montrent que l'efficacité pour l'élimination de la TC est fortement dépendante des conditions opératoires. En condition optimale, de hauts degrés de minéralisation peuvent néanmoins être obtenus. L'analyse du rôle respectif des radicaux générés en réaction, sulfate, hydroxyl ou superoxide, montre que les radicaux sulfates et hydroxyls sont les espèces réactives consommées lors de la réaction de dégradation.

Etude 4: L'ozone est, dans le cas de cette étude, employée comme oxydant car pouvant être activée à la surface des matériaux de type magnétite. La réaction de dégradation de la tétracycline est étudiée dans le procédé couplé US/Fe_3O_4/O_3. Une étude complète de l'effet des paramètres opérationnels sur la biodégradation et la toxicité de l'effluent a été effectuée. Les résultats obtenus indiquent que la vitesse de dégradation de la tétracycline est fortement influencée par le pH de la solution et la puissance des US, alors que celle-ci est peu dépendante de la concentration en catalyseur. Dans des conditions optimisées, la tétracycline est complètement convertie après 20 min de traitement, et l'abattement de DCO atteint 41.8%. Cet abattement atteint 89.1% quand le temps de réaction est étendu à 120 minutes, et la dégradation biochimique (DBO_5/DCO) atteint 0.694. La toxicité de l'effluent atteint son maximum après 60 min de traitement, et ensuite diminue avec l'augmentation du temps de réaction.

Etude 5: Du fait de l'activité intrinsèque élevée développée par les matériaux de type magnétite, des matériaux Fe_3O_4 de morphologie contrôlée ont été préparés par réduction thermique de α-Fe_2O_3 synthétisé en milieu liquide ionique (Etude 1). Les magnétites obtenues présentent des morphologies bien définies, microcube, nanosphère, nanotige poreuse. L'activité de ces solides a été évaluée pour les réactions de type Fenton, avec le phénol comme polluant modèle. Alors que les échantillons commerciaux Fe_3O_4 présentent des activités limitées, une activité exceptionnelle est obtenue sur les nanostructures de type nanotiges poreuses. La stabilité de ces matériaux a également été évaluée. Il s'avère que ces solides peuvent

être utilisés lors de plusieurs cycles réactionnels successifs sans désactivation notable. L'étude a également permis de montrer que l'activité des magnétites pouvait être améliorée significativement en ajustant le degré de réduction du solide, afin de former des composites Fe^0/Fe_3O_4. Ces derniers présentent des activités remarquables, supérieures à celles obtenues sur magnétite.

Etude 6: Connaissant l'impact de la mobilité d'oxygène et des propriétés de surface sur les propriétés catalytiques des solides, nous avons ensuite étudié la possibilité de préparer des matériaux nanocristallins de structure pérovskite $LaAO_3$ (A= Co, Mn) à partir d'une voie de synthèse non aqueuse. Ces matériaux de structure pérovskite trouvent un large écho auprès de la communauté scientifique proche de la catalyse environnementale pour des applications en dépollution aussi bien en phase gazeuse qu'en phase aqueuse. Les matériaux préparés ont été caractérisés par les techniques classiques de caractérisation des solides, et la mobilité d'oxygène a été mesurée par échange isotopique d'oxygène (OIE). Les matériaux préparés par synthèse non aqueuse présentent des surfaces spécifiques améliorées et des tailles de domaine cristallin réduites. Ces propriétés induisent d'importantes modifications des propriétés redox de ces solides. Les propriétés de mobilité d'oxygène sont également fortement modifiées par la réduction de la taille de cristal et l'augmentation de la surface spécifique. Ces évolutions varient en parallèle avec les évolutions d'activité catalytique, aussi bien dans le cas des réactions en phase gazeuse (oxydation du CO) que dans le cas des réactions en phase aqueuse (dégradation du phénol en présence de H_2O_2). En conclusion, l'utilisation de la voie de synthèse non aqueuse permet la préparation de matériaux présentant des propriétés catalytiques améliorées.

Mots clés: Fenton, hématite, magnétite, Procédés Avancés d'Oxydation, ultrason, peroxydisulfate, H_2O_2, oxydation du CO

Abstract

Fenton reaction (Fenton reagent: (Fe^{2+}/H_2O_2)) and persulfate oxidation process, as advanced oxidation processes, are powerful oxidations used world around. Fenton reaction has been evidenced to be a promising and attractive treatment method for the degradation of a wide variety of hazardous organic pollutants, which are difficult to be treated using traditional soft treatment technologies. During Fenton process, free hydroxyl radicals ($HO^{\bullet}$), strong oxidant molecules capable of reacting with practically all types of organic and inorganic compounds, are generated. In the meanwhile, due to the similar structure between H_2O_2 and peroxydisulfate ions, peroxydisulfate ions can be decomposed to sulfate radicals ($SO_4^{-\bullet}$), another kind of highly active oxidant that can react with organic compounds. However, the classical Fenton or peroxydisulfate activation processes present some disadvantages. Indeed, the solution needed acidification before carrying out the reaction and complex separation processes have to be applied after reaction. To overcome these drawbacks, heterogeneous catalytic oxidation processes were introduced for wastewater treatment. In this line, magnetite was evidenced as potential substituent to soluble iron ions, and it offers significant advantages such as an easy separation after reaction since the active material can be easily recovered by sedimentation or filtration for further used.

In this PhD work, iron oxides, hematite and magnetite, were synthesized using an ionic liquid mediated process. The morphology, structural properties, Fe^{II}/Fe^{III} surface ratios, specific surface areas (SSA), mean particle diameters, site densities, *etc.* were evaluated. Two different model pollutants (tetracycline (TC) and phenol), which are widely used chemicals all over the world, were selected to evaluate the performance of the prepared active materials. A significant part of the PhD study was then on the study of heterogeneous Fenton-like reaction for phenol and TC degradation. Experiments showed that many factors are affecting the heterogeneous Fenton-like system, some are related to the heterogeneous active phase properties, due to the surface reaction nature occurring over iron oxide surface, while other are relater to the process condition (nature of the oxidant, nature of the energy furnished for reaction). However, stability of this active phase, with progressive dissolution under reaction, is also a real challenge. This PhD manuscript, focusing on the design of highly active

materials for advanced oxidation processes (AOPs), is constituted of six experiment result parts:

First study: Hematite type materials (α-Fe_2O_3), with different morphologies, were synthesized using an original ionic liquid mediated process. Different morphologies can be obtained, amongst cubes, spheres, and porous nanotubes. Due to the different morphologies developed, accessible surface area varies from a few $m^2\ g^{-1}$ to more than 50 $m^2\ g^{-1}$. These differences result in largely different oxygen mobility properties, the porous nanorods presenting the highest bulk oxygen mobility. As a consequence, all these shaped materials present higher activity for oxidation reaction than classical hematite reference. In addition, the favorable physical properties, that are a high surface area and open porosity, allow the easy dispersion of noble metal nanoparticles (Pt, Pd, and Au). Some of these noble metal-containing high surface area materials exhibit remarkable catalytic activities for gas phase oxidation reaction. Indeed, porous nanorods-supported gold nanoparticles allow converting CO below 100 °C, which is far better than the performances obtained of commercial α-Fe_2O_3 supported gold for which dispersion of gold remains difficult due to the low surface area developed by the commercial support. This part is obviously a prerequisite to the synthesis of magnetite-type materials for water treatment, and these materials were used directly in gas phase oxidation reaction in order to characterize surface properties of the synthesized iron oxides.

Second study: Due to the importance of tetracycline (TC) in chemical industry, the oxidation of TC was studied over commercial Fe_3O_4 catalyst, using a coupled ultrasound/heterogeneous Fenton process, described in the literature as a powerful AOP. The effects of the reaction parameters, the evolution of the effluent toxicity, and the reaction mechanism were studied. The results demonstrated that the stability of the catalyst was significantly improved under ultrasound irradiation. Under optimized conditions, tetracycline was removed with an efficiency of 93.7% after 60 min of treatment. The total organic carbon (TOC) removal reached 14.9%, and the TOC value further increased to 31.8% when the reaction time was extended to 180 min. An original membrane separation system was used to explore the surface oxidation mechanism occurring during reaction. Then, surface hydroxyl radicals were determined as main reactive species for TC oxidation reaction.

Third study: Removal of tetracycline by magnetite (Fe_3O_4) activated peroxydisulfate ($Na_2S_2O_8$) under ultrasound irradiation was investigated ($Na_2S_2O_8$/Fe_3O_4/ultrasound oxidation process). The effects of $Na_2S_2O_8$ concentration, Fe_3O_4 loading, ultrasonic power, initial TC concentration and initial pH were addressed. The results showed that the TC removal efficiency increased with Fe_3O_4 loading, but decreased with the increase of initial pH and initial tetracycline concentration. Under optimal operation values of $Na_2S_2O_8$ concentration and ultrasound power intensity, high degradation efficiency can be achieved. Quenching effect was examined by using ethanol, *tert*-butyl alcohol and 1, 4-benzoquinone under ultrasound irradiation to evaluate the respective roles of sulfate radicals, hydroxyl radicals and superoxide radicals. The results indicated that sulfate radicals and hydroxyl radicals played the main roles for the degradation reaction.

Fourth study: Ozone was employed as oxidant, since it can be activated by magnetite surface. The degradation of tetracycline was investigated using ultrasound-enhanced magnetite catalytic ozonation process (US/Fe_3O_4/O_3). Thorough assessments of the operational parameters, biodegradability and acute toxicity were performed. The results indicated that the TC degradation rate was strongly influenced by the initial pH and the ultrasonic power, but it was almost independent of the dosage of Fe_3O_4 at the range from 0.3 to 1.0 g L^{-1}. Under optimized conditions, TC was almost completely removed after 20 min of treatment, and the COD removal reached 41.8%. The COD removal further increased to 89.1% when the reaction time was extended to 120 minutes, and the corresponding biochemical degradability (BOD_5/COD) rose to 0.694. The acute toxicity reached its maximum value after 60 min treatment and then decreased with further reaction time.

Fifth study: Due to the intrinsic activity of magnetite-type material for Fenton reaction, nanostructured Fe_3O_4 particles were obtained through hydrogen thermal reduction of α-Fe_2O_3 particles synthesized via an ionic liquid assisted hydrothermal process (first study). As-prepared magnetite materials show microcube, nanosphere, and porous nanorod morphologies. Activity of the nanostructures was evaluated for the Fenton reaction, using phenol as model molecule. While commercial Fe_3O_4 presents very limited activity, rod-type nanostructure exhibited exceptional activity toward phenol removal under mild conditions. The reusability of porous nanorods of Fe_3O_4 was also investigated, demonstrating promising properties for large scale

oxidative degradation of organic pollutants. Interestingly, the magnetite intrinsic activity can be strongly improved, tuning the reduction degree of the material. The beneficial effect of Fe^0/Fe_3O_4 mixed phase formation to achieve higher activity is clearly highlighted.

Sixth study: Knowing the impact of oxygen mobility and surface properties on the catalytic activity of materials, we studied the possibility to develop a route to nanocrystalline $LaAO_3$ (A = Co, Mn) materials. These perovskite type materials find wide application in environment field, for gas phase and water depollution reactions. Synthesized materials were characterised using classical techniques, and oxygen mobility in these nano-structures evaluated using oxygen isotopic exchange (OIE). The solids obtained by this non-aqueous route presents improved surface area, small crystal size, and improved redox properties (as measured by reduction by H_2), when compared to conventional materials. Oxygen mobility was also found to be strongly influenced by the material physico-chemical properties. These observations correlated well with the evolutions in catalytic activity for phenol degradation in Fenton reaction, but also for gas phase CO oxidation. The materials obtained by this original non-aqueous route presented excellent catalytic performances.

Keywords: Fenton, hematite, magnetite, AOP, ultrasound irradiation, peroxydisulfate, H_2O_2, CO oxidation

Table of content

Chapter 1. Introduction **2**

1.1 Background 3

1.2 Research goals and objective 5

1.3 Organization of thesis 6

Chapter 2. Literature review **12**

2.1 Pharmaceuticals and personal care products (PPCPs) 13

2.1.1 Physical and chemical properties – in case of tetracycline 17

2.1.2 Sources and occurrences – in case of tetracycline 17

2.1.3 Environmental toxicity – in case of tetracycline 18

2.1.4 Treatment methods – in case of tetracycline 18

2.2 Phenolic organic compounds 19

2.3 Advanced oxidation processes (AOPs) 19

2.3.1 Fenton process 20

2.3.2 Persulfate oxidation process 21

2.2.3 Catalytic ozonation process 22

2.4 Iron in heterogeneous catalysis - application in AOPs and oxidation 24

2.4.1 Iron oxide 24

2.4.2 Other iron oxide in environmental catalysis 28

2.4.3 Iron in mixed oxide materials, perovskite-based catalyst 29

Chapter 3 Ionic Liquid-Mediated α-Fe_2O_3 Shape-Controlled Synthesis **38**

3.1 Introduction 39

3.2 Structural properties 43

3.3 Textural properties 44

3.4 Reducibility of the composites 50

3.5 Conclusion 57

Chapter 4 Highly efficient AOP process using an ultrasound-assisted, heterogeneous Fenton-like reaction 70

4.1 Introduction 71

4.2 Materials and methods 73

4.3 Results and discussion 75

4.3.1 Physicochemical properties 75

4.3.2 Comparison of the catalytic activity under different oxidation conditions 79

4.3.3 Influence of the ultrasound power density on TC oxidation 82

4.3.4 Influence of the hydrogen peroxide concentration and catalyst loading on TC oxidation 83

4.3.5 Influence of temperature on TC oxidation. 85

4.3.6 Toxicity evolution 86

4.3.7 Catalytic mechanism 86

4.3.8 Stability of the Fe catalyst 89

4.3.9 Surface properties of magnetite nanoparticles effect on their catalytic performance 90

4.4. Conclusions 91

Chapter 5 Ultrasound enhanced heterogeneous activation of peroxydisulfate by magnetite catalyst 104

5.1 Introduction 105

5.2 Experimental section 105

5.3 Results and discussion 106

5.3.1 Degradation of tetracycline under different systems 106

5.3.2 The effect of initial pH on the degradation of tetracycline 108

5.3.3 The effect of sodium peroxydisulfate concentration on the degradation of tetracycline 110

5.3.4 The effect of magnetite addition on the degradation of tetracycline 111

5.3.5 The effect of power on the degradation of tetracycline 112

5.3.6 The effect of initial pollutant concentration on the degradation of tetracycline 113

5.3.7 Oxidative mechanism in the $Na_2S_2O_8/Fe_3O_4$/US system 114

5.3.8 Structural and catalytic stabilities 117

5.4 Conclusion 119

Chapter 6 Ultrasound-enhanced magnetite catalytic ozonation of tetracycline in water 122

6.1. Introduction 123

6.2. Experimental section 125

6.2.1 Materials 125

6.2.2 Procedure 125

6.2.3 Analysis methods 126

6.2.4 Acute toxicity test of tetracycline 127

6.3 Results and discussion 127

6.3.1 Degradation efficiency of tetracycline in the investigated processes 127

6.3.2 Effect of power density on the TC removal in the US/Fe_3O_4/O_3 system 130

6.3.3 Effect of pH on the TC removal in the US/Fe_3O_4/O_3 system 131

6.3.4 The effect of catalyst dosage on the removal of TC in the US/Fe_3O_4/O_3 system 133

6.3.5 Evidence of hydroxyl radical generation in the US/Fe_3O_4/O_3 system 134

6.3.6 COD removal efficiencies in the investigated processes 136

6.3.7 The change of biodegradability and toxicity in the US/Fe_3O_4/O_3 system 137

6.3.8 Catalyst stability tests in the US/Fe_3O_4/O_3 system 138

6.3.9 Electric energy cost estimation 139

6.4. Conclusions 141

Chapter 7 Shape-controlled nanostructured magnetite-type materials as highly efficient Fenton catalysts 148

7.1. Introduction 149

7.2 Experimental Section 152

7.2.1 Materials 152

7.2.2 Catalysts characterization 152

7.2.3 Catalytic activity measurement 154

7.3 Results and discussion 155

7.3.1 Characterization of the α-Fe_2O_3 precursors 155

7.3.2 Characterization of the Fe_3O_4 precursors 161

7.3.3 Comparison of the catalytic activity of different iron oxide nanoparticles 164

7.3.4 Evidence of heterogeneous Fenton reaction over Fe_3O_4-R 165

7.3.5 Role of morphology in the catalytic oxidation of phenol 167

7.3.6 Influence of hydrogen peroxide concentration and catalyst loading on phenol oxidation 169

7.3.7 Stability of Fe_3O_4-R catalyst and iron leaching 170

7.3.8 Effect of the iron crystal phase on the catalytic oxidation of phenol 172

7.4 Conclusion 173

Chapter 8 Simple non-aqueous route to nano-perovskite mixed oxides 184

8.1. Introduction 185

8.2 Experimental Section 188

8.3 Results and discussion 189

8.3.1 Physicochemical and structure properties 189

8.3.2 Redox properties as evaluated by H_2-TPR 193

8.3.3 Oxygen mobility capacity as evaluated by temperature-programmed oxygen isotopic exchange (TPOIE) 196

8.3.4 Catalytic acitivity evaluation 198

8.4 Conclusions 199

Chapter 9. General conclusion 208

Publications 211

Chapter 1. Introduction

1.1 Background

In recent years, the phenolic organic compounds, pharmaceuticals and personal care products can be found in waterbodies and the environment for as long as humans have been using them. The widespread of these non-biodegradable organic chemicals in environmental aqueous system or wastewater effluents is a serious environmental problem because of their significant threats on water resources and human health. Moreover, many types of them react with some metal ions to form complexes in aqueous environment, which are often more difficult to be degraded by conventional biological technologies, and physicochemical methods. These traditional processes are ineffective for many kinds of organic compounds, and the degradation rates are very slow. Furthermore, toxic by-products can be produced during the chemical treatment processes, which are more difficult to degradate and mineralize. In addition, physi/adsorption processes just transfer the pollutant from aqueous phase to solid phase, and further treatments are needed. Consequently, there is an increase in social pressure towards the wastewater treatment and an industrial interest in the improvement of the existing water treatment technologies.

Advanced oxidation processes (AOPs) have been defined as oxidation treatment based on the reaction of hydroxyl radical in an aqueous solution. Radicals are powerful and extremely reactive oxidant agent that can convert organic pollutants efficiently [1-7]. The oxidants most commonly employed to date include hydrogen peroxide, persulfate ions and ozone. Fenton reaction is one of the AOPs, It is one of the most powerful oxidation processes used world around. It has been used as an efficient treatment method for the degradation of many different organic pollutants. However, the conventional homogenous Fenton application was limited by the slurry system production, separation, and high metal concentrations in the final effluents. Hence, many researchs focused on the use of modified Fenton systems, the so called Fenton-like systems, to treat the organic pollutants. Nowadays, metal oxides were used instead of soluble metal ions, and their uses offer significant advantages in separation since the catalyst can be easily recovered by sedimentation or filtration and further use. Hence, the process operating conditions were significantly simplified. It is widely accepted that hydroxyl radicals ($^{\bullet}OH$) is the predominant reactive species generated in both the Fenton and Fenton-like systems [8-9]. This type of radicals has a strong and nonselective oxidizing ability ($E^0 = 2.7$ V); therefore, it can readily convert

organic molecules, and transform them into carbon dioxide and water. However, hydrogen peroxide is not a long-lived molecule and it rapidly decomposes in contaminated sites. In addition, H_2O_2 is easily influenced by the iron solubility, mineral species, cycling between the +2 and +3 states of iron valence, *etc*., which limit the process efficiency.

As a strong oxidant, persulfate ($S_2O_8^{2-}$, E^0 = 2.1 V) is another popular reagent in the wastewater treatment because it is more stable and more soluble than H_2O_2, and it can be transported over a long distance in the aqueous solution without alteration [10]. Furthermore, it can be activated by heat, light, soluble transition metal ions and metal oxide, releasing sulfate radicals ($SO_4^{-\bullet}$, E^0 = 2.6 V), which has high oxidative ability [11,12]. Therefore, it may quickly and effectively oxidize and remove pollutants from wastewater. Therefore, persulfate found wide application prospect in environmental pollution control field in recent years.

Ozone is another powerful oxidizing molecule that can either react directly with the organic pollutants or decompose into free radicals to attack the organic compounds with a very high rate. However, when ozone is used alone, it does not often lead to high level of mineralization and toxicity removal [13,14]. The use of ozone also has limitation with respect to the high implementation cost and the poor mass transfer rate. Consequently, ozone is usually combined with other technologies to improve its large scale utilization [15,16]. In recent years, heterogeneous catalytic ozonation has become a powerful treatment method for the degradation of refractory organic pollutants, and high removal and mineralization can be achieved [17 19]. Catalysts used include MgO [17], alumina [18], doped alumina catalysts [19], activated carbon supported catalyst (MnO_x/GAC) [21], α-FeOOH [22], cobalt oxides [23], β-MnO_2 [24], perovskite [25], and brucite [26]. Although some catalysts displayed considerable catalytic activity in the ozonation process, their production might be problematic and cost-intensive from an industrial viewpoint. Moreover, the separation step is often unfavorable. Considering this information, the application of magnetite particles (Fe_3O_4) in the pollution control has received great attention in the recent years [27-29]. Magnetic particles can be separated from the solution using a simple magnetic process, which shows its superiority to the other metal oxides (such as α-FeOOH, and α-Fe_2O_3, *etc.*) [22,30]. In addition, as one of transition metal oxides, Fe_3O_4 with multiple accessible oxidation states, is an active catalyst for ozone decomposition [31,32]. Despite the promising results of catalytic ozonation using

magnetic as catalyst, the catalyst deactivation due to organic intermediates accumulation on the surface is still a major obstacle for its industrial application. In the meanwhile, the release of metal ions decreased the stability and activity of the catalyst. Therefore, the development of an effective approach to improve the catalytic efficiency and durability remains an important issue that needs to be urgently addressed.

It has been found that ultrasound can enhance the activity of the catalyst in the ozonation process without prejudice on the stability of the heterogeneous iron species [30,33]. During the ultrasonic process, the cavitation effect can clean the surface of the catalyst, and improved stability in reaction can be achieved during the ultrasonic irradiation process [30,34]. In addition, ultrasound accelerates turbulence, which can reduce the liquid film thickness and subsequently increase the mass transfer of reactants and by-products between the liquid and solid phases [34,35]. Furthermore, hydroxyl radicals will be generated in the vapour phase of cavitation bubbles during the ultrasonic process [36,37].

In this work, Fenton-like process, sono-Fenton-like process and sono-catalytic ozonation processes in the presence of different oxidants and catalysts were studied. Tagets of the study were indentifying the means to overcome many disadvantages of the homogenous system, and it is very important and very meaningful to go deep into the study of these processes using metal oxides. Tetracycline (TC) has been used in numerous chemical applications, resulting in potential ecological damage [38]. In the same line, phenolic substances are one of the most common toxic pollutants in the natural environment around the world. These two types of pollutants were chosen as model pollutants in this PhD.

1.2 Research goals and objective

The objective of this work was to study degradation of model pollutants using different kinds of iron metal oxide (such as hematite, magnetite, perovskite) with different physic-chemical properties. We determined which are the suitable conditions and investigated main factors which affect the efficiency of the Fenton-like system, to gain insight into the heterogeneous Fenton reaction, and to get more information about the mechanism. Persulfate oxidation and ozonation systems were also studied to

improve the oxidation efficiency, and we investigated parameter effects to identify the best oxidation conditions; this can help us to know more deeply about the heterogeneous AOPs reaction. To meet these goals the following specific objectives were defined:

1. Conduct batch experiments to elucidate the role of iron species on the heterogeneous Fenton-like reaction, and to investigate the mechanism of the heterogeneous Fenton-like reaction.

2. Conduct experiments to investigate the influence of the operation parameters on the sono-persulfate oxidation process, and verify the main active species that affect the oxidation efficiency.

3. Conduct experiments to investigate the mechanism of sono-catalytic ozonation of tetracycline. The operation parameters on the sono-catalytic ozonation process were explored. Moreover, the acute toxicity of tetracycline was also verified after sono-catalytic ozonation.

4. Enhance the catalytic activity of the materials. Two kinds of iron oxide (α-Fe_2O_3, Fe_3O_4) with different morphologies by using ionic liquid assisted hydrothermal method were synthesized. Catalytic activities of these materials were measured.

5. Synthesis of highly crystalline $LaMO_3$ (M= Co, Mn). Compared with conventional citric acid method, the solids obtained by non-aqueous route present large differences in specific surface area, crystallite size, and redox properties (as measured by reduction by H_2).

1.3 Organization of thesis

This dissertation is divided into 9 chapters.

Chapter 1 is an introduction which included background, research goals and objectives, and organization of thesis.

Chapter 2 presents a review of recent research work related to this study. Four parts are described:

2.1. Pharmaceuticals and personal care products

2.2 Phenolic organic compounds

2.3 Advanced oxidation progresses (AOPs)

2.4. Heterogeneous catalysts application in AOPs

Chapter 3 to Chapter 8 are the parts devoted to the presentation of the experiments results.

Chapter 3 is entitled "Ionic liquid mediated α-Fe_2O_3 shape-controlled nanocrystals supported noble metal: highly active materials for CO oxidation". Shape-controlled iron oxide nanocrystals were prepared using an original ionic liquid mediated process. Differences in morphology and textural properties result in largely different oxygen mobility, the porous nanorods presenting the highest bulk oxygen mobility. In addition, the favorable physical properties, *i.e.* high surface area, allow the easy dispersion of noble metal nanoparticles (Pt, Pd, and Au), some of these noble metal-containing high surface area materials exhibiting remarkable catalytic activities.

Chapter 4 is entitled "Design of a highly efficient AOP process using an ultrasound-assisted, heterogeneous Fenton-like reaction: example of tetracycline degradation over a commercial magnetite catalyst". This part focused on the degradation of tetracycline over magnetite materials under ultrasound assisted Fe_3O_4/ H_2O_2 process. The effects of the reaction parameters, the evolution of the toxicity of the effluent, and the reaction mechanism were studied. A novel membrane separation system was used to explore the surface oxidation mechanism. Surface hydroxyl radicals were evidenced to be the main reactive species for the oxidation process.

Chapter 5 is entitled "Ultrasound enhanced heterogeneous activation of peroxydisulfate by magnetite catalyst for the degradation of tetracycline in water". In this chapter, the removal of tetracycline in the US/Fe_3O_4/$Na_2S_2O_8$ process was investigated. The effects of different operation parameters were investigated ($Na_2S_2O_8$ concentration, catalyst dosage, ultrasonic power, initial concentration of pollutant and initial pH). The roles of sulfate radicals, hydroxyl radicals and superoxide radicals were studied to go insight the catalytic mechanism.

Chapter 6 was named "Ultrasound-enhanced magnetite catalytic ozonation of tetracycline in water". In this section, commercial magnetic particles, Fe_3O_4, were

selected as the catalyst to evaluate its catalytic activity with ozone. Tetracycline (TC) was chosen as the target contaminant compound. An air-lift reactor was used owing to its efficient mixing with low shear stress and energy consumption and it provides the advantage of a high rate of gas-liquid mass transfer. Comparative experiments were performed to investigate the degradation efficiencies and removal rates of TC, including experiments with ozonation alone, ultrasound-enhanced ozonation (US/O_3), catalytic ozonation (Fe_3O_4/O_3), and ultrasound-enhanced catalytic ozonation ($US/Fe_3O_4/O_3$). The effects of the operating conditions on the removal of TC during the ultrasound-enhanced catalytic ozonation process were investigated. The mineralization and the variation of biodegradability and toxicity were also investigated. The solubility and the reusability of the catalyst were critical parameters that were also evaluated.

Chapter 7 is entitled "Shape-controlled nanostructured magnetite-type materials as highly efficient Fenton catalysts". In this study, magnetite materials were synthesized with different morphologies. The oxidation of phenol on the surface of magnetite has been investigated under various experimental conditions (initial pH, H_2O_2 concentration, material loading). Further activity improvement was achieved optimizing the Fe^0/Fe_3O_4 balance through reduction temperature.

Chapter 8 is named "A generic route to produce perovskite with improved oxygen transfer properties: to the design of highly active oxide catalysts". In this study, the successfully synthesis of crystalline $LaMO_3$ (M= Co, Mn) nanomaterials was reported. The results obtained for the oxygen exchange reaction showed that the activity was strongly influenced by the crystal size and surface accessibility. These observations correlated well with the evolution of catalytic activity for phenol conversion and low temperature CO oxidation. Indeed, the benzyl-derived materials showed large improvement in catalytic activity compared to classical materials.

Finally, *Chapter 9* provides the general conclusions and recommendations.

References:

[1] F. Mijangos, F. Varona, N. Villota, Changes in solution color during phenol oxidation by Fenton reagent, Environ. Sci. Technol. 2006 (40) 5538-5543.

[2] S. Esplugas, J. Giménez, S. Contreras, E. Pascual, M. Rodríguez, Comparison of different advanced oxidation processes for phenol degradation , Water Res. 2002 (36) 1034-1042.

[3] A. Santos, P. Yustos, A. Quintanilla, S. Rodríguez, F. García-Ochoa, Route of the catalytic oxidation of phenol in aqueous phase, Appl. Catal. B: Environ. 2002 (39) 97-113.

[4] D.L. Sedlak, A.W. Andren, Oxidation of chlorobenzene with Fenton reagent, Environ. Sci. Technol. 1991 (125) 777-782.

[5] F.J. Potter, J.A. Roth, Hazard. Oxidation of chlorinated phenols using Fenton reagent , Waste Hazard. Mater. 1993(10) 151-170.

[6] E. Neyens, J. Baeyens, A review of classic Fenton's peroxidation as an advanced oxidation technique, J. Hazard. Mater. 2002 (B98) 33-50.

[7] E. Chamarro, A. Marco, S. Esplugas, Use of Fenton reagent to improve organic chemical biodegradability, Water Res. 2001 (35) 1047-1051.

[8] W.P. Kwan, B.M. Voelker, Rates of hydroxyl radical generation and organic compound oxidation in mineral-catalyzed Fenton-like systems, Environ. Sci. Technol. 2003 (37) 1150-1158.

[9] A.L.T. Pham, F.M. Doyle, D.L. Sedlak, Inhibitory effect of dissolved silica on the H_2O_2 decomposition by iron (III) and manganese (IV) oxides: implications for H_2O_2-based in situ chemical oxidation, Environ. Sci. Technol. 2011 (46) 1055-1062.

[10] C. Cuypers, T. Grotenhuis, K.G.J. Nierop, E.M. Franco, A.D. Jager, W. Rulkens, Amorphous and condensed organic matter domains: the effect of persulfate oxidation on the composition of soil/sediment organic matter, Chemosphere 48 (2002) 919-931.

[11] R.E. Huie, C.L. Clifton, P. Neta, Electron transfer reaction rates and equilibria of the carbonate and sulfate radical anions, Radiat. Phys. Chem. 1991 (38) 477-481.

[12] G.P. Anipsitakis, D.D. Dionysiou, Radical generation by the interaction of transition metals with common oxidants, Environ. Sci. Technol. 2004 (38) 3705-3712.

[13] N.C. Shang, Y.H. Yu, H.W. Ma, C.H. Chang, M.L. Liou, Toxicity measurements in aqueous solution during ozonation of mono-chlorophenols, J. Environ. Manage. 78 (2006) 216–222.

[14] R.F. Dantas, M. Canterino, R. Marotta, C. Sans, S. Esplugas, R. Andreozzi, Bezafibrate removal by means of ozonation: primary intermediates, kinetics, and toxicity assessment, Water Res. 41 (2007) 2525–2532.

[15] R.H. Huang, B.Y. Lan, Z.Y. Chen, H.H. Yan, Q.Y. Zhang, J.H. Bing, L.S. Li, Catalytic ozonation of *p*-chlorobenzole acid over MCM–41 and Fe loaded MCM-41, Chem. Eng. J. 180 (2012) 19–24.

[16] C.V. Gómez-Pacheco, M. Sánchez-Polo, J. Rivera-Utrilla, J. López- Peñalver, Tetracycline removal from waters by integrated technologies based on ozonation and biodegradation, Chem. Eng. J. 178 (2011) 115–121.

[17] G. Moussavi, M. Mahmoudi, Degradation and biodegradability improvement of the reactive red 198 azo dye using catalytic ozonation with MgO nanocrystals, Chem. Eng. J. 152 (2009) 1–7.

[18] R. Keykavoos, R. Mankidy, H. Ma, P. Jones, J. Soltan, Mineralization of bisphenol A by catalytic ozonation over alumina, Sep. Purif. Technol. 107 (2013) 310–317.

[19] P. Pocostales, P. Álvarez, F.J. Beltrán, Catalytic ozonation promoted by alumina-based catalysts for the removal of some pharmaceutical compounds from water, Chem. Eng. J. 168 (2011) 1289–1295.

[20] J. Akhtar, N.S. Amin, A. Aris, Combined adsorption and catalytic ozonation for removal of sulfamethoxazole using Fe_2O_3/CeO_2 loaded activated carbon, Chem. Eng. J. 170 (2011) 136–144.

[21] J. Ma, M.H. Sui, T. Zhang, C.Y. Guan, Effect of pH on MnO_x/GAC catalyzed ozonation for degradation of nitrobenzene, Water Res. 39 (2005) 779–786.

[22] T. Zhang, C.J. Li, J. Ma, H. Tian, Z.M. Qiang, Surface hydroxyl groups of synthetic α-FeOOH in promoting $^{\bullet}OH$ generation from aqueous ozone: property and activity relationship, Appl. Catal. B: Environ. 82 (2008) 131–137.

[23] F.J. Beltrán, F.J. Rivas, R. Montero-de-Espinosa, Ozone-enhanced oxidation of oxalic acid in water with cobalt catalyst. 2. Heterogeneous catalytic ozonation, Ind. Eng. Chem. Res. 42 (2003) 3218–3224.

[24] Y.M. Dong, H.X. Yang, K. He, S.Q. Song, A.M. Zhang, β-MnO_2 nanowires: A novel ozonation catalyst for water treatment, Appl. Catal. B: Environ. 85 (2009) 155–161.

[25] F.J. Rivas, M. Carbajo, F. Beltrán, O. Gimeno, J. Frades, Comparison of different advanced oxidation processes (AOPs) in the presence of perovskites, J. Hazard. Mater. 155 (2008) 407–414.

[26] Y.M. Dong, K. He, B. Zhao, Y. Yin, L. Yin, A.M. Zhang, Catalytic ozonation of azo dye active brilliant red X-3B in water with natural mineral brucite, Catal. Commun. 8 (2007) 1599–1603.
[27] H.W. Chen, Y.L. Kuo, C.S. Chiou, S.W. You, C.M. Ma, C.T. Chang, Mineralization of reactive Black 5 in aqueous solution by ozone/H_2O_2 in the presence of a magnetic catalyst, J. Hazard. Mater. 174 (2010) 795–800.
[28] H. Zhao, Y.M. Dong, G.L. Wang, P.P. Jiang, J.J. Zhang, L. Wu, K. Li, Novel magnetically separable nanomaterials for heterogeneous catalytic ozonation of phenol pollutant: $NiFe_2O_4$ and their performances, Chem. Eng. J. 219 (2013) 295–302.
[29] H. Liu, B. Qing, X. Ye, Q. Li, K. Lee, Z. Wu, Boron adsorption by composite magnetic particles, Chem. Eng. J. 151 (2009) 235–240.
[30] Y. Wang, H. Zhang, L. Chen, Ultrasound enhanced catalytic ozonation of tetracycline in a rectangular air-lift reactor, Catal. Today 175 (2011) 283–292.
[31] A. Lv, C. Hu, Y.L. Nie, J.H. Qu, Catalytic ozoantion of toxic pollutants over magnetic cobalt and manganese co-doped γ-Fe_2O_3, Appl. Catal. B: Environ. 100 (2010) 62–67.
[32] A.H. Lv, C. Hu, Y.L. Nie, J.H. Qu, Catalytic ozonation of toxic pollutants over magnetic cobalt-doped Fe_3O_4 suspensions, Appl. Catal. B: Environ. 117–118 (2012) 246-252.
[33] L. Zhao, J. Ma, X.D. Zhai, Enhanced mechanism of catalytic ozonation by ultrasound with orthogonal dual frequencies for the degradation of nitrobenzene in aqueous solution, Ultrason. Sonochem. 17 (2010) 84–91.
[34] B. Neppolian, J.S. Park, H. Choi, Effect of Fenton-like oxidation on enhanced oxidative degradation of *para*-chlorobenzoic acid by ultrasonic irradiation, Ultrason. Sonochem. 11 (2004) 273–279.
[35] H. Zhang, Y.L. Lv, F. Liu, D.B. Zhang, Degradation of CI acid orange 7 by ultrasound enhanced ozonation in a rectangular air-lift reactor, Chem. Eng. J. 138 (2008) 231–238.
[36] J.K. Kim, F. Martinez, I.S. Metcalfe, The beneficial role of use of ultrasound in heterogeneous Fenton-like system over supported copper catalysts for the degradation of *p*-chlorophenol, Catal. Today 124 (2007) 224–231.
[37] Y. Wang, H. Zhang, L. Chen, S. Wang, D.B. Zhang, Ozonation combined with ultrasound for the degradation of tetracycline in a rectangular air-lift reactor, Sep. Purif. Technol. 84 (2012) 138–146.
[38] F. Baquero, J.L. Martinez, R. Canton, Antibiotics and antibiotic resistance in water environments, Current Opin. Biotechnol. 19 (2008) 260-265.

Chapter 2. Literature review

2.1 Pharmaceuticals and personal care products (PPCPs)

In recent years, pharmaceuticals and personal care products (PPCPs) were defined as a class of pollutants, which refered to any product used by individuals for personal health care or cosmetic or used by livestock for health or growth. PPCPs are comprised of thousands of chemical substances, including prescription and nonprescription, "over−the–counter" (OTC) therapeutic drugs, veterinary drugs, fragrances, lotions, and cosmetics [1]. Many of the drugs, which pertain to the human usage, also pertain to the veterinary usage, especially for antibiotics and steroids. A list of the PPCPs covered in this literature review, together with their chemical names, structures, and resources, modified from Daughton et al [6], is presented in Table 2-1.

These classes of PPCPs are present in the waterbodies influenced by raw sewage, including rivers, seas, atmospheres, ground water, and the source of drinking water. Some researchers suggest that some kind of PPCPs may cause ecological harm and have adverse effect on the human health [1–6]. Here, interest for PPCPs is related to: (1), their large usage in the human activity (e.g. bathing, shaving, and swimming), illicit drugs, veterinary drugs (antibiotics and steroids), agribusiness, the residences of pharmaceutical manufacturing, and the residences of hospitals [2–4]; (2), these substances can be adsorbed to sludge during wastewater treatment [5]; (3), the risks posed to aquatic environment and humans that are uncertain; (4) the number of PPCPs that is increasing in the aquatic environment and drinking water.

Among these compounds, tetracyclines (TCs) are one of the most widespread antibiotics currently prescribed for the treatment of urinary infection. Tetracycline (TC) is an antibiotic type of TCs that has been identified along with other pharmaceuticals in sewage treatment plants effluents at the concentrations ranged from ng L^{-1} to mg L^{-1}. However, the municipal sewage treatment plants are not equipped specifically for PPCPs, or other unregulated contaminants removal [2]. A typical case is that of tetracycline.

Table 2-1 PPCPs identified in environmental samples

Therapeutic class	Compounds	CAS name	CAS No., Formula Formula Weight (FW)	Concentrations after treated by Publicly Owned Treatment Works (POTW), surface waters and in sewages (μg L^{-1})
Analgesic/anti-inflammatory	Acetaminophen	*N*-(4-Hydroxyphenyl)acetamide;	103-90-2 151.17 $C_8H_9NO_2$	POTW Max.: 6.0
	Acetylsalicylic acid	2-(Acetyloxy)benzoic acid (Aspirin)	50-78-2 180.16 $C_9H_8O_4$	POTW max.: 1.5 Surface waters: 0.34 Sewage effluent: 1
Beta-blocker	Betaxolol	1-[4-[2-(Cyclopropylmethoxy) ethyl]-phenoxy]-3-[(1-methyl-ethyl)amino]-2-propanol	63659-18-7 307.43 $C_{18}H_{29}NO_3$	POTW max.: 0.19 Surface waters: 0.028
	Bisoprolol	1-[4-[[2-(1-Methylethoxy)-ethoxy] methyl]phenoxy]-3-[(1-methylethyl)amino]-2-propanol	66722-44-9 325.45 $C_{18}H_{31}NO_4$	POTW max.: 0.37 Surface waters: 2.9
Lipid regulator	Bezafibrate	2-[4-[2-[(4-Chlorobenzoyl)-amino]ethyl]phenoxy]-2-methylpropanoic acid	41859-67-0 361.82 $C_{19}H_{20}ClNO_4$	POTW max.: 4.6 Surface waters: 3.1 Sewage: 1.2 (Brazilian)
	Clofibrate	2-(4-Chlorophenoxy)-2-methyl-propanoic acid ethyl ester	637-07-0 242.70 $C_{12}H_{15}ClO_3$	River water : ~40 ng L^{-1}
Antiseptic, fungicide	Biphenylol	2-Biphenylol 2-Hydroxydiphenyl	90-43-7 170.21 $C_{12}H_{10}O$	POTW max.: 2.6 (Germany)
	4-Chlor-3,5-xylenol	4-Chloro-2-(phenylmethyl)phenol; (*o*-Benzyl-*p*-chlorophenol)	88-04-0 156.61 C_8H_9ClO	POTW max. : 0.71
Analgesic ; antiepileptic	Carbamazepine	5*H*-Dibenz[b,f]azepine-5-carboxamide	298-46-4 236.27 $C_{15}H_{12}N_2O$	POTW max. : 6.3 Surface waters : 1.1
B-Sympathomimetic (bronchodilator)	Clenbuterol	4-Amino-3,5-dichloro-α-[[(1,1-dimethylethyl)amino]-methyl]benzenemethanol	37148-27-9 242.70 $C_{12}H_{18}Cl_2N_2O$	POTW max. : 0.08 (effluent) Surface waters : 0.05

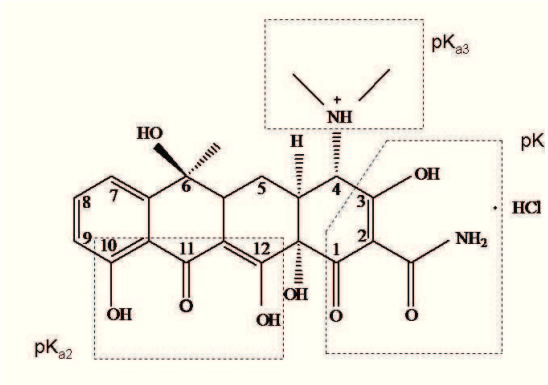
Antineoplastic	Cyclophosphamide	*N,N*-Bis(2-chloroethyl)tetra-hydro-2*H*-1,3,2-oxazaphos-phorin-2amine-2-oxide; e.g., Cycloblastin	50-18-0 261.09 $C_7H_{15}Cl_2N_2O_2P$	POTW max. effluent : 0.02 Hosptial sewage : 146 ng L^{-1}
X-Ray contrast media	Diatrizoate (Na)	3,5-Bis(acetylamino)-2,4,6-tri-lodobenzoic acid sodium salt	737-31-5 635.90 $C_{11}H_8I_3N_2NaO_4$	Surface waters : 0.23 (German)
	Iopromide	*N,N*' –Bis(2,3-dihydroxypropyl)-2,4,6-triiodo-5-[(methoxyacetyl)amino]-N-methyl-1,3-benzenedicarboxamide	73334-07-3 791.12 $C_{18}H_{24}I_3N_3O_8$	Sewage treatment plants: 11 (effluents)
Psychiatric drug	Diazepam	7-Chloro-1,3-dihydro-1-methyl-5-phenyl-2*H*-1,4-benzodiazepin-2-one	439-14-5 284.74 $C_{16}H_{13}ClN_2O$	POTW max. : 0.04
	Sulfonamides	Large class; e.g., Sulfomamethoxazole	723-46-6 253.48 $C_{10}H_{11}N_3O_3S$	landfill leachates: 0.04-6.47 mg L^{-1} on beneath and declining depending on depth and distance along plume
Antibiotics	Tetracyclines	Large class; e.g., Tetracycline hydrochloride	480.9 $C_{22}H_{25}N_2O_8Cl$	
	Fluoroquinolone carboxylic acids	Large class ; e.g., ciprofloxacin	e.g., 85721-33-1 331.35 $C_{17}H_{18}FN_3O_3$	Strongly sorbs to soil, highly active in hospital wastewaters
Oral contraceptive	17α-Ethinyl estradiol		57-63-6 296.41 $C_{20}H_{24}O_2$	POTW effluent: 7 ng L^{-1} Surface waters: 0.5 ng L^{-1} (German)
Sympathomimetic amine (anorexic)	Fenfluramine	*N*-Ethyl-α-methyl-3-[trifluoro-methyl] benzeneethanamine	458-24-2 231.26 $C_{12}H_{16}F_3N$	
Metabolite of acetylsalicylic acid	Gentisic acid	2,5-Dihydroxybenzoic acid	487-54-7 195.17 $C_9H_9NO_4$	POTW max.: 0.59 Surface waters: 1.2
Sunscreen agent	Methylbenzylidene camphor	3-(4-Methylbenzyliden) camphor	36861-47-9 254.37 $C_{18}H_{22}O$	Bioconcentrated in roach from German lakes

Musks fragances (synthetic)	galaxolide	1,3,4,6,7,8-Hexahydro-4,6,6,7,8,8-hexamethyl-cyclopenta-(g)-a-benzopyrane	1222-05-5 258.40 $C_{18}H_{26}O$	36-152 ng L^{-1}
	Tonalide (AHTN) (a polycyclic musk)	7-Acetyl-1,1,3,4,4,6-hexa-methyltetraline	1506-02-1 258.40 $C_{18}H_{26}O$	24-88 ng L^{-1}
	Celestolide (ADBI) (a polycyclic musk)	4-Acetyl-1,1-dimethyl-6-*tert*-butylindane	13171-00-1 244.38 $C_{17}H_{24}O$	2-8 ng L^{-1}

2.1.1 Physical and chemical properties – in case of tetracycline

To investigate the fate and transformation of PPCPs in the environment, we choose tetracycline (TC), which is a large group of antibiotics largely used in human beings and living stocks. As it is show in the Table 2-2, TC contains three functional groups: tricarbonylamide, phenolic diketone and a dimethylamine group [7]. The function group has three different pK_a values (3.3, 7.7, 9.7). When the pH was below 3.3 (pK_{a1}), TC is in its protonated form. With the increase of pH, deprotonation reaction takes place, and a zwitterion form of TC is present. Moreover, the fraction of TCH^- is the primary TC form while pH was increased to 9.0 [9].

Table 2-2. Chemical structures and relevant data for tetracycline hydrochloride

Name	Tetracycline hydrochloride
Formula	$C_{22}H_{25}N_2O_8Cl$
Structure	
Formula Weight (g mol^{-1})	480.9
λ (nm)	359, 270
pK_a	3.3, 7.68, 9.7

2.1.2 Sources and occurrences – in case of tetracycline

As one group of antibiotics, TC exhibits activity against a wide range of gram-positive and gram-negative bacteria, atypical organisms such as chlamydia, protozoan parasites. The favorable antimicrobial properties of TC and the absence of major adverse side effects have led to its extensive usage in the human therapy and livestock production. However, only 20%-50% were absorbed by human and animals, and excess returns to the environment via feces and urine. Therefore, TC is widely spread in the environment via municipal and industrial wastewater effluent, wastewater sludge and agricultural runoff [10]. Even, it was reported that TC was detected in milk [11].

During the therapeutic use of TC, up to the concentration of 200 mg tetracycline per kg slurry can be anticipated [12]. In U.S., Geological Survey reports the maximum concentration of TC on the surface water is 0.11 μg L^{-1} [13]. In Germany, the concentration of TC is around 100 μg kg^{-1} in agricultural fields [14]. Also, in municipal wastewater, 4 μg L^{-1} TC was detected in Germany [15]. In Canada, the average concentration of TC is 0.15 μg L^{-1} in the wastewater treatment plants (WTP) [16], indicating that the concentration of TCs in the aqueous water is at a trace level.

2.1.3 Environmental toxicity – in case of tetracycline

Although TC was in trace level, it may cause ecological damage to the environment [17]. Beside the direct toxicity to microorganisms [18], the acute and chronic toxic effects of TC on non-target organisms (such as diatoms, algae, crustaceans) are also reported. The acute toxicity toward *D. magna* is measured, and the values of EC_{50} and NOEC are 1000 mg L^{-1} (48 h) and 340 mg L^{-1} for oxytetracycline and tetracycline, respectively [19]. The EC_{50} values (chronic toxicity) with *D. magna* are 46.2 mg L^{-1} and 44.8 mg L^{-1} for oxytetracycline and TC, respectively [20,21]. Moreover, the intermediates of TC have the similar toxicity or are even more toxic than its parent form [22].

2.1.4 Treatment methods – in case of tetracycline

Generally, physi/adsorption and biodegradation processes are developed for the aqueous water and wastewater treatment. Adsorption methods, as the main conventional elimination processes, use adsorbents (activated carbon, metal ions, reverse osmosis *etc*.) to remove TCs from the aqueous phase to the solid phase (adsorbents). However, the elimination is site specific, and it cannot be relied upon on a global basis. Moreover, the structure of TC was not destructed.

Biodegradation method is another tool for TC removal. However, only partially PPCPs are eliminated by the conventional sewage treatment plant (STP), and it is inefficient for antibiotics removal [1]. Consequently, rest of the TC is directly discharged into the surface water and soil. The development of some novel methods to decrease the TC contents in the environment is then urgent.

Advanced oxidation processes (AOP) are considered good alternatives to the adsorption and biodegradation techniques. Among the various AOPs proposed in the literature, four main kinds can be distinguished [23]: (1) Photolysis (UV, VUV); (2) Ozonation (O_3, US/O_3, H_2O_2/O_3, catalytic ozonation etc.); (3) Hydrogen peroxide

(H_2O_2) (Fenton/Fenton-like/Photo-Fenton); (4) photocatalysis (homogenous or heterogeneous photocatalysis).

2.2 Phenolic organic compounds

Phenols, sometimes called phenolic organic compounds, are a class of chemical compounds consisting of a hydroxyl group (-OH) bonded directly to an aromatic hydrocarbon group. The simplest of the class is phenol also called as carbolic acid C_6H_5OH. Phenolic compounds are classified as simple phenols or polyphenols based on the number of phenol units in the molecule.

Phenols organic compounds exist in the environment in the areas of chemical, petroleum, and pharmaceutical industries. The compounds penetrate ecosystems via the municipal or industrial sewage [24]. Moreover, the occurrence of phenols in the environment stems from the numerous pesticides production and usage. The concentrations of phenol in surface water vary. In natural waters, its amounts are between 0.01-2.0 μg L^{-1} [24]. Phenol is also present in food, and the moderate concentration is 5 μg Kg^{-1} in honey [24]. Sometimes, transformation processes lead to its toxicity increase by the formation of electrophilic metabolites that may bind and damage DNA or enzymes. The noxious influence of phenols and their derivatives concerns acute toxicity, histopathological changes, mutagenicity and carcinogenicity [24].

Phenol irritates skin and causes its necrosis, it dam-ages kidneys, liver, muscle and eyes. Acute poison with phenol is characterized by dryness in throat and mouth, dark-colored urine and strong irritation of mucous membranes. In addition, the chronic toxicity of phenol leads to pathological changes in skin, esophagus, lungs, liver, kidneys and also urogenital tract. However, the municipal sewage treatment plants are not efferent to removal phenolic compounds.

2.3 Advanced oxidation processes (AOPs)

Advanced oxidation processes (AOPs), is a set of chemical treatment procedures designed to remove the organic pollutants in water or wastewater by oxidation through reactions with hydroxyl radicals ($^{\bullet}OH$). These reactive species are strong oxidants that can be applied in water and can virtually oxidize the pollutants in the water matrix. Consequently, $^{\bullet}OH$ reacts with the contaminants quickly, efficiently and

unselectively, leading to the mineralization of the pollutants. Hydroxyl radicals are produced with the help of one or more primary oxidants (e.g. hydroxyl peroxide, persulfate ions, and ozone), energy sources (*i.e.* UV, ultrasound) or catalysts in homogenous forms or heterogeneous forms (*i.e.* ferrous ions, titanium dioxide, and iron oxide). Precisely, the aim of these regents or processes combinations is to increase the production of $^{\bullet}OH$. Generally, when they apply in properly operation conditions, AOPs can reduce the concentrations of organic pollutants from trace quantity ppm to less than 5 ppb. Thus, the value of chemical oxygen demand (COD) and total organic carbon (TOC) are decreased, accordingly. They are considered as the promising processes for the water treatment in 21st century [25].

2.3.1 Fenton process

Fenton process (Fenton reagent: (Fe^{2+}/H_2O_2) as one of the AOPs has been proved to be a promising and attractive treatment method for the degradation of a large number of hazardous and organic pollutant [26-30]. These processes can generate free hydroxyl radical, a strong oxidant capable of reacting with practically almost all types of organic and inorganic compounds [26,27,31,32].

The generally accepted free radical mechanism for the classical homogeneous chain reaction involves the following steps [33]:

$$H_2O_2 + Me^n \rightarrow Me^{n+1} + {}^{\bullet}OH + OH^- \quad (2\text{-}1)$$

$$H_2O_2 + Me^{n+1} \rightarrow Me^n + {}^{\bullet}HO_2 + H^+ \quad (2\text{-}2)$$

$$^{\bullet}OH + Me^n \rightarrow Me^{n+1} + OH^- \quad (2\text{-}3)$$

$$Me^{n+1} + {}^{\bullet}HO_2 \rightarrow Me^n + O_2 + H^+ \quad (2\text{-}4)$$

$$Me^n + {}^{\bullet}HO_2 + H^+ \rightarrow Me^{n+1} + H_2O_2 \quad (2\text{-}5)$$

$$^{\bullet}HO_2 + {}^{\bullet}HO_2 \rightarrow H_2O_2 + O_2 \quad (2\text{-}6)$$

where Me represents the transition metals (Fe, Co, and Mn), and n represents the valence state.

Although the classic homogenous catalyst system is highly efficient, it operates at strict pH levels to prevent the precipitation of metal ions, and extra metal ions are considered pollution after treatment, thus limiting widespread application. Unlike the traditional homogenous catalysts, heterogeneous catalysts, with hydrogen peroxide, can effectively oxidise organic compounds at a wide pH range. However, we found that the catalytic activity of pure metal oxides (Fe_2O_3, MnO_2, etc.) was not effective in

degrading organic compounds; organics were only slightly degraded at slow rate in H_2O_2/Fe_2O_3, and H_2O_2/MnO_2 systems. Due to weak catalytic activity, heterogeneous catalysts often require the support of other advanced oxidation technologies, such as UV or ultrasound, to enhance the reaction rate.

2.3.2 Persulfate oxidation process

As mentioned above, traditional AOPs are some kinds of $^{\bullet}OH$ based technology, aiming to degrade organic compounds. More recently, another kind of AOPs, named persulfate oxidation process is considered as the active species, earn great concern. The similar structure of O-O bond were both contained in H_2O_2 and $S_2O_8^{2-}$ [34], and it can be decomposed to $SO_4^{-\bullet}$ radicals. $SO_4^{-\bullet}$ has a high oxidation potential (E_0= 2.6 V *vs* NHE) that is similar to $^{\bullet}OH$ (E_0= 2.73 V *vs* NHE) [35]. In addition, $Na_2S_2O_8$ is a strong and stable oxidizing agent (E_0=2.01 V *vs* NHE) and it has high aqueous solubility as compared to hydrogen peroxide (H_2O_2) [36]. Therefore, the organic compounds can be degraded completely by $SO_4^{-\bullet}$, especially benzene derivatives substances [37]. $S_2O_8^{2-}$ has to be effectively activated to generate $SO_4^{-\bullet}$ when it is activated by using ultraviolet light, heat or transition metal (Fe^{2+}, Co^{2+}) [38-41] or heterogeneous metal oxide (Zero-valent iron, supported cobalt catalysts, and iron–cobalt mixed oxide). All the reactions were based on the irradiation can generate $SO_4^{-\bullet}$ [42].

$$S_2O_8^{2-} + UV/Heat \rightarrow SO_4^{-\bullet} + SO_4^{2-} \quad (2\text{-}7)$$

Commonly, transition metal ions (Fe^{2+}, Co^{2+} etc.) were employed as activator for $Na_2S_2O_8$ in situ chemical oxidation due to its abundance in soil and sediment and environmentally friendly nature [38-40]. In the presence of metal ions, $S_2O_8^{2-}$ can be activated to produce $SO_4^{-\bullet}$, as depicted by the following equation [41].

$$S_2O_8^{2-} + Me^{n+} \rightarrow SO_4^{-\bullet} + SO_4^{2-} + Me^{(n+1)} \quad (2\text{-}8)$$

where Me represents the transition metals (Fe^{2+}, Co^{2+}), and n represents the valence state.

$SO_4^{-\bullet}$ normally reacts through electron transfer process, which is similar to the production of $^{\bullet}OH$ in Fenton process. Like classical Fenton process, the use of homogeneous iron catalysts as an activator is limited by the slurry system, the requirement of acid and high metal (iron or other transition metal) concentrations in the final effluent would raise the complexity and the costs of the process. To

overcome these drawbacks, cobalt catalyst, supported cobalt catalyst and zero-valent iron were introduced for the heterogeneous activation [35, 43-45].

In recent years, it was found that ultrasound treatment also could act as the activator of $S_2O_8^{2-}$, as can be seen by the equation below. It indicated that the use of $S_2O_8^{2-}$ for the initiation of oxidation process around room temperature is viable [46,47].

$$S_2O_8^{2-} +))) \rightarrow SO_4^{2-} + SO_4^{-\bullet} \quad (2\text{-}9)$$

In addition, during ultrasound irradiation, the collapse of cavitation bubbles induces localized high temperatures and pressures, which allows the formation of oxidizing species, such as $^{\bullet}OH$, superoxide radical ($O_2^{-\bullet}$) and H_2O_2. Therefore, the combination of ultrasound with heterogeneous oxidation reaction is a convenient approach in the degradation of organic compounds [47].

2.2.3 Catalytic ozonation process

Ozone is a powerful oxidizing molecule that can either react with organic pollutants directly or indirectly to produce free radicals. However, the high level of mineralization and toxicity removal cannot be achieved by using ozone alone [48,49]. Moreover, the high implementation cost and the poor mass transfer rate lead to the limitations of ozone use. To overcome these drawbacks, catalytic ozonation to improve degradation efficiency has emerged [50-53]. It has become a powerful treatment method for the degradation of refractory organic pollutants, leading to high removal and mineralization of the organic compounds.

Catalytic ozonation can be divided into the following sub-techniques, which facilitate ozone decomposition and the production of hydroxyl radicals [54]:

- *Homogeneous catalytic ozonation: ozone decomposition is initiated by transition metal ions.*
- *Heterogeneous catalytic ozonation: ozone decomposition is initiated by solid catalysts.*

For the homogenous catalytic ozonation, two major reaction mechanisms can be found in the literature [54]: 1) the decomposition of ozone by metal ions can enhance the generation of hydroxyl radicals; 2) A complex is formed between the organic compounds and metal ions, and subsequent oxidation of the complex occurs by ozone. Hence, the operating parameters, such as pH, catalyst concentration, and ozone

concentration, are essential for the catalytic reaction. However, the homogenous catalysts, used in the oxidation process, are difficult to be recycled, which limit their applications in wastewater treatment.

Compared with the homogeneous catalytic ozonation process, the heterogeneous catalytic ozonation has attractive advantages such as catalyst reusability, high mineralization degree and no secondary pollutants [52,53,55,56]. The catalysts include MgO [52], alumina [53], alumina based catalysts [55], activated carbon supported catalyst (MnO_x/GAC) [57], α-FeOOH [58], cobalt oxides [59], β-MnO_2 [60], perovskite [61], and brucite [62]. For the heterogeneous catalytic ozonation, there are three primary reaction mechanisms governing the catalytic ozone decomposition [54]: 1) Ozone decomposition on oxidized/reduced form of metal oxide or on the surface of the supported metal oxide; 2) decomposition of ozone on Lewis active sites of metal oxides; 3) ozone decomposition on the hydroxyl groups of metal oxides. It can be concluded that all active sites participate to the ozone decomposition.

Despite promising results through heterogeneous catalytic ozonation, the deactivation of the catalyst due to organic intermediates accumulation on the surface of the catalyst is still a major obstacle for its application. In the meanwhile, the release of metal ions decreased the stability and activity of the catalyst. Therefore, the development of an effective approach to improve the catalytic efficiency and durability remains an important issue that needs to be addressed.

It has been found that ultrasound can enhance the activity of the catalyst in the ozonation process without prejudice to the stability of the iron species [63,64]. During the ultrasonic process, the cavitation effect can clean the surface of the catalyst, and the catalyst can thereby present higher stability during the ultrasonic irradiation process [63,66]. In addition, ultrasound accelerates turbulence, which can reduce the liquid film thickness and subsequently increase the mass transfer of reactants and by-products between the liquid and solid phases [66,67]. Furthermore, hydroxyl radicals will be generated in the vapor phase of cavitation bubbles during the ultrasonic process [68,69].

2.4 Iron in heterogeneous catalysis - application in AOPs and oxidation

2.4.1 Iron oxide

Iron oxides are considered as the transition metal oxides, natural minerals and geocatalysts, existing in the natural aqueous environment, and they also suspend in aerosol, clouds, and fogs as fine particles [70,71]. Because iron is inexpensive and relatively nontoxic in comparison to other transition metals (including nickel, chromium, copper), it has been extensively used in different treatment processes, such as corrosion processes, electromagnetic devices [72], and catalytic reactions [73,74]. The versatility of the surface composition among Fe^0, Fe^{II} and Fe^{III} over different types of iron oxides (Fe^0, FeO, α-Fe_2O_3, γ-Fe_2O_3, Fe_3O_4, α-FeOOH, β-FeOOH, γ-FeOOH and δ-FeOOH) ensure tunable properties, conferring to some composition high activity for heterogeneous Fenton reactions at the catalyst / solution interface [10]. Significantly different catalytic activities are then observed depending of the material crystallographic and surface properties, due to variable valences of iron that can be stabilized [10].

Recently, iron compounds (e.g., in the Fenton reaction) have been intensively investigated for environmental applications [76]. For example, Fe^0 has been proposed as a low-cost and nontoxic material in environmental remediation processes [77]. Different iron compounds, such as Fe^0 and Fe_3O_4, have been reported to promote the Fenton reaction [78,79]. Although the kinetics of these processes is highly complex, an important rate-limiting step is the electron transfer from iron compounds to species in aqueous media. In this respect, the oxidation phases on the iron surface and the presence of oxide/hydroxide layers that cover the iron particles should strongly influence the rate of the process [80]. The development of processes to increase the electron transfer rate to improve the efficiency and widen the application of these systems in environmental remediation processes is of great interest.

Magnetite (Fe_3O_4)-based heterogeneous systems have attracted attention due to their unique properties and their potential applications in numerous fields [81-84], including ferrofluids, targeted drug delivery, and water treatment. Magnetite has also been reported to be an efficient catalyst for Fenton-like processes (Table 2-2) [85-97]. Magnetite exhibits several features that are important for a Fenton reaction: (i) it contains Fe^{2+}, which might play an important role as an electron donor to initiate the Fenton reaction; (ii) the octahedral site in the magnetite structure can easily

Table 2-3 Short summaries of recent studies on magnetite nanoparticles for Fenton-like reactions.

Refs.	Fe_3O_4 ressource	S_{BET} ($m^2\ g^{-1}$)	Pollutants	Morphology	Crystal size (nm)	Reaction conditions	Catalytic activity : Converstion/TOC removal	Fe_{tot} leaching (mg L^{-1})
[85]	Fe_3O_4-MWCNTs	-	Acid Orange II (AO7)	nanotubes	4.2-10.0	catalyst: 0.5 g L^{-1}, AO7: 0.25 mmol L^{-1}, H_2O_2: 15 mmol L^{-1}, 30 min, pH: 3.5	X_{AO7}: 94%	-
[86]	Fe_3O_4, co-precipitation of Fe(II) and Fe(III) in basic solutions	67.8	2,4-Dichlorophenol (2,4-DCP)	uniform	10	catalyst:1.0 g L^{-1}, 2,4-DCP 100 mg L^{-1}, H_2O_2: 12 mmol L^{-1}, 180 min, pH: 3.0, T: 30 ^oC	$X_{2,4\text{-DCP}}$: 100% TOC: 51%	0.2=2.5
[87]	Fe_3O_4, commerical, Prolabo (France)	2.4±0.2	Pentachlorophenol (PCP)	uniform	4000± 1000	catalyst:2.0 g L^{-1}, PCP: 50 mg L^{-1}, H_2O_2: 150 mM, 180 min, pH: 7.0, T: 20 ^oC	X_{PCP}: 90%, TOC:60%	<2.8
[88]	Fe_3O_4, coprecipitation method	55.73	Bisphenol A (BPA)	nanoparticles	10-20	catalyst: 585 mg L^{-1}, BPA:20 mg L^{-1}, H_2O_2: 160 mmol L^{-1}, 20 min, pH: 7.0, T= 20 ^oC	X_{BPA}: 100% TOC: 48.5%	0.003
[79]	Fe_3O_4, ultrasonic-assisted reverse co-precipitation method	82.5	Rhodamine B (RhB)	uniform	16.5	catalyst:0.6 g L^{-1}, RhB: 0.02 mmol L^{-1}, H_2O_2: 40 mmol L^{-1}, 60 min, pH: 5.4, T: 40 ^oC	X_{RhB}: 90%	<0.015
[89]	Fe_3O_4, chemical precipitation method	79.65	Reactive Black 5 (RB5)	core-shell	13	catalyst: 0.1 g L^{-1}, RB5: 10 mM, H_2O_2: 10 mM, 180 min, pH: 4.5, T : 25 ^oC	X_{RB5}: 90%	<0.6

[90]	Fe_3O_4, chemical coprecipitation method	-	phenol	quasi-spherical	10	catalyst:5.0 g L^{-1}, phenol: 1 mM, H_2O_2; 1.2 M, 360 min, pH:6-7, T: 25 ^oC	X_{phenol}: 100% TOC: 42.79%	<0.3
[91]	Fe_3O_4, commerical, Nanostructured & Amorphous Materials Inc. (Texas, USA)	48±2	*p*-Nitrophenol (*p*-NP)	quasi-spherical	30	catalyst: 1.5 g L^{-1}, *p*-NP: 25 mg L^{-1}, H_2O_2: 620 mM, 10 h, pH: 7.0, T: 22 ^oC	$X_{P\text{-}NP}$ > 90%	<0.25
[92]	Fe_3O_4, coprecipitation method	-	phenol	uniform	13	catalyst:0.096 g L^{-1}, phenol: 2 mM, H_2O_2:60 mM, 3 h, pH: 3.0, T: 20 ^oC	X_{phenol}: 85% TOC: 35%	-
[93]	Fe_3O_4, commerical, Prolabo (France)	2.4±0.2	Rhodamine B (RhB)	uniform	<5000	catalyst: 2 g L^{-1}, RhB: 20 mg L^{-1}, H_2O_2: 150 mM, 9h, pH: 7.0, T: 20 ^oC	*k*: 0.00326 min^{-1}	0.0015
[93]	Fe_3O_4, commerical, Aldrich Chemical Co.	40	Rhodamine B (RhB)	uniform	<50	catalyst: 2 g L^{-1}, RhB: 20 mg L^{-1}, H_2O_2: 150 mM, 9h, pH: 7.0, T: 21 ^oC	*k*: 0.011 min^{-1}	-
[94]	Fe_3O_4, co-precipitation	5.6	phenol	uniform	20-30	catalyst: 3 g L^{-1}, phenol: 25 mg L^{-1}, H_2O_2: 5 g L^{-1}, 24 h, pH: 7.0, T: 22 ^oC	X_{phenol}: 65%	0.01
[95]	Fe_3O_4, co-precipitation	-	polycyclic aromatic hydrocarbons (PAHs)	uniform	150000-300000	catalyst: 100 g L^{-1}, PAHs: 125 μg g^{-1}, H_2O_2/Fe: 20:1, 48 h, pH: 7.0, T: 25 ^oC	X_{PAHs}: 90%	-

[96]	Fe_3O_4, co-precipitation	-	methylene blue (MB)	uniform	85-112	catalyst: 30 mg, MB : 100 mg L^{-1}, H_2O_2: 0.3 mol L^{-1}, 120 min, pH: 6.0, T: 25 ^oC	X_{MB} : 30% TOC: 25%	-
[97]	Fe_3O_4, impregnation method	67.79	4-chlorophenol (4-CP)	uniform	10	catalyst: 1.0 g L^{-1}, 4-CP: 0.78 mM, H_2O_2: 30 mM, 120 min, pH: 3.0, T: 30 ^oC	$X_{4\text{-}CP}$: 21%	4.9

accommodate both Fe^{2+} and Fe^{3+}, which means that Fe^{2+} can be reversibly oxidized and reduced; and (iii) Fe_3O_4 has peroxidase-like activity and could activate H_2O_2. Table 2-3 showed some recent works about using magnetite in heterogeneous Fenton oxidation process. A wide variety of methods have been reported to synthesize Fe_3O_4 nanoparticles [98-101]. Because the properties of nanomaterials are influenced by their structure, size, and shape [102], the preparation of Fe_3O_4 nanoparticles with different sizes and morphologies is important. Various Fe_3O_4 nanostructures, including nanotubes, nanowires, *etc.* were then recently achieved.

2.4.2 Other iron oxide in environmental catalysis

While magnetite presents high activity for Fenton reactions, the activity of hematite is very low due to the presence of mainly Fe^{III} sites on its surface. However, activity of Fe_2O_3 is interesting for gas phase redox oxidations, such as CO oxidation [103,104]. In the last three decades, the development of the catalytic converters in the United States and Europe highlighted the exceptional activity of noble metals (Pt, Pd, Rh) for low temperature oxidation [105-108]. The specific role of oxides having a high OSC (Oxygen Storage Capacity) such as stabilized ceria and ceria-zirconia, allowing the noble metals to continue to work in cycled conditions, was also highlighted [105,109]. The relative activities of noble metals and base metals for CO oxidation, as reported by Heck and Farrauto [108], show that noble metals are more active than base metals. However, recent developments in α-Fe_2O_3 nanoparticle synthesis (nanobelts, nanotubes, nanoflowers, nanospheres [110-115]) allow improving physical properties, which will favour metal dispersion. In addition, solid exposed planes with high Fe atom concentration will provide more active sites for catalytic reactions. Moreover, activity of Fe_2O_3 alone [116] or after promotion by gold [117] or palladium [118] evidences that noble metal strongly improves catalytic activity. Especially, Au particles supported on reducible transition metal oxides (Fe_2O_3) can exhibit high activity that is ascribed to the activation and supplement of oxygen for the reaction, making this catalyst more active than with other supports

[119]. Unfortunately, iron oxide is conventionally presenting limited surface area, resulting in some difficulties to achieve high noble metal dispersion [117]. Consequently, when gold is dispersed on classical low surface area Fe_2O_3, relatively low catalytic activity is achieved ($T_{50\%}$ CO conversion between 36 and 80 °C over 1 wt.% Au/α-Fe_2O_3, 50 mg of catalyst in a gas mixture of 1 vol.% CO, 20 vol.% O_2 – bal. N_2 at a flow rate of 67 mL min^{-1}). Better dispersions can be logically awaited over high surface area nanostructured supports. In addition, other important factors, such as the size and morphology of the Au particles, the degree of coordinative unsaturation, the oxidation state of Au, *etc.* will play important roles on the activity of Au supported catalysts [120].

2.4.3 Iron in mixed oxide materials, perovskite-based catalyst

Perovskite-based catalysts, of general formula ABO_3, are important heterogeneous catalysts in industry due to their high potential, low cost and flexibility of composition ; they are especially useful in waste gas oxidation or combustion (NO_x, CO and methane) [121-123]. Indeed, some composites have been proposed as potential alternatives to the commercially used noble metals. Among perovskites, cobalt and manganese-based structures were found to be the most useful in the catalytic process due to their great versatility, excellent high-temperature thermal and hydrothermal stability, interesting activity, and low cost of the constituting elements [121,124-126]. More interestingly, in addition to their application in waste gas treatment, perovskites also act as efficient catalysts for wastewater treatment, due to the presence of transition metals with multiple valence states. $BiFeO_3$-type perovskites (BFO) are reported to be good catalysts for oxidative acetylation [127], photocatalysis [128] and catalytic activation of H_2O_2 [129]. A phase-pure layered perovskite (such as $LaNi_3O_{10}$) was employed as a catalyst for the removal of azo dyes [130].

It is known that the redox properties and catalytic performance of perovskites are critically dependent on their physical properties. Generally, conventional methods for

perovskite preparation, such as calcination-milling [122] and citric acid routes, lead to large grain size (*D*), low specific surface area (*SSA*) and poor activity [131,132]. To overcome these limitations, improved synthetic approaches, such as the so-called sol-gel method [122], reactive grinding [133], nanocasting [134] and flame-spray pyrolysis [135], allow achieving higher surface areas (30-50 m^2 g^{-1}) and smaller crystal sizes (< 20 nm). Reactive grinding is sufficient for LaA_xO_3 (Co, Mn) synthesis, but popularisation is largely restricted by the requirement for special equipment [133] Although a simple and efficient route for the preparation of supported nanocrystalline perovskites with sizes below 5 nm was developed by our group [136], it remains a challenge to directly synthesise size-limited and pure nanocrystalline perovskites. Therefore, to find a new way to improve the catalyst activity is of great importance.

References

[1] http://www.epa.gov/ppcp/faq.html#define

[2] Enick, O. V., Moore, M. M. (2007). Assessing the assessments: Pharmaceuticals in the environment. Environ. Impact Assess. Rev., 27 (8), 707-729.

[3] Westerhoff, P., Yoon, Y., Snyder, S., Wert, E. (2005). Fate of endocrine-disruptor, pharmaceutical, and personal care product chemicals during simulated drinking water treatment processes. *Environ. Sci. Technol.* 39 (17), 6649-6663.

[4] Rabiet, M., Togola, A., Brissaud, F., Seidel, J. L., Budzinski, H., Elbaz-Poulichet, F., (2006). Consequences of treated water recycling as regards pharmaceuticals and drugs in surface and ground waters of a medium-sized Mediterranean catchment. Environ. Sci. Technol. 40 (17), 5282-5288.

[5] Segura, P.A., François, M., Gagnon, C., Sauvé, S. (2009). Review of the occurrence of anti-infectives in contaminated wastewaters and natural and drinking waters. Environ. Health Perspec. 117 (5), 675–684.

[6] Daughton, C.G., Ternes, T.A. (1999). Pharmaceuticals and personal care prodcuts in the environment: agents of subtle change? Environ. Health Perspect. 107 (suppl. 6), 907-944.

[7] Vu, B.K., Shin, E.W., Snisarenko, O., Jeong, W.S., Lee, H. S. (2010). Removal of the antibiotic tetracycline by Fe-impregnated SBA-15. Korean J. Chem. Eng. 27(1), 116-120.

[8] Chen, Y., Hu, C., Hu, X., Qu, J. (2009). Indirect photodegradation of amine drugs in aqueous solution under simulated sunlight. Environ. Sci. Technol. 43 (8), 2760-2765.

[9] Sapadin, A.N., Fleischmajer, R. (2006). Tetracyclines: nonantibiotic properties and their clinical implications. J. Am. Academy Dermatol.54 (2), 258-265.

[10] Wang, P., He, Y.L., Huang, C.H. (2010). Oxidation of fluoroquinolone antibiotics and structurally related amines by chlorine dioxide: reaction kinetics, product and pathway evaluation. Water Res. 44 (20), 5989-5998.

[11] Fritz, J.W., Zuo, Y. (2007). Simultaneous determination of tetracycline, oxytetracycline, and 4-epitetracycline in milk by high-performance liquid chromatography. Food Chem. 105 (3), 1297-1301.

[12] Kühne, M., Ihnen, D., Möller, G., Agthe, O. (2000). Stability of tetracycline in water and liquid manure. J. Veterinary Medicine Series A, 47 (6), 379-384.

[13] Kolpin, D.W., Furlong, E.T., Meyer, M.T., Thurman, E.M., Zaugg, S. D., Barber, L.B., Buxton, H.T. (2002). Pharmaceuticals, hormones, and other organic wastewater contaminants in US streams, 1999-2000: A national reconnaissance. Environ. Sci. Technol. 36 (6), 1202-1211.
[14] Pawelzick, H. T., Hoper, H., Nau, H., Hamscher, G. (2004, April). A survey of the occurrence of various tetracyclines and sulfamethazine in sandy soils in northwestern Germany fertilized with liquid manure. In SETAC Euro 14th Annual Meeting (pp. 18-22). Czech Republic: Prague.
[15] Karthikeyan, K. G., Bleam, W. F., Gu, C. (2003). Occurrence of antibiotics in wastewater effluents and their mobility in soils: a case study for Wisconsin. DNR project, 169.
[16] Miao, X.S., Bishay, F., Chen, M., Metcalfe, C.D. (2004). Occurrence of antimicrobials in the final effluents of wastewater treatment plants in Canada. Environ. Sci. Technol. 38 (13), 3533-3541.
[17] Baquero, F., Martínez, J. L., Cantón, R. (2008). Antibiotics and antibiotic resistance in water environments. Current Opin. Biotechnol. 1 9(3), 260-265.
[18] Halling-Sørensen, B. (2000). Algal toxicity of antibacterial agents used in intensive farming. Chemosphere 40 (7), 731-739.
[19] Khetan, S.K., Collins, T.J. (2007). Human pharmaceuticals in the aquatic environment: a challenge to green chemistry. Chem. Rev.-Columbus, 107 (6), 2319-2364.
[20] Wollenberger, L., Halling-Sørensen, B., Kusk, K. O. (2000). Acute and chronic toxicity of veterinary antibiotics to *Daphnia magna*. Chemosphere, 40 (7), 723-730.
[21] di Delupis, G.D., Macrí, A., Civitareale, C., Migliore, L. (1992). Antibiotics of zootechnical use: Effects of acute high and low dose contamination on *Daphnia magna* Straus. Aquatic Toxicology, 22 (1), 53-59.
[22] Halling-Sørensen, B., Sengeløv, G., Tjørnelund, J. (2002). Toxicity of tetracyclines and tetracycline degradation products to environmentally relevant bacteria, including selected tetracycline-resistant bacteria. Archives Environ. Contamination Toxicology, 42 (3), 263-271.
[23] Parsons, S. Advanced oxidation processes for water and wastewater treatment. 2004. London: IWA Pub. xii.
[24] Michalowicz, J. Duda, W. (2007) Phenols-sources and toxicity. Polish J. Environ. Stud. 16 (3), 347-362.
[25] Munter, R. (2001). Advanced oxidation processes–current status and prospects. Proc. Estonian Acad. Sci. Chem, 50 (2), 59-80.
[26] Oliveira, R., Almeida, M. F., Santos, L., Madeira, L. M. (2006). Experimental design of 2, 4-dichlorophenol oxidation by Fenton's reaction. Ind. Eng. Chem. Res. 45 (4), 1266-1276.
[27] Pera-Titus, M., García-Molina, V., Banos, M.A., Giménez, J., Esplugas, S. (2004). Degradation of chlorophenols by means of advanced oxidation processes: a general review. Appl. Catal. B: Environ. 47 (4), 219-256.
[28] Lin, J. G., Ma, Y. S. (2000). Oxidation of 2-chlorophenol in water by ultrasound/Fenton method. J. Enviorn. Eng.126 (2), 130-137.
[29] Ormad, M. P., Ovelleiro, J. L., Kiwi, J. (2001). Photocatalytic degradation of concentrated solutions of 2, 4-dichlorophenol using low energy light: identification of intermediates. Appl. Catal. B: Environ. 32 (3), 157-166.
[30] Sabhi, S., Kiwi, J. (2001). Degradation of 2, 4-dichlorophenol by immobilized iron catalysts. Water Res.35 (8), 1994-2002.
[31] Huling, S. G., Arnold, R. G., Sierka, R. A., Jones, P. K., & Fine, D. D. (2000). Contaminant adsorption and oxidation via Fenton reaction. J. Environ. Eng. 1*26* (7), 595-600.
[32] Sun, Y., Pignatello, J.J. (1993). Photochemical reactions involved in the total mineralization of 2, 4-D by iron (3+)/hydrogen peroxide/UV. Environ. Sci. Technol., 27 (2), 304-310.
[33] Costa, R.C.C., Lelis, M.F.F., Oliveira, L.C.A., Fabris, J.D., Ardisson, J.D., Rios, R.R.V.A., Silva, C.N., Lago, R.M. (2006). Novel active heterogeneous Fenton system based on $Fe_{3-x}M_xO_4$ (Fe, Co, Mn, Ni): the role of M^{2+} species on the reactivity towards H_2O_2 reactions. J. Hazard. Mater. 129 (3), 171-178.
[34] Yan, J., Lei, M., Zhu, L., Anjum, M. N., Zou, J., Tang, H. (2011). Degradation of sulfamonomethoxine with Fe_3O_4 magnetic nanoparticles as heterogeneous activator of persulfate. J. Hazard. Mater. 186 (2), 1398-1404.
[35] Yang, Q., Choi, H., Chen, Y., Dionysiou, D. D. (2008). Heterogeneous activation of peroxymonosulfate by supported cobalt catalysts for the degradation of 2, 4-dichlorophenol in water: The effect of support, cobalt precursor, and UV radiation. Appl.Catal.B: Environ. 77 (3), 300-307.

[36] Cuypers, C., Grotenhuis, T., Nierop, K. G., Franco, E. M., de Jager, A., Rulkens, W. (2002). Amorphous and condensed organic matter domains: the effect of persulfate oxidation on the composition of soil/sediment organic matter. Chemosphere, 48 (9), 919-931.
[37] Neta, P., Madhavan, V., Zemel, H., & Fessenden, R. W. (1977). Rate constants and mechanism of reaction of sulfate radical anion with aromatic compounds. J. Am. Chem. Soc.99 (1), 163-164.
[38] Do, S. H., Jo, J. H., Jo, Y. H., Lee, H. K., & Kong, S. H. (2009). Application of a peroxymonosulfate/cobalt (PMS/Co (II)) system to treat diesel-contaminated soil. Chemosphere 77 (8), 1127-1131.
[39] Anipsitakis, G. P., Dionysiou, D. D. (2004). Radical generation by the interaction of transition metals with common oxidants. Environ. Sci. Technol. 38 (13), 3705-3712.
[40] Rastogi, A., Al-Abed, S. R., Dionysiou, D. D. (2009). Sulfate radical-based ferrous–peroxymonosulfate oxidative system for PCBs degradation in aqueous and sediment systems. Appl. Catal. B: Environ. 85 (3), 171-179.
[41] Kolthoff, I.M., Miller, I.K. (1951). The Chemistry of persulfate. I. The kinetics and mechanism of the decomposition of the persulfate ion in aqueous medium. J. Am. Chem. Soc. 73 (7), 3055-3059.
[42] House, D. (1962). Kinetics and mechanism of oxidations by peroxydisulfate. Chem. Rev. 62 (3), 185-203.
[43] Anipsitakis, G.P., Stathatos, E., Dionysiou, D.D. (2005). Heterogeneous activation of oxone using Co_3O_4. J.Phys. Chem. B, 109 (27), 13052-13055.
[44] Oh, S.Y., Kim, H.W., Park, J.M., Park, H.S., Yoon, C. (2009). Oxidation of polyvinyl alcohol by persulfate activated with heat, Fe^{2+}, and zero-valent iron. J. Hazard. Mater. 168 (1), 346-351.
[45] Zhao, J., Zhang, Y., Quan, X., Chen, S. (2010). Enhanced oxidation of 4-chlorophenol using sulfate radicals generated from zero-valent iron and peroxydisulfate at ambient temperature. Sep. Purif. Technol.71 (3), 302-307.
[46] Price, G.J., Clifton, A.A. (1996). Sonochemical acceleration of persulfate decomposition. Polymer, *37* (17), 3971-3973.
[47] Gayathri, P., Praveena Juliya Dorathi, R., Palanivelu, K. (2010). Sonochemical degradation of textile dyes in aqueous solution using sulphate radicals activated by immobilized cobalt ions. Ultrason. Sonochem., 17 (3), 566-571.
[48] N.C. Shang, Y.H. Yu, H.W. Ma, C.H. Chang, M.L. Liou, Toxicity measurements in aqueous solution during ozonation of mono-chlorophenols, J. Environ. Manage. 78 (2006) 216–222.
[49] R.F. Dantas, M. Canterino, R. Marotta, C. Sans, S. Esplugas, R. Andreozzi, Bezafibrate removal by means of ozonation: primary intermediates, kinetics, and toxicity assessment, Water Res. 41 (2007) 2525–2532.
[50] R.H. Huang, B.Y. Lan, Z.Y. Chen, H.H. Yan, Q.Y. Zhang, J.H. Bing, L.S. Li, Catalytic ozonation of *p*-chlorobenzole acid over MCM–41 and Fe loaded MCM-41, Chem. Eng. J. 180 (2012) 19–24.
[51] C.V. Gómez-Pacheco, M. Sánchez-Polo, J. Rivera-Utrilla, J. López- Peñalver, Tetracycline removal from waters by integrated technologies based on ozonation and biodegradation, Chem. Eng. J. 178 (2011) 115–121.
[52] G. Moussavi, M. Mahmoudi, Degradation and biodegradability improvement of the reactive red 198 azo dye using catalytic ozonation with MgO nanocrystals, Chem. Eng. J. 152 (2009) 1–7.
[53] R. Keykavoos, R. Mankidy, H. Ma, P. Jones, J. Soltan, Mineralization of bisphenol A by catalytic ozonation over alumina, Sep. Purif. Technol. 107 (2013) 310–317.
[54] J. Nawrocki, B. Kasprzy-Hordern, The efficiency and mechanisms of catalytic ozonation, Appl. Catal. B: Environ. 99 (2010) 27-42.
[55] P. Pocostales, P. Álvarez, F.J. Beltrán, Catalytic ozonation promoted by alumina-based catalysts for the removal of some pharmaceutical compounds from water, Chem. Eng. J. 168 (2011) 1289–1295.
[56] J. Akhtar, N.S. Amin, A. Aris, Combined adsorption and catalytic ozonation for removal of sulfamethoxazole using Fe_2O_3/CeO_2 loaded activated carbon, Chem. Eng. J. 170 (2011) 136–144.
[57] J. Ma, M.H. Sui, T. Zhang, C.Y. Guan, Effect of pH on MnO_x/GAC catalyzed ozonation for degradation of nitrobenzene, Water Res. 39 (2005) 779–786.
[58] T. Zhang, C.J. Li, J. Ma, H. Tian, Z.M. Qiang, Surface hydroxyl groups of synthetic α-FeOOH in promoting $^{\bullet}OH$ generation from aqueous ozone: property and activity relationship, Appl. Catal. B: Environ. 82 (2008) 131–137.
[59] F.J. Beltrán, F.J. Rivas, R. Montero-de-Espinosa, Ozone-enhanced oxidation of oxalic acid in water with cobalt catalyst. 2. Heterogeneous catalytic ozonation, Ind. Eng. Chem. Res. 42 (2003) 3218–3224.

[60] Y.M. Dong, H.X. Yang, K. He, S.Q. Song, A.M. Zhang, β-MnO_2 nanowires: A novel ozonation catalyst for water treatment, Appl. Catal. B: Environ. 85 (2009) 155–161.
[61] F.J. Rivas, M. Carbajo, F. Beltrán, O. Gimeno, J. Frades, Comparison of different advanced oxidation processes (AOPs) in the presence of perovskites, J. Hazard. Mater. 155 (2008) 407–414.
[62] Y.M. Dong, K. He, B. Zhao, Y. Yin, L. Yin, A.M. Zhang, Catalytic ozonation of azo dye active brilliant red X-3B in water with natural mineral brucite, Catal. Commun. 8 (2007) 1599–1603.
[63] Y. Wang, H. Zhang, L. Chen, Ultrasound enhanced catalytic ozonation of tetracycline in a rectangular air-lift reactor, Catal. Today 175 (2011) 283–292.
[64] L. Zhao, J. Ma, X.D. Zhai, Enhanced mechanism of catalytic ozonation by ultrasound with orthogonal dual frequencies for the degradation of nitrobenzene in aqueous solution, Ultrason. Sonochem. 17 (2010) 84–91.
[66] B. Neppolian, J.S. Park, H. Choi, Effect of Fenton-like oxidation on enhanced oxidative degradation of *para*-chlorobenzoic acid by ultrasonic irradiation, Ultrason. Sonochem. 11 (2004) 273–279.
[67] H. Zhang, Y.L. Lv, F. Liu, D.B. Zhang, Degradation of CI acid orange 7 by ultrasound enhanced ozonation in a rectangular air-lift reactor, Chem. Eng. J. 138 (2008) 231–238.
[68] J.K. Kim, F. Martinez, I.S. Metcalfe, The beneficial role of use of ultrasound in heterogeneous Fenton-like system over supported copper catalysts for the degradation of *p*-chlorophenol, Catal. Today 124 (2007) 224–231.
[69] Y. Wang, H. Zhang, L. Chen, S. Wang, D.B. Zhang, Ozonation combined with ultrasound for the degradation of tetracycline in a rectangular air-lift reactor, Sep. Purif. Technol. 84 (2012) 138–146.
[70] Kreysa, G., Hákansson, B. (1986). Electrocatalysis by amorphous metals of hydrogen and oxygen evolution in alkaline solution. J. Electroanalyt. Chem. Interf. Electrochem. 201 (1), 61-83.
[71] Heusler, K.E. (1985). Some remarks on the mechanism of the iron-group metal electrodes. Electrochimi. Acta, 30 (12), 1741-1742.
[72] Chien, C.L. (1995). Magnetism and giant magneto-transport properties in granular solids. *Annual Rev. Mater. Sci. 25* (1), 129-160.
[73] Preuß, U., Baerns, M. (1987). Chemical technology of natural gas–its present state and prospects. Chem. Eng. Technol. 10 (1), 297-305.
[74] Oliveira, L.C.A., Fabris, J.D., Rios, R.R.V.A., Mussel, W.D.N., Lago, R.M. (2004). $Fe_{3-x}Mn_xO_4$ catalysts: phase transformations and carbon monoxide oxidation. Appl. Catal. A: General, 259 (2), 253-259.
[75] Kwan, W.P., Voelker, B.M. (2003). Rates of hydroxyl radical generation and organic compound oxidation in mineral-catalyzed Fenton-like systems. Environ. Sci. Technol., 37 (6), 1150-1158.
[76] Szecsody, J.E., Fruchter, J.S., Williams, M.D., Vermeul, V.R., Sklarew, D. (2004). In situ chemical reduction of aquifer sediments: Enhancement of reactive iron phases and TCE dechlorination. Environ. Sci. Technol. 38 (17), 4656-4663.
[77] Joo, S.H.; Feitz, A.J.; Waite, T.D. (2004). Oxidative degradation of the carbothioate herbicide, molinate, using nanoscale zero-valent iron. Environ. Sci. Technol., 38 (7), 2242-2247.
[78] Moura, F.C.C.; Araujo, M.H.; Costa, R.C.C.; Fabris, J.D.; Ardisson, J.D.; Macedo, W.A.A.; Lago, R.M. (2005). Efficient use of Fe metal as an electron transfer agent in a heterogeneous Fenton system based on Fe^0/Fe_3O_4 composites. Chemosphere, 60 (8), 1118-1123.
[79] Wang, N.; Zhu, L.H.; Wang, D.L.; Wang, M.Q.; Lin, Z.F.; Tang, H.Q. (2010). Sono-assisted preparation of highly-efficient peroxidase-like Fe_3O_4 magnetic nanoparticles for catalytic removal of organic pollutants with H_2O_2. Ultrason. Sonochem., 17 (3), 526-533.
[80] Tratnyek, P.G.; Scherer, M.M.; Deng, B.; Hu, S. (2001). Effect of natural organic matter, anthropogenic surfactants, and model quinones on the reduction of contaminants by zero-valent iron. Water Res., 35 (18), 4435-4443.
[81] Hyeon, T.; Lee, S.S.; Park, J.; Chung, Y.; Na, H.B. (2001). Synthesis of highly crystalline and monodisperse maghemite nanocrystallites without a size-selection process. J. Am. Chem. Soc. 123, 12781-12801.
[82] Yu, S.H.; Yoshimura, M. (2002). Ferrite/metal composites fabricated by soft solution processing. Adv. Func. Mater. 12 (1), 9-15.
[83] Woo, K.; Lee, H.J.; Ahn, J.P.; Park, Y.S. (2003). Sol-gel mediated synthesis of Fe_2O_3 nanorods. Adv. Mater., 15 (20), 1761-1764.
[84] Teng, X.W.; Yang, H. (2004). Effects of surfactants and synthetic conditions on the sizes and self-assembly of monodisperse iron oxide nanoparticles. J. Mater. Chem., 14, 774-779.

[85] Deng, J., Wen, X., Wang, Q. (2012). Solvothermal in situ synthesis of Fe_3O_4-multi-walled carbon nanotubes with enhanced heterogeneous Fenton-like activity. Mater. Res. Bull., 47 (11), 3369-3376.
[86] Xu, L., Wang, J. (2012). Fenton-like degradation of 2, 4-dichlorophenol using Fe_3O_4 magnetic nanoparticles. Appl. Catal. B: Environ. 123, 117-126.
[87] X.F. Xue, K. Hanna, M. Abdelmoula, N.S. Deng, (2009). Adsorption and oxidation of PCP on the surface of magnetite: kinetic experiments and spectroscopic investigations. Appl. Catal. B: Environ. 89, 432-440.
[88] R.X. Huang, Z.Q. Fang, X.M. Yan, W. Cheng, (2012). Heterogeneous sono-Fenton catalytic degradation of bisphenol A by Fe_3O_4 magnetic nanoparticles under neutral condition. Chem. Eng. J. 197 (2012) 242-249.
[89] Shin, S., Yoon, H., Jang, J. (2008). Polymer-encapsulated iron oxide nanoparticles as highly efficient Fenton catalysts. Catal. Comm.,10 (2), 178-182.
[90] Zhang, S., Zhao, X., Niu, H., Shi, Y., Cai, Y., Jiang, G. (2009). Superparamagnetic Fe_3O_4 nanoparticles as catalysts for the catalytic oxidation of phenolic and aniline compounds. J. Hazard. Mater., 167 (1), 560-566.
[91] Sun, S.P., Lemley, A. T. (2011). *p*-Nitrophenol degradation by a heterogeneous Fenton-like reaction on nano-magnetite: process optimization, kinetics, and degradation pathways. J. Molecular Catal. A: Chem., 349 (1), 71-79.
[92] Zhang, J., Zhuang, J., Gao, L., Zhang, Y., Gu, N., Feng, J., Yan, X. (2008). Decomposing phenol by the hidden talent of ferromagnetic nanoparticles. Chemosphere, 73 (9), 1524-1528.
[93] Xue, X., Hanna, K., Deng, N. (2009). Fenton-like oxidation of Rhodamine B in the presence of two types of iron (II, III) oxide. J. Hazard. Mater., 166 (1), 407-414.
[94] Rusevova, K., Kopinke, F. D., Georgi, A. (2012). Nano-sized magnetic iron oxides as catalysts for heterogeneous Fenton-like reactions-Influence of Fe (II)/Fe (III) ratio on catalytic performance. J. Hazard. Mater., 241, 433-440.
[95] Usman, M., Faure, P., Ruby, C., Hanna, K. (2012). Remediation of PAH-contaminated soils by magnetite catalyzed Fenton-like oxidation. Appl. Environ. B: Environ., 117, 10-17.
[96] Costa, R.C., Moura, F.C., Ardisson, J.D., Fabris, J.D., Lago, R.M. (2008). Highly active heterogeneous Fenton-like systems based on Fe^0/Fe_3O_4 composites prepared by controlled reduction of iron oxides. Appl. Environ. B: Environ., 83 (1), 131-139.
[97] Xu, L., Wang, J. (2012). Magnetic nanoscaled Fe_3O_4/CeO_2 composite as an efficient Fenton-Like heterogeneous catalyst for degradation of 4-chlorophenol. Environ. Sci. Technol., 46 (18), 10145-10153.
[98] Prakash, A.; McCormick, A.V.; Zachariah, M.R. (2004). Aero-sol-gel synthesis nanoporous iron-oxide particles: a potential oxidizer for nanoenergetic materials. Chem. Mater., 16 (8), 1466-1471.
[99] Peng, S.; Wang, C.; Xie, J.; Sun, S.H. (2006). Synthesis and stabilization of monodisperse Fe nanoparticles. J. Am. Chem. Soc., 128 (33), 10676-10677.
[100] Zhang, D., Zhang, X., Ni, X., Song, J., Zheng, H. (2007). Fabrication and characterization of Fe_3O_4 octahedrons via an EDTA-assisted route. Crys.Growth Design, 7 (10), 2117-2119.
[101] Zhang, S., Wu, W., Xiao, X., Zhou, J., Ren, F., Jiang, C. (2011). Preparation and characterization of spindle-like Fe_3O_4 mesoporous nanoparticles. Nanoscale Res. Lett., 6 (1), 89-98.
[102] Alivisatos, A. P. (1996). Perspectives on the physical chemistry of semiconductor nanocrystals. J. Phys. Chem. 100 (31), 13226-13239.
[103] Yu, Y., Takei, T., Ohashi, H., He, H., Zhang, X., Haruta, M. (2009). Pretreatments of Co_3O_4 at moderate temperature for CO oxidation at 80° C. J. Catal. 267 (2), 121-128.
[104] Cunningham, D. A. H., Kobayashi, T., Kamijo, N., Haruta, M. (1994). Influence of dry operating conditions: observation of oscillations and low temperature CO oxidation over Co_3O_4 and Au/Co_3O_4 catalysts. Catal. Lett., 25 (3-4), 257-264.
[105] Yao, Y. F. Y. (1984). The oxidation of CO and hydrocarbons over noble metal catalysts. J. Catal., 87 (1), 152-162.
[106] Ertl, G. (1991). Oscillatory kinetics and spatio-temporal self-organization in reactions at solid surfaces. *Science*, *254*(5039), 1750-1755.
[107] Barbier, J., Duprez, D. (1993). Reactivity of steam in exhaust gas catalysis I. Steam and oxygen/steam conversions of carbon monoxide and of propane over PtRh catalysts. Appl. Catal. B: Environ. 3 (1), 61-83.
[108] Heck, R.M., Farrauto, R.J., Gulati, S.T. (2009). Catalytic air pollution control: commercial technology, 3rd ed., John Wiley & Sons, Inc.

[109] Trovarelli, A. (2002). Catalysis by ceria and related materials (Vol. 2). Imperial College Pr. 243-280.
[110] Gao, Q. X., Wang, X. F., Di, J. L., Wu, X. C., Tao, Y. R. (2011). Enhanced catalytic activity of α-Fe_2O_3 nanorods enclosed with {110} and {001} planes for methane combustion and CO oxidation. Catal. Sci. Tehchnol., 1 (4), 574-577.
[111] Li, L., Chu, Y., Liu, Y., Dong, L. (2007). Template-free synthesis and photocatalytic properties of novel Fe_2O_3 hollow spheres. J. Phys. Chem. C., 111 (5), 2123-2127.
[112] Ma, J., Wang, T., Duan, X., Lian, J., Liu, Z., Zheng, W. (2011). Ionothermal synthesis of aggregated α-Fe_2O_3 nanoplates and their magnetic properties. Nanoscale, 3 (10), 4372-4375.
[113] Woo, K., Lee, H. J., Ahn, J. P., Park, Y. S. (2003). Sol–gel mediated synthesis of Fe_2O_3 nanorods. Adv. Mater. 15 (20), 1761-1764.
[114] Y Zhao, Y. M., Li, Y. H., Ma, R. Z., Roe, M. J., McCartney, D. G., Zhu, Y. Q. (2006). Growth and characterization of iron oxide nanorods/nanobelts prepared by a simple iron-water reaction. Small, 2 (3), 422-427.
[115] Li, Z., Lai, X., Wang, H., Mao, D., Xing, C., Wang, D. (2009). Direct hydrothermal synthesis of single-crystalline hematite nanorods assisted by 1, 2-propanediamine. Nanotechnol., 20 (24), 245603.
[116] Zheng, Y., Cheng, Y., Wang, Y., Bao, F., Zhou, L., Wei, X., heng, Q. (2006). Quasicubic α-Fe_2O_3 nanoparticles with excellent catalytic performance. J. Phys. Chem. B, 110 (7), 3093-3097.
[117] Wang, G. H., Li, W. C., Jia, K. M., Spliethoff, B., Schüth, F., Lu, A. H. (2009). Shape and size controlled α-Fe_2O_3 nanoparticles as supports for gold-catalysts: Synthesis and influence of support shape and size on catalytic performance. Appl. Catal. A: General, 364 (1), 42-47.
[118] Jiang, X. C., Yu, A. B. (2009). Synthesis of Pd/α-Fe_2O_3 nanocomposites for catalytic CO oxidation. J. Mater. Process. Technol., 209 (9), 4558-4562.
[119] Kung, M. C., Davis, R. J., Kung, H. H. (2007). Understanding Au-catalyzed low-temperature CO oxidation. J. Phys. Chem. C., 111 (32), 11767-11775.
[120] Liu, X., Liu, J., Chang, Z., Sun, X., Li, Y. (2011). Crystal plane effect of Fe_2O_3 with various morphologies on CO catalytic oxidation. Catal. Comm., 12 (6), 530-534.
[121] Tejuca, L.G., Fierro, J.L.G. (1992). Properties and applications of perovskite-type oxides, Marcel Dekker, New York, USA, 271.
[122] Campagnoli, E., Tavares, A., Fabbrini, L., Rossetti, I., Dubitsky, Y. A., Zaopo, A., Forni, L. (2005). Effect of preparation method on activity and stability of $LaMnO_3$ and $LaCoO_3$ catalysts for the flameless combustion of methane. Appl. Catal. B: Environ., 55 (2), 133-139.
[123] Nishihata, Y., Mizuki, J., Akao, T., Tanaka, H., Uenishi, M., Kimura, M., Hamada, N. (2002). Self-regeneration of a Pd-perovskite catalyst for automotive emissions control. Nature, 418 (6894), 164-167.
[124] Kremenić, G., Nieto, J. M., Tascón, J. M., Tejuca, L. G. (1985). Chemisorption and catalysis on $LaMO_3$ oxides. J. Chem. Soc., Faraday Trans. 1, 81 (4), 939-949.
[125] T. Nitadori, T. Ichiki, M. Misono, Bull. Chem. Soc. Jpn, 61, 1988, 621.
[126] S. Royer, F. Bérubé, S. Kaliaguine, Effect of the synthesis conditions on the redox and catalytic properties in oxidation reactions of $LaCo_{1-x}Fe_xO_3$, Appl. Catal. A: Gen. 282, 2005, 273-284
[127] Farhadi, S., Zaidi, M. (2009). Bismuth ferrite ($BiFeO_3$) nanopowder prepared by sucrose-assisted combustion method: A novel and reusable heterogeneous catalyst for acetylation of amines, alcohols and phenols under solvent-free conditions. J. Mole. Catal. A: Chem., 299 (1), 18-25.
[128] Gao, F., Chen, X. Y., Yin, K. B., Dong, S., Ren, Z. F., Yuan, F., Liu, J. M. (2007). Visible-Light photocatalytic properties of weak magnetic $BiFeO_3$ nanoparticles. Adv. Mater., 19(19), 2889-2892.
[129] Luo, W., Zhu, L., Wang, N., Tang, H., Cao, M., She, Y. (2010). Efficient removal of organic pollutants with magnetic nanoscaled $BiFeO_3$ as a reusable heterogeneous Fenton-like catalyst. Environ. Sci. Technol., 44 (5), 1786-1791.
[130] Wu, J. M., Wen, W. (2010). Catalyzed degradation of azo dyes under ambient conditions. Environ. Sci. Technol., 44 (23), 9123-9127.
[131] Crespin, M., Hall, W. K. (1981). The surface chemistry of some perovskite oxides. J. Catal., 69 (2), 359-370.
[132] Ciambelli, P., Cimino, S., Lasorella, G., Lisi, L., De Rossi, S., Faticanti, M., Porta, P. (2002). CO oxidation and methane combustion on $LaAl_{1-x}Fe_xO_3$ perovskite solid solutions. Appl. Catal. B: Environ. 37 (3), 231-241.
[133] Kaliaguine, S., Van Neste, A., Szabo, V., Gallot, J. E., Bassir, M., Muzychuk, R. (2001). Perovskite-type oxides synthesized by reactive grinding: Part I. Preparation and characterization. Appl. Catal. A: General, 209 (1), 345-358.

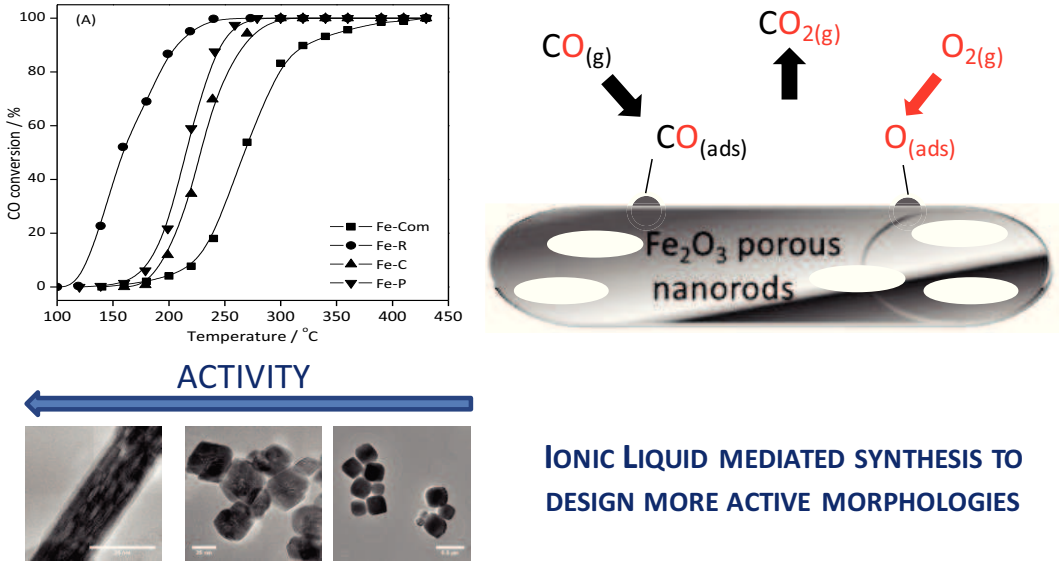
[134] Kleitz, F., Choi, S. H., Ryoo, R. (2003). Cubic Ia3d large mesoporous silica: synthesis and replication to platinum nanowires, carbon nanorods and carbon nanotubes. Chem. Comm., (17), 2136-2137.
[135] Chiarello, G. L., Rossetti, I., Forni, L. (2005). Flame-spray pyrolysis preparation of perovskites for methane catalytic combustion. J. Catal., 236 (2), 251-261.
[136] Bonne, M., Sellam, D., Dacquin, J. P., Lee, A. F., Wilson, K., Olivi, L., Duprez, D. (2011). A general route to synthesize supported isolated oxide and mixed-oxide nanoclusters at sizes below 5 nm. Chem. Comm., 47 (5), 1509-1511.

Chapter 3 Ionic Liquid-Mediated α-Fe_2O_3 Shape-Controlled Synthesis

Article:

Liwei Hou, Qinghua Zhang, François Jérôme, Daniel Duprez, Fabien Can, Xavier Courtois, Hui Zhang and Sébastien Royer, ChemCatChem 5 (2013) 1978-1988

Hematite (α-Fe_2O_3), an type of iron oxide and a n-type semiconductor, has been extensively investigated as catalysts, owing to its low processing cost, non-toxicity and high resistance to corrosion. Many recent researches have been directed toward the fabrication of nanostructured iron oxides for wastewater and wastegas treatment. Although Fe^{3+} in hematite is less active than that of Fe^{2+} in other iron oxides for the heterogeneous Fenton reaction, it is a good catalyst in the oxidation of carbon monoxide. However, the catalytic performances of the iron oxides are largely dependent on their physic-chemical properties, such as the unique sizes, surface areas, and shapes. Therefore, it is very important to control their crystal sizes and shapes to pursue high activity in environmental catalysis.



3.1 Introduction

Carbon monoxide (CO) is recognized as a major precursor gas of ground-level ozone [1] which can trigger off serious respiratory problems. CO is also a highly flammable gas: its combustion can occur for concentration between 12 and 75 vol.% in air [2]. However, in most cases, CO concentration in exhaust gases is much lower, typically in the range of 50-50000 ppm, making the homogeneous combustion impossible [1]. Therefore, the catalytic oxidation becomes a preferable choice. Since the beginning of the 20th century, some redox materials, such as hopcalite, have been known to oxidize CO at ambient temperature. Hopcalite is a binary amorphous

Mn-Cu oxide whose texture can be stabilized by addition of CaO, Al_2O_3 or bentonite clay [3]. Some oxides, especially those of cobalt and copper, also present an interesting activity for CO oxidation. The transition metal oxides relative activity, for different iron oxides and MnO_2, follows the order Fe_3O_4<Fe_2O_3<MnO_2 while copper and cobalt oxides are far more active but suffer from easy deactivation [4]. The main reason for the withdrawal of transition metal from catalytic converter formulation was their bad behaviour in cycled transient conditions and their high susceptibility to sulphur. The recent huge decrease of sulphur content in commercial fuels and progresses in oxide catalyst synthesis make base metal oxides to be again reconsidered and an intensive bare research is actually developed on nanoparticles properties. Then, a high-throughput investigation by Saalfrank and Maier in 2004, over $Mn_xCo_yO_w$, and $Al_xMn_yCo_zO_w$ confirmed the real potential of noble metal-free catalysts [5].

Among the metal oxides, hematite (α-Fe_2O_3), an n-type semiconductor, has been extensively investigated as catalysts, owing to its low processing cost, non-toxicity and high resistance to corrosion [6]. Many recent researches have been directed toward the fabrication of nanostructured iron oxides. Indeed, the unique size and shape-dependent properties of oxide materials (magnetic, catalytic, chemical properties, *etc.*) have attracted intensive attention [7,8]. In particular, many efforts have been devoted to the control of morphologies of oxides [9-13], due to their potential application in catalysis, energy storage, and so forth. Therefore, investigation on shape controllable synthesis of nanomaterials is of great interest and the activity of these materials in environmental catalysis is being pursued. To date, well-defined nanostructures of iron oxides with different morphologies such nanotubes, hollowspheres, nanocubes, as well as nanorods, naotubes, nanobelts have been obtained mainly using hydrothermal approach [10-18]. As expected, these α-Fe_2O_3 nanostructures present interesting size and shape-dependent properties [11-13, 19]. Among the various synthesis methods, template-directed processes including hard templates and soft-templates have been investigated for oxide of transition metal.

For example, Zhong *et al.* have reported the synthesis of flowerlike iron oxide nanostructures in the presence of urea and tetrabutylammonium bromide (TBABr) by a solvothermal process [20]. Zeng *et al.* have synthesized hollow hematite spindles and microspheres [21]. In this last example, microspheres can be transformed into iron oxide by calcination in air at 400 °C for 2 h. However, removal of the template is always needed. Furthermore, the proposed routes are often time-consuming and can involve the use of non-environmental-friendly template molecules. The nano-replication from a hard template open structure, exemplified by Davidson *et coll.* for manganese and iron oxide [22,23] or cobalt oxide by Schüth *et coll.* and Gao *et coll.*, [24-26] which involves multiple steps before obtaining the desired oxide structure, is clearly representative of the time consuming processes. Delahaye *et al.* then used this hard-templating approach to obtained hematite organized mesoporous structure [23]. The nanoparticles exhibit superparamagnetic behaviour around ambient temperature. Their magnetic properties, sizes and blocking temperatures increase with the pore diameter of silica template. This result highlights again the necessity of material structural control to design adapted systems to selected applications. Therefore, the development of a facile, environmental friendly and scaling-up route to synthesize morphology-controlled hematite nanoparticles is always needed to replace the time consuming previously presented routes.

Room-temperature ionic liquids (RTILs), considered as green and efficient recyclable solvents, are a class of organic solvents composed entirely of ions. They have gained a great deal of both academic and industrial attention as a potential effective green replacement of conventional organic solvents for long-lasting development of human society. Because of their highly favourable properties, such as extremely low volatility, good thermal stability, good dissolving ability, wide liquid temperature range, designable structures, high ionic conductivity, and wide electrochemical window, RTILs have been used effectively in organic chemical reactions, separation, and electrochemical processes but also for new material synthesis. The most important advantage of RTILs is that they can form extended

hydrogen bond systems in the liquid state and are therefore highly structured. These compounds can be used as "entropic driver" for spontaneous, well-defined, and extended ordering of nanostructures. It has also been demonstrated that RTILs are not only used as functional solvents, but can also act as templates for the preparation and stabilization of various inorganic nanomaterials with original and improved properties. Therefore, the potential of RTILs for the synthesis of porous structures or shape-selected nanoparticles was recently reviewed [6, 27-29]. Then, novel structures, including open framework aluminophosphate, metallic nanoparticles or oxides, metal organic framework structures and others were obtained in ionothermal processes or in RTIL-mediated hydrothermal/solvothermal approach [6,30,31].

However, as previously mentioned, the activity of iron oxide for CO oxidation remains limited compared to some other transition metal oxides [4,32]. In the last three decades, the development of the catalytic converters in the United States and Europe highlighted the exceptional activity of noble metals (Pt, Pd, Rh) for low temperature oxidation [33-36]. The specific role of oxides having a high OSC (Oxygen Storage Capacity) such as stabilized ceria and ceria-zirconia, allowing the noble metals to continue to work in cycled conditions, was also highlighted [33,37]. The relative activities of noble metals and base metals for CO oxidation, as reported by Heck and Farrauto,[36] show that noble metals are more active than base metals. However, recent developments in α-Fe_2O_3 nanoparticle synthesis (nanobelts, nanotubes, nanoflowers, nanospheres) allow improving physical properties, which will favour metal dispersion [10-18]. In addition, solid exposed planes with high Fe atom concentration will provide more active sites for catalytic reactions. Moreover, activity of Fe_2O_3 alone [34] or after promotion by gold [39] or palladium [40] evidences that noble metal strongly improves catalytic activity. Especially, Au particles supported on reducible transition metal oxides (Fe_2O_3) can exhibit high activity that is ascribed to the activation and supplement of oxygen for the reaction, making this catalyst more active than with other supports [41]. Unfortunately, iron oxide is conventionally presenting limited surface area, resulting in some difficulties

to achieve high noble metal dispersion [39,42]. Consequently, when gold is dispersed on classical low surface area Fe_2O_3, relatively low catalytic activity is achieved ($T_{50\%}$ CO conversion between 36 and 80 °C over 1 wt.% Au/α-Fe_2O_3, 50 mg of catalyst in a gas mixture of 1 vol.% CO, 20 vol.% O_2 – bal. N_2 at a flow rate of 67 mL min^{-1}). Better dispersions can be logically awaited over high surface area nanostructured supports. In addition, other important factors, such as the size and morphology of the Au particles, the degree of coordinative unsaturation, the oxidation state of Au, *etc.* will play important roles on the activity of Au supported catalysts [43].

In this work, RTILs was used as co-solvent/template during the hydrothermal synthesis of α-Fe_2O_3 nanostructures, as previously proposed [6]. Microcubes, nanoplates and porous nanorods are obtained in this ionic liquid mediated synthesis process. These structures where used after low temperature thermal stabilization for the CO oxidation reaction, to evidence the morphology effect on the activity. Thereafter, activity of highly dispersed noble metal (Pt, Pd and Au) was evaluated on the most active α-Fe_2O_3 nanorods.

3.2 Structural properties

XRD patterns of the α-Fe_2O_3 microcubes (Fe-C), nanoplates (Fe-P) and nanorods (Fe-R), all pretreated in air at 300 °C for 1 h, are shown in Figure S1 [the details were shown in the Supplementary information (SI), Figure S1]. Observed reflections are in good agreement with those of the standard pattern for pure hexagonal structure of α-Fe_2O_3 (JCPDS card No. 89-2355, added in the bottom of Figure S1 and 1). No other peaks are observed, suggesting the high purity of the synthesized samples. However, differences among the full width at half-maximum (FWHM) and relative intensities of the diffraction peaks are observed between these samples, which indicate differences in the crystal size and morphology. The narrow sharp peaks obtained for Fe-Com and Fe-C indicate that these materials are highly crystalline, i.e. exhibiting large crystal size. However, the peaks obtained for Fe-P are broadened with their intensities strongly decreased, showing that this last solid exhibits smaller crystal size than for

Fe-C and Fe-Com. Fe-R presents the broadest reflections suggesting that the smallest crystal size is obtained for this material. According to the FWHM evolution, the average crystallite sizes of the Fe-C, Fe-P and Fe-R are estimated to be 36.9, 27.2 and 16.1 nm, respectively (calculated with the main reflection at $2\theta = 35.7^{o}$, after Warrens' correction for instrumental broadening, Table 1). For comparison, the crystal size of the commercial α-Fe_2O_3 (Fe-Com) is evaluated at 36.0 nm.

The deposition of 1 wt.% of noble metal over Fe-R, Pd, Pt or Au, does not induce any modification of the crystal structure, with calculated crystal size of α-Fe_2O_3 remaining unchanged (Table 1). No significant difference could be discerned by XRD (Figure 1) between catalysts without and with noble metal, suggesting that very small noble metal particles form on the surface of the nanostructure.

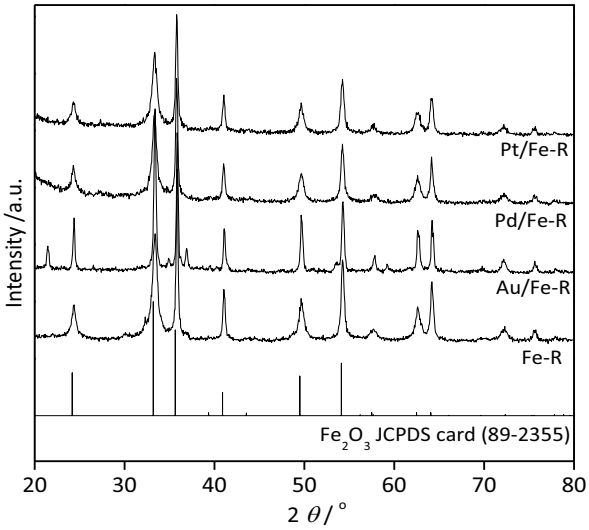


Figure 1. XRD patterns recorded for noble metal supported on the nanorods α-Fe_2O_3.

3.3 Textural properties

While the commercial low surface area material presents a SSA below 5 $m^2\ g^{-1}$, all the nanostructured materials present higher surface areas. Nevertheless, large differences can be observed between the materials. Indeed, relatively low surface areas, *c.a.* 10-15 $m^2\ g^{-1}$ are obtained for the cube (Fe-C) and pellet-type (Fe-P) morphology. The nanorod-like morphology allows achieving higher surface area (Fe-R, SSA = 56 $m^2\ g^{-1}$ in Table 1). As can be observed in Table 1, the surface area

does depend directly on the crystal size as evaluated by X-ray line broadening. Even if the highest surface area is displayed by the material presenting the lowest crystal domain size (Fe-R), Fe-Com and Fe-C present similar crystal size but largely different surface areas. The evolution of the SSA with crystal size over the ILs-mediated materials is however coherent with an exponential decrease of the SSA with the increase in D_{cryst}. Such a difference between classical material and the ILs-derived materials suggest an effect of the RTILs on either the morphology or size of the aggregates, or their density (*i.e.* the degree of agglomeration of the elementary particles in these aggregates). Despite the large differences in SSA, all materials display large mesopore (always above 5 nm) which is favourable for the diffusion of reactant and product molecules during reaction.

The noble metal impregnation does not induce any noticeable change in surface area, whatever the noble metal (Au, Pd or Pt). Only a small decrease in SSA is observed, the more important decrease being observed for 1% Pt/Fe-R which presents a SSA of 46.1 m^2 g^{-1} in Table 1. In addition, XPS analysis evidenced Au-surface enrichment over the Fe-R supported materials compared to Fe-Com sample (SI, Table S1). The Binding Energies (BE) of Au4f7/2 for 1%Au/Fe-Com and 1%Au/Fe-R were 84.1 and 83.9 eV, respectively, which are very closed to BE value of Au^0: 84.0 eV), indicating that the gold is predominantly present in the metallic form in both of our samples. Moreover, compared with 1%Au/Fe-Com, higher surface Au concentration was achieved for 1%Au/Fe-R catalyst, with the values of 1.2%. This result is in good agreement with the results of ICP presented in Table 1. Clearly, ILs assisted route resulted in the surface enrichment by Au atom, which is apparently favourable to the catalytic properties. Roughly, the concentration of Au increased along with the surface area of the supporters prepared through the impregnation method. The result may be mainly attributed to the decrease of crystal size and the high surface area of the supporters, leading to the good dispersion of Au particles on the supporter's surface.

3.3 Morphology

The morphology of the Fe-C, obtained by hydrothermal treatment in alkaline media of an iron chloride precursor and C_{10}mimCl additive, is observed to display highly geometrical symmetry as observed by scanning electron microscope (SEM) and transmission electron microscope (TEM), Fig. 2A-C. Typical low-magnification SEM image presented in Fig. 2A clearly shows that the material possesses a large-scale uniform cubic shape. The corresponding TEM images (Fig. 2B-C) evidence that the size of the Fe-C is about 300 nm in edge. However, size repartition is not mono-dispersed and a few smaller-sized cubes, as observed in Fig. 2C, can be found in the observed zone. Further observation of the Fe-C showed that the surfaces of the cubes are rough, showing that these cubes are aggregates of nanoparticles, which is consistent with results obtained by XRD. Indeed, crystal size as evaluated by XRD is largely lower than the observed size of the cubes.

Table 1. Physical and structural properties of the materials.

Sample	*SSA* [a] (m^2 g^{-1})	D_p [b] (nm)	V_p [c] (cm^3 g^{-1})	Noble metal *Conc.* (%)	Noble metal size (nm)	D_{cryst} [d] (nm)	$T_{50\%}$ (°C)
Fe-Com	3.4	24.5	0.04	–	–	36.0	267
Fe-C	10.4	43.3	0.13	–	–	36.9	228
Fe-P	28.5	32.8	0.15	–	–	27.2	215
Fe-R	56.0	16.5	0.22	–	–	16.1	158
1% Au/Fe-R[e]	57.9	16.9	0.23	1.27	2-6	–	< 25
1% Pd/Fe-R[e]	55.3	18.8	0.21	1.14	3-6	–	107
1% Pt/Fe-R[e]	46.1	17.3	0.19	1.19	0.5-1	–	209

[a] *SSA* is the specific surface area evaluated using the BET model, [b], D_p is the BJH mean pore size obtained on the desorption branch, [c], V_p is the pore volume evaluated at P/P_0 = 0,97; [d] $D_{crystal}$ is the crystal domain size evaluated from the X-ray line broadening using the Scherrer equation; [e] noble metal content is verified by ICP-OES to range at the expected value ± 0.2%.

A careful observation of the Fe-P sample, obtained with C_{10}mimCl in the CH_3COOK system, has been carried out (Figure 2D-F). Figure 2D shows a representative SEM image of the solid. A smooth-like morphology, with very small

particles highly agglomerated, is strongly suggested by SEM analysis (Figure 2D). The size of the nanoparticles is very small and cannot be clearly seen by SEM. Therefore, the morphology of the particles was further investigated by TEM (Figure 2E-F), illustrating the regular diamond-shaped of the hematite nanoplates. Figure 2F shows that the nanoplates obtained are crystallized. However, the surfaces of these nanoparticles, having an average size of 30 nm, are relatively rough.

Finally, Figure 2G presents a typical SEM image of the Fe-R obtained using hydrothermal treatment in alkaline media of an iron chloride precursor and C_{10}mimCl additive, but obtained at higher NaOH concentration than the Fe-C sample. Aggregate of rod-like particles, micrometric in length, can be detected by SEM. The material was further characterized by TEM to get more information on the morphology and porosity. The TEM image in Figure 2H shows representative aggregates of nanorods. The size of the obtained rods is however wide in diameter and length, with these rods displaying diameters of 20~60 nm and lengths of 200~600 nm. It is worth noticing that the nanorods were obtained with formation of pores in the rods (Figure 2I). The size of pores is in the range of 2~5 nm at the smaller zone, but is not presenting any defined form. Indeed, high magnification image in Figure 2I shows the formation of oblong-type pores while in other region of observation that the pores look spherical (see Figure 3). Such irregular intra-rod porosity formation is however in agreement with the N_2 physisorption results, given a high surface area and broad pore size distribution (Table 1).

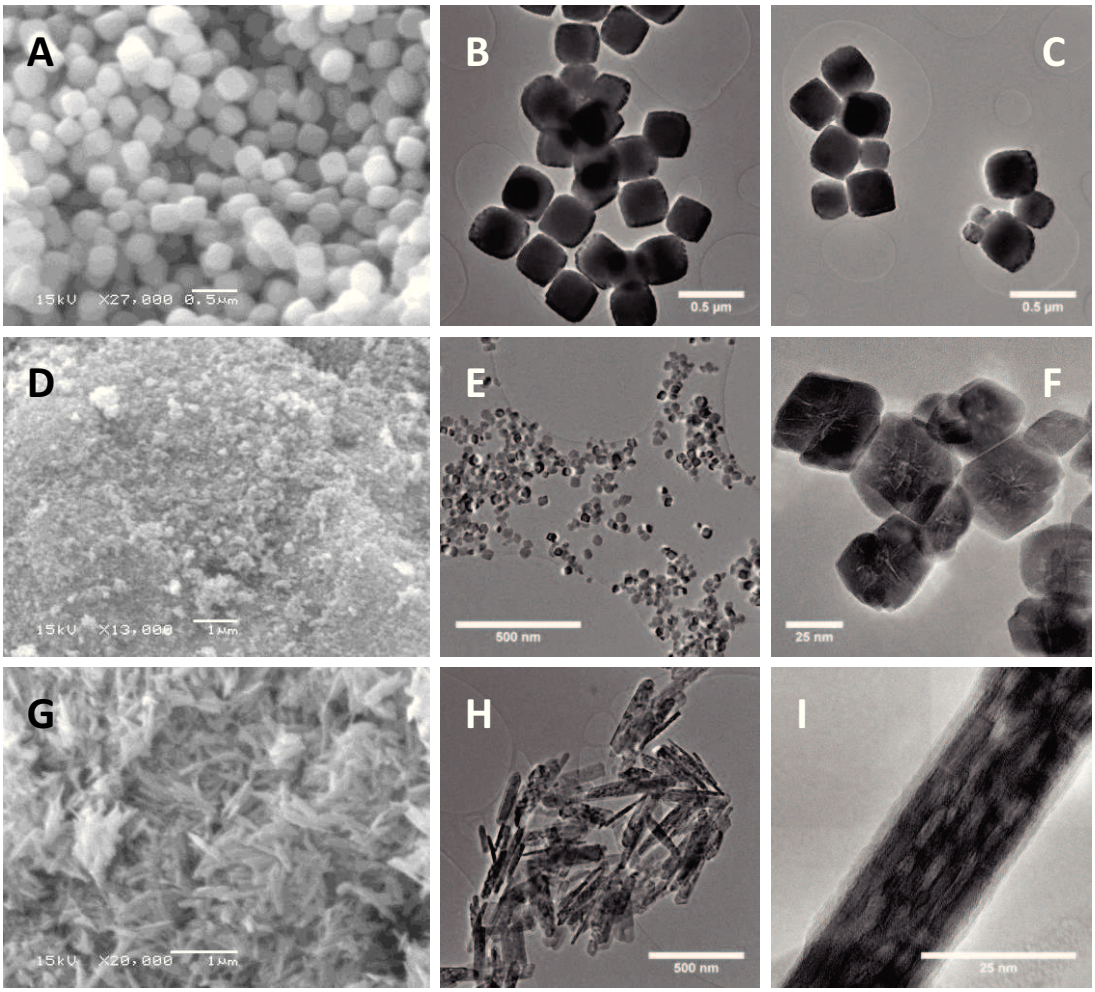


Figure 2. Representative SEM images of the different α-Fe_2O_3 morphologies (A) SEM for Fe-C; (D) SEM for Fe-P; (G) SEM for Fe-R; high magnification TEM images of the noble metal nanoparticles on Fe-R nanorods supported noble metal derived catalysts (B)-(C): Fe-C; (E)-(F): Fe-P; (H)-(I): Fe-R.

The morphology of α-Fe_2O_3 nanorods supported noble metals -including gold, palladium and platinum – are presented in Figure 3. Figure 3A-C show typical TEM image of Au/Fe-R composite obtained by deposition precipitation using $HAuCl_4$ precursor. The gold nanoparticles are observed to be uniformly dispersed without large external gold particle/aggregate formation. Most of the nanoparticles are located inside the Fe-R porosity. TEM analysis (Figure 3B) also shows that nanoparticles are relatively uniform in size. By measuring visible particles on Fe-R, the diameters of gold nanoparticles distribute in a narrow size range between 2.0-6.0 nm. Interestingly, the detection of large particle, at size higher than 10 nm, was not possible. A similar morphology is observed over the Pd/Fe-R material. As shown in Figure 3D, the composite obtained by impregnation procedure presents a satisfying dispersion of

palladium in the porosity of the nanorods, as observed in the case of the gold-containing material. Again, nanoparticles are highly-dispersed on Fe-R without large external particle/aggregate formation. The sizes of observed particles are within a narrow window, comprised between 3.0 nm and 6.0 nm which are directly comparable with the values obtained for the gold material.

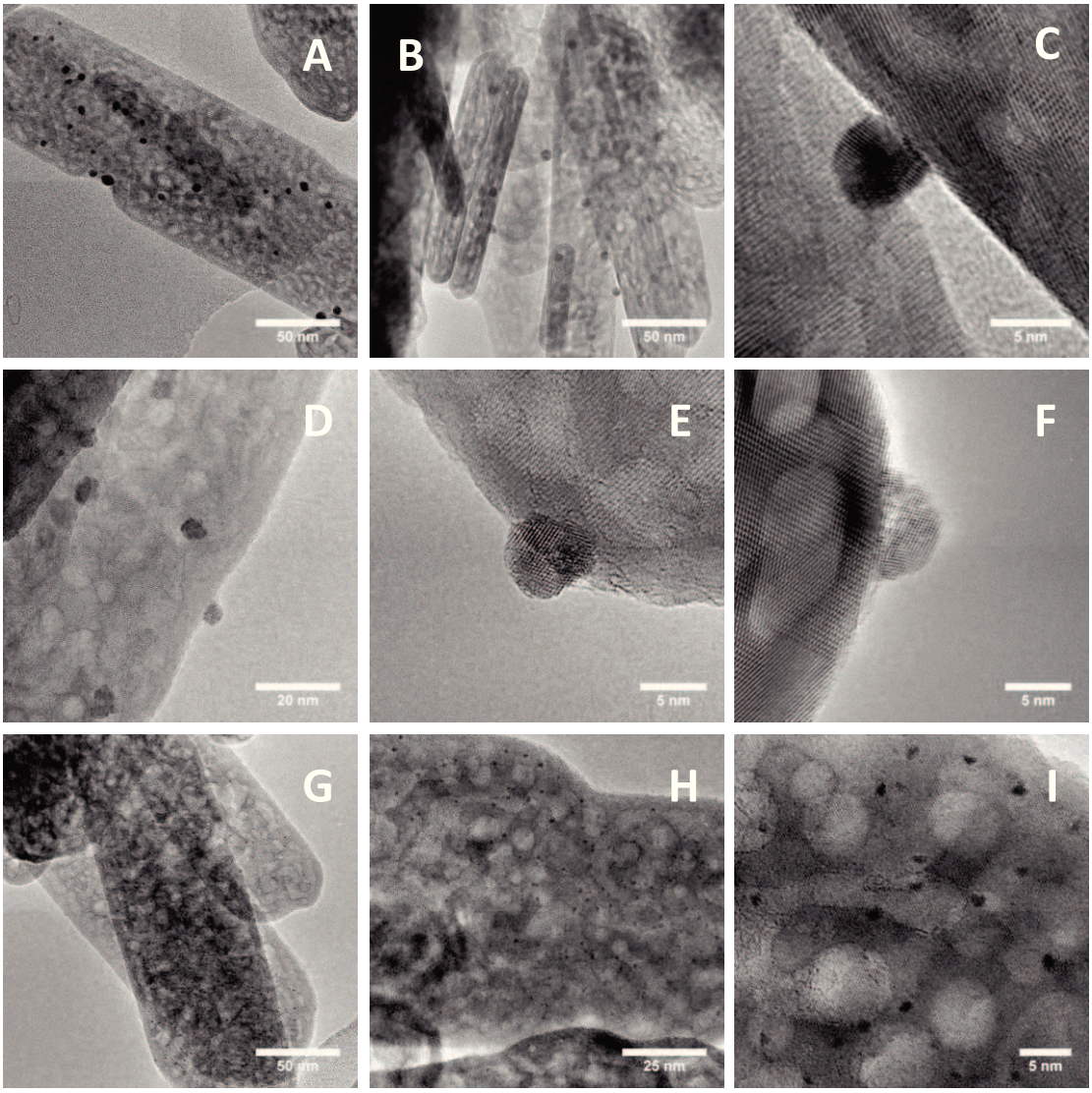


Figure 3. Representative TEM images of the different noble metal supported nanorod-type α-Fe_2O_3. (A)-(C): Au particles supported on Fe-R; (D)-(F): Pd particles supported on Fe-R; (G)-(K): Pt particles supported on Fe-R

As shown in the higher magnification image (Figure 3F), palladium nanoparticles are in strong interaction with iron oxide surface, always isolated on the nanorod surface. The morphology of platinum supported on α-Fe_2O_3 nanorods differs from the two previously presented materials. While the nanorod morphology is maintained, 2-5 nm

particles cannot be detected at low magnification (Figure 3G). The increase of the magnification allows however the detection of very small platinum nanoclusters located inside the porosity of the nanorods (Figures 3H-I). The measured sizes of the observed particles are very small, and are always in the range of 0.5-1.0 nm. Clearly, in this last case, high platinum dispersion inside the porosity is achieved.

3.4 Reducibility of the composites

The evolution of the iron reducibility with the different morphologies is displayed in Figure S2 (details shown in the SI data). Two broad peaks are observed, always located at similar temperature (250-450 °C and above 450 °C) whatever the morphology. These two successive reduction processes are assigned to the α-Fe_2O_3 to Fe_3O_4 (first step) and Fe_3O_4 to FeO and to Fe^0 (second step) reduction processes, respectively [40,43]. We observed a first reduction process centred at ~415 °C, in accordance with the results from Liu *et al.*[43] who reported the first step of reduction in the range of 404 °C to 520 °C (α-Fe_2O_3 synthesized by hydrothermal method and thermally activated at 140-180 °C for 2-12 h). In the low-temperature oxidation reaction, the Fe^{3+}/Fe^{2+} redox couple is responsible for the activity, as encountered for the CO oxidation reaction. Then, the oxygen ions considered as the active oxygen species for the CO oxidation are then directly related to the temperature of this reduction process [43]. The Fe-R material presents the highest surface area and the lowest crystal domain size. Surprisingly, the temperature at the maximum of the reduction peak for the first reduction process is located at exactly the same temperature of 415 °C than for the other morphologies. No notable improvement in reducibility can be achieved through the surface area increase or the crystal size decrease. However, only a small reduction peak appeared at 290 °C for Fe-R and 306 °C for Fe-P. It can be related to their higher surfaces areas and lower crystal sizes, which can promote surface reducibility [43], but in a very limited extend as can be deduced on the basis of these results. Figure 4 displays H_2-TPR profiles recorded for Au/Fe-R, Pd/Fe-R and Pt/Fe-R materials. A comparison with Figure S2 (details shown

in the SI files) reveals that upon the impregnation of noble metal, the reduction of hematite (α-Fe_2O_3) to magnetite (Fe_3O_4) is shifted to notably lower temperature, which can easily be explained by an hydrogen spill-over phenomenon from the noble metal sites to the support. Then, noble metal reduction occurs at the same time in the low temperature reduction step, and reduced sites will promote hydrogen activation and migration up to oxidized iron surface sites to favour their reductions. The profile of the Au/Fe-R shows then two main peaks located at 115 °C and 651 °C. The former one is ascribed to the simultaneous reduction of Au(III) to Au(0) and some Fe^{3+} to Fe^{2+}. The latter one corresponds to the reductions of Fe^{3+} to Fe^{2+} and even to Fe^0 [44,45]. The shift of Fe^{3+} reduction to lower temperature after the impregnation of gold may be ascribed to the weakening of the Fe-O bonds adjacent to the gold atoms, resulting in a higher mobility of lattice oxygen, as reported in previous investigation [46]. Similarly, Pd or Pt also lead to a lowering of the reduction temperature with respect to pure iron oxide, showing a reducibility rank for trivalent iron following the order: Au/Fe-R > Pd/Fe-R > Pt/Fe-R.

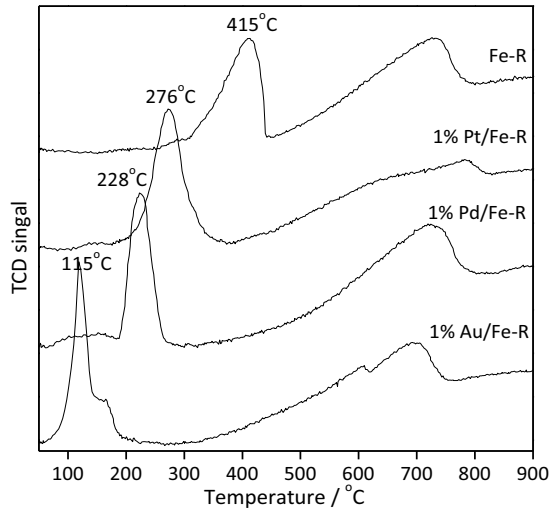


Figure. 4. TPR-H_2 profiles recorded for noble metal containing materials.

3.4 Oxygen Isotopic Exchange reaction (OIE)

Due to the lack in Fe^{3+} reducibility differences (Fig. S2 in the SI files), comparison of oxygen mobility in the different morphologies of α-Fe_2O_3 was undertaken by performing the temperature-programmed isotopic oxygen ($^{18}O/^{16}O$)

exchange reaction. From these experiments, we extracted the cumulative number of oxygen atoms exchanged, N_e (Figure 5A), and the evolution of the rate of exchange, R_e (Figure 5B), versus exchange temperature.

The number of oxygen atoms exchanged over the different morphologies of iron oxide material is strongly modified by the material morphology. Among the tested samples, a largely higher number of oxygen atoms was exchanged at 600 °C for Fe-R (Figure 5A), showing that a higher oxygen mobility is obtained for this high surface area nanocrystalline material than for the other morphologies. The evolution of the oxygen exchange rate, considered as a measure of the bulk oxygen diffusion rate, is presented in Figure 5B. The highest oxygen exchange rate is obtained for the Fe-R sample while the exchange reaction starts at higher temperature over Fe-P and Fe-C samples. Notably, the lowest exchange activity is measured for the Fe-Com sample.

The values of R_e, whose condition the number of oxygen atoms exchanged, are then associated with the specific surface area and crystal size of the materials. Then, the highest the surface area is and the lowest the crystal size is, the highest the oxygen mobility in α-Fe_2O_3 structure is. Indeed, crystal size reduction results in increase iron oxide surface sites, in addition to the possible modification of iron density exposed crystal faces, edges and corners.[47] Such low crystal size structures are then considered to favour molecule adsorption, which is obviously in favour of a catalytic reaction, but also of oxygen diffusion. These exposed iron sites are also the active sites for oxygen adsorption and activation, whose are the first steps of the exchange. Then, the highest the surface site concentration is, the highest the oxygen mobility is.

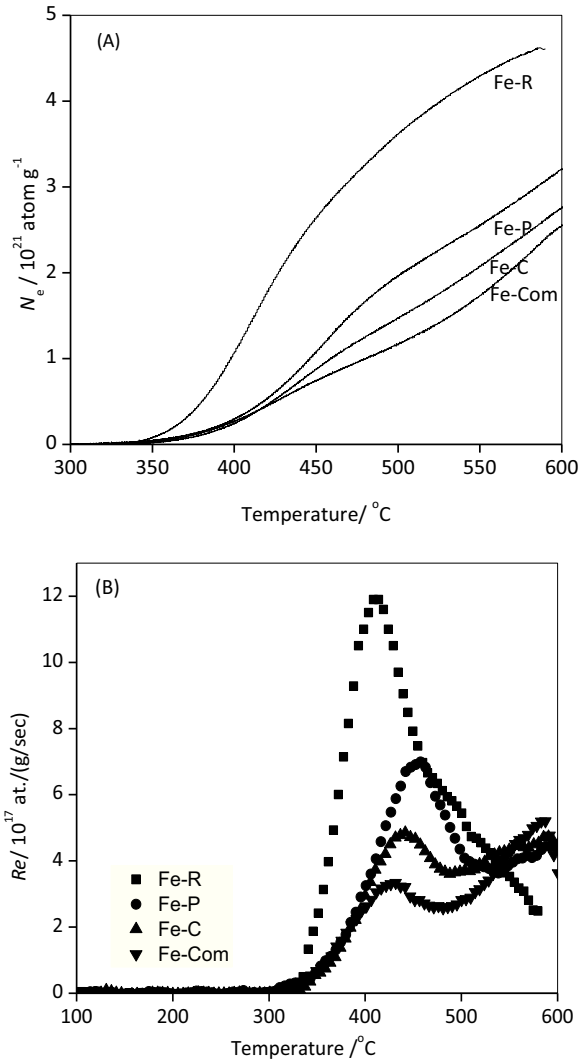


Figure 5. (A) Evolution of the number of oxygen atoms exchanged (N_e) versus temperature of reaction for the different morphologies of iron oxide. (B) Evolution of the oxygen isotopic exchange rate (R_e) versus temperature of reaction for the different morphologies.

3.5 Catalytic activity measurements

The evaluation of CO oxidation performances are performed over the morphologically-oriented Fe_2O_3 nanomaterials, as presented in Figure 6A. Among the designed morphologies, the Fe-C presents the lowest activity with a $T_{50\%}$ located at 228 °C. However, Fe-C still presents a higher activity than the commercial sample ($T_{50\%}$ = 267 °C). The best activity, with a $T_{50\%}$ of 158 °C, is obtained over Fe-R. The catalytic activities for CO oxidation over the different materials then rank as follow:

Fe-R >> Fe-P ＞ Fe-C >> Fe-Com (Table 1 and Figure 6A). This activity trend is in line with:

- The specific surface area evolution (Table 1)
- The crystal size evolution (Table 1)
- The oxygen mobility evolution (Figure 5A)

It is well known that the activity of the catalyst for CO oxidation is determined by the adsorption of CO and the Fe^{3+} surface site reducibility, allowing active oxygen atom available for oxidation.[49] Then, the different morphologies having different accessible surface iron concentration, lead to very different catalytic activities. As expected, nanorod-type morphology, due to its improved accessible surface, is favourable to the CO oxidation rate.

The effect of noble metal adding on Fe-R on the CO oxidation activity is shown in Figure 6B. The order of activity is: Au/Fe-R >> Pd/Fe-R＞Fe-R > Pt/Fe-R. While the deposition of palladium results in a net increase in catalytic activity, the platinum containing material presents lower activity than Fe-R alone despite a very high dispersion of the noble metal. Nevertheless, the limited activity of platinum can be related to the possible residual chlorine on platinum active site, due to the use of chlorine containing precursor and limited calcination temperature applied in this study. Such residual chlorine in interaction with noble metal surface can result in a poisoning of the active sites and reduced activity, which can explain the limited activity measured for Pt/Fe-R [48].

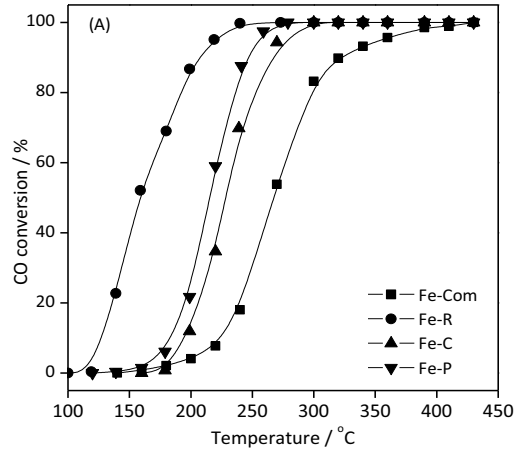
Compared to other noble metals such as Pt and Pd, oxidic gold species are very sensitive to ambient atmosphere and unstable at elevated temperature [42]. When the temperature is below 100 °C, the presence of highly active oxygen species on the surface of Au nanoparticles can results in high oxidation activity, as observed in our case for the Au/Fe-R material. The availability of reactive oxygen species are derived from surface OH group/adsorbed H_2O, absorbed oxygen species, or a combination of these [42,49]. Au/Fe-R catalyst then shows the highest activity on the CO oxidation at low temperature, showing the existence of highly active surface oxygen species in this

material. The activity of gold nanoparticles is however strongly related to the nanoparticle size [50]. To achieve a high activity for CO oxidation, gold particles must be under 10 nm.[51] Small Au clusters possess a high fraction of uncoordinated Au atoms that favour CO adsorption. Theoretical calculations indicated that low coordination Au atoms can strongly interact with adsorbates [52,53]. Low coordination sites are suggested to bind CO, whereas oxygen can be activated on Au nanoparticles. Some studies focused on the effect of Au nanoparticle size on the CO oxidation rate. The valence band density of gold nanoparticles oxidation states changed with decreasing the particle size, and results in the enhancement of activity for CO oxidation [55,56]. Goodman *et al.* reported then that CO oxidation reached a maximum conversion at a diameter of particles of 3.5 nm. The gold nanoparticles supported over nanorods we obtained in this study present sizes around 2-6 nm with excellent dispersion on the surface of Fe-R. These properties are then favourable to the reaction. Considering the excellent activity of the 1%Au/Fe-R at low temperature (>60 ^{o}C), we also conducted the experiments from 120 ^{o}C to 0 ^{o}C to test the CO conversion. As shown in the Figure S3 (details in SI files, Figure S3), CO conversion was always above 90%, showing high activity, even at 0 ^{o}C.

Gold on the α-Fe_2O_3 does not always present high activity. The support morphology is also observed to play an important role on the activity (Figure 6C). Au/Fe-R is far more active than the other materials, Au/Fe-P and Au/Fe-Com. The porous properties of Fe-R, high surface area and open porosity, which can result in increased surface defects sites, is suggested to be at the origin of the limited gold agglomeration into large particles. Compared to over Fe-R, gold presents heterogeneous dispersion in the Fe-P and Fe-Com support. In addition, large aggregates of gold particles can be detected over these two last solids (Figure S4, the details in the SI files). Then, the high and homogeneous dispersion of gold in the open porosity of Fe-R can explain its high activity compared to these obtained over the two lower surface area supports.

Furthermore, the stability of the catalysts of Fe-Com and Fe-R were also tested. Figure S5 shows the conversion of CO to CO_2 over Fe-Com and Fe-R catalysts. It is can be seen that the conversion of CO over 90% can be obtained over the two samples at 340 ^{o}C and 220 ^{o}C, respectively. The activity is stable for a certain period and then decreases with reaction time. The lifetimes of the Fe-Com and Fe-R are obviously different, the stability series is Fe-R>Fe-Com, indicating that the stability is depended on the crystal size and surface area.

The stability of Fe_2O_3 nanorods supported noble metals are presented in Figure S6 (1%Pd/Fe-R and 1%Pt/Fe-R). From the above results (Table 1 and Figure 3), it can be found that the noble particle size is strongly dependent on the properties of the supporters. Therefore, the stability of 1%Pt/Fe-R or 1%Pd/Fe-R catalysts are probably related to the particle size of noble metals, and the small Pd and Pt particle sizes are beneficial for enhancing the lifetime of the Pd/Fe-R and Pt/Fe-R catalysts.



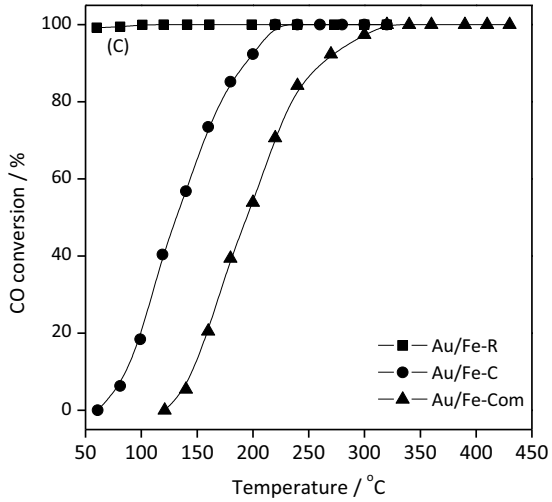


Figure 6. CO conversion versus reaction temperature on the synthesized materials. (A) Pure iron oxide morphologies (B) nanorods with different noble metals (C) gold supported on different iron oxide morphologies.

3.5 Conclusion

Different morphologies of α-Fe_2O_3 have been synthesized using an ionic liquid-assisted hydrothermal method. All materials are α-Fe_2O_3 pure phase. The TPR showed that α-Fe_2O_3 with various morphologies present comparable reduction properties. Reducibility is however strongly altered, with a first reduction process shifted to the low temperature, in the presence of noble metal on the surface. However, while the reducibility is only a few modified by the iron oxide morphology, large differences in oxygen mobility are observed. Then, oxygen mobility is favoured by the increase in surface area and decrease in crystal size, making the porous nanorod morphology the more active material for oxygen exchange.

Owing to the favourable physical properties of the iron oxides obtained using the ionic liquid-assisted route, high activity for CO oxidation can be achieved. In addition, due to the high noble metal dispersion obtained over the porous nanorod morphology, Pd and Au containing materials showed extremely high activity.

Experiment part:

Material synthesis

α-Fe_2O_3 synthesis in ionic liquid media. All the reagents were analytical grade, and were used without further purification. The ionic liquid 1-decyl-3-methyl imidazolium chloride (C_{10}mimCl) was purchased from the Centre for Green Chemistry and Catalysis (Lanzhou, China).

Nanoplate synthesis in the CH_3COOK system: At room temperature (~20 ^oC), an aqueous solution containing dissolved CH_3COOK (8 mmol) in de-ionized water (36.7mL) was mixed with $FeCl_3 \cdot 6H_2O$ (2.67 mmol) under vigorous stirring. Subsequently, 8 mmol of the C_{10}mimCl was added into the homogeneous brown solution under continuous stirring. After 30 min, the solution was transferred into a teflon-lined stainless-steel autoclave with a capacity of 55 mL, sealed and heated at 140 ^oC for 15 h. When the reaction was completed, the autoclave was cooled to the ambient temperature. The obtained red product was recovered by centrifugation at 10,000 rpm for 10 min, washed repeatedly with de-ionized water and ethyl alcohol until neutrality before being dried at 80 ^oC for 12 h. The final product was labelled as Fe-P.

Microcube synthesis in the NaOH system: 2.67 mmol of $FeCl_3 \cdot 6H_2O$ and 8 mmol of NaOH were mixed with 36.7 mL of de-ionized water under stirring. Subsequently, 8 mmol of C_{10}mimCl was added into the obtained solution. Then end of the procedure is similar than presented for the nanoplates, and the sample was denoted as Fe-C.

Porous nanorod synthesis in the NaOH system: Synthesis procedure, precursor and ionic liquid content are the same than those used for α-Fe_2O_3 microcube synthesis. Only the amount of NaOH was changed to 26.7 mmol. The final product was labelled as Fe-R.

All α-Fe_2O_3 materials were obtained by heating the as-prepared α-FeOOH compounds in air at 300 °C for 3 h (temperature increase rate = 5 °C min^{-1}).

Noble metal supported materials: Supported palladium and platinum materials were obtained by classical impregnation of an inorganic precursor in water. Palladium-containing solution (10 wt.% $Pd(NO_3)_2$ solution, Aldrich) was mixed with

5.5 mL of de-ioned water. The Pd precursor solution was then added dropwise into 0.1 g of Fe-R at room temperature under vigorous vibration. After overnight vibration, the resulted product was dried at 80 °C for 48 h. The dry solid was finally calcined under air at 300 °C for 1 h. The solid is denoted as (*1 wt.%*) Pd/Fe-R. For platinum impregnation, Platinum-containing solution (8 mg mL^{-1} H_2PtCl_6) was mixed with 5.5 mL of de-ioned water. The solution was thereafter added dropwise to 0.1 g Fe-R at room temperature under vigorous vibration. The end of the impregnation procedure was similar to that applied for Pd/Fe-R preparation. The solid is denoted Pt/Fe-R. Supported gold catalyst was prepared by deposition-precipitation method (denoted Au/Fe-R). $HAuCl_4$ solution (15 mg mL^{-1}) was mixed into 15 mL of de-ioned water. The solution was added dropwise to 0.1 g of Fe-R at room temperature under vigorous vibration. Ammonia solution (1 M) was used to adjust and keep the pH at ~8.0-9.0. After 6 h of aging at room temperature, the solid was washed with hot water several times until chloride could not be detected (using titration with 0.1 mol L^{-1} $AgNO_3$). Finally, the solid is recovered by centrifugation at 10,000 rpm for 10 min and dried at 80 °C for 12 h.

Physical and textural characterization

ICP-OES. Noble metal content was verified to be in accordance with the expected value by ICP-OES using an Optima 3000 XL spectrometer (PERKIN-ELMER).

X-ray photoelectron spectroscopy (XPS).

XPS was conducted on a Thermo-Fisher ESCALAB 250 system with Al*Kα* radiation under ultrahigh vacuum (UHV).

N_2 physisorption. N_2 adsorption measurements were performed on a Micromeritics TRISTAR 3000 instrument. Surface areas were obtained by the Brunauer-Emmett-Teller (BET) method. Desorption isotherm was used to determine the pore size distribution using the Barret Joyner Halenda (BJH) method.

XRD. Crystal structure was determined by X-ray diffraction, using a D5005 diffractometer from Bruker, equipped with a CuKα radiation (λ=1.5406 Å). Signal

was recorded for *2θ* between 20° and 80° with a recording step of 0.05° each 3 s. Phase identification was made by comparison with JCPDS database. Crystal size was determined using the Scherrer equation, after Warren's correction for instrumental broadening.

TEM. Morphology and pore structure were evaluated by Transmission Electronic Microscopy (TEM) coupled with Energy Dispersive X-ray Spectroscopy (EDXS). Micrographs were obtained on a JEOL 2100 instrument (operated at 200 kV with a LaB_6 source and equipped with a Gatan Ultra scan camera). EDX spectroscopy was carried out with a Hypernine (Premium) detector (active area: 30 mm^2) using the software SM-JED 2300T for data acquisition and treatment.

Temperature programmed reduction. TPR-H_2 experiments were performed on an AUTOCHEM instrument from Micromeritics. About 50 mg of sample was introduced in a microreactor. The material was initially activated under simulated air (total flow rate = 30 mL min^{-1}) at 300 °C for 1 h. After cooling down to room temperature, a reducing flow (5 vol.% of H_2 in Ar) was stabilized at a flow rate of 30 mL min^{-1}, and then the temperature of the reactor was increased from 25 °C to 1000 °C with a ramp of 5 °C min^{-1}. Evolution of the H_2 concentration with temperature was recorded on an on-line TCD.

CO oxidation activity measurement

CO oxidation reaction was performed in a tubular microreactor with 75 mg of catalyst. After activation at 300 °C of the catalyst under simulated air (30 mL min^{-1}), the reaction flow composed of 5 vol.% of CO - 20 vol.% O_2 - bal. N_2 at a total flow rate of 60 mL min^{-1} (given a GHSV of 22500 h^{-1}) was stabilized. The conversion was recorded under isothermal conditions each 20-30 °C (depending on the conversion). The concentration of CO and CO_2 in the effluent gas was on-line analyzed using a VARIAN (model CP-3800) gas chromatograph equipped with a TCD and a Porapak column for separation.

OIE (Oxygen Isotopic Exchange)

Background

The oxygen isotopic exchange (OIE) reaction is used to evaluate oxygen reactivity. The exchange mechanism and data treatment are fully described in Refs [55,56] and are shortly summarized herein. The exchange reaction can be described by the following equation, even if different mechanisms are depicted:

$$^{18}O_{(g)} + {}^{16}O_{(s)} \rightarrow {}^{16}O_{(g)} + {}^{18}O_{(s)}$$

Where (s) and (g) refer to oxygen from the solid and from the gas phase, respectively.

Three exchange mechanisms are distinguished in the literature: equilibration reaction, the simple heteroexchange and complex heteroexchange [56].

The equilibration reaction consists in the reaction between two isotopes from the gas phase, as described in the following equation:

$$^{18}O_{2\ (g)} + {}^{16}O_{2\ (g)} \rightarrow 2\ {}^{18}O^{16}O_{\ (g)}$$

In this last case, oxygen from the solid does not participate to the reaction. Equilibration supposes adsorption, equilibration, and desorption steps on the surface of a material [57,58]. Then, the ^{18}O and ^{16}O fractions in the gas phase remain constant all during the test.

The simple exchange supposes the participation (or exchange) of only one oxygen atom from the solid at each step. The two following equations characterize this mechanism:

$$^{18}O^{18}O_{(g)} + {}^{16}O_{(s)} \rightarrow {}^{18}O^{16}O_{(g)} + {}^{18}O_{(s)}$$

$$^{18}O^{16}O_{(g)} + {}^{16}O_{(s)} \rightarrow {}^{16}O^{16}O_{(g)} + {}^{18}O_{(s)}$$

In contrast to the simple heteroexchange, complex heteroexchange mechanism supposes the participation of two atoms of the solid at each step [59].

$$^{18}O^{18}O_{(g)} + 2{}^{16}O_{(s)} \rightarrow {}^{16}O^{16}O_{(g)} + 2{}^{18}O_{(s)}$$

The two following reactions also occur in the case of the occurrence of $^{16}O^{18}O$ isotopomers in the gas phase:

$$^{18}O^{16}O_{(g)} + 2{}^{16}O_{(s)} \rightarrow {}^{16}O^{16}O_{(g)} + {}^{18}O_{(s)} + {}^{16}O_{(s)}$$

$$^{18}O^{16}O_{(g)} + 2{}^{18}O_{(s)} \rightarrow {}^{18}O^{18}O_{(g)} + {}^{18}O_{(s)} + {}^{16}O_{(s)}$$

Some oxides were found to present mainly this mechanism of exchange. Boreskov *et al.* [60], who observed an oxygen reaction order near 0.5 for α-Fe_2O_3 presenting mainly this mechanism, assumed a dissociative adsorption on the anionic vacancies on the surface of the solid.

Experimental

The exchange experiment was carried out in a recycling U-shaped microreactor. The recirculation volume (V = 60 cm^3; recirculation rate = 170 cm^3 s^{-1}) was coupled to a quadrupolar mass spectrometer (PFEIFFER VACUUM). The gas sampling was regulated by a thermo-valve adjusted to maintain a constant pressure of 1×10^{-6} mbar in the ionization chamber of the mass spectrometer. An equivalent of 20.0 mg of the as-prepared sample is inserted in a microreactor, heat treated up to 300 °C under O_2 (ramp = 5 °C min^{-1}, total flow rate Q_{O2} = 20 mL min^{-1}) and cooled down to the test temperature. After temperature stabilization, the sample was evacuated under dynamic vacuum for 30 min. For the oxygen exchange experiments, around 65 mbar of pure $^{18}O_2$ was introduced into the recirculation volume. The temperature-programmed exchange experiments are performed from 100 °C to 600 °C (ramp = 2 °C min^{-1}), and partial pressure evolution of $^{18}O_2$ (mass 36), $^{16}O_2$ (mass 32), and $^{16}O^{18}O$ (mass 34) are recorded on the mass spectrometer allowing to quantify the ^{18}O fraction in the gas phase (α) and the number of oxygen atom exchanged (N_{ex}).

References

[1] S. Royer, D. Duprez, *ChemcatChem*, 2011, 3, 24-65.

[2] B. Lewis, G.V. Elbe, Combustion, flames, and explosions of gases, 3rd ed., Academic Press, Orlando, 1987.

[3] A.S. Kireev, V.M. Mukhin, S.G. Kireev, V.N. Klushin, S.N. Tkachenko, Rus. *J. Appl. Chem*. 2009, 82, 169-171.

[4] Y.B. Yu, T. Takei, H. Ohashi, H. He, X.L. Zhang, M. Haruta, *J. Catal.* 2009, 267, 121-128.

[5] J.W. Saalfrank, W.F. Maier, *Angew. Chem. Int. Ed.* 2004, 43, 2028-2031.

[6] J.B. Lian, X.C. Duan, J. Ma, P. Peng, T. Kim, W.J. Zheng, *ACS. Nano* 2009, 3, 3749-3761.

[7] J. Hulliger, *Angew. Chem. Int. Ed*. 1994, 33, 143-162.

[8] C.M. Lee, H.J. Jeong, S.T. Lim, M.H. Sohn, D.W. Kim, *Appl. Mater. Interfaces* 2010, 2, 756-759.

[9] J. H. Bang, K.S. Suslick, *J. Am. Chem. Soc.* 2007, 129, 2242-2243

[10] Q.X. Gao, X.F. Wang, J.L. Di, X.C. Wu, Y.R. Tao, *Catal. Sci. Technol.* 2011, 1, 574-577.

[11] C.J. Jia, L.D. Sun, F. Luo, X.D. Han, L.J. Heyderman, Z.G. Yan, C.H. Yan, K. Zheng, Z. Zhang, M. Takano, N. Hayashi, M. Eltschka, M. Kla#ui, U. Ru#diger, T. Kqsama, L. Cervera-Gontard, R.E. Dunin-Borkowski, G. Tzvetkov, J. Raabe, *J. Am. Chem. Soc.* 2008, 130, 16968-16977.

[12] C.J. Jia, L.D. Sun, Z.G. Yan, Y.C. Pang, L.P. You, C.H. Yan, *J. Phys. Chem. C.* 2007, 111, 13022-13027.

[13] C.J. Jia, L.D. Sun, Z.G. Yan, L.P. You, F. Luo, X.D. Han, Y.C. Pang, Z. Zhang, C.H. Yan, *Angew. Chem. Int. Ed.,* 2004, 4328-4333.

[14] L.L. Li, Y. Chu, Y. Liu, L.H. Dong, *J. Phys. Chem. C* 2007, 111, 2123-2127.

[15] J. Ma, J.B. Lian, X.C. Duan, X.D. Liu, W.J. Zheng, *J. Phys. Chem. C* 2010, 114, 10671-10676.

[16] K. Woo, H.J. Lee, J.P. Ahn, Y.S. Park, *Adv. Mater.* 2003, 15, 1761-1764.

[17] Y.M. Zhao, Y.H. Li, R.Z. Ma, M.J. Roe, D.G. McCartney, Y.Q. Zhu, *Small.* 2006, 2, 422-427.

[18] Z.M. Li, X.Y. Lai, H. Wang, D. Mao, C.J. Xing, D. Wang, *Nanotechnology* 2009, 20, 245603.

[19] C.Z. Wu, P. Yin, X. Zhu, C.Z. Ouyang, Y. Xie, *J. Phys. Chem. B.* 2006, 110, 17806-17812.

[20] L.S. Zhong, J.S. Hu, H.P. Liang, A.M. Cao, W.G. Song, L.J. Wan, *Adv. Mater.* 2006, 18, 2426-2431.

[21] S.Y. Zeng, K.B. Tang, T.W. Li, Z.H. Liang, D. Wang, Y.K. Wang, W.W. Zhou, *J. Phys. Chem. C.* 2007, 111, 10217-10225.

[22] V. Escax, Impéror-Clerc, D. Bazin, A. Davidson, C.R. *Chimie* 2005, 8, 663-677.

[23] E. Delahaye, V. Escax, N. Hassan, A. Davidson, R. Aquino, V. Dupuis, R. Perzynski, Y. L. Raikher, *J. Phys. Chem. B.* 2006, 110, 26001-26011.

[24] A. Rumplecker, F. Kleitz, E.L. Salabas, F. Schuth. *Chem. Mater*. 2007, 19, 485-496.

[25] Y. Q. Wang, C. M. Yang, W. Schmidt, B. Spliethoff, E. Bill, F. Schuth, *Adv. Mater.* 2005, 17, 53-56.

[26] S. J. Sun, Q.M. Gao, H. L. Wang, J. K. Zhu, H. L. Guo, *Appl. Catal. B* 2010, 97, 284-291.

[27] S. W. Cao, Y.J. Zhu, *Acta. Mater.* 2009, 57, 2154-2165.

[28] D. Freudenmann, S. Wolf, M. Wolff, C. Feldmann, *Angew. Chem. Int. Ed.* 2011, 50, 11050-11060.

[29] Z. Ma, J.H. Yu, S. Dai, *Adv. Mater.* 2010, 22, 261-285.

[30] E. R. Parnham, R. E. Morris, *Acc. Chem. Res.* 2007, 40, 1005-1013.

[31] A. Taubert, *Acta. Chim. Slov.* 2005, 52, 183-186.

[32] D.A.H. Cunningham, T. Kobayashi, N. Kamijo, M. Haruta, *Catal. Lett.* 1994, 25, 257-264.

[33] Y. Fang, Y. Yao, *J. Catal.* 1984, 87, 152-162.

[34] G. Ertl, *Science* 1991, 254, 1750-1755.

[35] J. Barbier, D. Duprez, *Appl. Catal. B* 1993, 3, 61-83.

[36] R.M. Heck, R.J. Farrauto, S.T. Gulati, Catalytic air pollution control: commercial technology, 3rd ed., John Wiley & Sons, Inc., 2009.

[37] D. Duprez, C. Descorme, in *Catalysis by Ceria and Related Materials* (Ed.: A. Trovarelli), Imperial College Press, 2002, 243-280.

[38] Y.H. Zheng, Y. Cheng, Y.S. Wang, F. Bao, L.H. Zhou, X.F. Wei, Y.Y. Zhang, Q. Zheng, *J. Phys. Chem. B*, 2006, 110, 3093-3097.

[39] G.H. Wang, W.C. Li, K. M. Jia, B. Spliethoff, F. Schuth, A.H. Lu, *Appl. Catal. A* 2009, 364, 42-47.

[40] X.C. Jiang, A.B. Yu, *J. Mater. Process. Technol.* 2009, 209, 4558-4562.

[41] M.C. Kung, R.J. Davis, H.H. Kung, *J. Phys. Chem. C.* 2007, 111, 11767-11775.

[42] Z.Y. Zhong, J. Highfield, M. Lin, J. Teo, Y.F. Han, *Langmuir* 2008, 24, 8576-8582.

[43] X.J. Liu, J.F. Liu, Z. Chang, X.M. Sun, Y.D. Li, *Catal. Comm.* 2011, 12, 530-534.

[44] Y. Zhu, L. Tian, Z. Jiang, Y. Pei, S. H. Xie, M. H. Qiao, K. N. Fan, *J. Catal.* 2011, 106-118.

[45] G. Munteanu, L. Ilieva, D. Andreeva, *Thermochimica. Acta* 1997, 291, 171-177.

[46] L.I. Ilieva, D.H. Andreeva, A.A. Andreev, *Thermochimica. Acta* 1997, 292, 169-174.

[47] P.K. Stoimenov, V. Zaikovski, K.J. Klabunde, *J. Am. Chem. Soc.* 2003, 125, 12907-12913.

[48] U. Oran, D. Uner, *Appl. Catal. B* 2004, 54, 183-191.

[49] D. Gavril, A. Georgaka, V. Loukopoulos, G. Karaiskakis, B.E. Nieuwenhuys, *Gold Bull*. 2006, 39, 192-199.

[50] M. Haruta, S. Tsubota, T. Kobayashi, H. Kageyama, M.J. Genet, B.J. Delmon, *J. Catal.* 1993, 144, 175-192.

[51] M. Comotti, W.C. Li, B. Spliethoff, F. Schùth, *J. Am. Chem. Soc.* 2006, 128, 917-924.

[52] N. Lopez, T.V.W. Janssens, B.S. Clausen, Y. Xu, M. Mavrikakis, T. Bligaard, J.K. Nøskov*, J. Catal.* 2004, 223, 232-235.

[53] L. Lopez, J.K. Nørskov, *J. Am. Chem. Soc.* 2002, 124, 11262-11263.

[54] L. Guczi, D. Horvath, Z. Paszti, G. Peto, *Catal. Today* 2002, 72, 101-105.

[55] L. Guczi, G. Peto, A. Beck, K. Frey, O. Geszti, G. Molnar, C. Daroczi, *J. Am. Chem. Soc.* 2003, 125, 4332-4337.

[56] G.K. Boreskov, *Adv. Catal.* 1964, 15, 285-339.

[57] S. Royer, D. Duprez, S. Kaliaguine, *J. Catal.* 2005, 234, 364-375.

[58] A. Galdikas, D. Duprez, C. Descorme, *Appl. Surf. Sci.* 2004, 236, 342-355.

[59] C. Descorme, D. Duprez, *Appl. Catal. A* 2000, 202, 231-241.

[60] G.K. Boreskov, V.S. Muzykantov, N.Y. Ann, *Acad. Sci.* 1973, 213, 137-160.

Sumplementary information for

Ionic Liquid-Mediated α-Fe_2O_3 Shape-Controlled Nanocrystal-Supported Noble Metals: Highly Active Materials for CO Oxidation

Liwei Hou, Qinghua Zhang, François Jérôme, Daniel Duprez, Fabien Can, Xavier Courtois, Hui Zhang* and Sébastien Royer*

Table S1. The XPS results for 1%Au/Fe-R and 1%Au/Fe-Com.

Samples	Surface atom concentration from XPS / %			Banding Energy / eV		FWHM /eV
	Fe	O	Au	Fe2P	$Au4f_{7/2}$	
1%Au/Fe-Com	33.90	65.13	0.97	710.6	84.1	1.5
1%Au/Fe-R	34.40	64.39	1.21	710.8	83.9	1.4

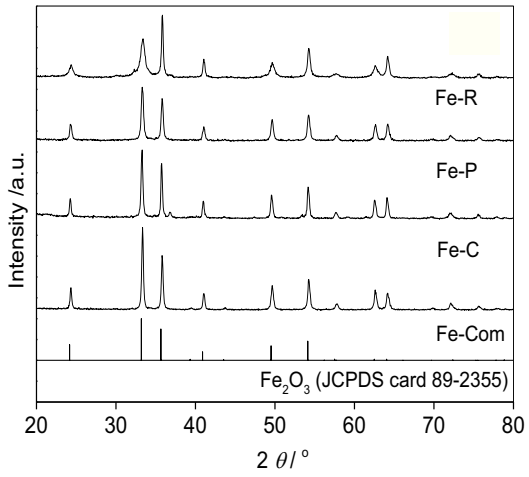


Figure S1. XRD patterns recorded for the different α-Fe_2O_3 morphologies.

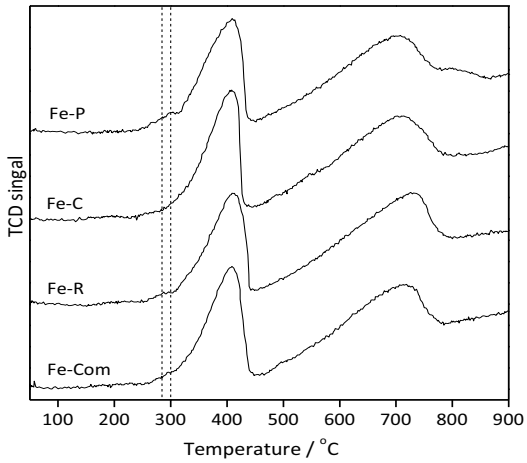


Figure S2. TPR-H_2 profiles recorded for iron oxide nanostructures.

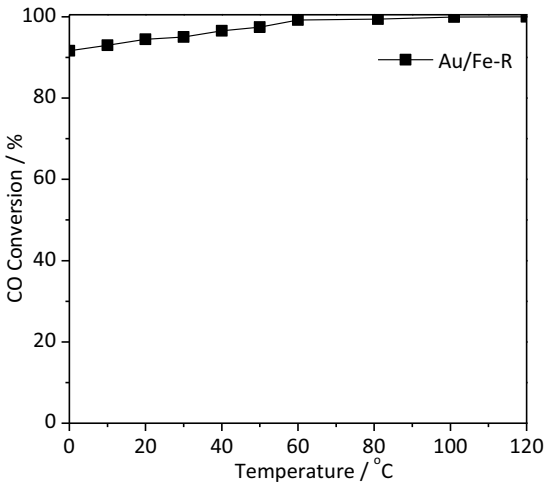


Figure S3. CO conversion versus reaction temperature on the synthesized material 1%Au/Fe-R

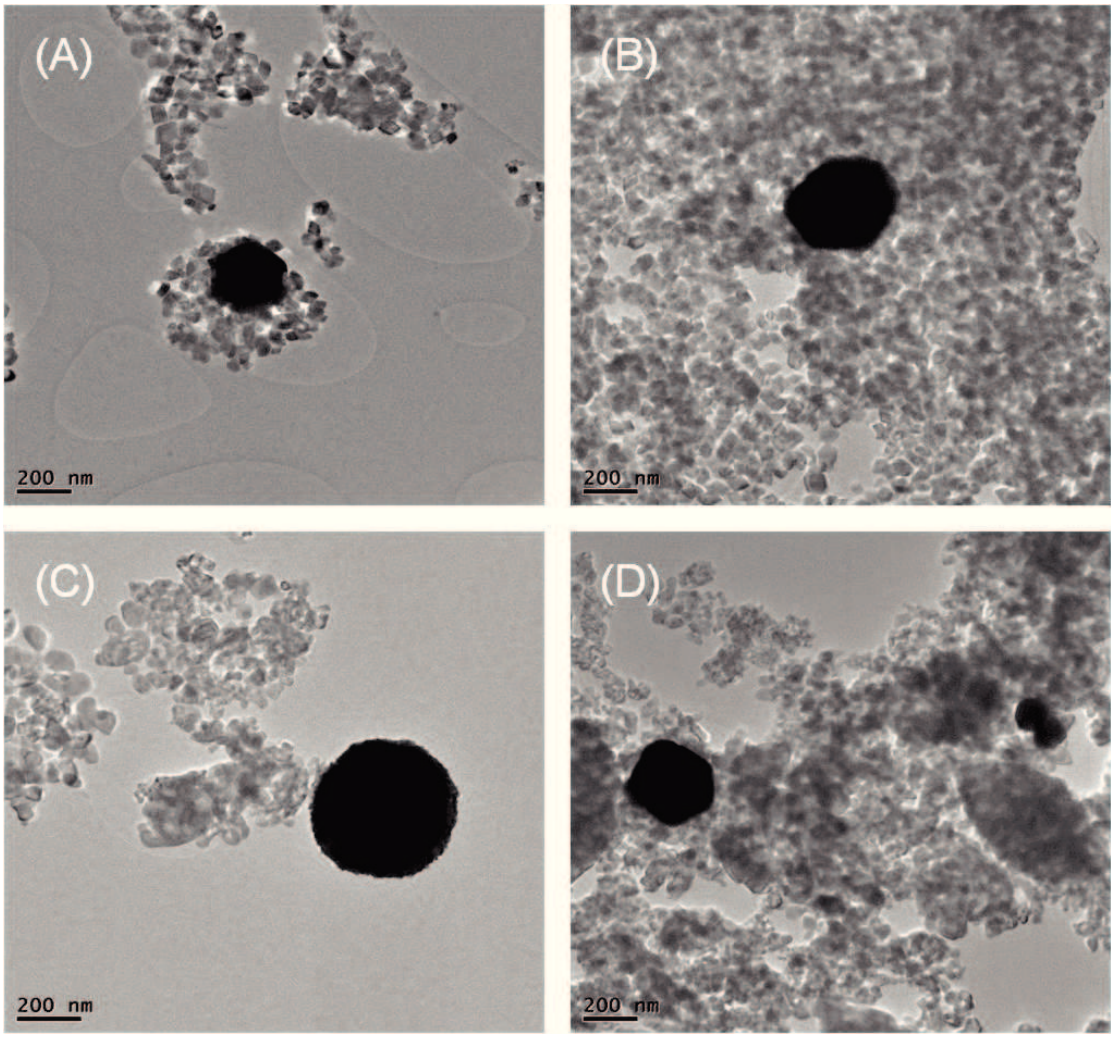


Figure S4. Evidence of large Au particles on the low surface area α-Fe_2O_3 materials: (A)-(B), Au particles supported on Fe-P; (C)-(D), Au particles supported on Fe-Com.

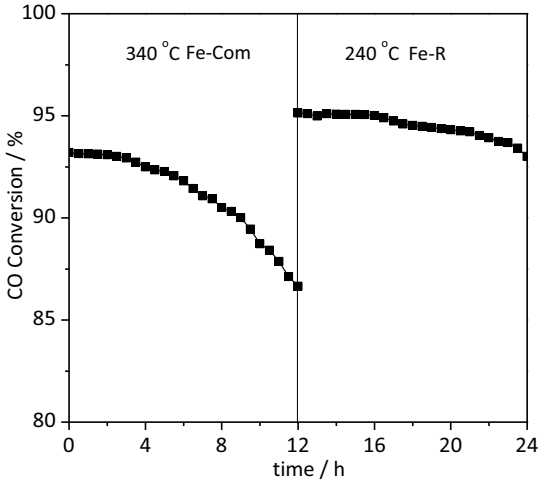


Figure S5. The stability test of the Fe-Com and Fe-R catalysts for 12 h

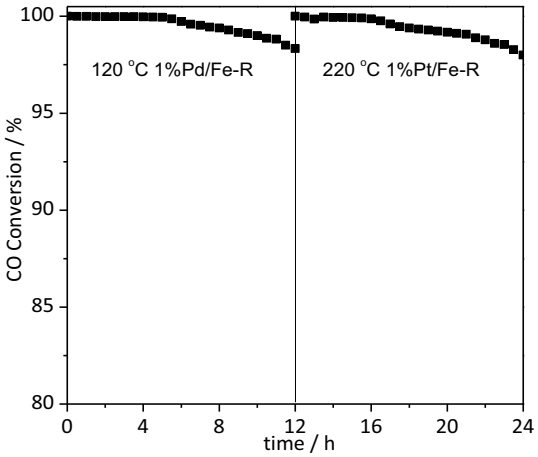


Figure S6. The stability test of the 1%Pd/Fe-R and 1%Pt/Fe-R catalysts for 12 h.

Chapter 4 Highly efficient AOP process using an ultrasound-assisted, heterogeneous Fenton-like reaction

Example of tetracycline degradation over a commercial magnetite catalyst

Article:

Liwei Hou, Sébastien Royer, Hui Zhang and Liguo Wang, to be submitted.

4.1 Introduction

Over the last few decades, advanced oxidation processes (AOPs) based on hydroxyl radical chemistry have been successfully employed for the degradation of tetracycline [1-8]. The activation of hydrogen peroxide (H_2O_2) over heterogeneous Fe-bearing minerals was recently demonstrated to be highly efficient for treating organic pollutants over a wide pH range [9-12]. Similar to the widely accepted free radical chain mechanism of the classic homogeneous Fenton reaction, the main reactions for the heterogeneous reaction involve the following steps [10]:

$$\equiv Fe(II) + H_2O_2 \rightarrow \equiv Fe(III) + OH^- + {}^{\bullet}OH \quad (5\text{-}1)$$

Then, the structural ≡Fe(III) reacts with H_2O_2 to form $\equiv Fe(OOH)^{2+}$.

$$\equiv Fe(III) + H_2O_2 \rightarrow \equiv Fe(OOH)^{2+} + H^+ \quad (5\text{-}2)$$

The limiting step in the Fenton reaction is the slow kinetic rate of the reduction of $\equiv Fe(OOH)^{2+}$ to ≡Fe(II) and ${}^{\bullet}HO_2$ (Eq. 5-3).

$$\equiv Fe(OOH)^{2+} \rightarrow \equiv Fe(II) + {}^{\bullet}HO_2 \quad (5\text{-}3)$$

The ≡Fe(III) reacts with ${}^{\bullet}HO_2$ to form ≡Fe(II), allowing the Fe to be recycled to ≡Fe(II) (Eq. 5-4).

$$\equiv Fe(III) + {}^{\bullet}HO_2 \rightarrow \equiv Fe(II) + O_2 + H^+ \quad (5\text{-}4)$$

One of the iron oxides, magnetite (Fe_3O_4) was selected as the catalyst for the following reasons: it contains Fe(II) sites; is cheap, non-toxic, environmentally friendly, easily recovered, and recyclable; and has low solubility in the reaction medium [13]. Consequently, Fe_3O_4 can be used for the efficient remediation of PAH-contaminated soils, Rhodamine B (RhB), and pentachlorophenol (PCP) in Fenton-like processes [14-15]. However, the catalyst is poisoned during the oxidation process due to the adsorption of the reaction intermediates on the surface active sites [16]. Moreover, the slow degradation rates observed for these recalcitrant organics may limit its practical application in industry. An effective means of improving catalytic efficiency and stability for the degradation of pollutants is thus urgently needed.

Sonochemical technology is an AOP that is widely used for the destruction of organic pollutants via pyrolysis near cavitation bubbles and/or sonochemically generated $^{\bullet}OH$ radicals [17]. However, high removal efficiency and mineralization are difficult to achieve with ultrasound technology alone [18]. Hence, recent research has focused on the combination of ultrasound with other AOPs because these novel combined techniques have proven to be more effective for the degradation of recalcitrant pollutants than ultrasound alone [19]. To date, several types of heterogeneous catalysts, such as CuO, Cu/Al_2O_3 [20], $CuO/ZnO/Al_2O_3$ [21], Fe_2O_3-Al_2O_3-meso [22], FeO_x-SBA-15 [10,23], and goethite [11] have been proposed for sono-enhanced, heterogeneous Fenton process-mediated degradation of organic pollutants. Particularly promising results have been obtained when Fe_3O_4 is used as the heterogeneous catalyst for the decolorization of RhB under coupled ultrasound/heterogeneous Fenton conditions [24]. In addition to enhancing degradation rates, ultrasonic irradiation can also remove the products from the surface of the catalyst, thereby leaving a clean and reactive catalyst surface for subsequent reactions [11,25].

In this study, the performance of an ultrasound-assisted, heterogeneous Fenton process is evaluated. The removal of tetracycline (TC), an antibiotic, from wastewater by conventional water treatment technologies is not as effective as anticipated [26]. An adequate catalyst system has not been reported for the degradation of TC, and the detailed degradation mechanism of the ultrasound/heterogeneous Fenton process has not been investigated. Hence, the present contribution investigates the performance of a sono-Fenton-like process that uses Fe_3O_4 as a heterogeneous catalyst for the removal of TC. The effects of operating parameters such as ultrasonic power, initial pH, Fe_3O_4 loading, H_2O_2 concentration, temperature, and initial TC concentration, are extensively examined. The mineralization of the solution is assessed by total organic carbon (TOC) abatement. The change in the acute toxicity profiles is obtained from the inhibition of *D. magna* immobilization essays. A $^{\bullet}OH$-based reaction mechanism is also proposed based on the results of the use of different types of scavengers.

Moreover, a membrane system is employed to investigate whether there is direct contact between the catalyst and existing TC during the reaction. Finally, the stability of the catalyst, which is also a crucial parameter, is evaluated.

4.2 Materials and methods

Tetracycline hydrochloride (TC, $C_{22}H_{25}N_2O_8Cl \geq 99\%$, Sigma-Aldrich) was used as received. Hydrogen peroxide (H_2O_2, 30 wt.% in H_2O) was obtained from Sinopharm Chemical Reagent Co., Ltd. (Shanghai, China). The magnetite catalyst (Fe_3O_4) was obtained from Prolabo Co. (Paris, France). Other chemicals were purchased from Shanghai Reagent Co., Ltd. (Shanghai, China). Dialysis bags (PVDF) with a 180 Dalton molecular weight cutoff (MWCO) were obtained from Union Carbide Corp. (State of Connecticut, Danbury, U.S.).

A tetracycline hydrochloride stock solution (100 mg L^{-1}) was prepared in deionized water. The initial pH of the stock solution was 3.7, and in consideration of the practical application of the TC treatment, the pH was not adjusted in our study. The catalysts are denoted Fe_3O_4-X, where X represents the number of times the catalyst was used. The commercial magnetite catalysts (Fe_3O_4) before and after each reaction were stored in the vacuum oven at room temperature to prevent oxidizing in the air. Then, they were systematically characterized using X-ray diffraction (XRD), X-ray Photoelectron Spectroscopy (XPS), N_2-physisorption and ICP-OES. Complete descriptions of the catalyst characterization and the conditions of the activity tests are provided in the Supporting Information (SI): catalyst characterizations and activity tests section.

The TC concentration was determined using a high-performance liquid chromatography (HPLC) instrument equipped with a Shim-Pack VP-ODS-C18 column (4.6 mm × 250 mm, 5 μm). The total organic carbon (TOC) content was measured with a Multi N/C® 2100 (Analytik Jena AG) TOC meter.

To investigate whether direct contact between the catalyst and TC is a prerequisite for Fenton-like degradation, a novel membrane separation setup was

designed. The setup of the separated system is shown in Figure 1. A PVDF dialysis bag was used that allowed components in the solution with molecular weights (MW) below 180 Dalton, such as ions and radicals ($^{\bullet}OH$), to diffuse through the pores. This type of dialysis bag does not react with the organic compounds and active species. Molecules larger than the membrane pores remained outside of it, permitting the separation of TC and Fe_3O_4. The dialysis bag contained 10 mL of a 100 mg L^{-1} TC solution. The outer system contained 100 mL of an aqueous suspension of 0.1 g Fe_3O_4, and the suspension was continuously stirred with a mechanical stirrer to keep the catalyst evenly distributed in the solution outside the container. Then, H_2O_2 was added to the outer system to start the reaction. After 60 min, 1.0 mL of the reacted solution from both sides of the container was sampled to measure the TC concentration. The outer system was replaced by water, US/H_2O, US/H_2O_2, and the sono-Fenton (US/Fe^{2+}/H_2O_2) system in succession.

Acute toxicity was evaluated with *Daphnia magna* immobilization essays. These tests were performed in accordance with the conditions prescribed by the OECD Guideline 202 method [27]. Complete description of the acute toxicity was shown in SI file: catalyst characterizations and activity tests.

To investigate the stability and reusability of the catalyst, the solids were immediately separated from the solution with a magnet at the end of each run, dried in a vacuum oven at 25 °C, and used without prior washing in the next run. The dissolved iron concentration in the reacted solution was quantified by ICP after each test. The residual H_2O_2 concentration after the reaction tests was also measured via colorimetry with a UV spectrophotometer (Secomam, RS232) after complexation of the hydrogen peroxide with a vanadate salt.

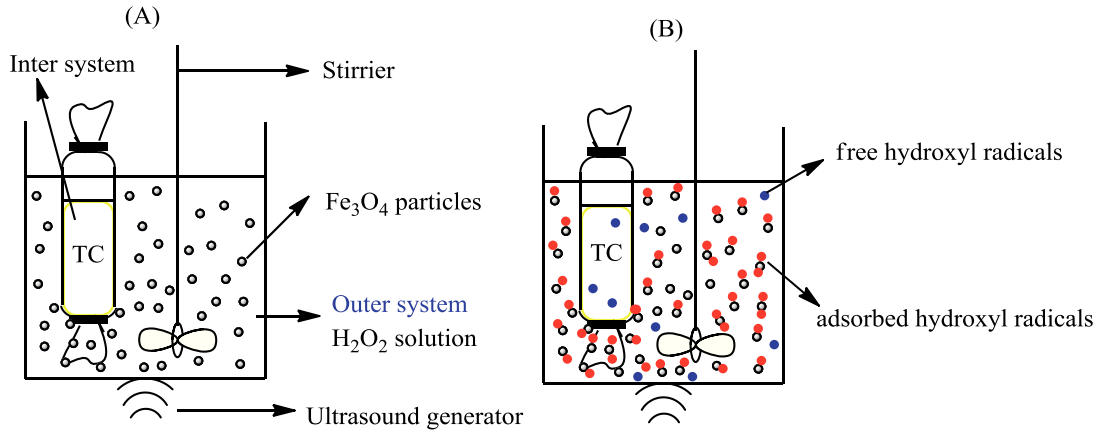


Figure 1 Schematic illustration of setup for the separation system

4.3 Results and discussion

4.3.1 Physicochemical properties

The X-ray diffraction patterns of the catalyst revealed that Fe_3O_4 had a pure magnetite structure (Figure 2). All peaks could be indexed to the pure face-centered cubic structure of magnetite (JCPDS Card 19-0629). The diffraction peaks located at $2\theta = 30.2$, 35.6, 43.2, 53.6, 57.1, 62.6, and 74.2° could be indexed to the (220), (311), (400), (422), (511), (440), and (553) planes of Fe_3O_4, respectively, by comparison with previously reported data for Fe_3O_4 nanoparticles [28]. The crystal sizes determined from the XRD results and the Scherrer equation were 77.3 nm for the catalyst before use. However, the XRD pattern of Fe_3O_4 is believed to be similar to that of γ-Fe_2O_3, which is also black in color. However, the compositions of these two types of materials are different. To verify that the material was Fe_3O_4 rather than γ-Fe_2O_3, the composition of the catalyst was determined from the Fe^{2+}/Fe^{3+} ratio both in the bulk and on the surface of the catalyst, which was measured by chemical analysis and XPS, respectively. First, the total iron content ($Fe^{(II)}$ and $Fe^{(III)}$) was measured by chemical analysis, and the $Fe^{(II)}/Fe^{(III)}$ ratio was found to be approximately 0.47 (Table 1). Because the stoichiometric Fe_3O_4 can also be expressed as $FeO{\bullet}Fe_2O_3$, the $Fe^{(II)}/Fe^{(III)}$ ratio should be 1:2, or 0.49. Clearly, this value is consistent with the calculated value. In addition, the surface element concentrations and valence states of the Fe_3O_4-0 and Fe_3O_4-3 samples were also characterized by

XPS. The attenuation length depends on the electron kinetic energy and emission angle. It has been reported that no satellite peak is present in the XPS spectrum for Fe_3O_4 [29-31], and it was also confirmed in our study (Figure 3). The peak positions of Fe $2p_{3/2}$ and Fe $2p_{1/2}$ were 710.5 and 724.1 eV, respectively, which are higher than the values obtained for γ-Fe_2O_3 [31]. The Fe $2p_{3/2}$ XPS spectra of Fe_3O_4-0 and Fe_3O_4-3 are shown in (Figure 3). Based on the Fe^{2+} and Fe^{3+} peak shape parameters and peak positions of Fe_3O_4 reported in the literature [31], the main relative areas of each constituent peak were calculated, and $Fe^{(II)}/Fe^{(III)}$ ratio was obtained (Table 1). Based on these result, we conclude that the magnetite material (Fe_3O_4-0) is pure with no γ-Fe_2O_3 present. However, the element composition changed after 3 runs (Erreur ! Source du renvoi introuvable.), an indication of the stability of the catalyst as discussed below in the catalyst stability section.

After the reaction, the surface area of the catalyst was larger than that of fresh catalyst. The SSA of the catalyst was significantly smaller prior to the reaction (Table 1). Notably, the SSA of Fe_3O_4-3 (4.3 m^2 g^{-1}) was larger than that of Fe_3O_4-0 (0.7 m^2 g^{-1}), and this sample had a smaller crystal size than the other samples, indicating that the ultrasound cracked the surface of the catalyst to increase the SSA during the reaction. Furthermore, the aggregated particles broke into pieces under the continuous ultrasound radiation, as supported by SEM and TEM analysis.

Representative SEM and TEM images of the catalyst before and after the heterogeneous or ultrasound-assisted heterogeneous reactions are shown in Figure 4 and Figure 5. A compact aggregation of many interconnected particles was observed for Fe_3O_4-0, resulting to large, uniform bulk structures (Figure 4). These Fe_3O_4-0 structures are consistent with the small SSA described above.

To further elucidate the morphology and structure of Fe_3O_4-0, TEM images were obtained (Figure 5). The average size of the Fe_3O_4-0 particles was 200-300 nm along the edge, a value that is much larger than the corresponding size calculated from the XRD pattern (Table 1). The results largely support the initial aggregation of the material observed in the SEM and TEM images (Figure 4A and Figure 5A).

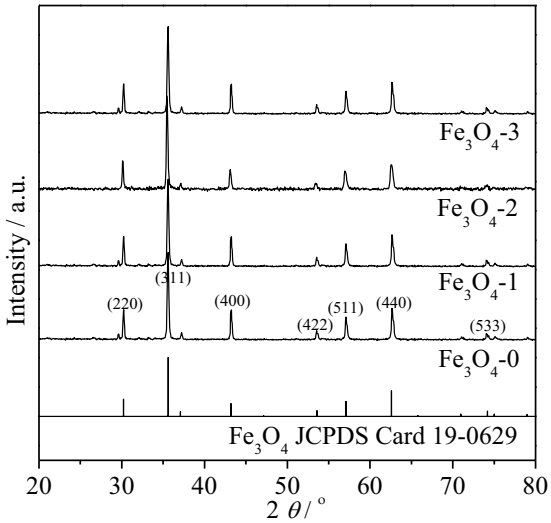


Figure 2. XRD patterns of Fe_3O_4 particles before and after the reactions

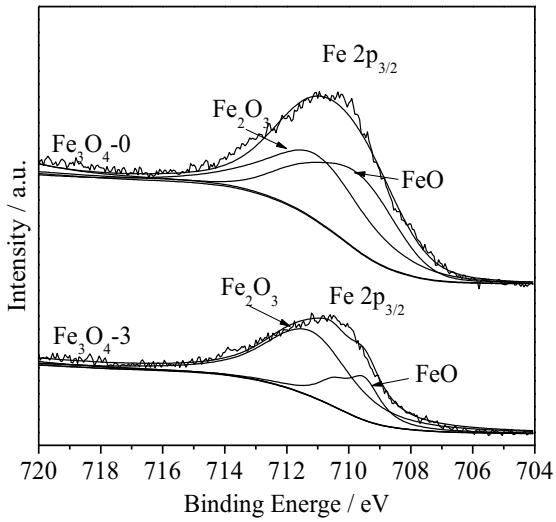


Figure 3 XPS details of the Fe $2p_{3/2}$ peaks of the as-synthesized Fe_3O_4-0 and the Fe_3O_4-3.

Table 1 Physico-chemical properties of fresh and recycled Fe_3O_4 in US/Fe_3O_4/H_2O_2 system

Sample	Morphology	Fe_{tot}[a]/ *wt%*	*DI*[b]/ (nm)	SSA[c]/ (m^2 g^{-1})	Atomic ratio Fe^{2+}/Fe^{3+} [d]		pH_{PZC}[e]
					Bulk	Surface	
Fe_3O_4-0	uniform	70if	77.3	0.7	0.47ormo	0.45ormo	7.2
Fe_3O_4-1		7025	64.4	2.9	—	—	—
Fe_3O_4-2		7094	61.1	3.5	—	—	—
Fe_3O_4-3		7051	59.9	4.3	0.38ormo	16.6ormo	—

[a], bulk ratio between Fe(II) and Fe(III) in Fe_3O_4 ; [b], the crystal domain size evaluated from the X-ray line broadening using the Scherrer equation; [c], the specific surface area evaluated using the BET model; [d], surface ratio of Fe(II) and Fe(III) obtained by XPS analysis; [e], the pH of point of zero charge

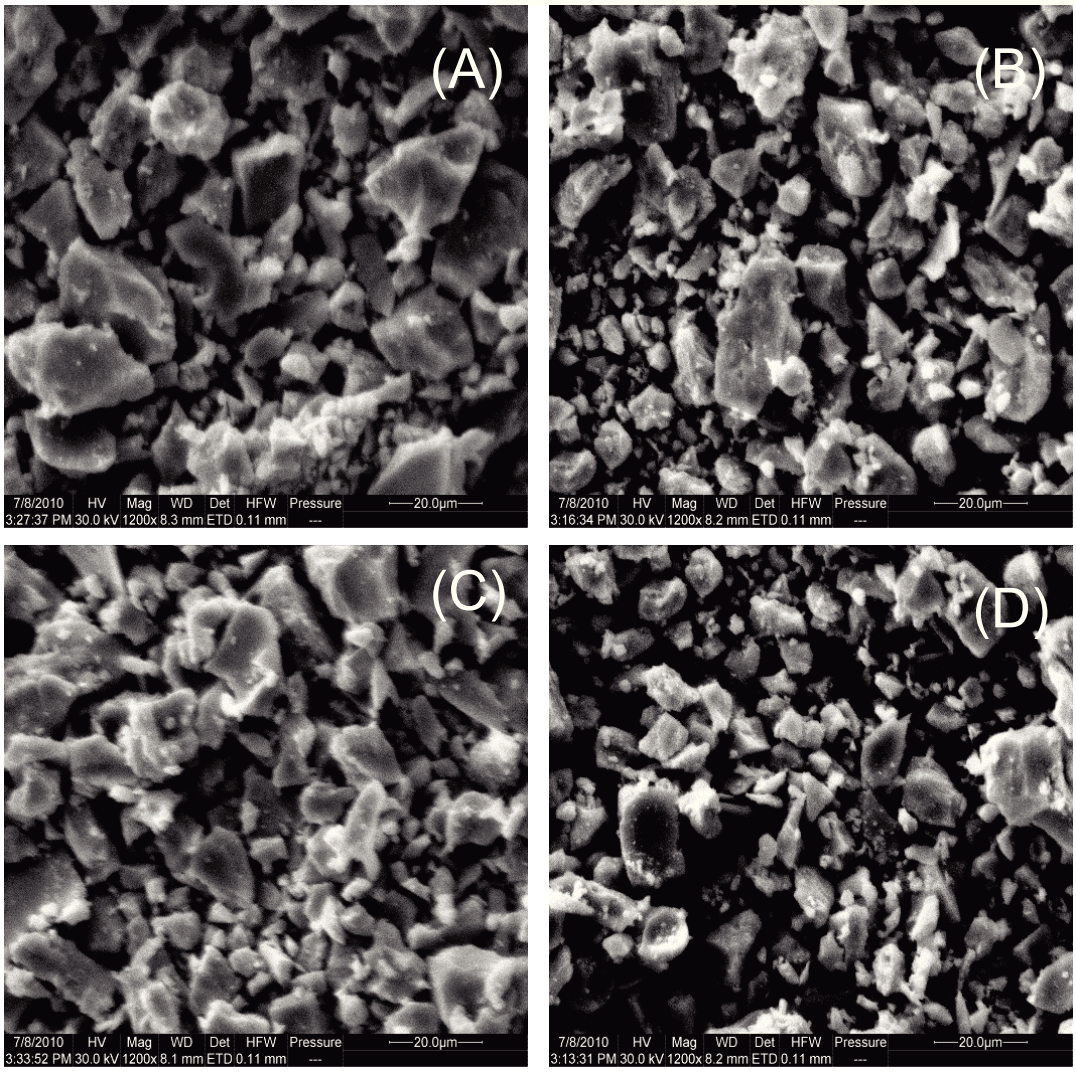


Figure 4. Representative SEM images of Fe_3O_4: A: Fe_3O_4-0; B: Fe_3O_4-1; C: Fe_3O_4-2; D: Fe_3O_4-3.

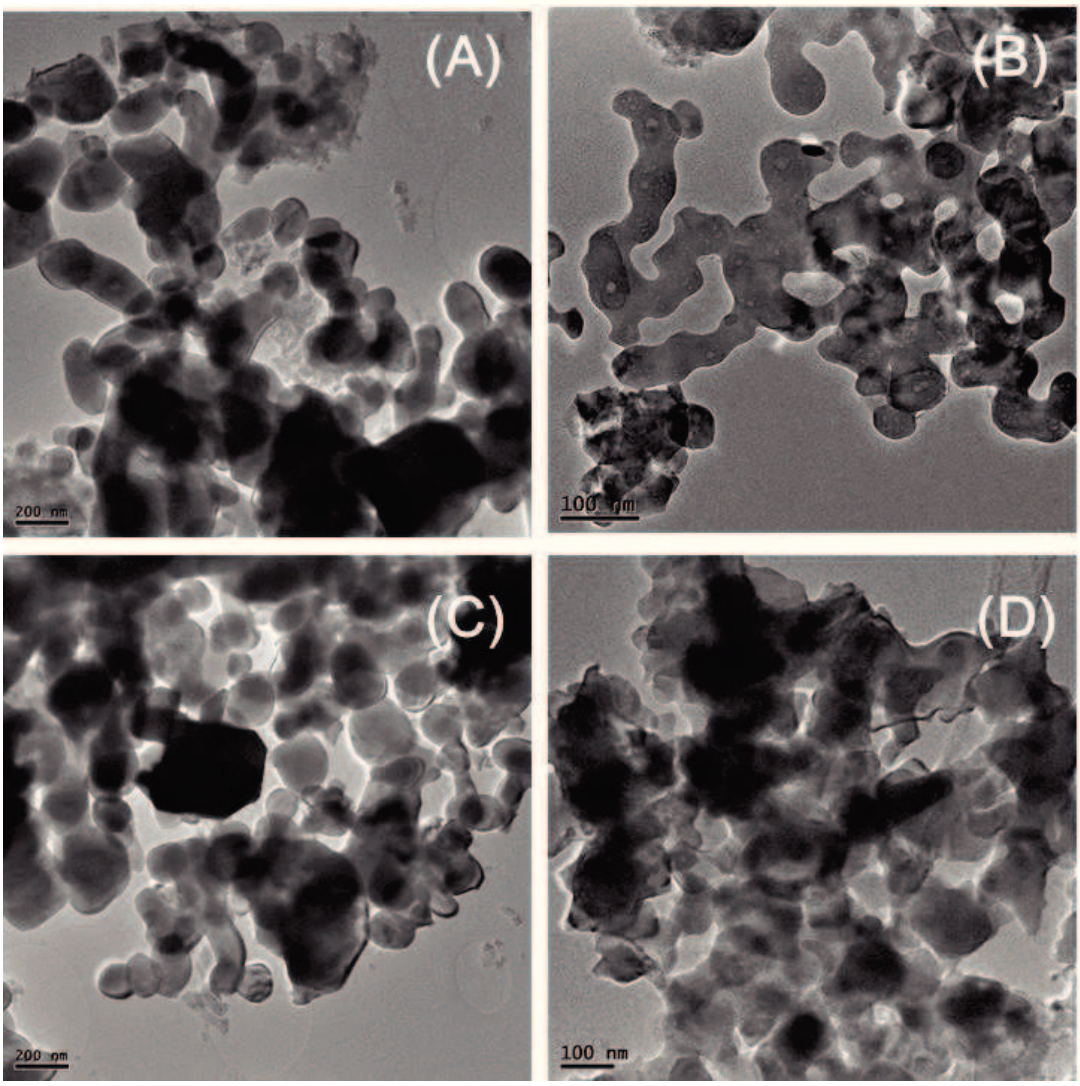


Figure 5. Representative high magnification TEM images of Fe_3O_4 in heterogeneous Fenton (A: Fe_3O_4-0; B: Fe_3O_4-3) or ultrasound assisted heterogeneous Fenton process (A, Fe_3O_4-0; B: Fe_3O_4-3).

4.3.2 Comparison of the catalytic activity under different oxidation conditions

Considering the acidic properties of TC in real condition, it is more meaningful to investigate its removal without pH adjustment. The catalytic activity of Fe_3O_4 in the degradation of TC was evaluated under different experimental conditions (0). In the control experiments, we confirmed that the removal efficiency of TC was less than 10% when only H_2O_2 or Fe_3O_4 was added into the solution or when the TC solution was only irradiated with ultrasound. Then, the sonolysis of TC was investigated in the absence and presence of Fe_3O_4 particles as well as with and without H_2O_2. Interestingly, as shown in 0and in Figure S2 (SI file), more of the TC was degraded

by US/H_2O_2 (18.0%) than by US/Fe_3O_4 (11.0%). This limited activity in the US/Fe_3O_4 system can be explained by the fact that the cavitation phenomenon cannot effectively enhance the degradation of organic compounds in the presence of the catalyst [32]. The few active radicals generated during the reaction can, however, are consumed by the iron oxide [33]. In contrast to the US/Fe_3O_4 system, the generation of hydroxyl radicals can be accelerated with the US/H_2O_2 process, resulting in higher degradation efficiency. Although TC can be removed more efficiently, the removal efficiency was also limited in the US/H_2O_2 system, indicating the reactive radicals were not sufficient for the TC removal.

In a simple catalytic system of Fe_3O_4/H_2O_2 without ultrasonic irradiation, the degradation efficiency and TOC abatement were 72.2% and 21.3%, respectively. In the Fe_3O_4/H_2O_2 system, the conversion of the H_2O_2 molecules into free radicals ($^{\bullet}OH$) plays an important role in the oxidation reaction by greatly increasing the degradation efficiency [34]. In a heterogeneous catalytic reaction, the heterogeneous active site (Fe^{II}) reacts with H_2O_2, resulting in the generation of hydroxyl radicals that degrade TC, as described in Eq. (1).

Significant higher degradation efficiency was achieved when both Fe_3O_4 and H_2O_2 present, indicating that the active sites on the catalyst surface strongly influenced the reaction rate (0A). Notably, the degradation of TC was significantly enhanced when this simple catalytic system was irradiated with ultrasound. Within 60 min of continuous ultrasonic irradiation, 93.7% of the TC was removed, a considerably greater removal efficiency than that yielded by the Fe_3O_4/H_2O_2 system without sonolysis (72.2%). The TOC removal was 31.8% within 60 min (0B**)**. The addition of ultrasonic irradiation might enhance the degradation of TC because the nucleation sites on the catalyst surface promote the formation of cavities and consequently increase the ultrasonic efficiency [35-36]. The mechanistic effect of ultrasound can change the morphology of the active phase. Although the particle size distribution did not show significantly changes after using the catalyst in 3 consecutive runs (SI Files, Figure S3), the physiochemical properties of the solid in

both the simple catalytic system and the ultrasound-assisted catalytic system changed (Figure 4 and Table 1).

In order to further evaluate the ultrasonic benefits, the degradation efficiency in heterogeneous Fenton and sono-heterogeneous Fenton process were conducted with three consecutive runs. As shown in Table 2, the degradation efficiency was decreased considerably after three consecutive tests and decreased from 72.2% to 48.2% in the simple catalytic system (Fe_3O_4/H_2O_2). In comparison, the removal efficiency did not decrease as significantly in the ultrasound-assisted system as in the simple catalytic system (Table 2) because ultrasound plays an important role in the activation of the catalyst. In addition, the aggregate sizes of the catalyst were measured before the initial oxidation test and after each subsequent test. In the process of $US/Fe_3O_4/H_2O_2$, the crystal size decreased from 77.3 to 59.9 nm after 3 recycle reactions, as calculated by XRD (Table 1). This result was further confirmed by the SEM and TEM observations. As can be seen in Figure 5D, a more compact aggregation of many interconnected particles was obtained under the heterogeneous Fenton process (Figure 5D), leading to the large bulk structures. In contrast, the magnetic particles, without large cluster or agglomerates after the reaction in the $US/Fe_3O_4/H_2O_2$ system (Figure 4B-D and Figure 5B) were observed. An increase in the number of accessible active sites and the improved mass transfer between the solute reagents and the solid particles were expected under ultrasonic conditions [37]. Moreover, the indirect chemical effects associated with cleaning the catalyst surface by continuous ultrasonic irradiation might result in the continuous removal of reaction intermediates from the surface, allowing new reactions to occur at the surface, as verified by TEM images (Figure 5A-B). Such result fully confirms the reason of highly removal efficiency of TC when the heterogeneous Fenton process combined with ultrasound. Therefore, we can conclude that the ultrasound can improve the activity of the catalyst in the heterogeneous Fenton process without prejudice to the stability of the solid phase in the successive runs.

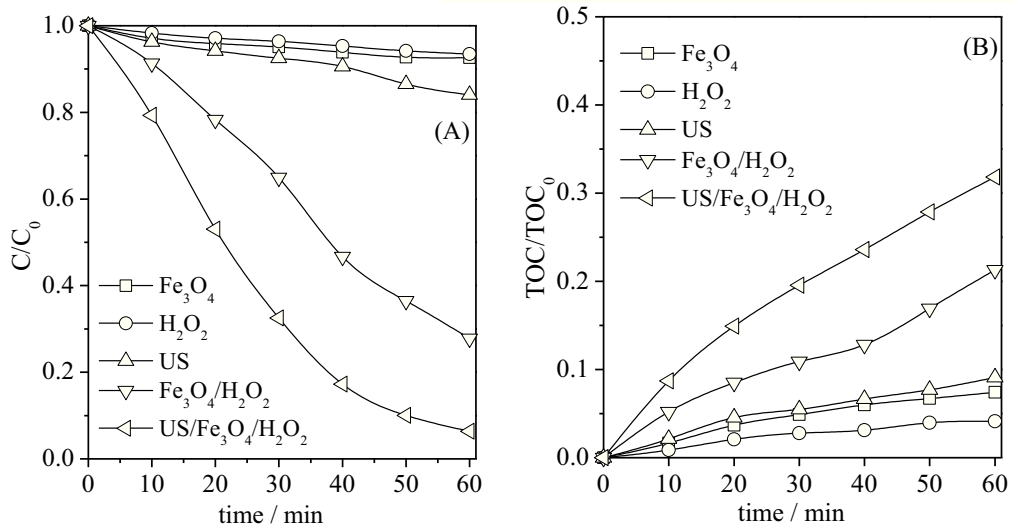


Figure 6. TC conversion (A) and TOC removal (B) obtained with different systems (TC: 100 mg L^{-1}, Fe_3O_4: 1.0 g L^{-1}, H_2O_2: 150 mM, pH_0: 3.7, T: 22 °C).

Table 2. Selected reaction results and catalyst stability for TC degradation under ultrasound assisted heterogeneous Fenton and heterogeneous Fenton process. (Fe_3O_4: 1.0 g L^{-1}; TC: 100 mg L^{-1}; H_2O_2: 150 mmol L^{-1}; pH: 3.7, T: 25 °C).

Sample	X_{TC}[b]/ % (X_{H2O2}[c]/ %)		Fe_{tot} leaching[f]/ mg L^{-1}		Fe_{tot} in solution[g] / %	
	Silence[d]	*US*[e]	*Silence*[a]	*US*[b]	*Silence*[a]	*US*[b]
Homogenous with 0.2 mg L^{-1} of Fe^{2+}	32.1		-		-	
Fe_3O_4-0[a]	-	-				
Fe_3O_4-1[a]	93.7/67.8	72.2/52.3	0.15	0.11	0.015	0.011
Fe_3O_4-2[a]	91.3/62.9	57.9/44.6	0.14	0.12	0.014	0.012
Fe_3O_4-3[a]	79.5/59.8	48.2/39.1	0.13	0.13	0.014	0.013

[a], Fe_3O_4-X (0, 1, 2, 3): fresh catalyst, and the catalyst used for one, two and three successive tests; [b], TC conversion after 60min of reaction in the process of US/Fe_3O_4/H_2O_2; [c], hydrogen peroxide conversion; [d], Fe_3O_4/H_2O_2 system; [e], US/Fe_3O_4/H_2O_2 system; [f], iron content in the solution at the end of the reaction; [g] percentage of total iron (Fe^{2+} and Fe^{3+}) leached from the catalyst at the end of the reaction.

4.3.3 Influence of the ultrasound power density on TC oxidation

Ultrasound produces acoustic cavitation, which involves the formation and subsequent collapse of microbubbles from acoustical wave-induced compression/rarefaction [17]. The implosion of the microscopic bubbles in the liquid generates energy, inducing the formation of reactive species in addition to producing other mechanical or physical effects [19]. However, the cavitation bubbles are

produced in such small quantities that they do not affect the overall reaction significantly when the sound intensity is lower than the cavitation threshold of the system [36]. As shown in Figure 7, the removal efficiency was 79.8% after 60 min of reaction with an ultrasonic power of 40 W, which is only slightly higher than the removal efficiency under silent conditions (72.2%).

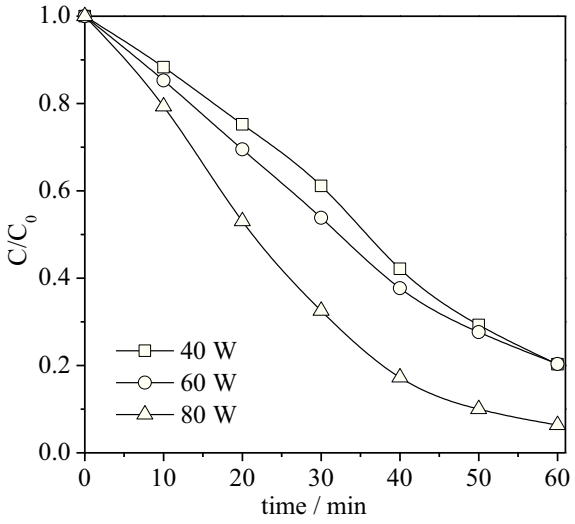


Figure 7 Effect of ultrasound power on the degradation of tetracycline (TC: 100 mg L^{-1}, Fe_3O_4: 1.0 g L^{-1}, H_2O_2: 150 mM, pH_0: 3.7, T: 22 ^oC).

When the ultrasound power density was increased to 60 W, no obvious increase in the efficiency was observed. However, when the ultrasound power was 80 W, a significant enhancement in the TC removal efficiency was observed. The mixing intensity due to the turbulence generated by cavitational bubble collapse as well as microstreaming at the solid surface [37] increased accordingly with the increase in the ultrasound power. Enhanced mixing at the solid-liquid interface and the continuous Fe_3O_4 surface cleaning [38] thereby enhance the $^{\bullet}OH$ production rate.

4.3.4 Influence of the hydrogen peroxide concentration and catalyst loading on TC oxidation

In the heterogeneous Fenton reaction, the concentration of the oxidant and the catalyst loading directly affected the concentration of active radicals produced for TC degradation. We investigated the effect of the hydrogen peroxide concentration by increasing the hydrogen peroxide concentration from 10 mmol L^{-1} to 150 mmol L^{-1}

(Figure S4, SI file). The decomposition reaction rate is dependent on either the surface site density or H_2O_2 concentration, and thus an increase in H_2O_2 concentration resulted in increased $^{\bullet}OH$ production. However, the degradation efficiency does not scale linearly with the initial H_2O_2 concentration. Further increases in the H_2O_2 concentration yield minimal changes in the degradation rates and final removal efficiencies. Here, we increased the H_2O_2 concentration to 250 mM, and the removal efficiency was 93.6% (data not shown). The $^{\bullet}OH$ preferentially attacked TC molecules below a certain H_2O_2 concentration. Whereas, $^{\bullet}OH$ has been suggested to react with H_2O_2 at high H_2O_2 concentrations with a reaction rate constant of 2.7×10^7 M^{-1} s^{-1} [39]. Thus, competing reactions between $^{\bullet}OH$ and TC or H_2O_2 occur at high H_2O_2 concentrations. The scavenging reaction of $^{\bullet}OH$ with H_2O_2 generates $HO_2^{\bullet}$ as described in Eq. 5

$$^{\bullet}OH + H_2O_2 \rightarrow HO_2^{\bullet} + H_2O \quad (5)$$

$HO_2^{\bullet}$ is, however, much less reactive than $^{\bullet}OH$ and does not contribute to the oxidation of TC. The consumption of the reactive radicals according to Eq. 5 explains why the degradation efficiency only increases slightly at H_2O_2 concentrations greater than 150 mM.

The effect of catalyst loading on phenol and TOC removal in the US/Fe_3O_4/H_2O_2 system was also evaluated. The impact of catalyst loading (from 0.5 g L^{-1} to 2.0 g L^{-1}) on TC degradation by the US/Fe_3O_4/H_2O_2 system is reported in the supporting information (Figure S5, SI file). When the Fe_3O_4 loading increased from 0.5 g L^{-1} to 1.5 g L^{-1}, the conversion rate significantly increased. The final conversions obtained were all greater than 80%. Logically, the increase in Fe_3O_4 loading provides more Fe(II)/Fe(III) active sites, leading to an enhanced degradation rate. In addition, the rate of cavity formation is expected to increase with the Fe_3O_4 concentration due to the formation of gas nuclei in the catalyst pores, as previously reported [40]. However, the degradation rate and removal efficiency did not increase significantly when the Fe_3O_4 loading exceeded 1.5 g L^{-1}. This result indicates that this loading corresponds

to the optimal $^{\bullet}OH$ generation, which is dependent on the H_2O_2 concentration [37] and cavity formation. Therefore, 1.5 g L^{-1} Fe_3O_4 was selected for our study.

4.3.5 Influence of temperature on TC oxidation.

The effects of temperature on sonochemical reaction rates are expected to differ from those on chemical reaction rates [33]. Therefore, the dependence of the global reaction rate on temperature (20-50 °C range) in the US/Fe_3O_4/H_2O_2 system was studied. As shown in Figure 8, the rate of TC conversion increased with an increase in temperature.

Increasing the reaction temperature during ultrasonic irradiation decreases the cavitation threshold, and the cavitation bubbles formed contain more water vapor. However, water vapor reduces the ultrasonic energy produced upon cavitation [36]. Consequently, larger sonochemical effects are observed at low temperatures because a majority of the bubbles are filled with gas. By contrast, increasing the reaction temperature enhances the reaction rate according to the Arrhenius equation [36]. The data obtained in this work (Figure 8**)** indicate that the effect of temperature on the chemical reaction is more pronounced than that on the cavitation process. Even if the initial reaction rate is strongly influenced by the reaction temperature, the final removal efficiencies are nearly the same at all temperatures (conversion always greater than 90%). The amount of hydroxyl radicals generated by ultrasound-enhanced, Fe_3O_4-catalyzed hydrogen peroxide decomposition is thus sufficient for decomposing TC within 60 min.

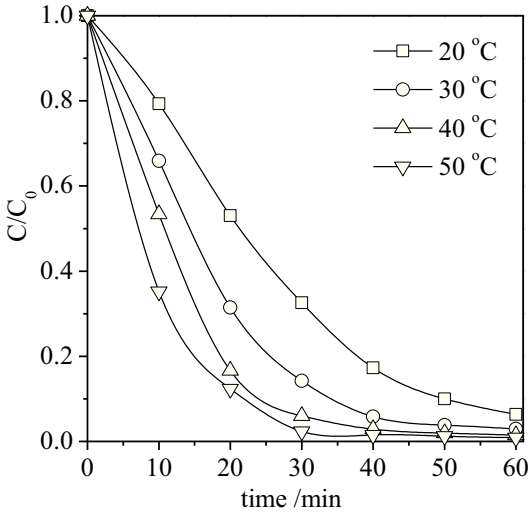


Figure 8 The effect of temperature on the degradation of tetracycline (TC: 100 mg L^{-1}, Fe_3O_4: 1.0 g L^{-1}, H_2O_2: 150 mM, P: 80 W, pH_0: 3.7).

4.3.6 Toxicity evolution

Even though 93.7% of the TC was converted after 60 min of reaction (Figure 6), the TOC conversion of TC was only approximately 14.9% after 60 min when the US/Fe_3O_4/H_2O_2 system was used. When the reaction time was increased to 180 min, the TOC abatement was 31.8%. After reaction under the US/Fe_3O_4/H_2O_2 conditions, the acute toxicity of the TC degradation effluents was evaluated by a 48-h immobilization assay with *D. magna*. The raw TC solution produced a mortality rate of 60% of *D. magna* after exposure to the solution for 48 h. After 60 min in the US/Fe_3O_4/H_2O_2 system, the toxicity reached a maximum value, and 100% of *D. magna* had died, indicating the formation of primary degradation by-products of considerably higher toxicity than TC. When the reaction time was increased to 180 min, the inhabitation percentage decayed, *i.e.,* the mortality rate was only 55%. Although the effluent of the first degradation stage produced death in all of the organisms, the toxicity of the solution decreased after only 180 min. This result fully supports the mineralization data obtained from the TOC abatement.

4.3.7 Catalytic mechanism

Whether direct contact of TC with the catalyst surface is necessary for the sono-catalytic degradation of TC remains an open question. Therefore, we constructed

a simple setup in which a dialysis bag was used to allow ions and radicals such as $^{\bullet}OH$ to move freely out of the bag, while TC can only diffuse slowly out of the bag as shown in Figure 1. Figure 9, shows the percentages of TC inside and outside the dialysis bag for different outer systems. When the outer system was water, 91.2% of the TC was maintained within the dialysis bag, and 8.8% diffused into the water after 60 min of reaction, indicating that no conversion occurred in water. No degradation of TC was observed after ultrasound alone for 60 min. Indeed, 88.0% of the TC remained in the membrane container, and 10.0% was detected in the outer system. These results indicate that the hydroxyl radicals generated by ultrasonic irradiation alone were insufficient, but showed a limited the decomposition of TC (2.0%). The removal efficiency of TC was also very limited under the US/H_2O_2 conditions. Indeed, only 9.0% of TC was converted, while 85.0% of the initial TC remained in the dialysis bag, indicating that more hydroxyl radicals were generated by H_2O_2 decomposition in the presence of ultrasound irradiation. This type of hydroxyl radical can be evenly dispersed in the bulk solution. When the outer system contains Fe_3O_4 and H_2O_2, the TC concentration in the inner system was 80.0% of the initial concentration after 60 min. The lack of significant differences in the TC concentrations in the dialysis bag in the Fe_3O_4/H_2O_2 and US/H_2O_2 systems indicates that there few hydroxyl radicals were present in the bulk solution. More importantly, the results also confirm that the function of ultrasound mainly focus on the surface activity enhancement. However, TC could not be detected in the Fe_3O_4/H_2O_2 outer system, indicating that the TC that leaked into the outer system was converted. Because no TC conversion occurred in the US/H_2O_2 system, the leaked TC must first be adsorbed on the Fe_3O_4 surface and then sono-catalytically degraded. These results indicate that direct contact between the Fe_3O_4 surface and TC is a prerequisite for the sono-catalytic degradation of TC. Under homogeneous conditions in which Fe^{2+} can diffuse through the membrane, 93% of the total TC was converted, further supporting our conclusions that the surface active species are the primary species and the

ultrasound mainly work on the catalyst surface during the ultrasound assisted heterogeneous reaction.

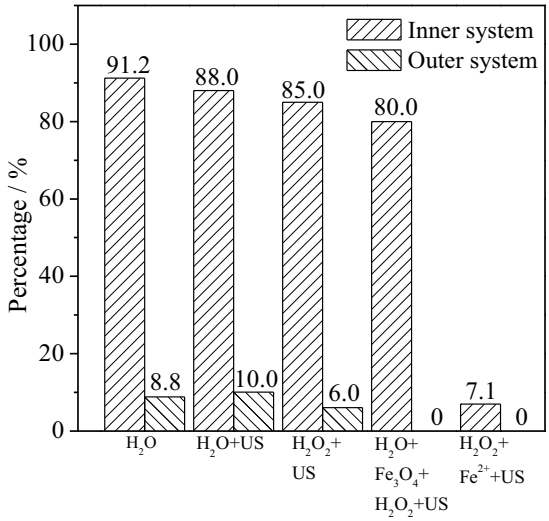


Figure 9. Percentages of tetracycline inside and outside a semipermeable membrane packaged container when the outer system is in various conditions. The initial concentration of TC is 100 mg L^{-1}. a, water; b, H_2O+US; c, H_2O_2+US; d, US+Fe_3O_4+H_2O_2; e, Fe^{2+}+H_2O_2+US (Fe_3O_4: 1.0 g L^{-1}, H_2O_2: 150 mM, P: 80 W, pH_0: 3.7, T: 22 ^oC).

To investigate the main active species during the ultrasound assisted heterogeneous Fenton reaction, two scavengers were employed to identify the specific reactive species in this sono catalytic process: KI for surface hydroxyl radical $^{\bullet}OH_s$ on the catalyst [41] and isopropanol for $^{\bullet}OH$ in the bulk (denoted $^{\bullet}OH_{free}$) [42,43]. The surface hydroxyl radical generated on the catalyst surface ($^{\bullet}OH_{ads}$) can then be scavenged by I^- with high reaction rate of 1.2×10^{10} $M^{-1}s^{-1}$ [41]. Isopropanol acts as a scavenger of $^{\bullet}OH_{free}$, with a reaction constant with $^{\bullet}OH_{free}$ of 1.9×10^{9} $M^{-1}s^{-1}$ [43].

When isopropanol was used as the $^{\bullet}OH$ scavenger, it is easily oxidized by $^{\bullet}OH$ and so it is usually used as a diagnostic tool for $^{\bullet}OH_{free}$ due to its low affinity to semiconductor surfaces in aqueous media [42]. Notably, as shown in Figure 10, the addition of isopropanol had little influence on the sono-degradation of TC, indicating that there is little $^{\bullet}OH_{free}$. However, in the presence of KI, the sono-degradation of TC decreased to 25.2% after 60 min of ultrasonic irradiation. Therefore, we conclude that the $^{\bullet}OH_s$ on the Fe_3O_4 surface is the major reactive species responsible for the sono-catalytic degradation of TC. As expected, greater adsorption of TC on Fe_3O_4 led to an increase in the sono-catalytic degradation efficiency of TC (Figure S5, SI files).

The results also fully confirm the reason of the direct contact between the catalyst and oxidants is a prerequisite for further oxidation we mentioned above.

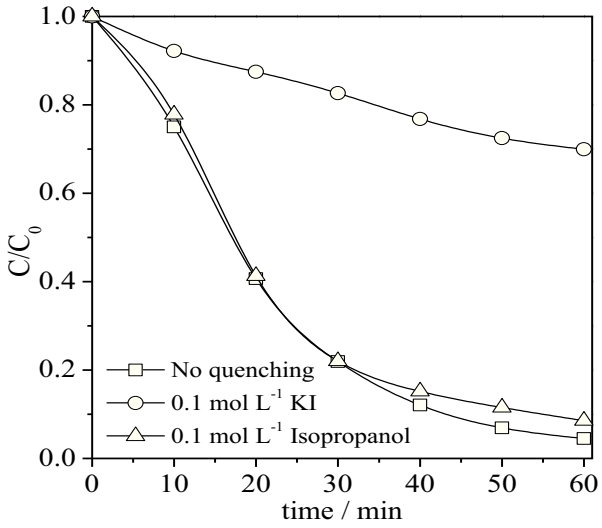


Figure 10. Effects of scavengers on the degradation of tetracycline (C_0 = 100 mg L^{-1}, Fe_3O_4: 1.0 g L^{-1}, H_2O_2:150 mM, P: 80 W, pH_0: 3.7, T: 22 ^oC).

4.3.8 Stability of the Fe catalyst

For the Fe_3O_4/H_2O_2 system, the stability of the catalyst is a critical factor for its successful application to wastewater treatment. The reusability of the solid was evaluated 3 times under identical oxidation conditions. At the end of each oxidation process, the solid was removed from the reactor and dried in a quartz tube at 60 °C overnight under N_2 at a flow rate of 60 min^{-1} to prevent further oxidation in air. As shown in Table 2, the removal efficiency decreased slightly after the 3 cycles. Due to the potential for oxidation of the catalyst surface during the reaction, XPS was employed to quantify the changes in the Fe^{2+}/Fe^{3+} ratio (Table 3). Part of the Fe^{2+} was oxidized to Fe^{3+} after the reaction, and the ratio of Fe^{2+}/Fe^{3+} changed from 25.09% to 14.31%. Meanwhile, the H_2O_2 decomposition also decreased after the 3 runs. As shown in Table 2, the conversion of H_2O_2 was measured after each run, and 67.8%, 62.9%, and 59.8% of the H_2O_2 was decomposed after the first, second, and third runs, respectively. These results demonstrate that the catalyst was slightly deactivated after 3 consecutive runs. However, these values were still much higher than those obtained in the simple catalytic process. In addition, the surface concentration of oxygen and

the Fe^{2+}/Fe^{3+} ratio decreased after the third run, leading to a corresponding decrease in the activity of the catalyst.

Table 3 The content changes of Fe^{2+} and Fe^{3+} content on the catalysts surface

Sample	Reaction time / min	Surface atom concentration from XPS / %		Banding Energe/ eV	Fe^{2+}/Fe^{3+} / %	Percentage of oxidation Fe^{2+} after reaction /%
		Fe	O			
Fe_3O_4-Com	0	85.55	14.45	710.43	25.09	33.47
	90	86.36	13.64	710.4	14.31	

Furthermore, the formation of soluble Fe^{2+} was also observed during the reaction (Table 2). However, because the iron leaching was on the order of ppm, the contribution of dissolved iron can be neglected based on the activities measured in this work at room temperature under slightly acidic conditions. Therefore, the conversion was attributed unambiguously to reaction over the heterogeneous active sites on the surface of the nanoparticles.

4.3.9 Surface properties of magnetite nanoparticles effect on their catalytic performance

As mentioned above, the catalytic activity of the commercial Fe_3O_4 is limited by its low surface area, large crystal size and the high agglomeration. Therefore, to improve the catalyst surface properties is necessary. Different morphologies exhibited different surface areas, adsorption abilities, and crystal sizes, which are considered to be the decisive parameters for catalytic performance [46-47]. Here, a novel nano crystal sized Fe_3O_4 with the shape of nanorod synthesized by ourselves was introduced. The characterizations (XRD，BET, and TEM) about this material are given in the SI files (Figure S6). As evident from the results we obtained, the surface areas of the catalysts were 24.7 $m^2\ g^{-1}$ for Fe_3O_4-R and 0.7 $m^2\ g^{-1}$ for the commercial one. The TC conversion and TOC abatement after the reaction are shown in Figure 11. After 60 min, Fe_3O_4-R exhibited superior catalytic activity in the Fe_3O_4/H_2O_2 process compared with the commercial one, and the TC conversion was 100%, TOC abatement was 74.8%. This process was a surface reaction as we elucidated in the

above section, increasing the surface area provided more active sites for catalytic oxidation. In addition, high surface area can also lead to the high adsorption ability of the catalyst, and more opportunity of the connection between the solid and liquid was achieved. More importantly, crystal size reduction also resulted in increased iron oxide surface sites in addition to the possible modification of iron density in the exposed crystal faces, edges, and corners [47] Therefore, much higher activity was achieved by nano-rods Fe_3O_4, and more details on this material will be carried out in our future study.

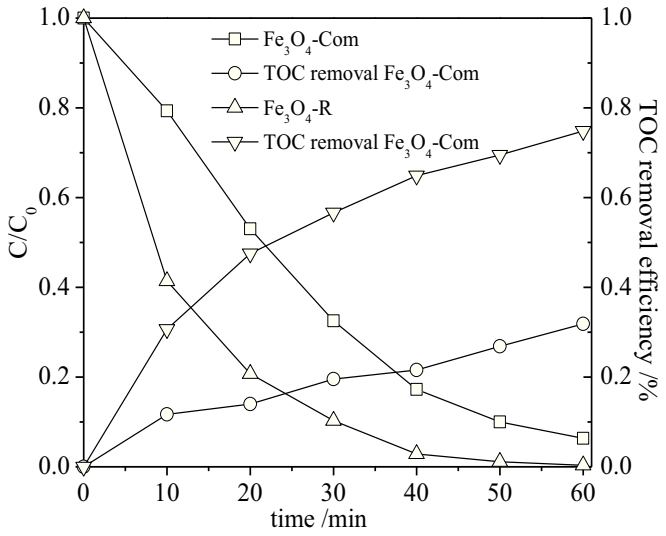


Figure 11. TC removal efficiency and TOC abatement obtained with nanorod and commercial Fe_3O_4 (TC: 100 mg L^{-1}, catalysts: 1.0 g L^{-1}, H_2O_2: 150mM, P: 80 W, pH_0: 3.7, T: 22 ^oC).

4.4. Conclusions

Magnetite catalysts in combination with H_2O_2 and ultrasound can efficiently convert TC. The catalyst exhibited good structural stability and a limited loss in performance upon reuse. The removal rate is affected by the initial TC, H_2O_2, and Fe_3O_4 concentrations; the temperature; and the ultrasonic power. The reaction is also affected by the initial pH; the reaction rate decreases with an increase in the initial pH. The toxicity, which was assessed using *D. magna*, decreased after it reached a maximum during the first period of the oxidation reaction. Experiments using different scavengers indicated that $^{\bullet}OH_{ads}$ plays a major role in the degradation process. More importantly, a semipermeable membrane system was introduced, and

the results demonstrated that the TC oxidation mechanism proceeds through a TC intermediate adsorbed on the Fe_3O_4 surface. These findings suggest that the US/Fe_3O_4/H_2O_2 system could be a promising method for enhancing the degradation of TC or other toxic and non-biodegradable molecules.

References

[1] Bautitz, I. R., Nogueira, R. F. P. (2007). Degradation of tetracycline by photo-Fenton process- Solar irradiation and matrix effects. Journal of Photochemistry and Photobiology A: Chemistry, 187(1), 33-39.

[2] Chen, Y., Hu, C., Hu, X., Qu, J. (2009). Indirect photodegradation of amine drugs in aqueous solution under simulated sunlight. Environmental science & technology,n43(8), 2760-2765.

[3] G], 2760-2765.cience & technology2009). Indirect photodegradation oeñalver, J. (2011). Tetracycline removal from waters by integrated technologies based on ozonation and biodegradation. Chemical Engineering Journal, 178, 115-121.

[4] Hou, L., Zhang, H., Xue, X. (2012). Ultrasound enhanced heterogeneous activation of peroxydisulfate by magnetite catalyst for the degradation of tetracycline in water. Separation and Purification Technology, 84, 147-152.

[5] Wang, Y., Zhang, H., Chen, L. (2011). Ultrasound enhanced catalytic ozonation of tetracycline in a rectangular air-lift reactor. Catalysis Today, 175(1), 283-292.

[6] Wang, Y., Zhang, H., Chen, L., Wang, S., Zhang, D. (2012). Ozonation combined with ultrasound for the degradation of tetracycline in a rectangular air-lift reactor. Separation and Purification Technology, 84, 138-146.

[7] Wang, Y., Zhang, H., Zhang, J., Lu, C., Huang, Q., Wu, J., Liu, F. (2011). Degradation of tetracycline in aqueous media by ozonation in an internal loop-lift reactor. Journal of hazardous materials, 192(1), 35-43.

[8] Wu, J., Zhang, H., Oturan, N., Wang, Y., Chen, L., Oturan, M. A. (2012). Application of response surface methodology to the removal of the antibiotic tetracycline by electrochemical process using carbon-felt cathode and DSA (Ti/RuO_2–IrO_2) anode. Chemosphere, 87(6), 614-620.

[9] Caudo, S., Centi, G., Genovese, C., Perathoner, S. (2006). Homogeneous versus heterogeneous catalytic reactions to eliminate organics from waste water using H_2O_2. Topics in catalysis, 40(1-4), 207-219.

[10] Molina, R., Martinez, F., Melero, J.A., Bremner, D.H., Chakinala, A.G. (2006). Mineralization of phenol by a heterogeneous ultrasound/Fe-SBA-15/H_2O_2 Process: multivariate study by factorial design of experiments. Applied Catalytic B: Environmental, 66, 198-207.

[11] Muruganandham, M., Yang, J. S., Wu, J. J. (2007). Effect of ultrasonic irradiation on the catalytic activity and stability of goethite catalyst in the presence of H_2O_2 at acidic medium. Industrial & engineering chemistry research, 46(3), 691-698.

[12] Zhang, S., Zhao, X., Niu, H., Shi, Y., Cai, Y., Jiang, G. (2009). Superparamagnetic Fe_3O_4 nanoparticles as catalysts for the catalytic oxidation of phenolic and aniline compounds. Journal of hazardous materials, 167(1), 560-566.

[13] Dhakshinamoorthy, A., Navalon, S., Alvaro, M., Garcia, H. (2012). Metal nanoparticles as heterogeneous Fenton catalysts. ChemSusChem, 5(1), 46-64.

[14] Xue, X., Hanna, K., Abdelmoula, M., Deng, N. (2009). Adsorption and oxidation of PCP on the surface of magnetite: kinetic experiments and spectroscopic investigations. Applied Catalysis B: Environmental, 89(3), 432-440.

[15] Usman, M., Faure, P., Hanna, K., Abdelmoula, M., Ruby, C. (2012). Application of magnetite catalyzed chemical oxidation (Fenton-like and persulfate) for the remediation of oil hydrocarbon contamination. Fuel, 96, 270-276.

[16] Sreedhar, B., Arundhathi, R., Reddy, M. A., Parthasarathy, G. (2009). Highly efficient heterogenous catalyst for acylation of alcohols and amines using natural ferrous chamosite. Applied Clay Science, 43(3), 425-434.

[17] Adewuyi, Y. G. (2005). Sonochemistry in environmental remediation. 1. Combinative and hybrid sonophotochemical oxidation processes for the treatment of pollutants in water. Environmental science & technology, 39(10), 3409-3420.

[18] Adewuyi, Y. G. (2001). Sonochemistry: environmental science and engineering applications. Industrial & Engineering Chemistry Research, 40(22), 4681-4715.

[19] Adewuyi, Y. G. (2005). Sonochemistry in environmental remediation. 2. Heterogeneous sonophotocatalytic oxidation processes for the treatment of pollutants in water. Environmental science & technology, 39(22), 8557-8570.

[20] Vajnhandl, S., Majcen Le Marechal, A. (2005). Ultrasound in textile dyeing and the decolouration/mineralization of textile dyes. Dyes and Pigments, 65(2), 89-101.

[21] Kim, J. K., Martinez, F., Metcalfe, I. S. (2007). The beneficial role of use of ultrasound in heterogeneous Fenton-like system over supported copper catalysts for degradation of p-chlorophenol. Catalysis today, 124(3), 224-231.

[22] Zhong, X., Xiang, L., Royer, S., Valange, S., Barrault, J., Zhang, H. (2011). Degradation of CI Acid Orange 7 by heterogeneous Fenton oxidation in combination with ultrasonic irradiation. Journal of Chemical Technology and Biotechnology, 86(7), 970-977.

[23] Bremner, D.H., Molina, R., Martínez, F., Melero, J.A., Segura, Y. (2009). Degradation of phenolic aqueous solutions by high frequency sono-Fenton systems (US–Fe_2O_3/SBA-15–H_2O_2). Applied Catalyst B: Environmental, 90, 380-388.

[24] Wang, N., Zhu, L., Wang, M., Wang, D., Tang, H. (2010). Sono-enhanced degradation of dye pollutants with the use of H_2O_2 activated by Fe_3O_4 magnetic nanoparticles as peroxidase mimetic. Ultrasonics sonochemistry, 17(1), 78-83.

[25] Papadaki, M., Emery, R. J., Abu-Hassan, M. A., Dıaz-Bustos, A., Metcalfe, I. S., Mantzavinos, D. (2004). Sonocatalytic oxidation processes for the removal of contaminants containing aromatic rings from aqueous effluents. Separation and purification technology, 34(1), 35-42.

[26] Halling-Sørensen, B., Nors Nielsen, S., Lanzky, P. F., Ingerslev, F., Holten Lützhøft, H. C., Jørgensen, S. E. (1998). Occurrence, fate and effects of pharmaceutical substances in the environment-a review. Chemosphere, 36(2), 357-393.

[27] Organization for Economic Cooperation and Development (OECD), 2004. Daphnia sp. acute immobilization test. Test Guideline No. 202, OECD Guidelines for Testing of Chemicals.

[28] Yan, H., Zhang, J., You, C., Song, Z., Yu, B., Shen, Y. (2009). Influences of different synthesis conditions on properties of Fe_3O_4 nanoparticles. Materials Chemistry and Physics, 113(1), 46-52.

[29] Hawn, D. D., DeKoven, B. M. (1987). Deconvolution as a correction for photoelectron inelastic energy losses in the core level XPS spectra of iron oxides. Surface and interface analysis, 10(2-3), 63-74.

[30] Muhler, M., Schlögl, R., Ertl, G. (1992). The nature of the iron oxide-based catalyst for dehydrogenation of ethylbenzene to styrene 2. Surface chemistry of the active phase. Journal of Catalysis, 138(2), 413-444.

[31] Yamashita, T., Hayes, P. (2008). Analysis of XPS spectra of Fe^{2+} and Fe^{3+} ions in oxide materials. Applied Surface Science, 254(8), 2441-2449.

[32] Melero, J. A., Martinez, F., Molina, R. (2008). Effect of ultrasound on the properties of heterogeneous catalysts for sono-Fenton oxidation processes. Journal of Advanced Oxidation Technologies, 11(1), 75-83.

[33] Mason, T.J., Lorimer, J.P. (2002). Wiley-VCH Verlag GmbH, Weinheim, 42-52.

[34] Voinov, M. A., Pagán, J. O. S., Morrison, E., Smirnova, T. I., Smirnov, A. I. (2010). Surface-mediated production of hydroxyl radicals as a mechanism of iron oxide nanoparticle biotoxicity. Journal of the American Chemical Society, 133(1), 35-41.

[35] Zhang, H., Zhang, J., Zhang, C., Liu, F., Zhang, D. (2009). Degradation of CI Acid Orange 7 by the advanced Fenton process in combination with ultrasonic irradiation. Ultrasonics sonochemistry, 16(3), 325-330.

[36] Thompson, L. H., Doraiswamy, L. K. (1999). Sonochemistry: science and engineering. Industrial & engineering chemistry research, 38(4), 1215-1249.

[37] Zhang, H., Fu, H., Zhang, D. (2009). Degradation of CI Acid Orange 7 by ultrasound enhanced heterogeneous Fenton-like process. Journal of hazardous materials, 172(2), 654-660.

[38] Gogate, P. R., & Pandit, A. B. (2004). A review of imperative technologies for wastewater treatment II: hybrid methods. Advances in Environmental Research, 8(3), 553-597.

[39] Buxton, G. V., Greenstock, C. L., Helman, W. P., Ross, A. B. (1988). Critical review of rate constants for reactions of hydrated electrons, hydrogen atoms and hydroxyl radicals. Phys. Chem. Ref. Data, 17, 513-886.

[40] Chand, R., Ince, N. H., Gogate, P. R., Bremner, D. H. (2009). Phenol degradation using 20, 300 and 520kHz ultrasonic reactors with hydrogen peroxide, ozone and zero valent metals. Separation and Purification Technology, 67(1), 103-109.

[41] Martin, S. T., Lee, A. T., Hoffmann, M. R. (1995). Chemical mechanism of inorganic oxidants in the TiO_2/UV process: increased rates of degradation of chlorinated hydrocarbons. Environmental science & technology, 29(10), 2567-2573.

[42] Zhang, L. S., Wong, K. H., Yip, H. Y., Hu, C., Yu, J. C., Chan, C. Y., Wong, P. K. (2010). Effective photocatalytic disinfection of E. coli K-12 using AgBr-Ag-Bi_2WO_6 nanojunction system irradiated by visible light: The role of diffusing hydroxyl radicals. Environmental science & technology, 44(4), 1392-1398.

[43] Buxton, G. V., Greenstock, C. L., Helman, W. P., Ross, A. B. (1988). Critical review of rate constants for reactions of hydrated electrons, hydrogen atoms and hydroxyl radicals. Phys. Chem. Ref. Data, 17, 513-886.

Supplementary Information for

Highly efficient AOP process using ultrasound assisted heterogeneous Fenton-like reaction

Example of tetracycline degradation over commercial magnetite-type catalyst

Liwei Hou, Hui Zhang, Sébastien Royer, Liguo Wang

1.Catalyst characterizations and activity tests

XRD characterization. The catalysts structures were measured by XRD using a D5005 diffractometer from Bruker equipped with a CuKα radiation (λ = 1.5406 Å) source. The diffractogram are recorded in the range of 20-80° 2θ with each step of 0.05° every 5s. Phase identification was made by comparison with JCPDS database and the crystallite sizes were calculated using Scherrer equation after Warren's correction for instrumental broadening.

N_2 physical adsorption. A TRISTAR 3000 instrument was used to measure the specific surface area (SSA) of the samples using Brunauer-Emmett-Teller (BET) method, with outgas pretreatment at 250 ^{o}C under vacuum.

XPS analysis. X-ray photoelectron spectroscopy (XPS) was conducted on a Thermo-Fisher ESCALAB 250 system with Al$K\alpha$ radiation under ultrahigh vacuum (UHV). X-ray photoelectron spectroscopy (XPS) was conducted on a Thermo-Fisher ESCALAB 250 system with Al$K\alpha$ radiation under ultrahigh vacuum (UHV). The attenuation length depends on the electron kinetic energy and emission angle (S1-S3). The peak positions of Fe 2p3/2 and Fe 2p1/2 are, respectively, 710.5 (S.D. = 0.05) and 724.1 eV (S.D. = 0.07). The symmectric peak shape without low-intensity side binds proves the cleanliness of the surface. The ratio of Fe^{2+}/Fe^{3+} is also presented in Table 2.

SEM. Scanning electron microscopy (SEM, FEI Quanta 200, Holland) was used to characterize the surface morphology of Fe_3O_4 (the applied acceleration voltage was 20 kV). All samples were coated with a conductive layer of sputtered gold before collecting the SEM images.

TEM. Transmission electron microscopy (TEM) investigations were performed on a JEOL 2100 instrument (operated at 200 kV a LaB_6 source and equipped with a Gatan Ultra scan camera).

Iron leaching test. The Fe^{2+} content in the bulk of Fe_3O_4 was determined by chemical analysis after the samples were dissolved in acid at 60 °C for 48 h under a nitrogen atmosphere. 6 M HCl was added to ensure dissolution of the iron oxide. The dissolved

ferrous iron concentration was measured via the 1,10-phenanthroline method using a UV spectrophotometer with λ fixed at 510 nm (S4). Furthermore, surface Fe^{2+} content on the catalysts were also analyzed by XPS [See details in SI, XPS part]. The total aqueous iron content after dissolution was determined using inductively coupled plasma optical emission spectroscopy (ICP-OES).

Particle size distribution. The particle size distribution of Fe_3O_4 before and after ultrasound irradiation was evaluated by a dynamic light scattering method using a laser scattering particle size analyzer (MASTER-SIZER 3500, Microtrac, US).

Catalytic tests. Catalytic tests were performed under ultrasound irradiation (KQ-100 KDB ultrasonic generator, 100 W, 20 kHz, Kunshan Ultrasonic Instrument Co., Ltd.) in a 250 mL plastic reactor continuously stirred with a mechanical stirrer at 350 rpm min^{-1} (RW 20, IKA, Germany). The setup is shown in the SI files (Figure S1). Tetracycline hydrochloride (TC) was used as the reactant, and hydrogen peroxide was used as the oxidant. We initially verified that no external or internal diffusional limitations existed and that the reaction was performed in a kinetic regime. In consideration of the original pH of the reactant, the pH was not adjusted before the oxidation began (pH 3.7). In a typical experiment, 200 mL of a TC solution was prepared with an initial concentration of 100 mg L^{-1}. The catalyst was subsequently added to the solution, which was then stirred in the dark for 60 min to ensure adsorption-desorption equilibrium prior to the initiation of oxidation. Appropriate amounts of hydrogen peroxide were then added to start the reaction.

The reaction solution (1.5 mL) was sampled at fixed time intervals and mixed with the same volume of 0.1 M NaOH to quench the reaction. The reaction solution was then filtered through a 0.22 μm membrane (Millipore Corp.) before the residual TC concentration and total organic carbon (TOC) content were measured.

The changes of the acute toxicity test. *D. magna* was cultivated in the laboratory for more than 3 generations. The acute toxicity experiments were performed in a 50 mL test beaker with *D. magna* organisms that were less than 24 h old. The *D. magna* organisms were divided into 5 groups of 25. Four groups were used as test groups,

and the remaining group was used as the control group. All groups were placed in the incubator along with the samples to be evaluated. The incubator was set to room temperature (20 °C) with a 16 h light: 8 h dark cycle. Food was administered during the test. The mobile surviving *D. magna* organisms were counted after 48 h.

2. Experimental setup

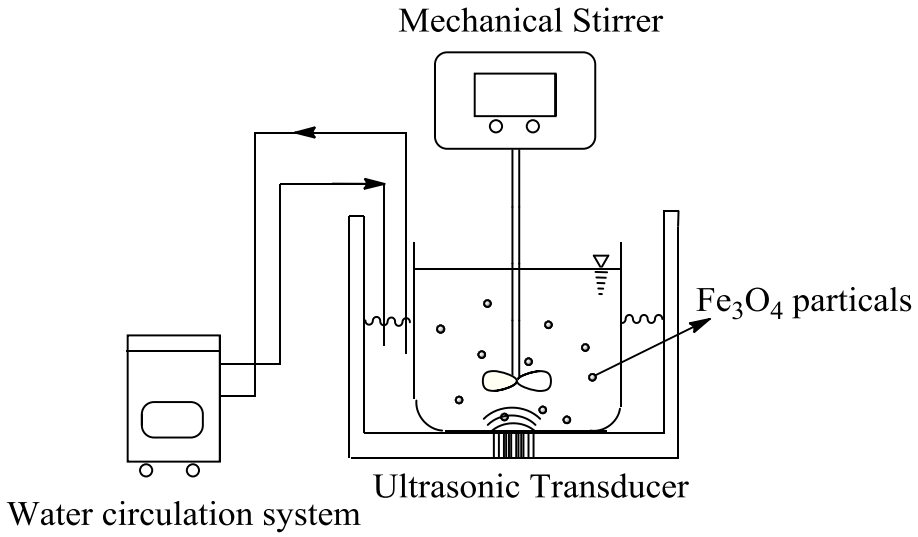


Figure S1. The experimental setup used in our study.

3. Degradation of TC in different systems

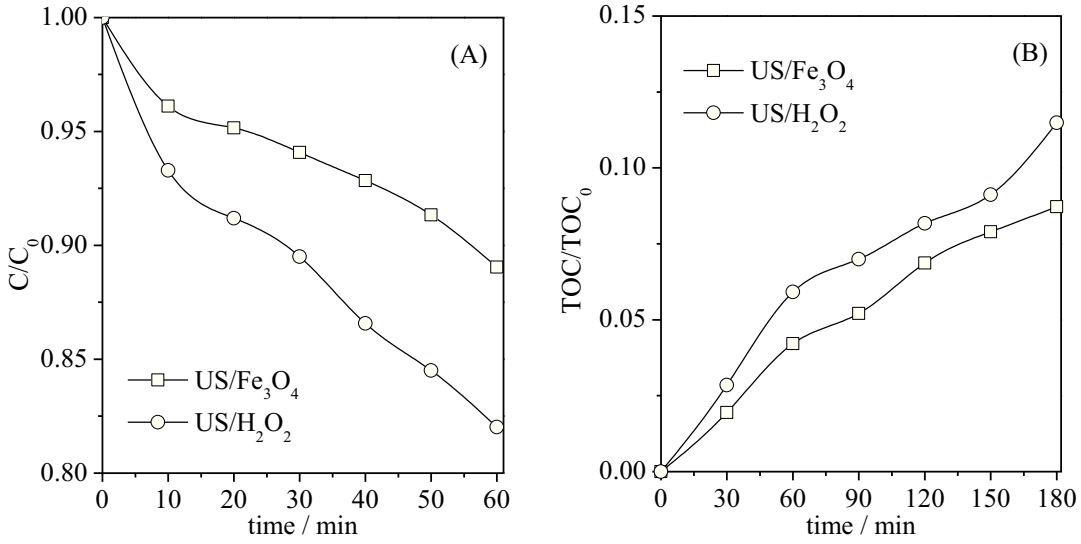


Figure S2. Degradation of TC in systems of US/Fe_3O_4 and US/Fe_3O_4. (Fe_3O_4: 1.0 g L^{-1}, H_2O_2: 150 mM, P: 80 W, pH_0: 3.7).

4. Particle size distribution analysis

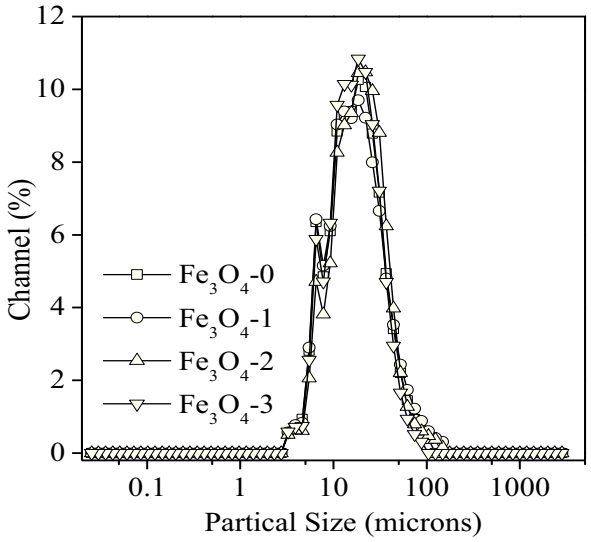


Figure S3. Fe_3O_4 catalyst particle size distribution dispersed in water and representative samples.

5. Influence of catalyst dosage and hydrogen peroxide concentration on the TC removal

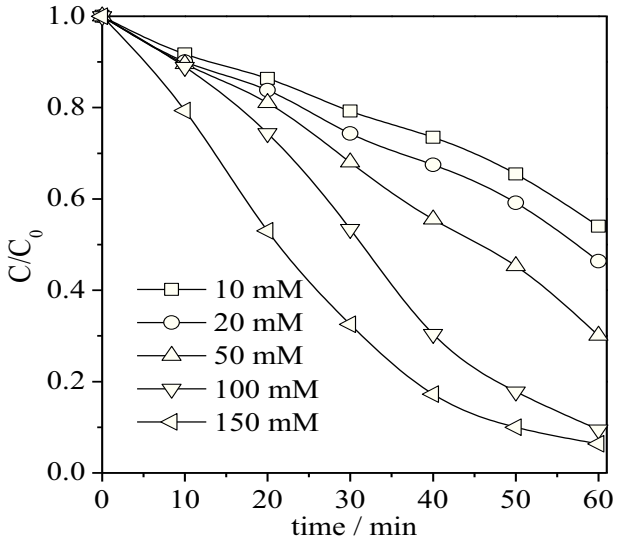


Figure S4. The effect of hydrogen peroxide concentration on the degradation of tetracycline (TC: 100 mg L^{-1}, Fe_3O_4: 1.0 g L^{-1}, P: 80 W, pH_0: 3.7).

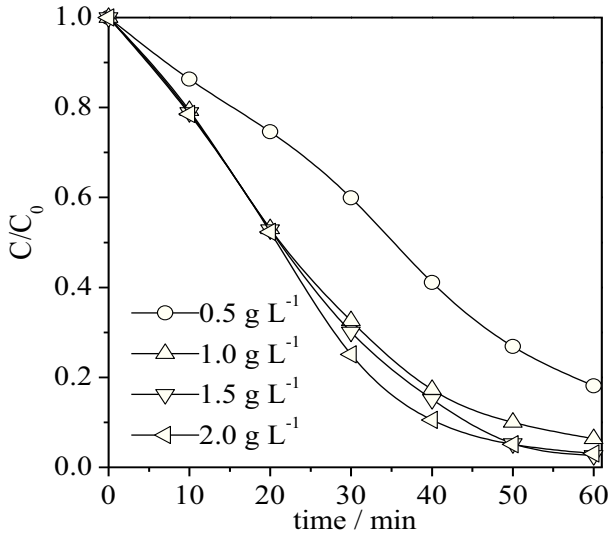


Figure S5. The effect of the dosage of Fe_3O_4 on the degradation of tetracycline (TC: 100 mg L^{-1}, H_2O_2: 150 mM, P: 80 W, pH_0: 3.7).

6. Characterizations of Fe_3O_4 nanrods

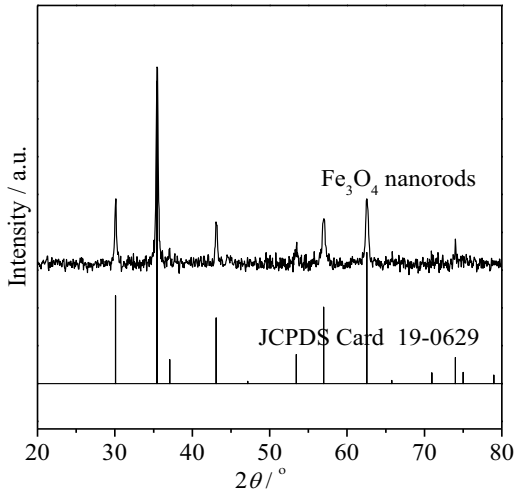


Figure S6. XRD patterns of Fe_3O_4 nanrods. Reference X-ray lines attributed to Fe_3O_4 (JCPDS card 19-0629)

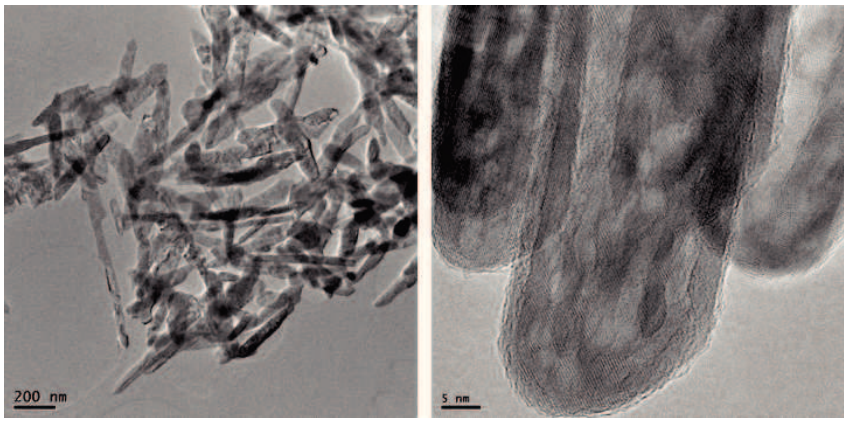


Figure S7 TEM images of Fe_3O_4 nanorods

7. References

[S1] D.D. Hawn, B.M. Koven, Surf. Interface Anal. 10 (1987) 63-74.

[S2] M. Muhler, R. Schlögl, G. Ertl, J. Catal. 138 (1992) 413-444.

[S3] T. Yamashita, P. Hayes, Appl. Surf. Sci. 254 (2008) 2441-2449.

[S4] A.E. Harvey, J.A. Smart, E.S. Arms, Anal. Chem. 27(1955) 26-29.

Chapter 5 Ultrasound enhanced heterogeneous activation of peroxydisulfate by magnetite catalyst

Degradation of tetracycline in water

Article:

Liwei Hou, Hui Zhang and Xiaofei Xue, Separation and Purification Technology 84 (2012) 147-152.

Except for the Fenton and heterogeneous Fenton processes, another kind of oxidant, peroxydisulfate, has the similar structure of O-O bond with H_2O_2. It is more stable and higher aqueous solubility than H_2O_2, and it can be decomposed to sulfate radicals ($SO_4^{-\bullet}$). Hence, in this study, peroxydisulfate was chosen as an oxidant, and tetracycline was selected as the target antibiotic compound in the process of US/$Na_2S_2O_8$/Fe_3O_4. The present work here not only aimed at providing insight into the effects of operating parameters, such as $Na_2S_2O_8$ concentration, initial pH, ultrasonic power, Fe_3O_4 power addition and initial tetracycline concentration on degradation of tetracycline, but also the activation mechanism of tetracycline in the system of US/$Na_2S_2O_8$/Fe_3O_4 were explored. In addition, the surface modification of Fe_3O_4 before and after ultrasound irradiation was performed by using laser particle size analyzer.

5.1 Introduction

Except for the Fenton and heterogeneous Fenton processes, another kind of oxidant, peroxydisulfate, has the similar structure of O-O bond with H_2O_2. It is more stable and higher aqueous solubility than H_2O_2, and it can be decomposed to $SO_4^{-\bullet}$ radicals. Hence, in this study, peroxydisulfate was chosen as an oxidant, and tetracycline was selected as the target antibiotic compound in the process of $Na_2S_2O_8$/Fe_3O_4/US. The present work here not only aimed at providing insight into the effects of operating parameters, such as $Na_2S_2O_8$ concentration, initial pH, ultrasonic power, Fe_3O_4 power addition and initial tetracycline concentration on degradation of tetracycline, but also the activation mechanism of tetracycline in the system of $Na_2S_2O_8$/Fe_3O_4/US were explored. In addition, the surface modification of Fe_3O_4 before and after ultrasound irradiation was performed by using laser particle size analyzer.

5.2 Experimental section

All degradation runs were carried out by employing the experimental setup sketched in Fig. 3-1. A stock solution of tetracycline was prepared fresh with deionized water before each run and the initial concentration (C_0) was fixed at 100 mg

L^{-1}. Then Fe_3O_4 was added into 200 mL of tetracycline solution with constant stirring by using a mechanical stirrer (RW 20, IKA, Germany) for 15 min to achieve adsorption-desorption equilibrium. Finally, $Na_2S_2O_8$ was added to start the reaction. Sonication was performed with a KQ-100 KDB ultrasonic generator (100 W, 20 kHz, Kunshan Ultrasonic Instrument Co., Ltd.). The reactor was immersed into the ultrasonic batch. All experiments were conducted at ambient temperature (22±2°C). A small volume of the solution (2 mL) was taken by syringe at different time intervals, filtered through 0.22 μm membranes (Millipore Co.) and mixed with the same volume of methanol to quench the reaction.

The concentration of tetracycline in aqueous solution was analyzed by HPLC. It is consisted of a Shimadzu LC-20 AB pump, Shim-Pack VP-ODS-C18 column (4.6 mm × 250 mm, 5 μm) with a flow rate of 1.0 mL min^{-1} and UV detector (Shimadzu UV-1600 spectrophotometer). The detected wavelength for tetracycline is 359 nm [1]. The mobile phase was acetonitrile- 0.1 M oxalic acid solution (31:69, v/v). The injection volume was 20 μL. The retention time of tetracycline was 3.6 min. The total iron (Fe^{2+}, Fe^{3+}) leached from the Fe_3O_4 into the reaction solution was determined by using the 1, 10-phenanthroline method [2]. Particle size distribution of solid catalysts before and after ultrasound irradiation was investigated by using a Microtrac S-3500 laser particle size analyzer (Microtrac, U.S.).

5.3 Results and discussion

5.3.1 Degradation of tetracycline under different systems

Figure 1 shows tetracycline removal efficiency achieved by different systems. The concentration of tetracycline was hardly sono-Catalytic ozonation decreased when 20 kHz ultrasound was applied to the tetracycline solution (data not shown). It is due to the reason that only a very small amount of $^{\bullet}OH$ is formed in the presence of ultrasound alone. $Na_2S_2O_8$ is stable and the chemical reaction rate is relatively slow at ambient temperature, so the concentration of tetracycline is not significantly decreased with the addition of $Na_2S_2O_8$ alone (Figure 1). In control experiments, we also confirmed that little removal occur when adding into the solution with the catalyst only (Figure 1). The result indicates that the effect of adsorption on

tetracycline removal is not obvious under the condition investigated. Even though the catalyst was combined with ultrasound, no significant enhancement was observed. It is due to the reason that only a small amount of active radicals can be produced during the catalytic ultrasound reactions in the absence of oxidant [3].

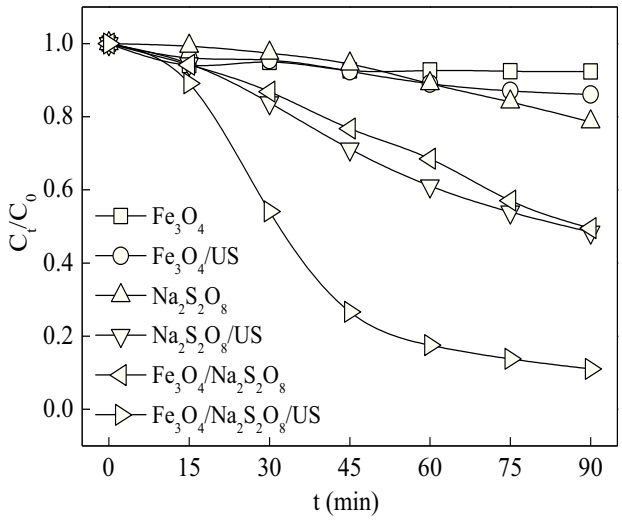


Figure 1. The effect of different systems on the degradation (Fe_3O_4: C_0=100 mg L^{-1}, [Fe_3O_4] =1 g L^{-1}, pH_0=3.7; Fe_3O_4/US: C_0=100 mg L^{-1}, [Fe_3O_4] =1 g L^{-1}, P= 80 W, pH_0=3.7; $Na_2S_2O_8$: C_0=100 mg L^{-1}, [$Na_2S_2O_8$] =200 mM, pH_0=3.7; $Na_2S_2O_8$/US: C_0=100 mg L^{-1}, [$Na_2S_2O_8$] =200 mM, P= 80 W, pH_0=3.7; Fe_3O_4/$Na_2S_2O_8$: C_0=100 mg L^{-1}, [Fe_3O_4] =1 g L^{-1}, [$Na_2S_2O_8$] =200 mM, pH_0=3.7; Fe_3O_4/$Na_2S_2O_8$/US: C_0=100 mg L^{-1}, [Fe_3O_4] =1 g L^{-1}, [$Na_2S_2O_8$] =200 mM, P= 80 W, pH_0=3.7)

When $Na_2S_2O_8$ was combined with Fe_3O_4 or ultrasound at ambient temperature, the degradation efficiency increased to some large extent (Figure 8-1). The results clearly indicate that $Na_2S_2O_8$ can be activated by Fe_3O_4 or ultrasound irradiation. When $Na_2S_2O_8$ is activated by Fe_3O_4, the degradation efficiency can be achieved at 50.5%. It can be explained that $SO_4^{-\bullet}$ and $^{\bullet}OH$s could be formed on the surface of Fe_3O_4 for the degradation process of tetracycline. When $Na_2S_2O_8$ was activated by ultrasound, the removal efficiency is 51.5%. The result can be explained by the following reasons. Firstly, the cavitation is intensified under low temperature, which could accelerate the decomposition of $Na_2S_2O_8$ [4]. Moreover, ultrasound irradiation could induce the production of $^{\bullet}OH$, which could also participate in the following oxidation reaction.

The degradation efficiency is 89% in the process of $Na_2S_2O_8/Fe_3O_4$/US, which is much higher than the silent condition at ambient temperature. This is due to the fact that $Na_2S_2O_8$ can be activated by Fe_3O_4 to generate $SO_4^{-\bullet}$ at ambient temperature. The reaction can be described according to the following equation (Eq. 1).

$$\equiv Fe(II) + S_2O_8^{2-} \rightarrow \equiv Fe(III) + SO_4^{-\bullet} + SO_4^{2-} \quad (1)$$

Furthermore, ultrasound can enhance the decomposition of $Na_2S_2O_8$ to generate $SO_4^{-\bullet}$ [4]. Since the tetracycline degradation is relatively low under the ultrasound irradiation and the oxidation process of $Na_2S_2O_8/Fe_3O_4$, the very fast degradation of tetracycline is a clear synergetic effect between the sonochemical and catalytic degradation of tetracycline.

5.3.2 The effect of initial pH on the degradation of tetracycline

To investigate the pH effect on the degradation of tetracycline, the initial pH values was varied as 3.7, 7.0 and 9.0. As can be seen in Figure 2, the results pointed out that the degradation rate of tetracycline increased with the decrease of pH. However, the removal efficiency was nearly the same after 1.5 h. It is reported that $SO_4^{-\bullet}$ can be scavenged by $^{\bullet}OH$ at high pH (Eq. 2) [5,6].

$$SO_4^{-\bullet} + {}^{\bullet}OH \rightarrow HSO_4^{-} + \frac{1}{2}O_2 \quad (2)$$

The same condition might be expected during the sonochemical oxidation of tetracycline leading to a decrease in the degradation rate of tetracycline under alkaline pH. Also, $SO_4^{-\bullet}$ are converted to $^{\bullet}OH$ under alkaline condition as shown in Eq. 3 [7].

$$SO_4^{-\bullet} + H_2O \rightarrow SO_4^{2-} + {}^{\bullet}OH + H^+ \quad (3)$$

However, no significant effect or influence of pH on the degradation efficiency was observed. The finial removal efficiency was 89%, 85.6% and 84.6% at pH_0 3.7, 7.0 and 9.0, respectively as presented in Figure 2. In this study, the effect of initial pH value was investigated without adding any buffer solution (such as $NaHCO_3/KHSO_4$, Na_2HPO_4/KH_2PO_4) to avoid potential complications to the reaction. They may act as the scavengers of $SO_4^{-\bullet}$ and the reaction equations were showed in Eqs. 4,5 [8].

$$SO_4^{-\bullet} + HCO_3^- \rightarrow SO_4^{2-} + HCO_3 \quad (4)$$

$$HCO_3 \rightleftharpoons H^+ + CO_3^- \quad (5)$$

In addition, buffer solution may also cause the additional environmental problems (such as phosphorus pollution). Therefore, we not adjust the pH during the process of the reaction.

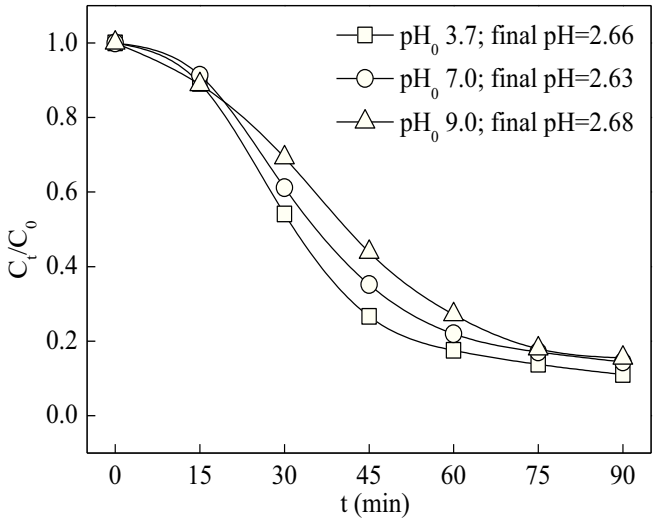


Figure 2. The effect of initial pH on the degradation (C_0=100 mg L^{-1}, [Fe_3O_4] =1 g L^{-1}, [$Na_2S_2O_8$] =200 mM, P=80 W)

It is very clear that the initial pH does not affect the degradation efficiency of tetracycline in the $Na_2S_2O_8/Fe_3O_4$/US system from pH_0 3.7 to 9.0. Our results are in accordance with the result of Zhao et al. [9] and Gayathri et al. [10]. Carboxyl acids such as acetic acid and sulfate acid are produced during the reaction. Therefore, it is expected that pH values would drop during the reaction in the absence of buffer solution. The final pH value was decreased to 2.66 after 1.5 h reaction when initial pH was 3.7, and this value dropped to 2.63, 2.68 at pH_0 7.0 and 9.0, respectively. Therefore, this may be the reason for the same degradation efficiency at the end of the reaction with different initial pH value.

5.3.3 The effect of sodium peroxydisulfate concentration on the degradation of tetracycline

Different concentrations of $Na_2S_2O_8$ in the range from 20 mM to 400 mM were investigated in this study with constant Fe_3O_4 dosage of 1.0 g L^{-1} and the results are displayed in Figure 3. It can be seen that the degradation efficiency increased with the increase of $Na_2S_2O_8$ concentration from 20 mM to 200 mM. It can be activated to generate $SO_4^{-\bullet}$ on the surface of Fe_3O_4. It is similar to the mechanism of H_2O_2 activated by Fe_3O_4 as the pervious study described [11]. Therefore, more $SO_4^{-\bullet}$ can be generated when increasing the concentration of $Na_2S_2O_8$. Notably, when the dosage exceeds 200 mM, the removal efficiency decreased. Excess addition of $Na_2S_2O_8$ leads to produce sulfate anions without producing active $SO_4^{-\bullet}$. It is also reported that radical-radical reactions may be prior to the radical-organic reactions and $SO_4^{-\bullet}$ can also be scavenged by $S_2O_8^{2-}$ (Eqs. 6,7) [6, 12]. Moreover, the interaction between excess $SO_4^{-\bullet}$ on the surface of Fe_3O_4 and ≡Fe(II) may directly quench $SO_4^{-\bullet}$ through Eq. 8 [13]. In addition, SO_4^{2-} also inhibits the generation of $^{\bullet}OH$. Therefore, the overall efficiency is reduced when $Na_2S_2O_8$ concentration is 400 mM.

$$SO_4^{-\bullet} + SO_4^{-\bullet} \rightarrow S_2O_8^{2-} \qquad k = 4.0\times10^8\ M^{-1}S^{-1} \qquad (6)$$

$$SO_4^{-\bullet} + S_2O_8^{2-} \rightarrow SO_4^{2-} + S_2O_8^{-\bullet} \qquad k = 6.1\times10^5\ M^{-1}S^{-1} \qquad (7)$$

$$SO_4^{-\bullet} + Fe^{2+} \rightarrow Fe^{3+} + SO_4^{2-} \qquad k = 4.6\times10^9\ M^{-1}S^{-1} \qquad (8)$$

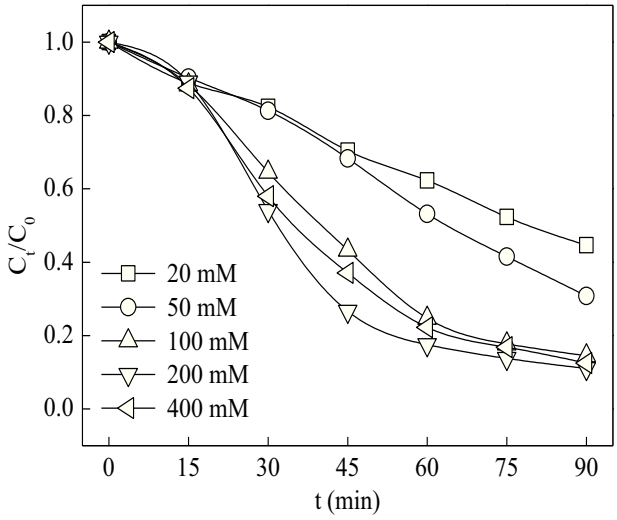


Figure 3. The effect of sodium peroxydisulfate concentration on the degradation, (C_0=100 mg L^{-1}, [Fe_3O_4] =1.0 g L^{-1}, P=80 W, pH_0=3.7)

5.3.4 The effect of magnetite addition on the degradation of tetracycline

The degradation of tetracycline at different addition of Fe_3O_4 was investigated in this study. As depicted in the Figure 4, the degradation efficiency increased with various dosages of Fe_3O_4 in the range from 0 g L^{-1} to 2.0 g L^{-1}. The degradation efficiency was only 50.5% after 1.5 h in $Na_2S_2O_8$/US system. As expected, the addition of iron oxides powder significantly improved the removal efficiently of the tetracycline. Fe_3O_4 is multivalent oxides, which act as a good provider of ≡Fe (II) for the activation of $Na_2S_2O_8$.

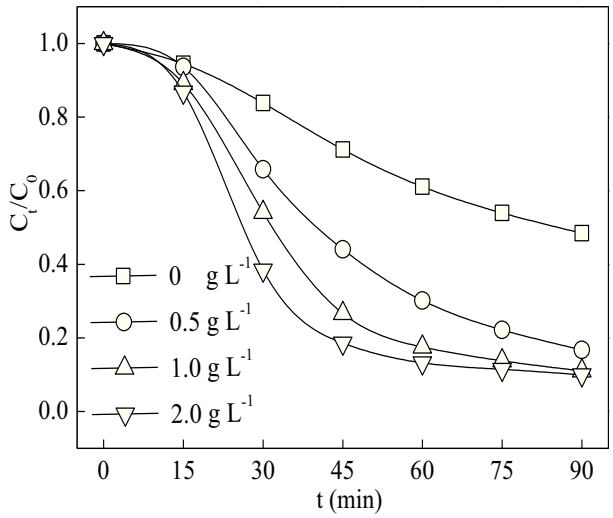


Figure 4. The effect of the catalyst addition on the degradation (C_0=100 mg L^{-1}, [$Na_2S_2O_8$] =200 mM, P=80 W, pH_0=3.7)

As an initiator, Fe_3O_4 activate $Na_2S_2O_8$ to generate $SO_4^{-\bullet}$, and then accelerate the decomposition of tetracycline. Therefore, the higher loading of Fe_3O_4, the higher degradation rate of tetracycline can be achieved. In addition, it would lead to the faster decomposition of $Na_2S_2O_8$ to obtain $SO_4^{-\bullet}$. Once it was activated, $SO_4^{-\bullet}$ and $^{\bullet}OH$ might initiate a series number of chain reactions during the ultrasound irradiation. At 0.5 g L^{-1} of Fe_3O_4, the degradation efficiency was low. It may be due to the fact that insufficient amount of $SO_4^{-\bullet}$ were produced with low concentration of Fe_3O_4. Despite different initial degradation rates of tetracycline at different Fe_3O_4 powder addition, the final removal efficiency was similar as a result of the same concentration of $Na_2S_2O_8$. It is the fact that the amount of $SO_4^{-\bullet}$ generated is only dependent on the

concentration of $Na_2S_2O_8$. When the concentration of $Na_2S_2O_8$ was fixed at 200 mM, it is sufficient enough to generate $SO_4^{-\bullet}$. Therefore, 1.0 g L^{-1} is chosen as an optimum addition for the catalyst.

5.3.5 The effect of power on the degradation of tetracycline

In order to study the effect of ultrasound power on the degradation of tetracycline, experiments with different level of ultrasound power were performed in this study. The heterogeneous reaction could be enhanced with the increase of ultrasound power, and the degradation efficiency could increase to some extent, as observed in Figure 5. The increase of ultrasound power increases the amount of $^{\bullet}OH$ generated in the system. Microstreaming could be formed during the ultrasound irradiation. The appearance resulted in the promoted mixing the metal-liquid interfaces and the continuous cleaning the surface of Fe_3O_4 for further surface reactions. In addition, due to the turbulence generated by cavitational bubble collapse as well as microstreaming, it will increase the mixing intensity with the increase of the ultrasound power [14]. Further, when the intensity of ultrasound increased to a certain high level, both the more decomposition of $Na_2S_2O_8$ and production of $^{\bullet}OH$ could lead to the enhancement decay of tetracycline [15]. Therefore, the rate of tetracycline oxidation increases with increasing ultrasound power.

Besides, it also should be noted that there is an optimum intensity of ultrasound power, in the case of 80 W, by further increasing it, the benefit is not observed. This is due to the fact that the oxidation rate will be limited by both amount and size of the cavitation events in radical production [16]. Cavitation bubble grows to extend and then collapse during the compression cycle of the cavitation process. Moreover, large bubble field will terminated the transmission of sound through the liquid. In that case, the cavitation effect may be weakened at a higher intensity of ultrasound.

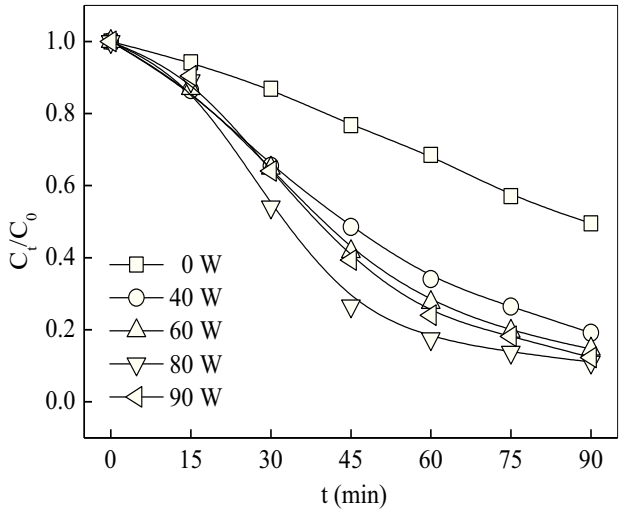


Figure 5. The effect of ultrasound power on the degradation (C_0=100 mg L^{-1}, [Fe_3O_4] =1 g L^{-1}, [$Na_2S_2O_8$] =200mM, pH_0=3.7)

5.3.6 The effect of initial pollutant concentration on the degradation of tetracycline

Figure 6 depicts degradation of tetracycline at different initial concentration. It can be seen that the degradation rate decreased with the increase of the initial tetracycline concentration. In the constant conditions of oxidation system such as $Na_2S_2O_8$ concentration, amount of Fe_3O_4, etc., $SO_4^{-\bullet}$ and $^{\bullet}OH$ formed in this process is also a constant [14].

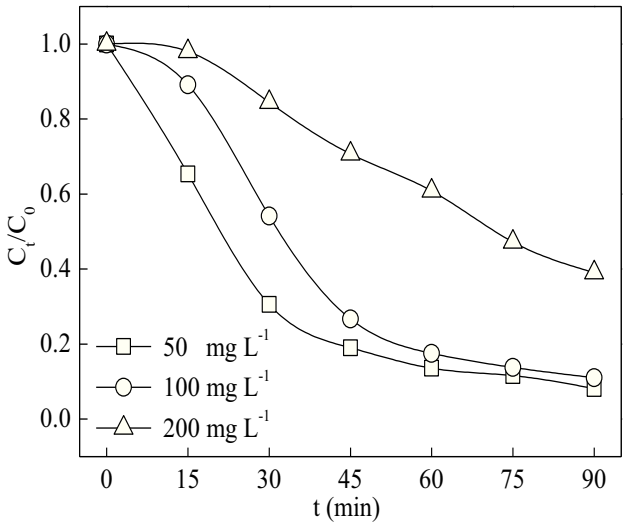


Figure 6. The effect of initial pollutant concentration on the degradation of tetracycline ([Fe_3O_4] =1 g L^{-1}, [$Na_2S_2O_8$] =200 mM, P=80 W, pH_0=3.7)

The increase of initial concentration of tetracycline would decrease the probability of reaction between the model pollutant molecules and reactive species. In addition, the intermediates which were produced during the reaction may cause the side reactions and $SO_4^{-\bullet}$ and $^{\bullet}OH$ were consumed. This may lead to the competition between the model pollutant and their products in reacting with $SO_4^{-\bullet}$ and $^{\bullet}OH$. Therefore, the degradation rate was declined at high initial concentration of tetracycline in the process of $Na_2S_2O_8/Fe_3O_4$/US.

However, it also can be seen that the total amount of tetracycline increases with the increase of initial concentration of tetracycline. Within 1.5 h of sono-reaction, 45.9 mg L^{-1}, 88.9 mg L^{-1} and 121.9 mg L^{-1} were oxidized when the initial concentrations were 50 mg L^{-1},100 mg L^{-1} and 200 mg L^{-1}, respectively. The amount of reactive species is determined by the addition of ultrasound power, catalyst dosage and $Na_2S_2O_8$ concentration in the dispersion.

5.3.7 Oxidative mechanism in the $Na_2S_2O_8/Fe_3O_4$/US system

$SO_4^{-\bullet}$, $^{\bullet}OH$, $O_2^{-\bullet}$ and H_2O_2 were generally considered as the oxidants in organic compounds degradation on the surface of the catalyst [17]. In order to evaluate the effect of the oxidizing species, three kinds of scavengers were employed to confirm the specific reactive species in the $Na_2S_2O_8/Fe_3O_4$/US process: *t*-BuOH, EtOH and BQ. Their quenching effect has been a signal for verifying the roles of $^{\bullet}OH$, $O_2^{-\bullet}$ and $SO_4^{-\bullet}$ (Figure 7).

tert-Butanol is generally used as $^{\bullet}OH$ scavenger and the reaction constant is 3.8-7.6×10^8 $M^{-1}S^{-1}$ [18]. Excess *tert*-Butanol (1.05 M) was added to the solution to check the contribution percentage of $^{\bullet}OH$s in this work. It is investigated that $^{\bullet}OH$s could be formed by the reaction of $SO_4^{-\bullet}$ with water at all pH values [9].

EtOH contains α-hydrogen, which acts as a scavenger of $SO_4^{-\bullet}$ and also can react with $^{\bullet}OH$. According to the literature report, the reaction constant of EtOH with $SO_4^{-\bullet}$ and $^{\bullet}OH$ are 1.6-7.7×10^7 $M^{-1}S^{-1}$ and 1.2-2.8×10^9 $M^{-1}S^{-1}$, respectively [18]. The results showed that the oxidation process was almost suppressed in the addition of 1.05 M

EtOH. It is proved that $SO_4^{-\bullet}$ and $^{\bullet}OH$ are the dominant radicals for the degradation of tetracycline in our study. In addition to $^{\bullet}OH$ and $SO_4^{-\bullet}$, $O_2^{-\bullet}$ is also an efficient reactive radical, which may also play an important role in the degradation of tetracycline. To investigate the role of $O_2^{-\bullet}$ in the process of $Na_2S_2O_8/Fe_3O_4$/US, 1,4-Benzoquinone (BQ) is used as $O_2^{-\bullet}$ quencher in this study. The decrease of the rate of degradation, with BQ in the $Na_2S_2O_8/Fe_3O_4$/US system can be attributed to the quenching of $O_2^{-\bullet}$ produced in the oxidizing process through rapid electron transfer to BQ that produces ground-state O_2 and BQ radical anion as given in the Eq. 9 [19]. The addition of 20 mM BQ does not seem to affect the degradation in the initial stages as seen in Figure 7.

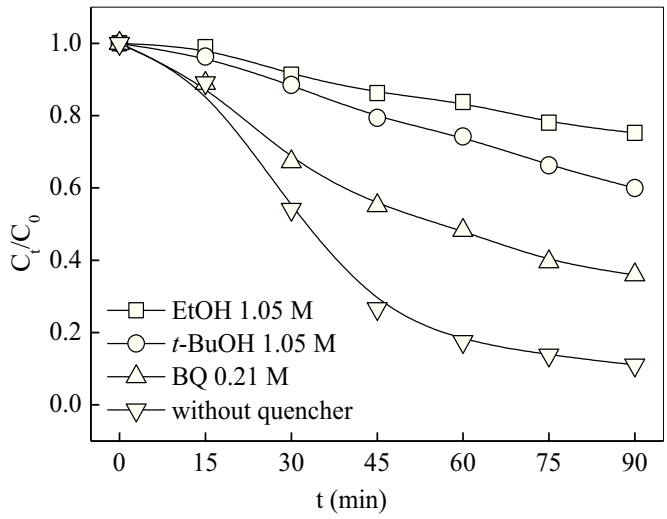
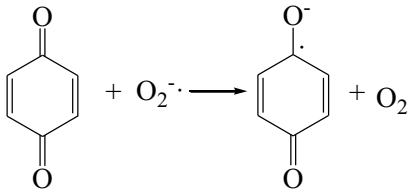


Figure 7. Effects of scavengers on the degradation of tetracycline (C_0=100 mg L^{-1}, [Fe_3O_4] =1 g L^{-1}, [$Na_2S_2O_8$] =200 mM, P=80 W, pH_0=3.7)

However, the suppression becomes larger after 30 min. The results indicated the delayed formation of $O_2^{-\bullet}$ during the sonochemistry reaction. $O_2^{-\bullet}$ can be formed through the Fenton-like reaction, and then a series of chain reactions can be achieved.



(9)

Figure 8 shows the possible degradation mechanism of tetracycline over iron oxides surface. $Na_2S_2O_8$ molecules are adsorbed on the surface of Fe_3O_4 and then

activated by the bound ≡Fe(II) and ≡Fe(III) to generate $SO_4^{-\bullet}$. Also, as discussed above, ultrasound irradiation could accelerate the decomposition of $Na_2S_2O_8$ [4]. Then H_2O_2 is formed by the hydrolysis of $S_2O_8^{2-}$ (Eq. 10). Furthermore, the $^{\bullet}OH$ can be formed as shown in Eqs. 11. The rate constant for Eq. 8-12 is 6.12×10^{-5} min^{-1} in the condition of 0.05 M H^+, and the rate constant is about 4.82×10^{-4} min^{-1} and 5.2×10^{-2} min^{-1} under the acid and alkaline conditions (Eqs. 13,14), respectively [20]. Furthermore, ≡Fe (III) is an electron acceptor, which can be reacted with HSO_5^- [19] as shown in Eq. 15. So the ≡Fe (II) is recycled. Then, a consecutive Fenton reaction can be conducted in $Na_2S_2O_8/Fe_3O_4$/US system.

$$2H_2O + S_2O_8^{2-} \rightarrow 2HSO_4^- + H_2O_2 \quad (10)$$

$$SO_4^{-\bullet} + H_2O \rightarrow SO_4^{2-} + {}^{\bullet}OH + H^+ \quad (11)$$

Acidic pH:

$$S_2O_8^{2-} + H^+ \rightarrow HS_2O_8^- \quad (12)$$

$$HS_2O_8^- \rightarrow SO_4^{-\bullet} + SO_4^{2-} + H^+ (8\text{-}13)$$

Alkaline pH:

$$SO_4^{-\bullet} + OH^- \rightarrow SO_4^{2-} + {}^{\bullet}OH \quad (14)$$

All pHs:

$$Fe^{3+} + HSO_5^- \rightarrow Fe^{2+} + SO_5^{-\bullet} + H^+ \quad (15)$$

Also, ≡Fe(III) reacts with H_2O_2 to generate $O_2^{-\bullet}$, then it is followed by ≡Fe(II) regeneration with formation of the $^{\bullet}OH$. Furthermore, the dissolved oxygen may also play an important role in the generation of $O_2^{-\bullet}$ [21].

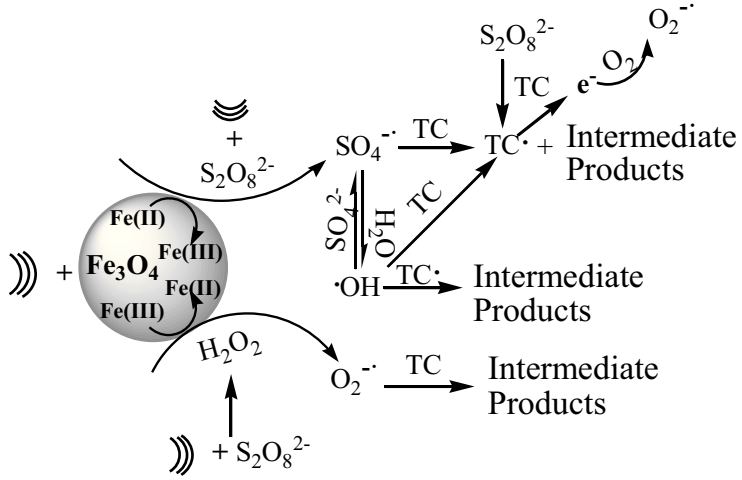


Figure 8. Mode of degradation of tetracycline for the activation of $Na_2S_2O_8$ on the surface of Fe_3O_4.
- TC is presented tetracycline;
-))) represents ultrasound irradiation

Due to the high oxidizing ability of the reactive oxygen species, the formed $SO_4^{-\bullet}$, $^{\bullet}OH$ and $O_2^{-\bullet}$ radicals initiate the subsequent degradation of tetracycline. Subsequently, a series of radical chain reactions will be initiated, where organic compounds are usually removed.

5.3.8 Structural and catalytic stabilities

The sequential experiments were performed to test the stability of the catalyst. The reusability of the solids had been evaluated in the optimum oxidation process as for the first oxidation cycle. The solid is easily removed from the reactor at the end of each repetitive oxidation process, then washed by distilled water, dried in the vacuum oven and stored at ambient temperature. As can be seen in Figure 9, in the primary experiment, tetracycline was decomposed 89% after 1.5 h. The decrease trend in final degradation efficiency was 73.5% after three repetitive experiments. It is generally believed that the decrease of the degradation efficiency is attributed to the leaching of metal ions from the catalyst or the changing of the surface characteristic of the catalyst [10]. Low dissolved iron concentration (<0.2 mM) was detected in the solution. In addition, as we known, Fe(III)-bearing iron oxides will be formed on the surface of the catalyst, which may be more soluble, less active and stable. Therefore,

we deduced that the major reason for the decline of removal efficiency is the conversion of the ≡Fe(II) to ≡Fe(III) on the surface of Fe_3O_4, which leads to less activity and stable of the catalyst.

The ultrasound irradiation may affect the particle size of heterogeneous catalysts [3]. To further verify the ultrasonic effects, the particle size distribution of fresh Fe_3O_4 catalyst and the used catalysts after ultrasound run were also evaluated. As shown in Figure 8-10, the particle size distribution of used catalysts is similar to the fresh catalysts. The result indicates that Fe_3O_4 is stable in the presence of ultrasound, and the cavitation physical effect on the catalyst is not obvious.

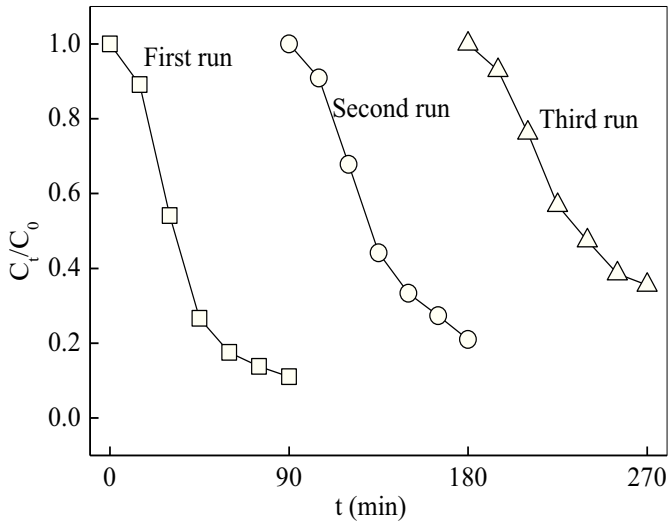


Figure 9. Repetitive degradation of tetracycline using Fe_3O_4 as catalyst (C_0=100 mg L^{-1}, $[Na_2S_2O_8]$ = 200 mM, $[Fe_3O_4]$ =1 g L^{-1}, P=80 W, pH_0=3.7)

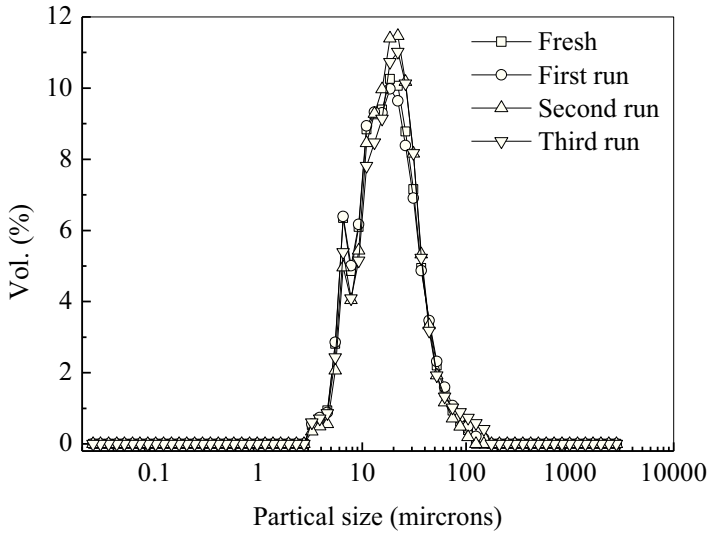


Figure 10. Fe_3O_4 catalyst particle size distribution dispersed in water before reaction and after $Na_2S_2O_8$/Fe_3O_4/US treatment.

5.4 Conclusion

This study shows that employing Fe_3O_4 in combination with $Na_2S_2O_8$ and ultrasound process can degrade tetracycline effectively. The degradation reaction mainly takes place on the surface of Fe_3O_4 and the leaching ion during the reaction could be neglected. The decrease of initial tetracycline concentration and the increase of Fe_3O_4 addition favor the enhancement of the degradation rate. The decomposition of tetracycline increased with the concentration of $Na_2S_2O_8$ and then decreased. The ultrasound can be used to crucially accelerate the decomposition of $Na_2S_2O_8$ at room temperature. The maximum power efficiency is reached at 80 W and a further increase of power does not affect degradation rate of the reaction. Both the degradation rate and removal efficiency reach the highest level at the optimal initial pH of 3.7. The presence of $SO_4^{-\bullet}$, $^{\bullet}OH$ and $O_2^{-\bullet}$ scavengers would hinder the degradation reaction.

Our results suggest that Fe_3O_4/US activated $Na_2S_2O_8$ process may be an optional method for enhancing the degradation of tetracycline in natural and engineering systems.

References

[1] Zhang, H., Liu, F., Wu, X., Zhang, J., Zhang, D. (2009). Degradation of tetracycline in aqueous medium by electrochemical method. *Asia - Pacific Journal of Chemical Engineering*, *4*(5), 568-573.

[2] Harvey, A.E., Smart, J.A., Arms, E.S., (1955). Simultaneous spectrophotometric determination of iron (II) and total iron with 1,10-phenanthrolin. *Analytical Chemistry,* 27, 26-29.

[3] Molina, R., Martinez, F., Melero, J.A., Bremner, D.H., Chakinala, A.G. (2006). Mineralization of phenol by a heterogeneous ultrasound/Fe-SBA-15/H_2O_2 process: multivariate study by factorial design of experiments. *Applied Catalysis B: Environmental,* 66, 198-207.

[4] Price, G. J., Clifton, A. A. (1996). Sonochemical acceleration of persulfate decomposition. *Polymer*, *37*(17), 3971-3973.

[5] Lau, T.K., Chu, W., Graham, N.J.D. (2007). The aqueous degradation of buthylated hydroxyanisole by UV/$S_2O_8^{2-}$: study of reaction mechanisms via dimerization and mineralization. *Environmental Science Technology*, 41 (2), 613-619.

[6] Liang, C., Wang, Z. S., Bruell, C. J. (2007). Influence of pH on persulfate oxidation of TCE at ambient temperatures. *Chemosphere*, *66*(1), 106-113.

[7] Wu, C. H. (2008). Effects of operational parameters on the decolorization of CI Reactive Red 198 in UV/TiO_2-based systems. *Dyes and Pigments*, *77*(1), 31-38.

[8] Huie, R. E., Clifton, C. L. (1990). Temperature dependence of the rate constants for reactions of the sulfate radical, $SO_4^{-\bullet}$, with anions. *Journal of physical chemistry*, *94*(23), 8561-8567.

[9] Zhao, J., Zhang, Y., Quan, X., Chen, S. (2010). Enhanced oxidation of 4-chlorophenol using sulfate radicals generated from zero-valent iron and peroxydisulfate at ambient temperature. *Separation and Purification Technology*, *71*(3), 302-307.

[10] Gayathri, P., Praveena Juliya Dorathi, R., Palanivelu, K. (2010). Sonochemical degradation of textile dyes in aqueous solution using sulphate radicals activated by immobilized cobalt ions. *Ultrasonics sonochemistry*, *17*(3), 566-571.

[11] Xue, X., Hanna, K., Abdelmoula, M., Deng, N. (2009). Adsorption and oxidation of PCP on the surface of magnetite: kinetic experiments and spectroscopic investigations. *Applied Catalysis B: Environmental*, *89*(3), 432-440.

[12] Peyton, G. R. (1993). The free-radical chemistry of persulfate-based total organic carbon analyzers. *Marine Chemistry*, *41*(1), 91-103.

[13] Yan, J., Lei, M., Zhu, L., Anjum, M. N., Zou, J., Tang, H. (2011). Degradation of sulfamonomethoxine with Fe_3O_4 magnetic nanoparticles as heterogeneous activator of persulfate. *Journal of hazardous materials*, *186*(2), 1398-1404.

[14] Zhang, H., Fu, H., Zhang, D. (2009). Degradation of CI Acid Orange 7 by ultrasound enhanced heterogeneous Fenton-like process. *Journal of hazardous materials*, *172*(2), 654-660.

[15] Neppolian, B., Doronila, A., Ashokkumar, M. (2010). Sonochemical oxidation of arsenic (III) to arsenic (V) using potassium peroxydisulfate as an oxidizing agent. *Water research*, *44*(12), 3687-3695.

[16] Price, G. J., Clifton, A. A., Keen, F. (1996). Ultrasonically enhanced persulfate oxidation of polyethylene surfaces. *Polymer*, *37*(26), 5825-5829.

[17] Huang, K. C., Couttenye, R. A., Hoag, G. E. (2002). Kinetics of heat-assisted persulfate oxidation of methyl *tert*-butyl ether (MTBE).*Chemosphere*, *49*(4), 413-420.

[18] Anipsitakis, G. P., Stathatos, E., Dionysiou, D. D. (2005). Heterogeneous activation of oxone using Co_3O_4. *The Journal of Physical Chemistry B*, *109*(27), 13052-13055.

[19] Herath, A. C., Rajapakse, R. M. G., Wicramasinghe, A., Karunaratne, V. (2008). Photodegradation of triphenylamino methane (magenta) by photosensitizer in oxygenated solutions. *Environmental science & technology*, *43*(1), 176-180.

[20] House, D. (1962). Kinetics and mechanism of oxidations by peroxydisulfate. *Chemical reviews*, *62*(3), 185-203.

[21] Huang, Y. F., Huang, Y. H. (2009). Behavioral evidence of the dominant radicals and intermediates involved in Bisphenol A degradation using an efficient Co^{2+}/PMS oxidation process. *Journal of hazardous materials*, *167*(1), 418-426.

CHAPTER 5 ULTRASOUND ENHANCED HETEROGENEOUS ACTIVATION OF PEROXYDISULFATE BY MAGNETITE CATALYST

Chapter 6 Ultrasound-enhanced magnetite catalytic ozonation of tetracycline in water

Article:

Liwei Hou, Hui Zhang, Liguo Wang, Lu Chen, Chemical Engineering Journal (2013) in press.

In this section, ozone acts another kind of oxidant, and it also can be activated by magnetite. Commercial magnetic particles, Fe_3O_4, were selected as the catalyst to evaluate its catalytic activity with ozone. Comparative experiments were performed to investigate the degradation efficiencies and removal rates of TC, including experiments with ozonation alone, ultrasound-enhanced ozonation (US/O_3), catalytic ozonation (Fe_3O_4/O_3), and ultrasound-enhanced catalytic ozonation ($US/Fe_3O_4/O_3$). The effects of the operating conditions on the removal of TC during the ultrasound-enhanced catalytic ozonation process were investigated. The mineralization and the variation of biodegradability and toxicity were also investigated in this study. The solubility and the reusability of the catalyst were critical parameters that were also evaluated to investigate the stability of the catalyst.

6.1. Introduction

Over the past decades, contaminated water has been treated in biological treatment plants using biological and physic-chemical methods. However, conventional treatment processes are ineffective for antibiotic agents, both in their parent form and as metabolites, which are widely detected in wastewater, surface and ground waters and have been observed to be resistant to the conventional sewage treatment process [1,2]. Furthermore, considerable volumes of toxic by-products may be produced during the treatment process. Advanced oxidation processes (AOPs) such as Fenton and photo-Fenton-like oxidation, have been extensively applied to address this problem [3,4]. Some of the AOPs are based on the use of ozone to degrade toxic compounds in wastewater [2,5]. Ozone is a powerful oxidizing molecule that can either react directly with organic pollutants or decompose to free radicals to attack the organic compounds with a very high rate constant. However, when ozone is used alone, it does not often lead to high level of mineralization and toxicity removal [6-7]. The use of ozone also has limitations with respect to the high implementation cost and the poor mass transfer rate. Consequently, ozone is usually combined with other technologies to improve its utilization and application [8,9]. In recent years, heterogeneous catalytic ozonation has become a powerful treatment method for the degradation of refractory organic pollutants, and high removal and mineralization can be achieved correspondingly [10–13]. The catalysts include MgO [10], alumina [11], alumina based catalysts [12], activated carbon supported catalyst (MnO_x/GAC) [14], α-FeOOH [15], cobalt oxides [16], β-MnO_2 [17], perovskite [18], and brucite [19]. Although some catalysts have shown considerable catalytic activity in the ozonation process, their production might be problematic and cost-intensive from an industrial viewpoint. Moreover, the separation step is often unfavourable.

Considering this information, the application of magnetite particles (Fe_3O_4) in the pollution control has received great attention in the recent years [20–22]. Magnetic particles can be separated from the solution using a simple magnetic process, which shows its superiority to the other metal oxides (such as α-FeOOH, and α-Fe_2O_3 *etc.*) [15,23]. In addition, as one of transition metal oxides, Fe_3O_4 with multiple accessible oxidation states is a good catalyst for ozone decomposition [24,25]. Despite the promising results of catalytic ozonation using magnetic as the catalyst, the deactivation of the catalyst due to the organic intermediates accumulation on the surface of the catalyst is still a major obstacle for its application. In the meanwhile, the release of metal ions decreased the stability and activity of the catalyst. Therefore, the development of an effective approach to improve the catalytic efficiency and durability remains an important issue that needs to be urgently addressed.

It has been found that ultrasound can enhance the activity of the catalyst in the ozonation process without prejudice to the stability of the iron species [23,26]. During the ultrasonic process, the cavitation effect can clean the surface of the catalyst, and the catalyst can thereby avoid being poisoned during the ultrasonic irradiation process [23,27]. In addition, ultrasound accelerates turbulence, which can reduce the liquid film thickness and subsequently increase the mass transfer of reactants and by-products between the liquid and solid phases [27,29]. Furthermore, hydroxyl radicals will be generated in the vapour phase of cavitation bubbles during the ultrasonic process [29,30].

In this study, magnetic particles, Fe_3O_4, were selected as the catalyst to evaluate its catalytic activity with ozone. Tetracycline hydrochloride (TC), which is a typical class of antibiotics that is widely used for the treatment of infectious diseases in humans and in veterinary applications, was chosen as the target contaminant compound. An air-lift reactor was used owing to its efficient mixing with low shear stress and energy consumption and it provides the advantage of a high rate of gas–liquid mass transfer [23,28,30]. Comparative experiments were performed to investigate the degradation efficiencies and removal rates of TC, including experiments with ozonation alone, ultrasound-enhanced ozonation (US/O_3), catalytic ozonation (Fe_3O_4/O_3), and ultrasound-enhanced catalytic ozonation ($US/Fe_3O_4/O_3$). The effects of the operating conditions on the removal of TC during the ultrasound-enhanced catalytic ozonation process were investigated. The mineralization and the variation of biodegradability and toxicity were also investigated in this study. The solubility and the reusability of the catalyst were critical parameters that were also evaluated to investigate the stability of the catalyst.

6.2. Experimental section

6.2.1 Materials

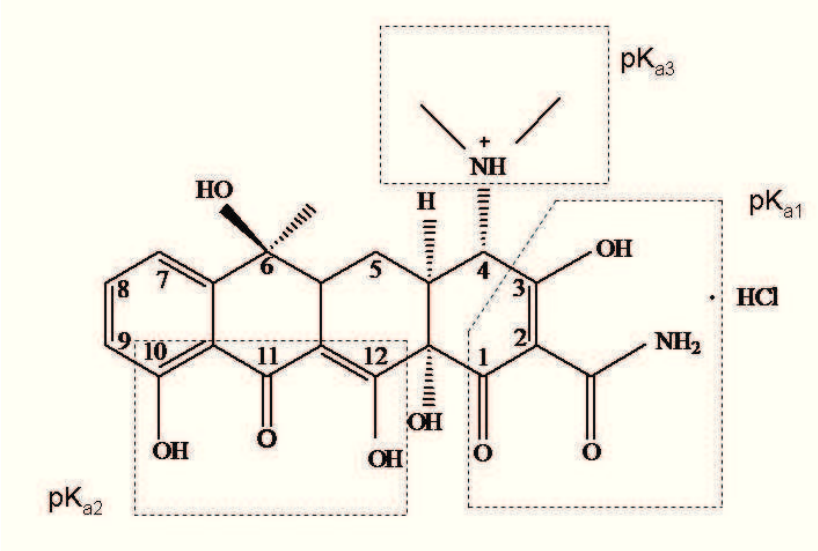
Commercial tetracycline hydrochloride ($C_{22}H_{25}N_2O_8Cl$, Sigma–Aldrich, >99%) with a molecular weight of 480.9 was used as received without further purification. The structure and relative data on TC are presented in Table 1. Magnetite was purchased from Prolabo (Paris, France). The structure of the catalyst and the spent samples were verified via X-ray diffraction using a Bruker D5005 diffractometer equipped with a Cu Kα radiation source (λ = 1.5406 Å). The diffraction intensity data were recorded between 20° and 80° 2θ with a recording step of 0.05° 2θ each 3 s. Phase identification was performed by comparison of the diffraction results with those from the JCPDS database (Supplementary information, Fig. S1). The specific surface areas of the catalyst before and after the oxidation process were obtained using the N_2 adsorption measurements. Furthermore, the primary physico-chemical properties of the fresh and spent samples were summarized in Table 2. *Tert*–butanol, isopropanol and NaF were purchased from Shanghai Chemical Reagent Co., Ltd. (Shanghai, China). The other chemicals used in this study were of reagent grade.

6.2.2 Procedure

A fresh solution of TC was prepared in a buffer solution with an initial concentration (C_0) of 100 mg L^{-1} before each run. The phosphate buffer solution was used in this study, i.e., 0.05 mol L^{-1} H_3PO_4 and appropriate quantities of NaOH for pH 9.0 [31], and 0.05 mol L^{-1} NaH_2PO_4 and Na_2HPO_4 for other pH values (3.0, 5.0, 7.0).

Semi-batch experiments were carried out in a rectangular air-lift reactor made of plexy glass with working volume of 200 mL [23]. Ozone was generated using a laboratory ozone generator (XFZ-5BI, China). The concentrations of ozone in the gas and liquid phases were measured using the iodometric method with a potassium iodide solution [32] and the indigo method [33], respectively. The catalyst was subsequently added to the reactor and stirred by a magnetic stirrer to maintain thorough mixing of the solution during the reaction.

Table 1. Chemical structures and relevant data for tetracycline hydrochloride

Name	Tetracycline hydrochloride
Formula	$C_{22}H_{25}N_2O_8Cl$
Structure	
Formula Weight (g mol^{-1})	480.9
λ (nm)	359, 270
pK_a	3.3, 7.68, 9.7

Sonication was performed using a KS-250 ultrasonic generator (250 W, 20 kHz, Ningbo Kesheng Instrument, China) equipped with a titanium probe transducer. The tip of the probe was 1.0 cm in diameter, and it was inserted 1.5 cm into the liquid layer. The sonication was administered in a pulse mode of 2.5 s on and 2.1 s off. The acoustic power was transferred to the solution, and it was measured using the calorimetric method [34]. The reactor was immersed into a water bath at 22 ± 2 °C during the reaction. At different time intervals, 1.5-mL aliquots of the reaction solution were sampled and then filtered through 0.22–μm membrane filters (Millipore) before analysis.

6.2.3 Analysis methods

The concentration of TC at each interval was measured using a reversed-phase high-performance liquid chromatography (HPLC) unit that consisted of a Shimadzu LC-20AB pump, a Shim-Pack VP-ODS-C18 column (4.6 mm × 250 mm, 5 μm) and a UV detector (Shimadzu UV-1600 spectrophotometer); the flow rate was 1.0 mL min^{-1}. The detected wavelength for TC was 359 nm. The mobile phase was composed of 31% (v/v) acetonitrile and a 69% oxalic acid solution (0.01 mol L^{-1}). The injection volume was 20 μL. COD was determined via the colorimetric method at 440 nm using a Hach spectrophotometer (Hach DR/2000, Loveland) based on the standard method [35]. The five-day biochemical oxygen demand (BOD_5) was measured via the respirometric method using an Oxi-top BOD analyser (WTW Oxitop IS6, Germany). The total iron (Fe^{2+}, Fe^{3+}) leached from the Fe_3O_4 was determined using the 1, 10-phenanthroline method [36]. The density of surface hydroxyl

groups of the catalyst was measured with a saturated deprotonation method [15]. Briefly, 0.3 g of oxide particles was added to a series of NaOH solutions (2–200 mM). After being shaken at 25 ^{o}C for more than 4 h, the solution was titrated with a standard HNO_3 solution to determine the rest concentration of NaOH in the solution. The surface acid hydroxyl groups and the surface basic hydroxyl groups should be equal due to the charge balance in the solution. Thus, the sum of acid and basic hydroxyl groups is confirmed to be the total density of surface hydroxyl groups (Table 2).

Table 2. The surface characteristics of fresh and spent catalysts.

Sample	Morphology	*D* (nm)	SSA (m^2 g^{-1})	Density of surface hydroxyl groups (mmol g^{-1})
fresh	uniform	78.6	0.7	1.22
spent	uniform	72.6	2.6	1.36

D, the crystal domain size evaluated from the X-ray line broadening using the Scherrer equation; SSA, the specific surface area evaluated using the BET model.

6.2.4 Acute toxicity test of tetracycline

The acute toxicity tests were conducted with *Daphnia magna* (*D. magna*) immobilisation assays. These assays were evaluated using the conditions prescribed by the OECD guideline 202 method [37]. *D. magna* was cultivated in the laboratory for at least three offspring. The acute toxicity experiments were performed in 50-mL-capacity test beakers using 25 *D. magna* that were less than 24 h old, which were divided into five groups. Four groups were used as test groups, whereas the remaining group was used as the control group. These groups were placed in the incubator along with the testing samples. The incubator was set to room temperature in a 16 h–light and 8 h–dark cycle. Food was not administered during the test. The surviving and mobile *D. magna* were counted at different time intervals.

6.3 Results and discussion

6.3.1 Degradation efficiency of tetracycline in the investigated processes

The experiments were conducted using the ozonation, US/O_3, catalytic ozonation and $US/Fe_3O_4/O_3$ processes with the pH adjusted to neutral with a buffer solution. The gas flow rate was 30 L h^{-1}, and the gas ozone concentration was 17.9 mg L^{-1} (in this case, 35.8 mg ozone was bubbled into 200 mL solution within 20 min reaction, i.e., 179 mg of ozone dose per liter solution). The ultrasound power was 85.7 W L^{-1} for the US/O_3 system and the $US/Fe_3O_4/O_3$ system, and a catalyst loading of 0.3 g L^{-1} Fe_3O_4 was used for the Fe_3O_4/O_3 and the $US/Fe_3O_4/O_3$ systems.

In this study, the experiments conducted using the above processes followed apparent pseudo-first-order kinetics according to the following equation (1):

$$-\frac{dC}{dt} = kC \quad (1)$$

where C is the concentration of TC at time t, k is the pseudo–first–order degradation rate constant.

As evident in Fig. 1, the enhanced value of k indicated that the use of ultrasonic irradiation promoted the reaction between ozone and TC. Ozonation of TC is a gas–liquid reaction, and mass transfer rate of ozone from gas phase to liquid phase is a crucial parameter to the process [23]. With the combination of ultrasonic irradiation, greater mixing caused turbulence, which reduced the gas–liquid film thickness [38]. When the film thickness was decreased, the liquid-side mass transfer coefficient (k_L) increased accordingly. Moreover, the mechanical effects of ultrasound broke the ozone gas bubbles, which led to a larger specific surface area (a). Therefore, the volumetric mass transfer coefficient $k_L a$ should increase in the presence of ultrasonic irradiation. Furthermore, when US/O_3 was used, the production of $^{\bullet}$OH increased, which primarily resulted from the additional thermal decomposition of ozone [39]:

$$O_3(g) +))) \rightarrow O_2(g) + O(^3P)(g) \quad (2)$$

$$O_3(g) + H_2O(g) \rightarrow 2^{\bullet}OH \quad (3)$$

where the symbol "))) " represents ultrasonic irradiation

The generated $^{\bullet}$OH might diffuse into the bulk solution to oxidize the TC. Therefore, as shown in Fig. 1, the rate constant was 0.354 min^{-1} when ozone was used alone, whereas it increased to 0.461 min^{-1} when ozonation was combined with ultrasonic irradiation (US/O_3).

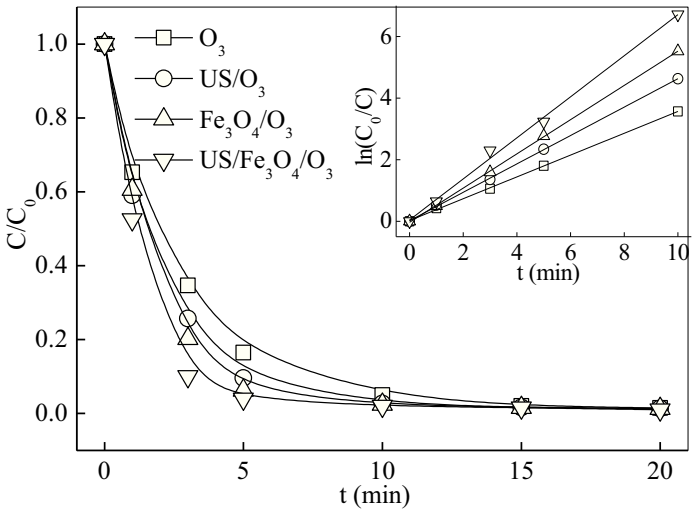


Fig. 1 Comparative performance for the selected processes on TC removal (C_0 = 100 mg L^{-1}, $[O_3]_g$ = 17.9 mg L^{-1}, Q = 30 L h^{-1}, P = 85.7 W L^{-1}, $[Fe_3O_4]$ = 0.3 g L^{-1}, pH = 7.0).

In parallel, the rate constant in the catalytic ozonation system was also greater than the rate constant of ozonation alone. It is generally accepted that the catalyst can initiate the decomposition of ozone on its surface and subsequently enhance the formation of hydroxyl radicals ($^{\bullet}OH$) on the catalyst surface [14,15,40-42]. Specifically, the surface hydroxyl groups on the catalyst surface, as the active surface sites, are believed to be critical for the generation of $^{\bullet}OH$ in the catalytic ozonation of TC in aqueous solution [43,44]. When the catalyst was introduced into water, H_2O was quickly adsorbed on the catalyst surface, forming surface hydroxyl groups [45], and the surface hydroxyl groups on the catalyst (≡Fe-OH) were the active sites in the catalytic ozonation process, and then $^{\bullet}OH$ was generated [15,44].

Since iron is in a mixed-valence state in magnetite, it is expected that ozone can be decomposed on oxidized/reduced form of metal to produce $^{\bullet}OH$ [42], whereas ≡Fe(II) that is oxidized to ≡Fe(III) could be returned to its initial state by $^{\bullet}OOH$ [25]. This speculation will be further explored in our future work.

$$O_3 + \equiv Fe(II) + H^+ \rightarrow \equiv Fe(III) + {}^{\bullet}OH_{ads} + O_2 \quad (4)$$

where $^{\bullet}OH_{ads}$ represents the hydroxyl radicals on the catalyst surface.

The oxidizing potential of $^{\bullet}OH$ was significantly greater than that of molecular ozone, and a faster degradation rate (0.555 min^{-1}) was observed in catalytic ozonation process.

When both ultrasonic irradiation and Fe_3O_4 were introduced into the ozonation system, the degradation rate of TC reached 0.664 min^{-1}, which was nearly two times greater than that with ozonation alone and was also greater than that in US/O_3 system or in the catalytic ozonation system. As previously mentioned, the degradation rate of TC by ozonation would be improved when ozonation is combined with ultrasonic irradiation or catalyst. However, the active sites of Fe_3O_4 could be gradually occupied by the by-products formed during the catalytic ozonation reaction, which would result in the deactivation of the catalyst [16,23]. When ultrasound was introduced into the system, more available active sites would be obtained. Simultaneously, the turbulent effect of cavitation could enhance mass transfer between the catalyst and the reactants or products [23]. In addition, the removal rate was increased because of the ultrasonic cavitation effect [23,29]. Therefore, compared to ozonation, US/O_3 and the catalytic ozonation processes, a considerably greater degradation rate was achieved with the US/Fe_3O_4/O_3 process. Based on the experimental results and the literatures [40-42], the ultrasound-enhanced catalytic ozonation mechanism on the Fe_3O_4 is proposed and illustrated in Fig. 2.

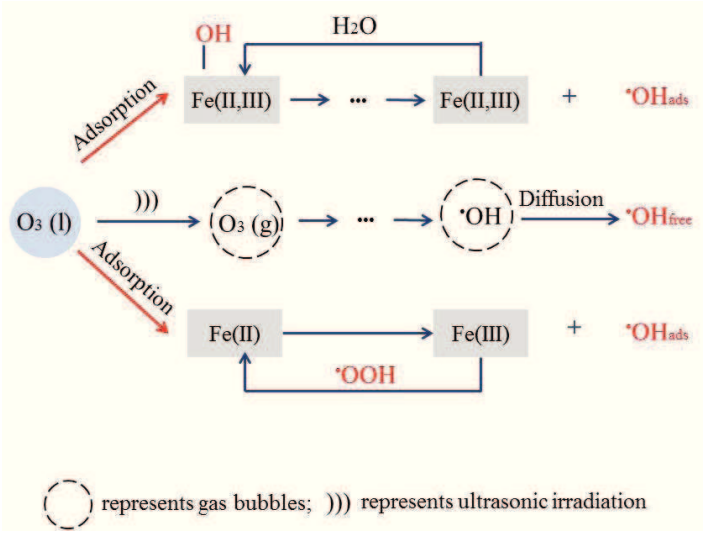


Fig. 2 Proposed ultrasound-enhanced catalytic ozonation mechanism on the Fe_3O_4 suspension.

When oxygen rather than ozone was bubbled into the reactor, the removal of TC was negligible in the presence of ultrasound alone because the production of •OH in the solution at a frequency of 20 kHz was insufficient to ensure the removal of the organic pollutant (Supplementary information, Fig. S2). Furthermore, almost no removal of TC occurred when catalyst was used alone (Supplementary information, Fig. S2). It indicated that the role of adsorption phenomenon on TC removal was limited. Even when ultrasound was introduced, no significant removal efficiency was obtained (Supplementary information, Fig. S2), and it can be concluded that the generation of free radicals was negligible in the US/Fe_3O_4 system. As the US/Fe_3O_4/O_3 process was the most effective route for the treatment of TC, it was employed in the following laboratory experiments.

6.3.2 Effect of power density on the TC removal in the US/Fe_3O_4/O_3 system

To investigate the effect of the ultrasonic power density on the degradation of TC, an ultrasonic horn (20 kHz) with different power settings was used. The initial pH was 7.0, the TC concentration was 100 mg L^{-1}, the gaseous ozone concentration was 16.2 mg L^{-1}, and the catalyst dosage was 0.3 g L^{-1} (Fig. 3). When the ultrasonic power density ranged from 39.6 W L^{-1} to 101.3 W L^{-1}, the degradation rate increased with increasing power density. The rate constants were 0.444, 0.502, and 0.567 min^{-1} at power densities of 39.6, 85.7, and 101.3 W L^{-1}, respectively. When ultrasound was

introduced into the system, it would lead to the greater mixing intensity and then the turbulence of the liquid phase. An increase in the power density would increase turbulence and the mechanical effect, which increased liquid-side mass transfer coefficient k_L and specific surface area a. Then the mass transfer rate of ozone was increased accordingly. In addition, due to the cleaning action of the ultrasonic irradiation, more available active sites on the catalyst surface were available when the ultrasound power density was increased. Moreover, the surface hydroxyl groups are the major active species, which are generated on the catalyst surface during the reaction. Therefore, the density and the status of surface hydroxyl groups are important factors to understand the ozone decomposition on the catalyst surface. Table 2 indicated that the density of the surface hydroxyl groups of the spent magnetite was higher than that of the fresh one. Therefore, the decomposition of ozone to •OH at catalyst surface were enhanced and TC removal rate was increased.

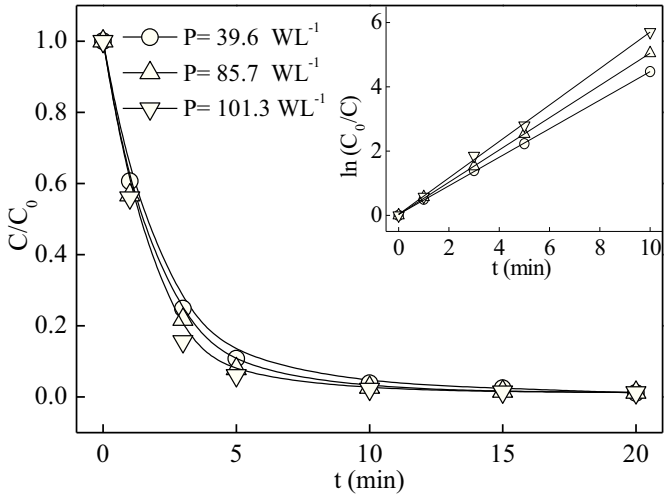


Fig. 3 The effect of ultrasonic power density on the degradation of tetracycline (C_0 = 100 mg L^{-1}, $[O_3]_g$ = 16.2 mg L^{-1}, Q = 30 L h^{-1}, $[Fe_3O_4]$ = 0.3 g L^{-1}, pH = 7.0);

6.3.3 Effect of pH on the TC removal in the US/Fe_3O_4/O_3 system

As deduced in the above section, the active species are •OH on the catalyst surface and •OH in the aqueous solution. The number of these active species is strictly dependent upon pH. Therefore, the pH value is usually considered to be one of the most important factors in the heterogeneous ozonation system. In this study, the

degradation of TC was conducted at fixed pH values of 3.0, 5.0, 7.0, and 9.0, which were controlled using a buffer solution. As evident in Fig. 4, an increase in the pH resulted in a significant enhancement in the TC degradation rate.

The structure of TC is presented in different forms ($TCH_3^+ \rightarrow TCH_2 \rightarrow TCH^- \rightarrow TC^{2-}$) at different pH value. When the pH was below 3.3 (pK_{a1}), TC was in its protonated form, which was less susceptible to ozone attack. With the increase of pH, deprotonation reactions took place, the deprotonated TC with negatively charged group could be more easily attacked by ozone molecules than TC itself when the solution pH was less than 7.68 (pK_{a2}) [46,47]. Moreover, the fraction of TCH^- was the primary TC form while pH was increased to 9.0, and its effect on the TC removal rate was also easier than that of TCH_2 when pH was further increased to 9.0.

In addition, the pH may influence the surface activity of the metal oxides in the catalytic ozonation system. Proton transfer occurs on the surface of the metal oxides at different pH values [14]. The different forms of the catalysts are associated with the decomposition rate of ozone on the catalyst surface [14]. Magnetite is an amphoteric solid that can develop charges in the protonation and deprotonation reactions on its surface under different pH [43]. And, it is reported that the density of surface hydroxyl groups on the catalyst surface largely depends on the pH at the point of zero charge (pH_{PZC}) of the catalyst [15]. The majority of the surface hydroxyl groups is in a neutral state when the pH is close to the pH_{PZC} of the catalyst. On the other hand, the oxide surface becomes protonated or deprotonated when the pH of the aqueous solution is greater than or less than the pH_{PZC}. Therefore, the surface hydroxyl groups have different charge states, which depend on not only the pH of aqueous solution but also the pH_{PZC} of the catalyst [44]. This situation is described in the following equations:

$$pH < pH_{PZC}: \quad \equiv FeOH + H^+ \rightarrow \equiv FeOH_2^+ \qquad (5)$$

$$pH > pH_{PZC}: \quad \equiv FeOH + OH^- \rightarrow \equiv FeO^- + H_2O \qquad (6)$$

At neutral and basic pH levels, ozone is decomposed to non-selective $^{\bullet}OH$ (equation 7), which could easily attack organic molecules [20].

$$2O_3 + OH^- \rightarrow {}^{\bullet}OH + O_2^- + 2O_2 \quad (7)$$

Thus, the removal rate of TC was increased from 0.167 to 0.366 min^{-1} when pH was increased from 3.0 to 9.0.

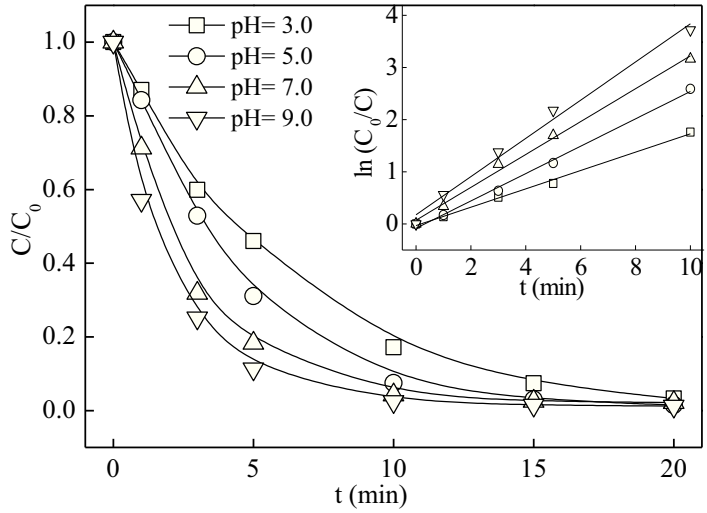


Fig. 4 The effect of pH on the degradation of tetracycline (C_0 = 100 mg L^{-1}, $[O_3]_g$ = 12.5 mg L^{-1}, Q = 30 L h^{-1}, P = 85.7 W L^{-1}, $[Fe_3O_4]$ = 0.3 g L^{-1})

6.3.4 The effect of catalyst dosage on the removal of TC in the US/Fe_3O_4/O_3 system

Compared to the US/O_3 system, the catalyst addition exerted a positive influence on the conversion of TC (Fig. 1), and the removal rate increased from 0.461 min^{-1} to 0.664 min^{-1} when the catalyst dosage rose from 0 to 0.3 g L^{-1}. The production of $^{\bullet}OH$ increased with the addition of Fe_3O_4, and the $^{\bullet}OH$ showed greater oxidizing power than ozone itself. Thus, the catalyst dosage played an important role in the US/Fe_3O_4/O_3 process. To make effective use of the catalyst in practical applications, it was reasonable to explore the effect of the catalyst dosage on the degradation rate of TC. The experiments were conducted using catalyst concentrations that were ranged from 0.3 to 1.0 g L^{-1}, and the lower catalyst loading was not investigated due to the limitation of experimental conditions.

As can be seen in Fig. 5, TC degradation rate was almost independent of the dosage of Fe_3O_4 over the range investigated. Similar results were also observed by other catalytic ozonation processes [10,11,48]. It can be hypothesized that there exists a minimum amount of catalyst offering a sufficient number of active sites. Further

increase in the catalyst loading may generate excessive •OH, which will recombine forming hydrogen peroxide [49]. Therefore, the removal rate of TC was nearly independent of the catalyst dosage in the range of 0.3–1.0 g L^{-1} during the US/Fe_3O_4/O_3 process.

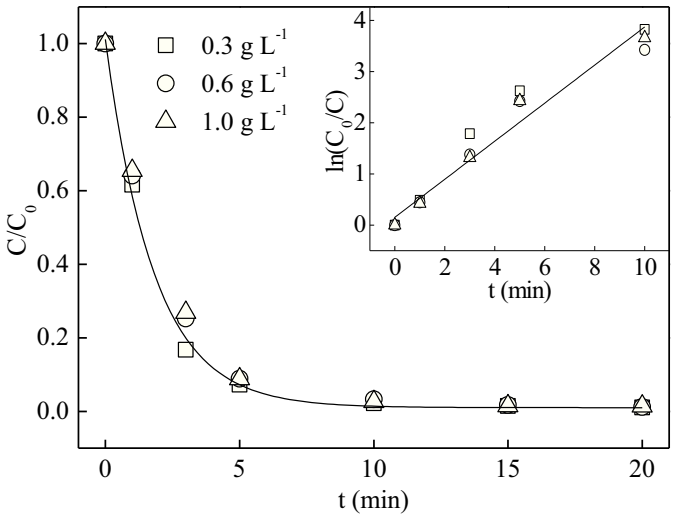


Fig. 5 The effect of Fe_3O_4 dosage on the degradation of tetracycline (C_0 = 100 mg L^{-1}, $[O_3]_g$ = 13.7 mg L^{-1}, Q = 30 L h^{-1}, P = 85.7 W L^{-1}, pH = 7.0).

6.3.5 Evidence of hydroxyl radical generation in the US/Fe_3O_4/O_3 system

As proposed in the mechanism in Fig. 2, for the ultrasound-enhanced catalytic ozonation, the increased oxidative capacity in the presence of a catalyst is commonly attributed to the enhanced generation of •OH [49]. The hydroxyl radical is considered to be the strongest oxidative species during the reaction. In the ultrasound–enhanced catalytic ozonation process, •OH could be generated through homogeneous decomposition of ozone initiated by hydroxide ions, thermal decomposition of ozone in cavitation bubbles, and heterogeneous ozone decomposition on oxidized/reduced form of metal or hydroxyl groups of metal oxide. Because hydroxyl radials are a short–lived species, they are difficult to be measured directly by conventional analytical techniques. Hence, we cannot directly determine how Fe_3O_4 nanoparticles act in the radical chain reaction. We made an indirect evaluation using trapping agents by measuring the removal efficiency and removal rate in the process of US/Fe_3O_4/O_3, and the results are shown in Fig. 6. Two different radical scavengers (*tert*-butanol and

isopropanol) and a reactive surface hydroxyl group indicator (NaF) were employed. The respective quenching effects of the reagents allowed the roles of the total hydroxyl radicals ($^{\bullet}OH$) both in the solution and on the surface of the catalyst, and the hydroxyl radicals in solution ($^{\bullet}OH_{free}$), to be verified.

Tert-butanol is generally used as the scavenger of hydroxyl radicals both generated in the heterogeneous and homogenous catalytic reactions. It can be adsorbed on the surface of the catalyst to occupy the reactive sites, and then to inhibit the reaction process [43]. On the other hand, *tert*-butanol can also be used as the scavenger of hydroxyl radicals in aqueous ozonation process [46]. Therefore, the excessive *tert*-butanol serve as a scavenger for all the hydroxyl radicals both generated in the solution and on the catalyst surface. As shown in Fig. 4, the removal rate of TC was 0.238 min^{-1} when 0.1mol L^{-1} *tert*-butanol was added, whereas the reaction rate of TC was 0.464 min^{-1} in the absence of scavenger. This result confirmed the significant role of $^{\bullet}OH$ for the degradation of TC. To further determine the role of $^{\bullet}OH_{free}$ and $^{\bullet}OH_{ads}$ on the degradation of TC, isopropanol and NaF were used, respectively.

Isopropanol is easily oxidized by $^{\bullet}OH$, and it is usually used as a diagnostic tool for $^{\bullet}OH_{free}$ because of its low affinity to semiconductor surfaces in aqueous media [50]. When isopropanol was added, a very limited quenching effect was observed (0.342 min^{-1}) at the beginning of the experiment (Fig. 6), which suggested that the $^{\bullet}OH_{free}$ generated in bulk solution was not mainly attributed to the removal of TC.

The concentration of surface hydroxyl group generated on the catalyst surface can be controlled by adopting the fluoride–exchange process [51,52]. When 0.1 mol L^{-1} NaF was added to the reaction system, the degradation rate was suppressed, and the rate constant was 0.256 min^{-1}. That is to say, the hydroxyl groups on the surface of Fe_3O_4 were almost replaced by fluoride ions, and the process of ozone decomposition on the surface of Fe_3O_4 as mentioned in Fig. 2 was greatly inhibited. Consequently, the $^{\bullet}OH_{ads}$ generated on the catalysts surface was suppressed accordingly. Therefore, besides the direct oxidation of molecular ozone to organic degradation,

ultrasound-enhanced catalytic ozonation of TC occurred mainly with the adsorbed state of hydroxyl radical over the Fe_3O_4 surface.

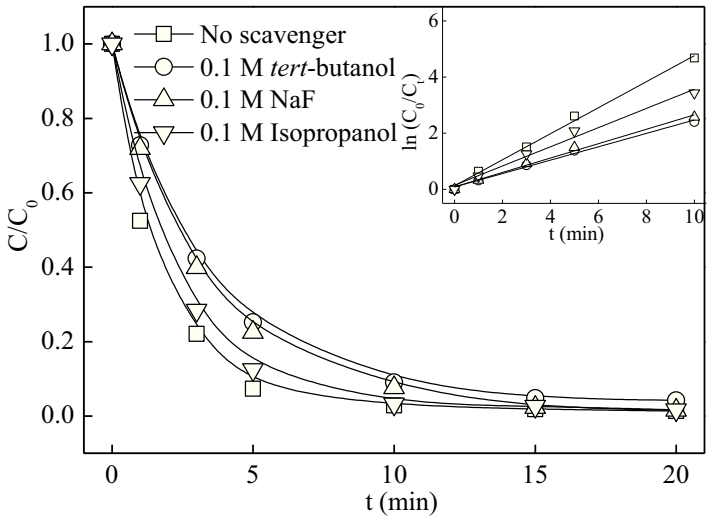


Fig. 6 Effects of scavengers and surface hydroxyl group caption on the removal of TC under US/Fe_3O_4/O_3 process (C_0 = 100 mg L^{-1}, $[O_3]_g$ = 14.1 mg L^{-1}, Q = 30 L h^{-1}, P = 85.7 W L^{-1}, $[Fe_3O_4]$ = 0.3 g L^{-1}, pH = 7.0, [*tert*-butanol] = 0.1 mol L^{-1}, [Isopropanol] = 0.1 mol L^{-1}, [NaF] = 0.1 mol L^{-1}).

6.3.6 COD removal efficiencies in the investigated processes

Due to the importance of the mineralization of organic pollutants, experiments were performed to determine the removal efficiency of COD in the selected processes. As indicated in Fig. 7, the US/O_3 process was more effective (67.8%) than ozonation alone (53.4%) when COD removal was concerned. Simultaneously, the enhancement on COD removal was more pronounced in the Fe_3O_4/O_3 process compared to ozonation alone, and 75.7% of COD was removed after 120 min treatment.

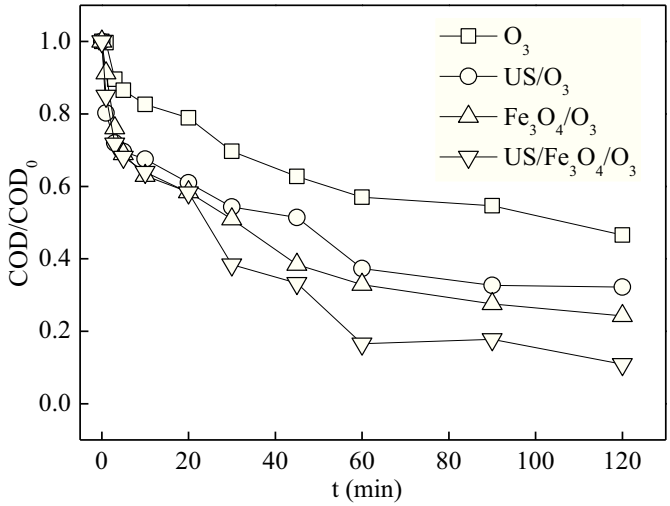


Fig. 7 The variation of COD with reaction time under the selected processes (C_0 =100 mg L^{-1}, $[O_3]_g$ = 13.2 mg L^{-1}, Q = 30 L h^{-1}, P = 85.7 W L^{-1}, $[Fe_3O_4]$ = 0.3 g L^{-1}, pH = 7.0).

When US/Fe_3O_4/O_3 was used, 89.1% COD removal efficiency was achieved. It was observed that the removal rate of COD was considerably less than that of TC. This was accounted for the formed intermediates which were difficult to be further oxidized.

6.3.7 The change of biodegradability and toxicity in the US/Fe_3O_4/O_3 system

Although COD was not completely removed in the US/Fe_3O_4/O_3 system after 120 min reaction, AOPs may improve the biodegradability and decrease the toxicity of the pollutants. Therefore, biodegradability experiments were conducted on non-treated and treated TC to assess the effects of the US/Fe_3O_4/O_3 process on the biodegradability of the treated wastewater. The BOD_5/COD ratio was selected as the biodegradability index. The value of the initial TC was almost zero, indicating that TC was difficult to biodegrade. After 120 min of treatment, the BOD_5/COD ratio increased to 0.694. These results confirmed that the formed intermediate products were considerably easier to be biodegraded than their parent constituents.

To investigate the potential environmental impact of the treated wastewater, the variation in the acute toxicity during the US/Fe_3O_4/O_3 process was investigated using a 24–h immobilisation test with *D. magna*. As can be seen in Fig. 8, the initial TC solution led to a 22% death of *D. magna*. The acute toxicity increased during the first stage of treatment, and it reached the maximum at 60 min, i.e., 55% death of D. magna. It indicated the primary degradation by–products that possessed a considerably high toxicity were formed during the oxidation process. After 120 min treatment, the inhibition percentage decayed to 20%. The result indicated that the complete removal of the target pollutant could not be used as the end point of the treatment, and the decrease of the toxicity to a certain point was required before discharge.

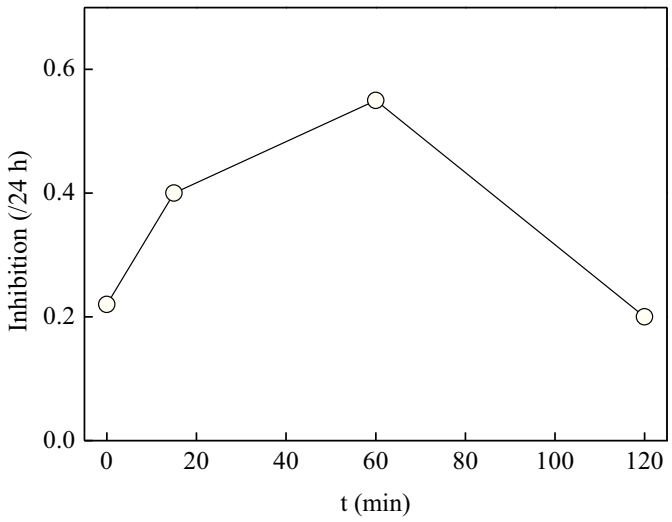


Fig. 8 The change of acute toxicity of TC under US/Fe_3O_4/O_3 process (C_0 = 100 mg L^{-1}, $[O_3]_g$ = 13.8 mg L^{-1}, Q = 30 L h^{-1}, P = 85.7 W L^{-1}, $[Fe_3O_4]$ = 0.3 g L^{-1}, pH = 7.0).

6.3.8 Catalyst stability tests in the US/Fe_3O_4/O_3 system

The activity of the catalyst and its stability and reusability are important factors for its application. If the catalyst is unstable or easily deactivated, it will fail in practical applications. Therefore, an investigation of the stability and reusability of the Fe_3O_4 catalyst was performed by repeatedly using the solid sample in three consecutive runs under identical oxidation conditions. No significant loss of activity was observed, and the TC removal rate remained consistent throughout the sequential runs. The degradation values were 0.340, 0.338 and 0.329 min^{-1} in the three successive cycles. Furthermore, the structure of Fe_3O_4 was also observed by the XRD characterization after being used for three times (Supplementary information, Fig. S1), and no difference was shown compared with the fresh one, indicating that the catalyst was relatively stable.

The amount of iron dissolved in the solution was determined at the end of the three consecutive experiments (Supplementary information, Fig. S3). The concentration of leached iron ions in the solution was 0.21 mg L^{-1} in the first run, whereas the further leaching of Fe_3O_4 was not detected during the third run. This result suggested that the iron dissolution could be neglected during the reaction and

further confirmed the stability and reusability of Fe_3O_4 in the subsequent reaction cycle.

6.3.9 Electric energy cost estimation

In sono-catalytic ozonation process, electric energy represents an important fraction of the operating costs. A simple economical assessment by means of the calculation of electric energy per order of pollutant removal (EE/O) was employed [46,53,54]. The EE/O value was adopted to compare the energy efficiency of different systems. In case of TC, the EE/O (kW h m^{-3} $order^{-1}$) can be determined from the following equation:

$$EE/O = \frac{P_{elec} \times t \times 1000}{V \times 60 \times \log(C_0 / C_f)} \quad (8)$$

where P_{elec} is the rated power (kW) of the oxidation system (0.15 kW for ozone generator and 0.25 kW for ultrasonic generator); t is the time reaction time (min), and V is the reaction volume (L); C_0 and C_f are the initial and final TC concentrations (mmol L^{-1}), respectively.

Compared to the α-FeOOH used in our previous study [23], less electrical energy was consumed by using Fe_3O_4 as a catalyst in this study (Table 3), and we confirmed that Fe_3O_4 was a more efficient catalyst than α–FeOOH. The presence of catalyst could improve ozonation and catalytic ozonation, and the associated energy consumption decreased. However, the ultrasound-enhanced systems were less energy saving than the silent systems, though higher removal efficiencies were achieved in the first systems. Therefore, the optimization of the sonochemical reactor is needed in the future work to further improve ozone utilization and catalyst activity.

Table 3. Comparison of electrical consumption under the different reaction systems.

Process	pH	Q ($L\ h^{-1}$)	$[O_3]_g$ ($mg\ L^{-1}$)	Catalyst loading ($g\ L^{-1}$)	P (WL^{-1})	P_{elec} (kW)	k (min^{-1})	EE/O ($kWh\ m^{-3}\ order^{-1}$)	Reference
O_3	7	30	17.9	0	0	0.15	0.354	81.3	this study
Fe_3O_4/O_3	7	30	17.9	0.3	0	0.15	0.461	62.4	this study
US/O_3	7	30	17.9	0	85.7	0.40	0.555	138.3	this study
$US/Fe_3O_4/O_3$	7	30	17.9	0.3	85.7	0.40	0.664	115.6	this study
O_3	3	30	13.8	0	0	0.15	0.096	299.8	[23]
α-FeOOH /O_3	3	30	13.8	0.5	0	0.15	0.129	223.1	[23]
US/O_3	3	30	13.8	0	85.7	0.40	0.115	667.4	[23]
US/α-FeOOH /O_3	3	30	13.8	0.5	85.7	0.40	0.174	441.1	[23]

Q, ozone gas flow rate ; $[O_3]_g$, gaseous ozone concentration; P, ultrasound power density; P_{elec}, total power of the oxidation system, including the electric consumption of ozone generator and ultrasound generator; EE/O, energy consumption per unit of the pollutant

6.4. Conclusions

TC can be rapidly removed in the US/Fe_3O_4/O_3 process. The degradation rate increased with pH, power density and ozone concentration, but was nearly independent of the catalyst dosage over the range investigated. The enhanced $^{\bullet}OH$ generation in the presence of Fe_3O_4 was verified using different radical scavengers. The Fe_3O_4 catalyst was confirmed to be stable and reusable. Although TC was almost completely removed after 20 min, the toxicity increased and reached the maximum after 60 min treatment. It then decreased when the reaction time was extended to 120 min, and the BOD_5/COD ratio increased to 0.694 accordingly.

Based on the electric energy cost estimation, the catalyzed systems consumed less energy than the uncatalyzed systems, but the ultrasound–enhanced systems were less energy saving than the silent systems. Therefore, the devolvement of highly efficient sonochemical reactor is needed for ultrasound–enhanced catalytic ozoantion process.

References

[1] M. Carballa, F. Omil, J.M. Lema, M. Liompart, C. García-Jares, I. Rodríguez, M. Gómez, T. Ternes, Behavior of pharmaceuticals, cosmetics and hormones in a sewage treatment plant. Water Res. 38 (2004) 2918–2926.

[2] P. Westerhoff, Y. Yoon, S. Snyder, E. Wert, Fate of endocrine-disruptor, pharmaceutical, and personal care product chemicals during simulated drinking water treatment processes, Environ. Sci. Technol. 39 (2005) 6649–6663.

[3] I. Arslan-Alaton, F. Gurses, Photo-Fenton-like and photo-Fenton-like oxidation of procaine penicillin G formulation effluent, J. Photochem. Photobiol. A: Chem. 165 (2004) 165–175.

[4] F. Gozzi, A.M. Jr, V.S. Ferreira, M.E. Osugi, A.P. F. Santos, J.A. Nogueira, R.F. Dantas, S. Esplugas, S.C.D. Oliveira, Investigation of chlorimuron–ethyl degradation by Fenton, photo-Fenton and ozonation processes, Chem. Eng. J. 210 (2012) 444–450.

[5] I.A. Balcioğlu, M. Otker, Treatment of pharmaceutical wastewater containing antibiotics by O_3 and O_3/H_2O_2 processes, Chemosphere 50 (2003) 85–95.

[6] N.C. Shang, Y.H. Yu, H.W. Ma, C.H. Chang, M.L. Liou, Toxicity measurements in aqueous solution during ozonation of mono-chlorophenols, J. Environ. Manage. 78 (2006) 216–222.

[7] R.F. Dantas, M. Canterino, R. Marotta, C. Sans, S. Esplugas, R. Andreozzi, Bezafibrate removal by means of ozonation: primary intermediates, kinetics, and toxicity assessment, Water Res. 41 (2007) 2525–2532.

[8] R.H. Huang, B.Y. Lan, Z.Y. Chen, H.H. Yan, Q.Y. Zhang, J.H. Bing, L.S. Li, Catalytic ozonation of *p*-chlorobenzole acid over MCM–41 and Fe loaded MCM-41, Chem. Eng. J. 180 (2012) 19–24.

[9] C.V. Gómez-Pacheco, M. Sánchez-Polo, J. Rivera-Utrilla, J. López- Peñalver, Tetracycline removal from waters by integrated technologies based on ozonation and biodegradation, Chem. Eng. J. 178 (2011) 115–121.

[10] G. Moussavi, M. Mahmoudi, Degradation and biodegradability improvement of the reactive red 198 azo dye using catalytic ozonation with MgO nanocrystals, Chem. Eng. J. 152 (2009) 1–7.

[11] R. Keykavoos, R. Mankidy, H. Ma, P. Jones, J. Soltan, Mineralization of bisphenol A by catalytic ozonation over alumina, Sep. Purif. Technol. 107 (2013) 310–317.

[12] P. Pocostales, P. Álvarez, F.J. Beltrán, Catalytic ozonation promoted by alumina-based catalysts for the removal of some pharmaceutical compounds from water, Chem. Eng. J. 168 (2011) 1289–1295.

[13] J. Akhtar, N.S. Amin, A. Aris, Combined adsorption and catalytic ozonation for removal of sulfamethoxazole using Fe_2O_3/CeO_2 loaded activated carbon, Chem. Eng. J. 170 (2011) 136–144.

[14] J. Ma, M.H. Sui, T. Zhang, C.Y. Guan, Effect of pH on MnO_x/GAC catalyzed ozonation for degradation of nitrobenzene, Water Res. 39 (2005) 779–786.

[15] T. Zhang, C.J. Li, J. Ma, H. Tian, Z.M. Qiang, Surface hydroxyl groups of synthetic α-FeOOH in promoting $^{\bullet}OH$ generation from aqueous ozone: property and activity relationship, Appl. Catal. B: Environ. 82 (2008) 131–137.

[16] F.J. Beltrán, F.J. Rivas, R. Montero-de-Espinosa, Ozone-enhanced oxidation of oxalic acid in water with cobalt catalyst. 2. Heterogeneous catalytic ozonation, Ind. Eng. Chem. Res. 42 (2003) 3218–3224.

[17] Y.M. Dong, H.X. Yang, K. He, S.Q. Song, A.M. Zhang, β-MnO_2 nanowires: A novel ozonation catalyst for water treatment, Appl. Catal. B: Environ. 85 (2009) 155–161.

[18] F.J. Rivas, M. Carbajo, F. Beltrán, O. Gimeno, J. Frades, Comparison of different advanced oxidation processes (AOPs) in the presence of perovskites, J. Hazard. Mater. 155 (2008) 407–414.

[19] Y.M. Dong, K. He, B. Zhao, Y. Yin, L. Yin, A.M. Zhang, Catalytic ozonation of azo dye active brilliant red X-3B in water with natural mineral brucite, Catal. Commun. 8 (2007) 1599–1603.

[20] H.W. Chen, Y.L. Kuo, C.S. Chiou, S.W. You, C.M. Ma, C.T. Chang, Mineralization of reactive Black 5 in aqueous solution by ozone/H_2O_2 in the presence of a magnetic catalyst, J. Hazard. Mater. 174 (2010) 795–800.

[21] H. Zhao, Y.M. Dong, G.L. Wang, P.P. Jiang, J.J. Zhang, L. Wu, K. Li, Novel magnetically separable nanomaterials for heterogeneous catalytic ozonation of phenol pollutant: $NiFe_2O_4$ and their performances, Chem. Eng. J. 219 (2013) 295–302.

[22] H. Liu, B. Qing, X. Ye, Q. Li, K. Lee, Z. Wu, Boron adsorption by composite magnetic particles, Chem. Eng. J. 151 (2009) 235–240.

[23] Y. Wang, H. Zhang, L. Chen, Ultrasound enhanced catalytic ozonation of tetracycline in a rectangular air-lift reactor, Catal. Today 175 (2011) 283–292.

[24] A. Lv, C. Hu, Y.L. Nie, J.H. Qu, Catalytic ozoantion of toxic pollutants over magnetic cobalt and manganese co-doped γ-Fe_2O_3, Appl. Catal. B: Environ. 100 (2010) 62–67.

[25] A.H. Lv, C. Hu, Y.L. Nie, J.H. Qu, Catalytic ozonation of toxic pollutants over magnetic cobalt-doped Fe_3O_4 suspensions, Appl. Catal. B: Environ. 117–118 (2012) 246-252.

[26] L. Zhao, J. Ma, X.D. Zhai, Enhanced mechanism of catalytic ozonation by ultrasound with orthogonal dual frequencies for the degradation of nitrobenzene in aqueous solution, Ultrason. Sonochem. 17 (2010) 84–91.

[27] B. Neppolian, J.S. Park, H. Choi, Effect of Fenton-like oxidation on enhanced oxidative degradation of *para*-chlorobenzoic acid by ultrasonic irradiation, Ultrason. Sonochem. 11 (2004) 273–279.

[28] H. Zhang, Y.L. Lv, F. Liu, D.B. Zhang, Degradation of CI acid orange 7 by ultrasound enhanced ozonation in a rectangular air-lift reactor, Chem. Eng. J. 138 (2008) 231–238.

[29] J.K. Kim, F. Martinez, I.S. Metcalfe, The beneficial role of use of ultrasound in heterogeneous Fenton-like system over supported copper catalysts for the degradation of *p*-chlorophenol, Catal. Today 124 (2007) 224–231.

[30] Y. Wang, H. Zhang, L. Chen, S. Wang, D.B. Zhang, Ozonation combined with ultrasound for the degradation of tetracycline in a rectangular air-lift reactor, Sep. Purif. Technol. 84 (2012) 138–146.

[31] F.J. Benitez, J. Beltrán-Heredia, T. González, Ozonation of aqueous solutions of Fenuron, Ind. Eng. Chem. Res. 30 (1991) 2390–2395.

[32] D.L. Flamm, Analysis of ozone at low concentrations with boric acid buffered potassium iodide, Environ. Sci. Technol. 11 (1977) 978–983.

[33] H. Bader, J. Hoingé, Determination of ozone in water by the indigo method, Water Res. 154 (1981) 449–456.

[34] T. Kimura, T. Sakamoto, J.M. Leveque, H. Sohmiya, M. Fujita, S. Ikeda, Standardization of ultrasonic power for sonochemical reaction, Ultrason. Sonochem. 3 (1996) S157–S161.

[35] APHA, AWWA, WPCF, Standard methods for the examination of water and wastewater, 20th edition. American Public Health Association, American Water Works Association, Water Pollution Control Federation, Washington DC, USA, 1998.

[36] A.E. Harvey, J.A. Smart, E.S. Arms, Simultaneous spectrophotometric determination of iron (II) and total iron with 1, 10-phenanthrolin, Anal. Chem. 27 (1955) 26–29.

[37] Organization for Economic Cooperation and Development (OECD), Daphnia sp. Acute immobilization test. Test Guideline No. 202, OECD guidelines for testing of chemicals, 2004.

[38] H. Zhang, L.J. Duan, D.B. Zhang, Decolorization of methyl orange by ozonation in combination with ultrasonic irradiation, J. Hazard. Mater. 138 (2006) 53–59.

[39] P.R. Gogate, A.B. Pandit, A review of imperative technologies for wastewater treatment II: hybrid methods, Adv. Environ. Res. 8 (2004) 553–597.

[40] B. Legube, N.K.V. Leitner, Catalytic ozonation: a promising advanced oxidation technology for water treatment, Catal. Today 53 (1999) 61–72.

[41] B. Kasprzyk-Hordern, M. Ziółek, J. Nawrocki, J., Catalytic ozonation and methods of enhancing molecular ozone reactions in water treatment, Appl. Catal. B: Enivron. 46 (2003) 639–669.

[42] J. Nawrocki, B. Kasprzyk-Hordern, The efficiency and mechanisms of catalytic ozonation, Applied. Catal. B: Enivron. 99 (2010) 27–42.

[43] F. Qi, B.B. Xu, Z.L., Chen, L.Q. Zhang, P.Y. Zhang, D.Z. Sun, Mechanism investigation of catalyzed ozonation of 2-methylisoborneol in drinking water over aluminum (hydroxyl) oxides: role of surface hydroxyl group, Chem. Eng. J. 165 (2010) 490–499.

[44] L. Zhao, Z.Z. Sun, J. Ma, Novel relationship between hydroxyl radical initiation and surface group of ceramic honeycomb supported metal for the catalytic ozonation of nitrobenzene in aqueous solution, Environ. Sci. Technol. 43 (2009) 4157–4163.

[45] Y. Joseph, W. Ranke, W. Weiss, Water on FeO (111) and Fe_3O_4 (111): adsorption behavior on different surface terminations, J. Phys. Chem. B 104 (2000) 3224–3226.

[46] Y. Wang, H. Zhang, J.H. Zhang, C. Lu, Q.Q. Huang, J. Wu, F. Liu, Degradation of tetracycline in aqueous media by ozonation in an internal loop-lift reactor, J. Hazard. Mater. 192 (2011) 35–43.

[47] Y. Chen, C. Hu, J.H. Qu, M. Yang, Photodegradation of tetracycline and formation of reactive oxygen sepcies in aqueous tetracycline solution under simulated sunlight irradiation, J. Photochem. Photobiol. A: Chem. 197 (2008) 81–87.

[48] M. Carbajo, F.J. Beltrán, O. Gimeno, B. Acedo, F.J. Rivas, Ozonation of phenolic wastewaters in the presence of a pervoskite type catalyst, Appl. Catal. B: Environ. 74 (2007) 203–210.

[49] F. Qi, B,B, Xu, L. Zhao, Z.L. Chen, L.Q. Zhang, D.Z. Sun, J. Ma, Comparison of the efficiency and mechanism of catalytic ozonation of 2,4,6-trichloroanisole by iron and manganese modified bauxite, Appl. Catal. B: Environ. 121–122 (2012) 171–181.

[50] L.S. Zhang, K.H. Wong, D.Q. Zhang, C. Hu, J.C. Yu, C.Y. Chan, P.K. Wong, Zn:$In(OH)_yS_z$ solid solution nanoplates: synthesis characterization, and photocatalytic mechanism, Environ. Sci. Technol. 43 (2009) 7883–7888.

[51] P. Calza, E. Pelizzetti, Photocatalytic transformation of organic compounds in the presence of inorganic ions, Pure Appl. Chem. 73 (2001) 1893–1848.

[52] Y. Chen, S. Yang, K. Wang, L. Lou, Role of primary active species and TiO_2 surface characteristic in UV-illuminated photodegradation of Acid Orange 7, J. Photochem. Photobiol. A–Chem. 172 (2005) 47–54.

[53] C.H. Wu, H.Y. Ng, Degradation of C.I. Reactive Red 2 (RR2) using ozone-based systems: Comparisons of decolorization efficiency and power consumption, J. Hazard. Mater. 152 (2008) 120–127.

[54] N. Daneshvar, A. Aleboyeh, A.R. Khataee, The evaluation of electrical energy per order (EEO) for photooxidative decolorization of four textile dye solutions by the kinetic model, Photochem. Photobiol. Sci. 8 (2009) 620–627.

Supplementary information for

Ultrasound-enhanced magnetite catalytic ozoantion of tetracycline in water

Liwei Hou, Hui Zhang*, Liguo Wang, Lu Chen

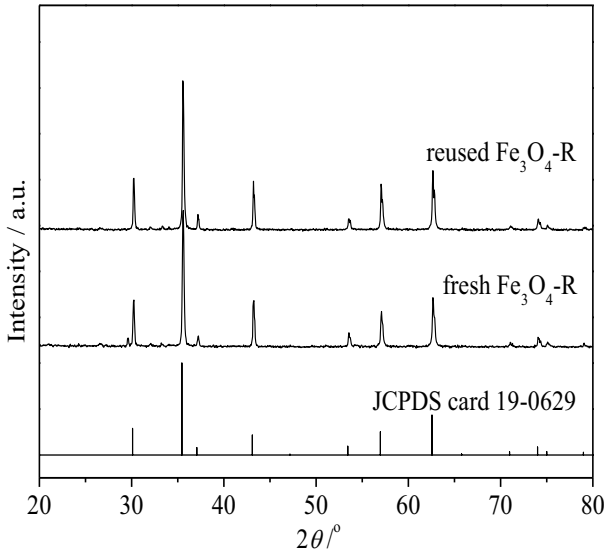


Figure (S1): XRD pattern of Fe_3O_4 particles (fresh and reused samples). Reference X-ray belonging to Fe_3O_4 (JCPDS card no 89-2355) is given at the bottom of the figure.

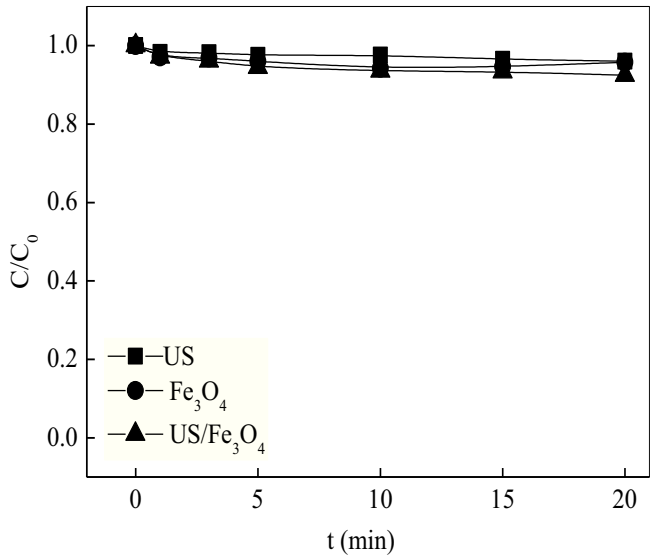


Figure (S2): The effect of ultrasound and catalyst on the degradation of tetracycline (C_0 = 100 mg L^{-1}, $[Fe_3O_4]$ = 0.3 g L^{-1}, P = 85.7 W L^{-1}, pH = 7.0)

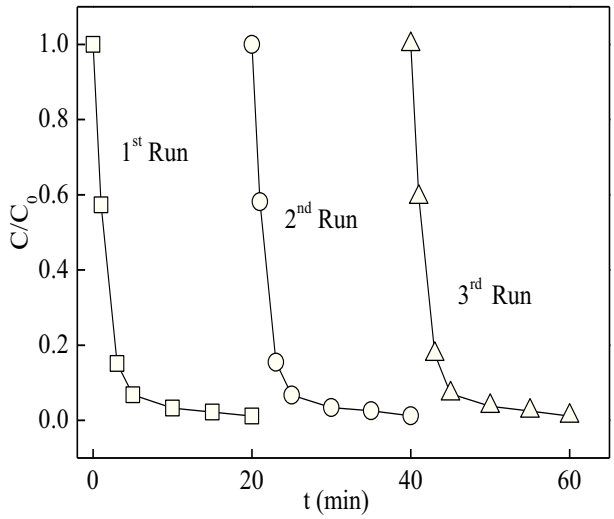


Figure (S3): Reusability study of the degradation of TC (C_0 = 100 mg L^{-1}, $[O_3]_g$ = 13.2 mg L^{-1}, Q = 30 L h^{-1}, P = 85.7W L^{-1}, $[Fe_3O_4]$ = 0.3 g L^{-1}, pH = 7.0)

Chapter 7 Shape-controlled nanostructured magnetite-type materials as highly efficient Fenton catalysts

Article:

Liwei Hou, Daniel Duprez, Hui Zhang and Sébastien Royer, Applied Catalysis B (2013) submitted.

Nanostructured Fe_3O_4 particles were obtained through hydrogen thermal reduction of α-Fe_2O_3 particles synthesized via an ionic liquid assisted hydrothermal process. The morphology and microstructure of the nano-sized Fe_3O_4 particles were characterized by using X-ray diffraction, N_2 physisorption, transmission electron microscopy, and temperature-programmed reduction. As-prepared magnetite samples show microcube, nanosphere, and porous nanorod morphologies. Activity of the nanostructures was evaluated for the Fenton reaction, using phenol as model molecule. While commercial Fe_3O_4 presents very limited activity, rod-type nanostructure exhibited exceptional activity toward phenol removal under mild conditions; 98% phenol was converted, and the total organic carbon (TOC) abatement was 74%. The reusability of porous nanorods of Fe_3O_4 was also investigated after three successive runs, which demonstrated the promising application of the catalyst in the oxidative degradation of organic pollutants. In addition, the material activity is strongly affected by the reduction degree, highlighting the beneficial effect of Fe^0/Fe_3O_4 mixed phase formation to achieve higher activity.

7.1. Introduction

Iron oxides are transition metal oxides, natural minerals and geocatalysts, existing in the natural aqueous environment, and also suspending in aerosol, clouds, and fogs as fine particles [1,2]. Because iron oxides are inexpensive and relatively non-toxic in comparison to other transition metals (including nickel, chromium, copper), they are preferred for the extensively application in many fields, such as corrosion processes [3,4], electromagnetic devices [5], and catalytic reactions [6-9]. The versatility of the surface composition among Fe^0, Fe^{II} and Fe^{III} over different types of iron oxides (Fe^0, FeO, α-Fe_2O_3, γ-Fe_2O_3, Fe_3O_4, α-FeOOH, β-FeOOH, γ-FeOOH and δ-FeOOH) ensure tunable properties, conferring to some composition high activity for heterogeneous Fenton reactions at the catalyst / solution interface [10]. Significantly different catalytic activities are then observed depending of the

material crystallographic and surface properties, due to variable valences of iron that can be stabilized [10].

More recently, several environmental applications of iron compounds (*e.g.*, as reducing agents and as promoters in the Fenton reaction) have been intensively investigated [11]. For example, Fe^0 has been proposed as a low-cost and nontoxic material in environmental remediation processes [12,13]. Different iron compounds, such as Fe^0, Fe_3O_4 [14] and Fe^0/Fe_3O_4 [15] have been reported to promote the Fenton reaction. Although the kinetic of these processes is highly complex and dependent on numerous different parameters, an important rate-limiting step is the production of radicals. In this respect, the oxidation phases on the iron surface and the presence of oxide/hydroxide layers that cover the iron particles should strongly influence the rate of the process [16]. The development of new processes to increase their efficiencies and widen the application of these systems in environmental remediation processes is of great interest.

Magnetite (Fe_3O_4)-based heterogeneous systems have attracted attention due to their unique properties and their potential applications in numerous fields, including ferrofluids, targeted drug delivery, and water treatment [17-20]. Especially, magnetite has also been reported to be an efficient catalyst for Fenton-like processes [21-31]. Magnetite exhibits several features that are important for a Fenton reaction: (i) it contains Fe^{2+}, which might play an important role as an electron donor to initiate the Fenton reaction; (ii) the octahedral site in the magnetite structure can easily accommodate both Fe^{2+} and Fe^{3+}, which means that Fe^{2+} can be reversibly oxidized and reduced in the same structure; and (iii) Fe_3O_4 has peroxidase-like activity and could activate H_2O_2 [14]. In addition, recent works demonstrated that bringing Fe^0 particles into contact with Fe_3O_4 particles through grinding increases the electron-transfer ability [15]. Thus, activity in the Fenton reaction was improved over these mixed phase materials.

As far, a wide variety of method has been reported to synthesize Fe_3O_4 nanoparticles, including sol-gel methods [32], wet-chemical methods [33],

hydrothermal methods [34], and co-precipitation [35]. However, these methods tend to form Fe_3O_4 particles with isotropic shapes. Nevertheless, various Fe_3O_4 nanostructures with different morphologies have been successfully synthesized, including nanotubes, nanowires, nanofilms, spheres, nanorods, and other novel structures using routes such as coprecipitation, microemulsion, and so on [36]-[38].

Recently, reduction of premade isotropic β-FeOOH or α-Fe_2O_3 particles into Fe_3O_4 was proposed [39]-[41]. Compared with other methods, reduction of premade α-Fe_2O_3 is a simple and effective method. Generally, the reduction of α-Fe_2O_3 involves an annealing process under reductive atmosphere at moderate temperature (about 300-500 ^oC). However, the annealing treatment of the premade materials may result in undesirable aggregation and sintering. Since the shape of formed Fe_3O_4 particles is dependent on that of premade α-Fe_2O_3, it is important to achieve α-Fe_2O_3 synthesis with various shapes prior to the reduction process. As reported in our previous work [42], Ionic Liquids (ILs) assisted hydrothermal route is found to be an effective method to synthesize α-Fe_2O_3 nanoparticles of various shapes, such as cubes, nanorods as well as nanoplates. Compared with the traditional hydrothermal methods, high surface area can be achieved due to reduction in crystal size by employing the ILs as the soft template. Because the properties of nanomaterials are influenced by their structure, size, and shape [36], the preparation of Fe_3O_4 nanoparticles with different sizes and morphologies is an important issue.

Herein, we report an environmentally benign “green” route to the synthesis of Fe_3O_4 nanoparticles with various morphologies, achieved by reduction of pre-made α-Fe_2O_3 materials. The physical and chemical characterization of Fe_3O_4 was performed, and the effect of the morphology and crystal structure of Fe_3O_4 on the Catalytic Wet Peroxide Oxidation process was investigated. Because of their unique porous structure, the potential applicability of nanorods of Fe_3O_4 in heterogeneous Fenton reactions was evaluated with respect to changes in the catalyst, and the H_2O_2 concentration, as well as with respect to the material’s stability. Further activity

improvement was achieved optimizing the Fe^0/Fe_3O_4 balance through reduction temperature.

7.2 Experimental Section

7.2.1 Materials

All chemicals employed in the preparation of the α-Fe_2O_3 in ionic liquid media and derived Fe_3O_4 catalysts were used as purchased: 1-methylimidazole ($C_4H_6N_2$, ≥99%, Sigma-Aldrich), 1-Chlorodecane [$(CH_3(CH_2)_9Cl$, 98%, Sigma-Aldrich], ethyl acetate ($CH_3COOC_2H_5$, 99.8%, Sigma-Aldrich), $FeCl_3 \cdot 6H_2O$ (≥98%, Sigma-Aldrich), potassium acetate (CH_3COOK, ≥99%, Sigma-Aldrich), and sodium hydroxide (NaOH, ≥98%, Sigma-Aldrich). For the heterogeneous Fenton reaction, phenol (C_6H_5OH, ≥99%, Sigma-Aldrich) and hydrogen peroxide solution (H_2O_2, 32 wt.% in H_2O, Sigma-Aldrich) were used as received. The ionic liquid (C_{10}mimCl) used here was synthesized and used to prepare three kinds of α-Fe_2O_3 with different morphologies via the hydrothermal method [see details in SI, Materials]. Fe_3O_4-M catalysts, where M represents the morphology of the catalyst, were obtained through the reduction of the α-Fe_2O_3 under H_2 at a flow rate of 60 mL min^{-1} at 300 °C for 1 h. The samples were denoted Fe_3O_4-C ('C' for microcube), Fe_3O_4-S ('S' for microsphere), and Fe_3O_4-R ('R' for nano-rods).

7.2.2 Catalysts characterization

The α-Fe_2O_3 and Fe_3O_4 catalysts were systematically characterized using X-ray diffraction (XRD), N_2 physisorption, transmission electron microscopy (TEM), ICP-OES, and temperature-programmed reduction (TPR).

The catalyst structures were verified by X-ray diffraction using a D5005 diffractometer from Bruker equipped with a CuKα radiation (λ=1.5406 Å) source. The signal was recorded for 2θ between 20° and 80° with a recording step of 0.05° every 3 s. Phase identification was made through comparison with the JCPDS database. The crystallite sizes were determined using the Scherrer equation after Warren's correction

for instrumental broadening was applied. (113) reflection was used for calculation of Fe_2O_3 crystal size, while (311) reflection was used in the case of Fe_3O_4 phase.

The N_2 adsorption measurements were performed on a Micromeritics TRISTAR 3000 instrument. The specific surface area of the catalysts was measured at liquid N_2 temperature (-196 ^oC), using the Brunauer–Emmett–Teller (BET) method. Prior to analysis, sample was heated under vacuum at 250 ^oC for 3 h.

The material morphologies were evaluated by transmission electron microscopy (TEM) coupled with energy-dispersive X-ray spectroscopy (EDXS). Micrographs were obtained on a JEOL 2100 instrument (operated at 200 kV with a LaB_6 source and equipped with a Gatan Ultra scan camera).

TPR experiments were performed on an AUTOCHEM instrument from Micromeritics. Approximately 50 mg of sample was introduced into the microreactor. The material was initially activated under simulated air (total flow rate = 30 mL min^{-1}) at 300 °C for 1 h. After the sample was cooled to room temperature, a reducing flow (1 vol.% of H_2 in Ar) was stabilized at a flow rate of 30 mL min^{-1}, and the temperature of the reactor was subsequently increased from 50 °C to 1000 °C with a ramp of 5 °C min^{-1}. The change in the H_2 concentration as a function of temperature was recorded using an online TCD.

The total Fe^{2+} content in the bulk of Fe_3O_4 was determined by chemical analysis after the samples were dissolved in acidic media at 60 °C for 48 h under a nitrogen atmosphere. According to Xue et al. [9], 6 mol L^{-1} HCl ensures the dissolution of the catalysts. 1.0 mL of 1,10-phenanthroline (1.0 g L^{-1}) was then added 1.0 mL of dissolved sample to form a colored complex. Finally, complex concentration was measured by UV spectrophotometer at λ fixed at 510 nm [44].

Furthermore, the surface ratio of Fe^{II}/Fe^{III} on the Fe_3O_4 surface was also analyzed by X-ray Photoelectron Spectroscopy (XPS). Analyses were conducted on a Thermo-Fisher ESCALAB 250 system with Al*Kα* radiation under ultrahigh vacuum (UHV). Binding energies were calibrated with the C1s binding energy fixed at 285 eV

as internal reference. Curve fittings were achieved with the XPS Peak software using the Fe2p binding energies region for the analysis.

7.2.3 Catalytic activity measurement

Catalytic tests were performed under mild conditions (atmospheric pressure and room temperature, 25 °C) in a 150 mL glass reactor continuously stirred with magnetic using phenol as a reactant and hydrogen peroxide as the oxidant. We initially verified that no external or internal diffusional resistances occurred and that the reaction was performed in a kinetic regime. The reaction pH value was adjusted to 4.0 before the oxidation began. In a typical experiment, 100 mL of phenol aqueous solution was prepared with an initial concentration of 600 mg L^{-1}. The catalyst was subsequently added to the solution, which was then stirred in the dark the adsorption–desorption equilibrium was obtained prior to initiation of oxidation. At the end of this step, we obtain the C_0 concentration. Then, the H_2O_2 solution is added dropwise at a constant rate to the solution during the 5 first minutes of the reaction. The initial reaction time, t_0, is defined at the starting of the H_2O_2 adding. The reaction solution was sampled at fixed time intervals and mixed with 0.1 g of manganese oxide for at least 15 min to eliminate residual H_2O_2. The reaction solution was then filtered through a 0.22 μm membrane before the residual phenol concentration and the total organic carbon (TOC) were measured. The calculation of phenol conversion is performed, taken into account the initial adsorption on the material surface (Eq. 1):

$$X_{phenol} = \frac{C_t}{C_0} \times 100\% \quad (1)$$

where C_t is the phenol concentration at time t (min) and C_0 is the initial phenol concentration after stabilization due to the adsorption on the catalyst surface.

The calculation of TOC abatement is also performed, taken into account the initial adsorption on the material surface (Eq. 2):

$$X_{TOC} = \frac{C_{TOC}}{C_{TOC_0}} \times 100\% \quad (2)$$

where C_{TOC} is the TOC concentration at time t (min) and C_{TOC_0} is the initial TOC concentration after stabilization due to the adsorption on the catalyst surface.

Methods: The phenol concentration was determined using a high-performance liquid chromatography (HPLC) instrument equipped with an Aminex HPX-87 (Biorad) column. TOC content was measured using a 1020A Bioritech TOC meter. The leaching of iron into the solution was systematically evaluated by ICP analyses through quantification of the dissolved iron concentration in the solution after the tests. The concentration of H_2O_2 after the reaction tests was measured via colorimetry using a UV spectrophotometer (Secomam, RS232) after complexation of the hydrogen peroxide with a vanadate salt.

At the end of the catalytic test, the dissolved ferrous iron concentration was also measured via the 1,10-phenanthroline method at 510 nm [44], while the total aqueous iron leaching into the solution was systematically evaluated by inductively coupled plasma optical emission spectroscopy (ICP-OES) analyses through quantification of the dissolved iron concentration in the solution after the tests.

7.3 Results and discussion

7.3.1 Characterization of the α-Fe_2O_3 precursors

The final properties of the active Fe_3O_4 materials are conditioned by the properties displayed by the α-Fe_2O_3 precursors. Consequently, structural and textural properties of the precursors, as well as their reducibility, are presented thereafter.

X-ray diffraction results

The α-Fe_2O_3 precursors with different morphologies were prepared using a hydrothermal method. The purity and crystallinity of the as-prepared samples were examined using powder XRD measurements. Figure 1 displays the XRD patterns of the as-prepared α-Fe_2O_3 microcubes (Fe_2O_3-C), microspheres (Fe_2O_3-S), and nanorods (Fe_2O_3-R, prepared by annealing of the as-prepared α-FeOOH nanorods in air at 300 °C for 3 h). All the peaks could be indexed to the hexagonal structure of α-Fe_2O_3, which was in good agreement with literature results (JCPDS Card 33-0664).

No other peaks were observed, which indicated the high purity of the prepared samples. The diffraction peaks located at 2θ = 24.3, 33.3, 35.7, 41.1, 49.7, 54.1, 62.5 and 64.1° could be indexed to the (012), (104), (110), (113), (024), (116), (214) and (300) planes of α-Fe_2O_3, respectively. However, the differences among the full-width at half-maximum (FWHM) and relative intensities of the diffraction peaks indicated differences in the crystal sizes and morphologies of the particles. The narrow, sharp peaks obtained for the commercial α-Fe_2O_3 (Fe_2O_3-Com) and Fe_2O_3-C indicated that these materials present large crystal size. However, the peaks obtained for Fe_2O_3-S were broadened with decreased intensities, which suggested that the crystal size of this sample was smaller than that of Fe-C and Fe-Com. The Fe_2O_3-R sample exhibited the broadest reflections, which suggested that this material exhibited the smallest crystal size among the investigated samples. According to the FWHM evolution, the average crystallite sizes of the Fe_2O_3-C, Fe_2O_3-S, and Fe_2O_3-R were estimated to be 38, 34, and 24 nm, respectively (Table 1). For comparison, the average crystal size of the commercial α-Fe_2O_3 (Fe-Com) was 49 nm.

Table 1. Physico-chemical properties of different morphologies of α-Fe_2O_3 precursors and Fe_3O_4

Sample	Morphology	α-Fe_2O_3		Fe_3O_4			
		SSA[a]/ (m^2g^{-1})	D[b]/ (nm)	SSA/ (m^2g^{-1})	Total Fe^{II}/Fe^{III} ratio[c]	Surface Fe^{II}/Fe^{III} ratio [d]	D[b]/ (nm)
Fe_xO_y-C	microcube	3.4	38	2.8	0.49±0.2	—	65
Fe_xO_y -S	nanosphere	12.3	34	10.9	0.53±0.2	—	42
Fe_xO_y -R	nanorods	46.5	24	24.7	0.56±0.2	0.53±0.2	37
Fe_xO_y-Com	uniform	0.4	49	0.5	0.32±0.2	0.25±0.2	79

[a], SSA is the specific surface area evaluated using the BET model; [b], *D* is the crystal domain size evaluated from the X-ray line broadening using the Scherrer equation; [c], bulk ratio between Fe(II) and Fe(III) in Fe_3O_4 (molar ratio of Fe^{2+} and Fe^{3+} in the Fe_3O_4 content); [d], surface ratio of Fe(II) and Fe(III) obtained by XPS analysis.

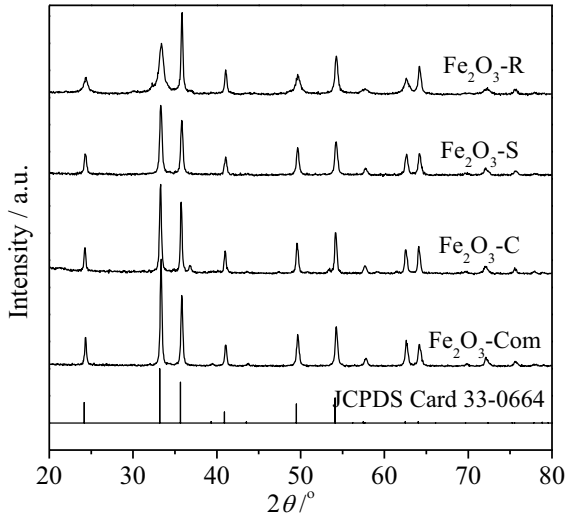


Figure 1. XRD patterns recorded for different morphologies of α-Fe_2O_3 precursor.

Evolution of physical properties

As shown in Table 1, all the nanostructured materials exhibited greater surface areas than the commercial material. With different morphologies of α-Fe_2O_3, different surface areas were obtained. Indeed, relatively low surface areas of 3.4 m^2 g^{-1} were obtained for Fe_2O_3-C. The sphere morphology led to a greater surface area (12.3 m^2 g^{-1}), and, for the nanorod-like material, the surface area was 46.5 m^2 g^{-1}. As evident from the results in Table 1, the surface area depended on the crystal size evaluated by X-ray line broadening. The evolution of the surface area with crystal size over the IL-mediated materials showed an exponential decrease with increasing crystal size. Compared with the classical material, the ILs-derived materials showed great enhancement in physical properties (morphology, crystal size, surface area, and density), indicating that the ionic liquid not only affected the morphologies of the materials, but also affected the porosity or density of the formed aggregates. Due to a higher surface area, the nanorod-like material (Fe_2O_3-R) is believed to favor the adsorption/reaction of organic pollutants in water-treatment applications.

Morphology of α-Fe_2O_3

TEM images of the four materials are shown in Figure 2. Figures 2A-B show the results for the α-Fe_2O_3 microcubes with an average size of 300 nm on the edges, which is much larger than the crystal size obtained from X-ray line broadening (38

nm). However, the size repartition was not monodispersed, and a few smaller-sized cubes were observed in Figure 2B. Moreover, as shown in Figures 2A-B, the surfaces of the cubes were rough, which indicated that the cubes were aggregated nanoparticles. Figure 2C-D show the TEM images of the α-Fe_2O_3-S, which exhibited a spherical morphology with an average diameter of approximately 150 nm.

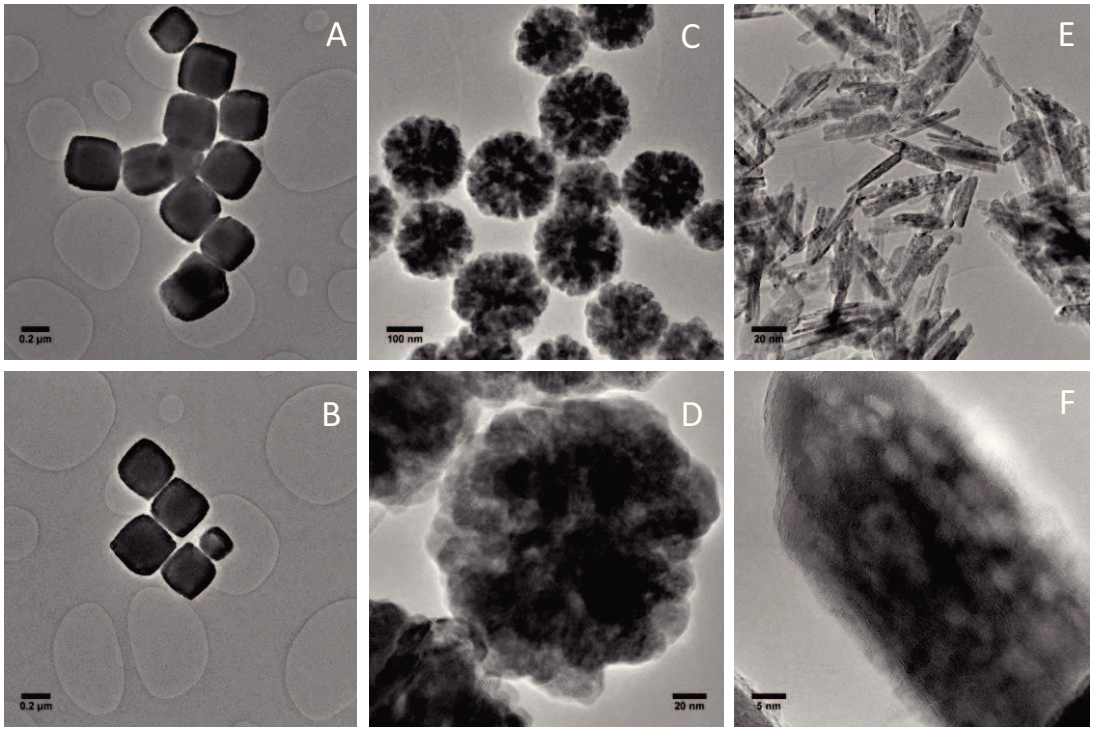


Figure 2. Representative high magnification TEM images of the different morphologies of α-Fe_2O_3

Although the average diameter of Fe_2O_3-S was significantly larger than the particle based on XRD analysis, the high-magnification TEM images (Figure 2D) indicated that the nanospheres were composed of individual nanoparticles with an average size of approximately 30-40 nm, which was consistent with the results calculated from the Scherrer formula. Finally, Figures 2E-F present typical TEM images of the α-Fe_2O_3 with nanorod morphology (Fe_2O_3-R) obtained through the hydrothermal treatment in alkaline media of an iron chloride precursor and a C_{10}mimCl additive, but with a NaOH concentration greater than that used to prepare the Fe_2O_3-C samples. Figures 2E-F show that the nanorods exhibited diameters in the range of 20-60 nm and lengths of 200-600 nm. Unfortunately, N_2 physisorption was

not appropriate to determine a mean pore size in this material, due to the very wide repartition in size of the pores. However, such pores broad in size and not regular are visible by TEM, at the outer surface within the annealed Fe_2O_3-R nanoparticles. Such intra-rod porosity is probably at the origin of the observed high surface area for this material (Table 1).

TPR results for Fe_2O_3-R and the commercial material

The reduction behaviors of hematite type materials were examined using TPR under H_2. Results obtained for Fe_2O_3-R and Fe_2O_3-Com are shown in Figure 3. The experimental TPR profile of α-Fe_2O_3 exhibited two well-resolved reduction peaks, located at 400 °C and 700 °C. Comparable reduction profiles were obtained for the Fe_2O_3-C and Fe_2O_3-S materials, showing that crystal size and aggregate morphology do not strongly impact the reduction process. The first reduction process occurred in the temperature range of 300-420 °C with a peak centered at 400 °C. As suggested by the XRD analyses and by previous works [30][44], the results for the sample obtained via a TPR experiment interrupted at 400 °C and the sample quenched to room temperature indicated that this reduction was related to the presence of α-Fe_2O_3 that was reduced to FeO at 400 °C, with the formation of Fe_3O_4 phase as intermediate product of reduction [45]:

$$Fe_2O_3 + H_2 \rightarrow 2.FeO + H_2O \quad (3)$$

At temperatures greater than 450 °C, another reduction process was observed (Figure 3). The peaks with maxima were located near 700 °C were due to the second reduction step from FeO to metallic iron:

$$FeO + H_2 \rightarrow Fe^0 + H_2O \quad (4)$$

Given that the total experimental H_2 consumption was lower than the theoretical H_2 consumed for complete reduction of Fe^{3+} to Fe^0, the Fe^{3+} reduction in the first stage could be assigned to $Fe_2O_3 \rightarrow FeO$ with 100% of the Fe^{3+} participating in this reduction step, while the second reduction step consists in the incomplete reduction of FeO to Fe^0 (Table 2). For comparison, the reduction behavior of commercial α-Fe_2O_3 was also investigated. For the Fe_2O_3-Com sample, reduction peaks centered at 405 °C

and 685 °C were observed. A comparison of the reduction behavior of Fe_2O_3-Com with that of Fe_2O_3-R revealed that the reduction of Fe_2O_3-R led to a slightly increased total H_2 consumption, and 16.1 mmol g^{-1} H_2 was consumed (Table 2). Furthermore, the Fe^{2+} reduction at the second stage could be considered as $FeO \rightarrow Fe^0$, and 78.9% of the Fe^{2+} participated in this reduction for Fe_2O_3-R. For comparison, 67.2% of Fe^{2+} was reduced to Fe^0 in Fe_2O_3-Com. Such an improvement in iron reducibility in Fe_2O_3-R was attributed to the adequate physicochemical properties, which included a significantly greater surface area, a smaller crystal size and the suppression of crystal agglomeration that are all in favor of an increased reducibility.

Table 2. H_2-TPR results for α-Fe_2O_3 and Fe_3O_4.

Samples	Theoretical H_2 consumption [a] / mmol g^{-1}			Experimental H_2 consumption / mmol g^{-1}			
	$Fe_2O_3 \rightarrow$ FeO	$Fe_3O_4 \rightarrow$ FeO	FeO→ Fe^0	Total [b]	$Fe_2O_3 \rightarrow$ FeO[c] (%)	$Fe_3O_4 \rightarrow$ FeO (%)	FeO→ Fe^0 (%)
Fe_2O_3-Com	6.3	—	12.5	14.7	100.0	—	67.2
Fe_2O_3-R	—	—	—	16.1	100.0	—	78.9
Fe_3O_4-Com	—	4.3	12.9	10.9	—	100.0	51.3
Fe_3O_4-R	—	—	—	13.4	—	100.0	70.0

[a], calculated values of H_2 to be consumed for the complete reduction of the cations (reduction reactions considered depicted in the Table); [b], total molar of H_2 consumed for per gram of materials, issued from H_2-TPR experiment; [c], reduction proportion calculated by comparing each experimental H_2 consumptions with theoretical H_2 consumption.

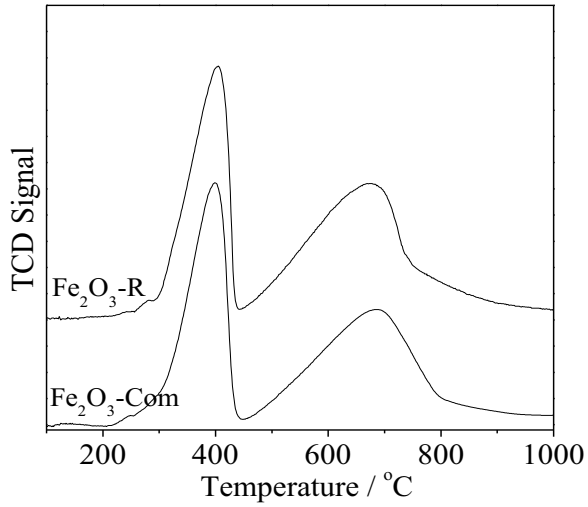


Figure 3. TPR-H_2 profiles recorded for α-Fe_2O_3 precursor (Fe_2O_3-Com, Fe_2O_3-R).

7.3.2 Characterization of the Fe_3O_4 precursors

X-ray diffraction results

Fe_3O_4 phases were obtained through the reduction of the α-Fe_2O_3 [36]. Conditions applied are reduction under H_2 at 300 °C for 1 h. The XRD pattern in Figure 4 reveals that all of the diffraction peaks of the three powders could be unambiguously assigned to the pure face-centered cubic structure of Fe_3O_4 magnetite (JCPDS Card 19-0629). The diffraction peaks located at 2θ = 30.2, 35.6, 43.2, 53.6, 57.1, 62.6, and 74.2° could be indexed to the (220), (311), (400), (422), (511), (440), and (553) planes of Fe_3O_4, respectively, by comparison with previously reported data for Fe_3O_4 phase [15,46,47]. As shown in Table 1 and Figure 4, the difference in the FWHM and in the intensities of the diffraction peaks suggested differences in the crystal sizes and morphologies. Compared to the α-Fe_2O_3, the Fe_3O_4 materials presents larger crystal size (Table 1) showing that the phase transformation is accompanied by a sensible crystal growth. The crystal sizes determined from the XRD results using the Scherrer equation were 65.1, 42.3, and 36.6 nm for Fe_3O_4-C, Fe_3O_4-S, and Fe_3O_4-R, respectively. For comparison, the crystal size of the commercial Fe_3O_4 was 78.6 nm.

Evolution of physical properties

The reducing transformation of the α-Fe_2O_3 into Fe_3O_4 induces some change in textural properties. After reduction, the surface area was relatively smaller than that of the α-Fe_2O_3 precursor. The specific surface areas obtained from N_2 adsorption measurements for the corresponding samples were, 2.8, 10.9, and 24.7 m^2 g^{-1}, respectively. Notably, the specific surface area of Fe_3O_4-R was larger than that of the other Fe_3O_4 nanoparticles, and this sample exhibited a smaller crystal size than the other samples. In addition, Fe^{II}/Fe^{III} ratios were also measured both in the bulk and on the material surface by chemical analysis (Table 1) and XPS (Figure S1 and Table 1), respectively. It is evident that the same trends of Fe^{II}/Fe^{III} ratio both in the bulk and on the surface were obtained (Table 1). Theoretical Fe^{II}/Fe^{III} ratio is 0.5 for Fe_3O_4

materials. As can be observed in Table 1, ratios obtained over the IL mediated materials are close to this theoretical value. Lower ratios were obtained for the Fe_3O_4-Com material, despite that a pure magnetite phase was obtained by XRD. As mentioned above, the favorable physical properties of Fe_3O_4-R, such as small crystal size, large surface area, in addition to a high Fe^{II}/Fe^{III} ratio, is suspected to lead to excellent catalytic performances.

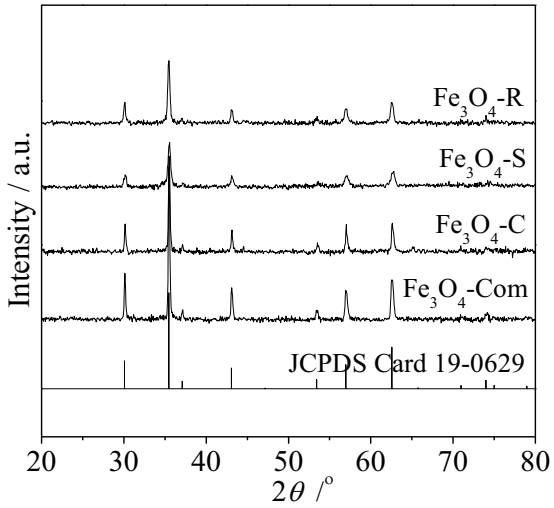


Figure 4. XRD patterns recorded for different morphologies of Fe_3O_4 (Fe_3O_4-C, Fe_3O_4-S, Fe_3O_4-R).

Morphology of Fe_3O_4

The morphologies of magnetite catalysts were successfully maintained after thermal transformation of the precursor to Fe_3O_4. The morphology of the Fe_3O_4-C nanoparticles with highly geometrical symmetry was visualized using TEM. The images showed that the average size of the cubes was 350 nm on edge, which was slightly larger than the corresponding size of the Fe_2O_3-C precursor. The TEM images also revealed that the surfaces of the microcubes were relatively rough (Figure 5A), which was further confirmed using high-magnification TEM (Figure 5B). Some pale areas between the dark nanoparticles were observed, which suggests the existence of mesopores inside the microcubes that can be at the origin of the surface area developed by this material. Figures 5C-D represent typical TEM images of the Fe_3O_4-S. A spherical morphology, with an average diameter of 200-400 nm, is easily observed. As in the case of the microcubes, the nanospheres were constructed by the self-assembly of nanoparticles. Finally, a typical TEM image of the Fe_3O_4-R obtained

through reduction of the as-prepared Fe_2O_3-R precursor was presented. Figures 5E-F show nanorods with diameters in the range of 40 to 80 nm and lengths from 200 to 600 nm. A high-magnification TEM image of the tip portion of a nanorod showed clear fringes (Figure 5F). As observed on the Fe_2O_3-R precursor, pores of irregular shape and broad in size are clearly observed by TEM.

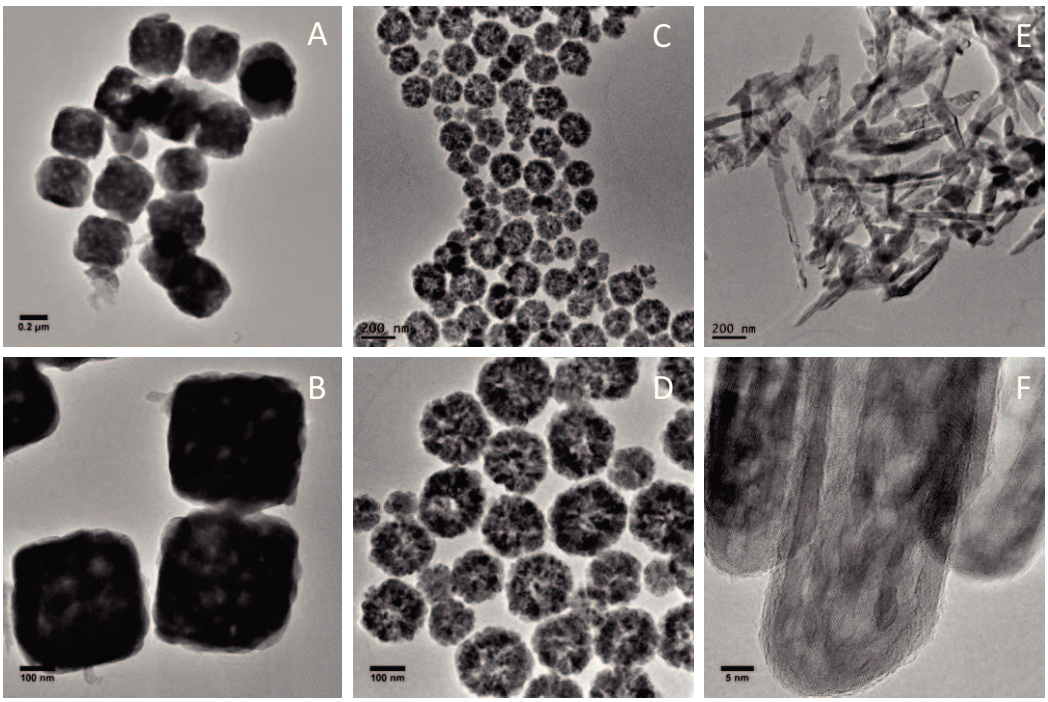


Figure 5. Representative high magnification TEM images of the different morphologies of Fe_3O_4: A-B: Fe_3O_4-C; C-D: Fe_3O_4-S; E-F: Fe_3O_4-R.

TPR results of Fe_3O_4-R and Fe_3O_4-Com

Figure 6 shows the TPR results of Fe_3O_4-R and Fe_3O_4-Com in the temperature range of 50 to 1000 °C. As in the case of the reduction of the hematite materials, similar reduction profiles were obtained over the Fe_3O_4-C and Fe_3O_4-S materials. Two reduction peaks are observed. H_2 consumptions at each step were calculated; the results are listed in Table 2. The reduction at the first stage (maximal consumption at 400-450 °C) was assigned to the Fe_3O_4 to FeO transition, with 100% of Fe^{3+} present in Fe_3O_4 reducing at this step into Fe^{2+}. When the temperature was greater than 500 °C, the second reduction process was observed (Figure 6). This reduction step (maximal consumption at 700-750 °C) was attributed to the reduction $FeO \rightarrow Fe^0$. However, only a limited fraction of Fe^{2+} participated in this second reduction process.

The total H_2 consumption measured for Fe_3O_4-R indicates that only 70.0% of Fe^{2+} reduced to Fe^0, which was however greater than the reduction degree in the commercial material (51.3%) (Table 2). This result shows that the improved reducibility of iron in nanorod morphology was maintained even in the Fe_3O_4 structure that is not surprising since the intermediate reduction step was performed at relatively low temperature (e.g. 300 °C).

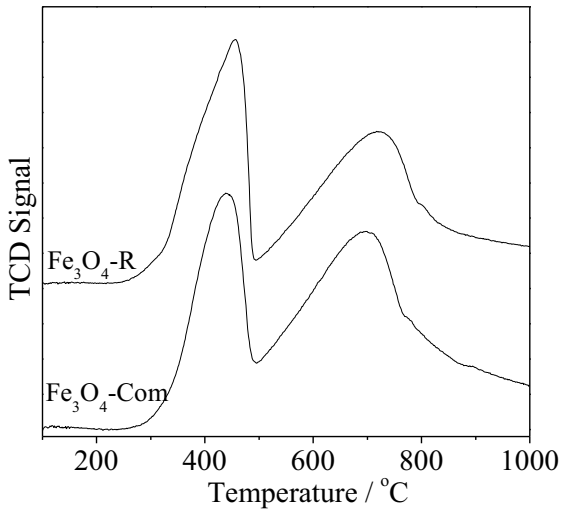


Figure 6. TPR-H_2 profiles recorded for Fe_3O_4 (Fe_3O_4-Com, Fe_3O_4-R).

7.3.3 Comparison of the catalytic activity of different iron oxide nanoparticles

Magnetite (Fe_3O_4) and hematite (α-Fe_2O_3) were used to investigate the effect of surface ferrous species (Fe^{II}) on iron oxide during Fenton-like reactions. In our study, Fe_2O_3-R and Fe_3O_4-R were used because of their high surface areas, small crystal sizes, and porous structures. Phenol conversion and TOC abatement curves obtained for Fe_2O_3-R and Fe_3O_4-R were presented in Figure 7. Almost no conversion of phenol was observed (5.7%), and only 4.0% TOC was removed, using Fe_2O_3-R as catalyst. However, iron oxides containing mainly surface ferric species (Fe^{III}), *e.g.* α-Fe_2O_3, are known to be nearly inactive for H_2O_2 decomposition into active radicals [30]. Consequently, this material leads to very limited phenol conversion. The concentration of H_2O_2 was measured at the end of the Fe_2O_3-R/H_2O_2 reaction. A H_2O_2 concentration of 4.3 mmol L^{-1} was obtained despite the very limited phenol conversion. This result shows that H_2O_2 adsorbs rather than decomposes on the

surface of Fe_2O_3-R. It agrees with the observation that the adsorption of H_2O_2 onto Fe^{III} sites (Eq. 5) was faster than the adsorption of organic molecules [48].

$$Fe^{III} + H_2O_2 \rightarrow Fe^{III}H_2O_2 \quad (5)$$

Compared with Fe_2O_3-R, Fe_3O_4-R showed a much greater removal efficiency of phenol, with almost complete conversion after 90 min, while the TOC was 74.0%. These results clearly indicated that Fe^{II} surface site played an important role in the activation of the H_2O_2 molecule. Moreover, the Fe_3O_4-R catalyst could be conveniently separated from the reaction mixture through the application of an external magnetic field. In the case of reaction with Fe_3O_4-R (Table 3), the conversion of H_2O_2 was 87.3% at the end of the reaction that is consistent with the high phenol conversion and high TOC abatement.

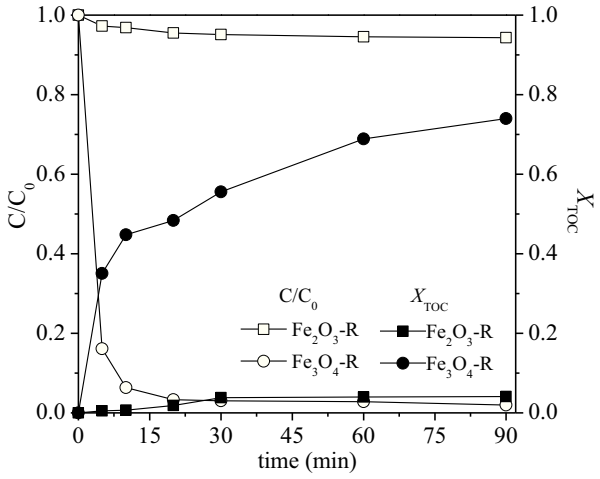


Figure 7. Degradation and mineralization of phenol over rod-type morphology in the presence of H_2O_2 (phenol: 600 mg L^{-1}, Fe_2O_3-R: 0.25 g L^{-1} or Fe_3O_4: 0.25 g L^{-1}, H_2O_2: 40 mmol L^{-1}, pH: 4.0, T: 25 °C).

7.3.4 Evidence of heterogeneous Fenton reaction over Fe_3O_4-R

An evaluation of the catalytic activity in the degradation of phenol by Fe_3O_4-R was performed under different experimental conditions (Figure 8A-B). The results showed that phenol conversion was limited with hydrogen peroxide alone (33.0%), with a TOC removal efficiency of 25.3%. When the catalyst was added to the phenol solution, 45.1% of the TOC was removed. When we separated the catalyst, and added the new phenol solution (600 mg L^{-1}) to the catalyst for another 90 min, no more than 10.0% phenol disappear with less than 5.0% TOC abatement in the second run, which

shows that the observed removal of phenol can be attributed to material surface adsorption (SI, Figure S2). It is probably due the porous structure and high surface area of Fe_3O_4-R, which is in favor of phenol adsorption. Furthermore, the phenol removal efficiency of the heterogeneous catalytic system is highlighted in Figure 8, and as previously mentioned, high phenol conversion and TOC abatement were obtained in the Fe_3O_4-R/H_2O_2 process.

The high activity of Fe_3O_4 is obviously related to the capability of the material surface to convert H_2O_2 molecules into free radicals ($^{\bullet}OH$) [48]. Under acidic conditions, the mechanism of H_2O_2 decomposition over Fe_3O_4 may involve either adsorption on Fe^{2+} and Fe^{3+} surface sites. Adsorption and formation of a complex between surface Fe^{III} site and H_2O_2 (Eq. 6) can occur, allowing the production of $^{\bullet}HO_2$ radical that can thereafter react to form dioxygen (Eq. 7). However, the rates of radical formation over Fe^{III} are slow [49], compared to the rate of radical production over Fe^{II} surface sites (Eq. 8), that are responsible for the phenol degradation.

$$Fe^{III}H_2O_2 \rightarrow Fe^{II} + {}^{\bullet}HO_2 + H^+ \quad (6)$$

$$Fe^{III} + {}^{\bullet}HO_2 \rightarrow Fe^{II} + O_2 + H^+ \quad (7)$$

$$Fe^{II} + H_2O_2 \rightarrow Fe^{III} + {}^{\bullet}OH + OH^- \quad (8)$$

Furthermore, formation of soluble Fe^{2+} was also measured during the reaction (Table 3). However, the iron leaching remains at the ppm level in the solution. A blank experiment, performed with a similar content in Fe^{2+} as homogeneous catalyst (Table 3, 0.2 mg L^{-1} in Fe^{2+} experiment), was performed. Limited phenol conversion (32.1 %) and TOC abatement (27.3%) was obtained, indicating that the contribution of dissolved iron is limited, especially when we compare these values to the values obtained for the more active materials. Then, the high phenol conversion and TOC abatement measured for the Fe_3O_4-R can be attributed to reaction over heterogeneous active sites on the material surface.

Table 3. Selected reaction results and catalyst stability for the phenol degradation. (Fe_3O_4: 0.25 g L^{-1}; Phenol: 600 mg L^{-1}; H_2O_2: 40 mmol L^{-1}, pH: 4.0, T: 25 °C).

Sample	C_0[a]/ mg L^{-1}	X_{phenol}[b]/ %	X_{TOC}[c]/ % ($X_{H_2O_2}$[d] / %)	Fe_{tot} leaching[f]/ mg L^{-1}	Fe_{tot} in solution[g]/ %
Homogenous with 0.2 mg L^{-1} of Fe^{2+}	587	32.1	27.3	—	—
Fe_3O_4-C	576	67.1	38.4 (82.3)	0.03	0.01
Fe_3O_4-S	405	93.2	52.4 (83.2)	0.50	0.20
Fe_3O_4-R-1[e]	304	98.0	74.0 (87.3)	0.17	0.07
Fe_3O_4-R-2[e]		97.1	72.3	0.14	0.06
Fe_3O_4-R-3[e]		92.9	67.9	0.15	0.06
Fe_3O_4-Com	598	54.7	32.1 (72.5)	0.27	0.11

[a], C_0 is the initial phenol concentration, after adsorption on the catalyst surface; [b], X_{phenol} presents the phenol conversion after 90 min of reaction; [c], X_{TOC} presents the TOC abatement after 90 min of reaction; [d], X_{H2O2} presents the hydrogen peroxide conversion; [e], Fe_3O_4-R-1, -2 and -3 present the catalyst used for one, two and three successive tests; [f], Fe_{tot} leaching in solution presents the iron content in the solution at the end of the reaction; [g], Fe_{tot} leaching (%) presents the percentage of total iron (Fe(II) and Fe(III)) leached from the catalyst at the end of the reaction.

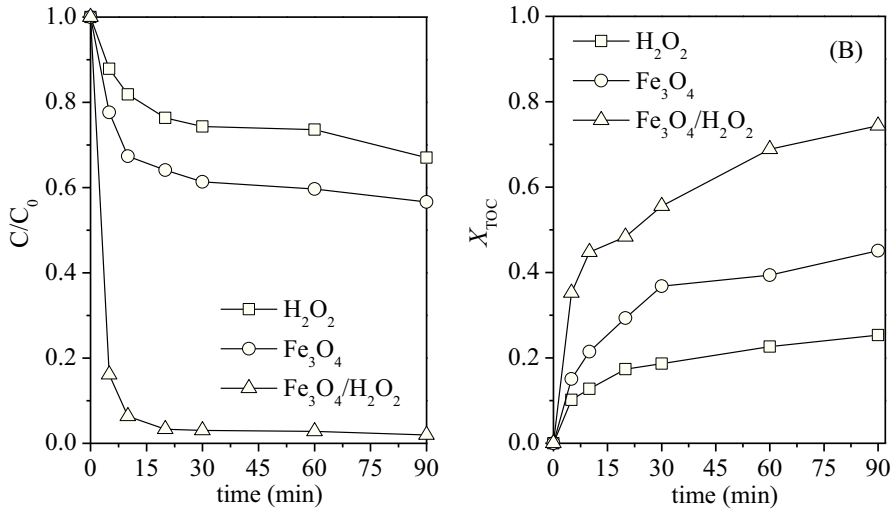


Figure 8. Phenol removal efficiency (A) and TOC removal (B) obtained with hydrogen peroxide alone (blank), catalyst alone (adsorption test), and hydrogen peroxide and catalyst (catalytic degradation) (phenol: 600 mg L^{-1}, Fe_3O_4-R: 0.25 g L^{-1}, H_2O_2: 40 mmol L^{-1}, pH: 4.0, T: 25 °C).

7.3.5 Role of morphology in the catalytic oxidation of phenol

Different morphologies exhibited different surface areas, adsorption abilities, and crystal sizes, which are considered to be the decisive parameters that contribute to catalytic performance [50][51]. In our study, different shapes of Fe_3O_4 (Fe_3O_4-C,

Fe_3O_4-S, or Fe_3O_4-R, representing microcubes, nanospheres, and nanorods, respectively) were chosen to estimate the effect of catalyst morphology on the catalytic activity when H_2O_2 was used as an oxidant. The phenol, TOC removal efficiencies, and H_2O_2 conversions obtained at the end of the tests are summarized in Table 3. As evident in Figure 9 and Table 3, Fe_3O_4-R exhibited superior catalytic activity in the Fe_3O_4/H_2O_2 process compared with the other morphologies of Fe_3O_4. Notably, the three different catalysts synthesized here were much more active than the commercial material (Fe_3O_4-Com), for which only 54.7% of the phenol was converted, 32.1% of the TOC was removed, and 72.5% of the H_2O_2 was decomposed. The results in Figure 9, Table 1, and Table 3 then revealed that a greater surface area was beneficial to the reaction, leading to high phenol mineralization degree. Evolution of the Pseudo-first order reaction rate with the surface area is presented in Figure 10. The activity trend obtained was: Fe_3O_4-R > Fe_3O_4-S >> Fe_3O_4-C > Fe_3O_4-Com. The results clearly indicated that this process was a surface reaction since increased surface area provided more active sites for catalytic oxidation, and consequently higher constant rate. Higher content of surface hydroxyl radicals can be produced over high surface area materials, enhancing the degradation of phenol [51]. Consequently, the very limited activity of the catalyst prepared by reduction of the commercial hematite, that is Fe_3O_4-Com, results from its poor textural properties.

Greater Fe^{II}/Fe^{III} ratios led to more Fe^{II} sites and resulted in higher removal efficiency for organic compounds [52]. As evident from the results in Table 1, comparable bulk Fe^{II}/Fe^{III} ratios are obtained between the different morphologies of the synthesized Fe_3O_4. These are however slightly higher than the ratio measured in the commercial catalyst (0.32±0.2). Therefore, the significantly higher catalytic activities of the synthesized samples mainly originated from the higher surface areas, as demonstrate by Figure 10, due to the increase in exposed active site number with the surface area at iso-Fe^{II}/Fe^{III} ratios.

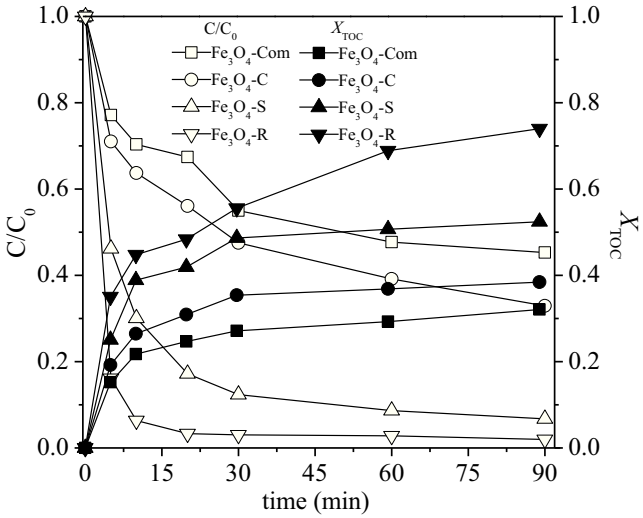


Figure 9. Phenol removal efficiency and TOC removal obtained with different morphology of Fe_3O_4 (phenol: 600 mg L^{-1}, catalysts: 0.25 g L^{-1}, H_2O_2: 40 mmol L^{-1}, pH: 4.0, T: 25 °C).

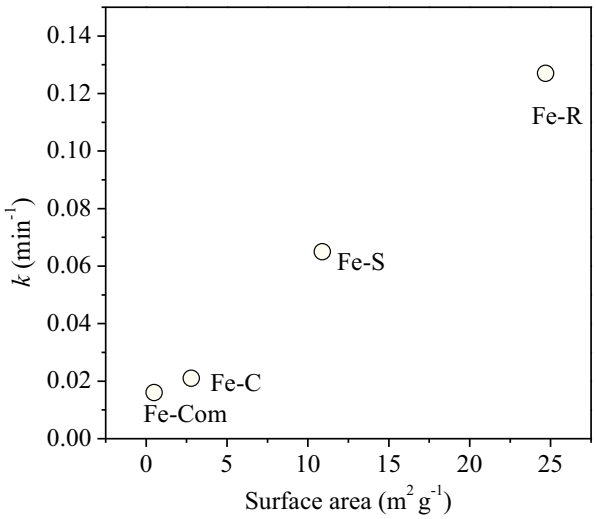


Figure 10. The relationship between the decay constant and surface areas for different catalysts.

7.3.6 Influence of hydrogen peroxide concentration and catalyst loading on phenol oxidation

In the heterogeneous Fenton reaction, the concentration of oxidant and catalyst loading are essential to the reaction and directly affect the concentration of active radicals produced for phenol degradation. We investigated the effect of hydrogen peroxide concentration by increasing the hydrogen peroxide concentration from 10 mmol L^{-1} to 50 mmol L^{-1} (SI, Figure S3). The effect of catalyst loading on phenol and TOC removal in the Fe_3O_4-R/H_2O_2 system was also evaluated (Details seen in SI,

Figure S5). TOC abatement increased with increasing H_2O_2 concentration and increasing catalyst loading (SI, Figure S3-4). Logically, the removal efficiency is dependent on H_2O_2 concentration. An increase in H_2O_2 concentration, resulting in increased $^{\bullet}OH$ production, lead to increased phenol conversion and TOC abatement. As evident in Figure S3, the TOC abatement increased linearly with increasing H_2O_2 dosage up to 40 mmol L^{-1}. However, further increase in the concentration of H_2O_2 to 50 mmol L^{-1} does not induce significant increase the TOC abatement (82.3%). According to the stoichiometry for the complete phenol degradation by H_2O_2, 14 mol of H_2O_2 is theoretically required to completely convert 1 mol phenol to CO_2 and H_2O.

In our study, 10, 20, 30 or 40 mmol L^{-1} of H_2O_2 is added to 100 mL of phenol solution (at the initial concentration of ~300-305 mg L^{-1} after adsorption stabilization). These concentrations in H_2O_2 are however below the stoichiometric value needed to completely mineralize phenol (45.3 mmol L^{-1} of H_2O_2). Consequently, complete phenol conversion and TOC abatement cannot be achieved under these conditions. When H_2O_2 concentration increases to 50 mmol L^{-1}, the H_2O_2/phenol molar ratio is 15.4, which is 1.1 times larger than the stoichiometric value needed to completely mineralize phenol into inorganic compounds (CO_2, H_2O). However, complete TOC abatement cannot be obtained even at the highest H_2O_2 value, and TOC abatement of only 82.3% is obtained. The effect of Fe_3O_4 loading was also given for sake of information. As can be awaited, an increase in catalyst loading induces an increase in final phenol conversion (Figure S4). The increase in catalyst loading results in an increase in Fe^{II} surface active site number that logically results in enhanced final phenol conversion.

7.3.7 Stability of Fe_3O_4-R catalyst and iron leaching

For the Fe_3O_4/H_2O_2 system, the stability of the catalyst is a critical factor for its successful application to wastewater treatment. The reusability of the solid was evaluated by three successive runs under identical oxidation conditions. At the end of each oxidation process, the solid was removed from the reactor, dried in a quartz tube

under N_2 at a flow rate of 60 min^{-1} at 60 °C overnight, and stored at room temperature. As shown in Figure 11, the removal efficiency slightly decreased after the three cycles. Due to the possible oxidation of the catalyst surface during reaction, XPS was employed to quantify the changes of Fe^{2+}/Fe^{3+} ratio (SI files, Table S1, Figure S1). A significant part of the Fe^{2+} is observed to be oxidized to Fe^{3+} after reaction (the ratio of Fe^{2+}/Fe^{3+} reduced to 41.0%, compared with 52.5% for the fresh material). This evolution can explain the slight decrease in final conversion between the three successive cycles. However, the phenol removal still remained high, which indicates that satisfying catalytic performance was maintained after three runs even if the Fe_3O_4 was observed to slightly dissolve at each cycle (the total iron ion concentration in solution was 0.14-0.17 mg L^{-1} at the end of each test, Table 3). The morphology of Fe_3O_4 after the three consecutive uses was similar to the fresh material (SI, Figure S5). In addition, XRD diffractograms collected before and after the oxidation reaction were found to be close to those of fresh catalyst samples (SI, Figure S6). Satisfying stability of the structure, and activity maintain under cyclic reaction tests (*i.e.*, limited deactivation of the surface catalytic sites by the adsorption/oxidation process was observed after three successive tests) is thus obtained.

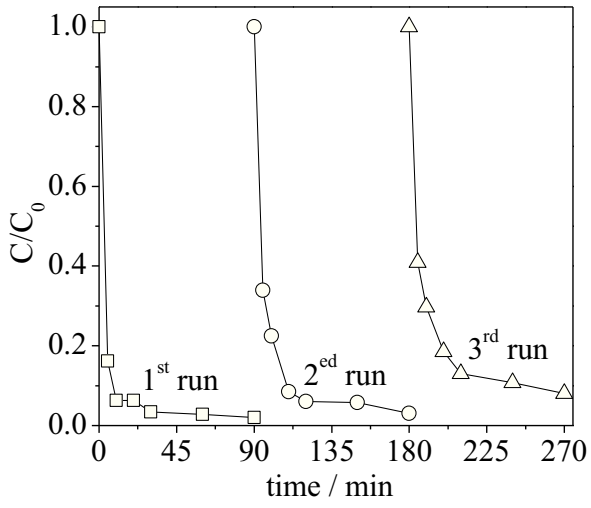


Figure 11. Evaluation of the catalyst stability during the reaction. (phenol: 600 mg L^{-1}, Fe_3O_4-R: 0.25 g L^{-1}, H_2O_2: 40 mmol L^{-1}, T: 25 °C).

7.3.8 Effect of the iron crystal phase on the catalytic oxidation of phenol

Different crystal phases contain different amounts of active sites, which is a decisive parameter that contributes to catalytic performance. Therefore, we deduced that the material phase composition can affect the degradation of phenol during catalytic oxidation. Different iron phases were thus obtained through reduction of the α-Fe_2O_3 under H_2 at 300 °C, 400 °C, and 600 °C for 1 h. The crystalline phases of the catalyst samples were then assessed based on their XRD patterns (Figure 12). The XRD patterns showed that the iron crystal phase depended on the reduction temperature. The diffraction peaks of Fe_2O_3-R reduced at 300 °C was assigned to Fe_3O_4-R. No additional phases were detected in the samples, which suggested that the Fe_3O_4-R was highly pure. When the reduction temperature was increased to 400 °C, the iron phase Fe_3O_4/Fe^0 was obtained, which was also reported by Moura et al. [15]. When the reduction temperature was increased to 600 °C, the Fe_3O_4 phase vanished completely and was transformed into pure Fe^0. This result is not in agreement with results obtained by TPR experiments for which incomplete reduction is measured even at 1000 °C (Table 2). However, the low H_2 concentration used for the TPR experiments could be at the origin of the incomplete reduction.

To investigate whether the crystal phase of the iron was correlated with the degradation of phenol, samples with different crystal phase combinations were used to compare removal efficiencies. TOC removal efficiency, which is an important parameter for evaluating the mineralization degree of organic compounds, was used to affirm the efficiency of catalytic degradation of phenol with H_2O_2. The phenol conversion and TOC abatement after 90 min are presented in the Figure S7 (SI file). The final conversion increased with increasing reduction temperature and then decreased when the reduction temperature reached 600 °C, showing the variable contribution of the different phases to the apparent activity. In addition, Fe^0 exhibited some activity, with 68.1% TOC removal, even if greater degradation were obtained for Fe_3O_4-R. The Fe_3O_4/Fe^0 phase (reduction at 400 °C, Figure 12) exhibited the highest catalytic activity and TOC removal efficiency (82.0%), and the catalytic

activity followed the order $Fe_3O_4/Fe^0 > Fe_3O_4 > Fe^0$. A positive effect on the catalytic activity was observed with the formation of Fe^0 phase over Fe_3O_4-R surface (SI, Figure S7). The formation of an interface between Fe^0 with Fe_3O_4, not only by physical contact but also via a surface chemical reaction to form the interfacial phase FeO could be at the origin of this high activity [15]. Therefore, we can conclude that the formation of mixed Fe^0/Fe^{II} phase was appropriate to generate high activity for heterogeneous Fenton reactions.

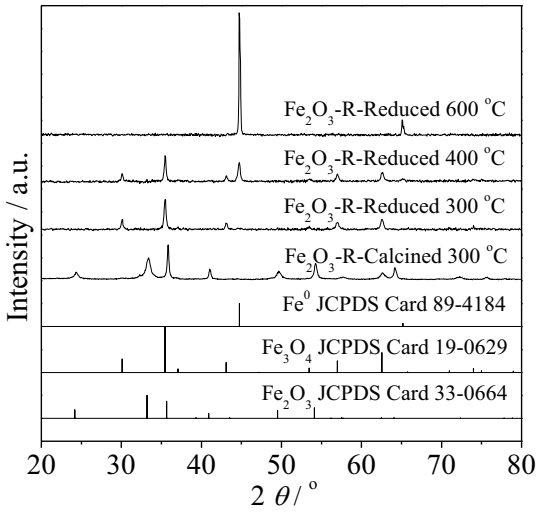


Figure 12. XRD patterns recorded of α-Fe_2O_3-R precursor oxidized at 300 °C and reduced at different temperatures (300 °C, 400 °C and 600 °C) for 1 h.

7.4 Conclusion

Magnetite, Fe_3O_4, with various morphologies has been successfully synthesized through the thermal reduction of α-Fe_2O_3 particles fabricated via a hydrothermal process. TEM analysis indicated that the microcubes, nanospheres, and nanorods of the Fe_3O_4 particles were porous structures. The nanorods of Fe_3O_4 exhibited the greatest activity, with a phenol conversion of 98.0% and a TOC abatement of 74.0%. In addition to the evident effect of the material morphology, studies revealed that the crystal phase was directly responsible for the catalytic degradation through Fe^{II} active site. Stability studies evidenced satisfying stability of these nanomaterials of Fe_3O_4 structure, with limited loss in catalytic activity. In addition, the optimization of the reduction temperature to form Fe^0/Fe_3O_4 mixed phase allows achieving improved

catalytic activity. These heterogeneous catalytic processes may be regarded as promising hydroxyl-radical-based systems for the oxidative degradation of organic compounds.

References

[1] R.M. Cornell, U. Schwertmann, 2nd ed., Wiley-VCH, Weinheim, 2003.
[2] F.B. Li, X.Z. Li, X.M. Li, T.X. Liu, J. Dong, J. Colloid Interface Sci. 311 (2007) 481-490.
[3] G. Kreysa, B. Hákansson, J. Eletroanal. Chem. 201 (1986) 61-83.
[4] K.E. Heusler, Electrochimica Acta 30 (1985) 1741-1742.
[5] C.L. Chien, Annu. Rev. Mater. Sci. 25 (1995) 129-160.
[6] U. Preuβ, M. Baerns, Chem. Eng. Technol. 10 (1987) 297-305.
[7] L.C.A. Oliveira, J.D. Fabris, R.R.V.A. Rios, W.N. Mussel, R.M. Lago, Appl. Catal. A: Gen. 259 (2004) 253-259.
[8] L.J. Xu, J.L. Wang, Appl. Catal. B: Environ. 123-124 (2012) 117-126.
[9] X.F. Xue, K. Hanna, M. Abdelmoula, N.S. Deng, Appl. Catal. B: Environ. 89 (2009) 432-440.
[10] W.P. Kwan, B.M. Voelker, Environ. Sci. Technol. 37 (2003) 1150-1158.
[11] P.G. Tratnyek, M.M. Scherer, T.J. Johnson, L.J. Matheson, M.A. Tarr, (Ed.), New York, Marcel Dekker, 2003, 371-421.
[12] J.E. Szecscody, J.S. Fruchter, M.D. Williams, V.R. Vermeul, D. Sklarew, Environ. Sci. Technol. 38 (2004) 4656-4663.
[13] S.H. Joo, A.J. Feitz, T.D. Waite, Environ. Sci. Technol. 38 (2004) 2242-2247.
[14] N. Wang, L.H. Zhu, D.L. Wang, M.Q. Wang, Z.F. Lin, H.Q. Tang, Ultrason. Sonochem. 17 (2010) 526-533.
[15] F.C.C. Moura, M.H. Araujo, R.C.C. Costa, J.D. Fabris, J.D. Ardisson, W.A.A. Macedo, R.M. Lago, Chemosphere 60 (2005) 1118-1123.
[16] P.G. Tratnyek, M.M. Scherer, B. Deng, S. Hu, Water Res. 35 (2001) 4435-4443.
[17] T. Hyeon, S.S. Lee, J. Park, Y. Chung, H.B. Na, J. Am. Chem. Soc. 123 (2001) 12798-12801.
[18] S.H. Yu, M. Yoshimura, Adv. Funct. Mater. 12 (2002) 9-15.
[19] K. Woo, H.J. Lee, J.P. Ahn, Y.S. Park, Adv. Mater. 15 (2003) 1761-1764.
[20] X.W. Teng, H. Yang, J. Mater. Chem. 14 (2004) 774-779.
[21] J.H. Deng, X.H. Wen, Q.N. Wang, Mater. Res. Bull. 47 (2012) 3369-3376.
[22] R.X. Huang, Z.Q. Fang, X.M. Yan, W. Cheng, Chem. Eng. J. 197 (2012) 242-249.
[23] S. Shin, H. Yoon, J. Jang, Catal. Comm. 10 (2008) 178-182.
[24] S.X. Zhang, X.L. Zhao, H.Y. Niu, Y.L. Shi, Y.Q. Cai, G.B. Jiang, J. Hazard. Mater. 167 (2009) 560-566.
[25] S.P. Sun, A.T. Lemley, J. Mol. Catal. A: Chem. 349 (2011) 71-79.
[26] J.B. Zhang, J. Zhuang, L.Z. Gao, Y. Zhang, N. Gu, J. Feng, D.L. Yang, J.D. Zhu, X.Y. Yan, Chemosphere 73 (2008) 1524-1528.
[27] X.F. Xue, K. Hanna, N.S. Deng, J. Hazard. Mater. 166 (2009) 407-414.
[28] K. Rusevova, F.D. Kopinke, A. Georgi, J. Hazard. Mater. 241-242 (2012) 433-440.

[29] M. Usman, P. Faure, C. Ruby, K. Hanna, Appl. Catal. B: Environ. 117-118 (2012) 10-17.

[30] R.C.C. Costa, F.C.C. Moura, J.D. Ardisson, J.D. Fabris, R.M. Lago, Appl. Catal. B: Environ. 83 (2008) 131-139.

[31] L.J. Xu, J.L. Wang, Environ. Sci. Technol. 46 (2012) 10145-10153.

[32] A. Prakash, A.V. McCormick, R.M. Zachariah, Chem. Mater. 16 (2004) 1466-1471.

[33] S. Peng, C. Wang, J. Xie, S.H. Sun, J. Am. Chem. Soc. 128 (2006) 10676-10677.

[34] D.E. Zhang, X.J. Zhang, X.M. Ni, J.M. Song, H.G. Zheng, Cryst. Growth Des. 7 (2007) 2117-2119.

[35] Z. Li, B. Tan, M. Allix, A. I. Cooper and M. J. Rosseinsky, Small, 4 (2008) 231-239.

[36] A.P. Alivisatos, J. Phys. Chem. 100 (1996) 13226-13239.

[37] J. Chen, F.B. Wang, K.L. Huang, Y.N. Liu, S.Q. Liu, J. Alloys. Compd. 475 (2009) 898-902.

[38] N. Du, Y.F. Xu, H. Zhang, C.X. Zhai, D.R. Yang, Nanosacle Res. Lett. 5 (2010) 1295-1300.

[39] S.F. Zhang, W. Wu, X.H. Xiao, J. Zhou, F. Ren, C.Z. Jiang, Nanoscale Res. Lett. 6 (2011) 89-97.

[40] J. Bachmann, J. Jing, M. Knez, S. Barth, H. Shen, S. Mathur, U. Gösele and K. Nielsch, J. Am. Chem. Soc., 129 (2007) 9554-9555.

[41] Y. L. Chueh, M. W. Lai, J. Q. Liang, L. J. Chou and Z. L. Wang, Adv. Funct. Mater., 16 (2006) 2243-2251.

[42] L.W. Hou, Q.H. Zhang, F. Jérôme, D. Duprez, F. Can, X. Courtois, H. Zhang, S. Royer, ChemcatChem, 5 (2013) 1978-1988.

[43] Y.L. Nie, C. Hu, L. Zhou, J.H. Qu, Appl. Catal. B: Environ. 82 (2008) 151-156.

[44] A.E. Harvey, J.A. Smart, E.S. Arms, Anal. Chem. 27 (1955) 26-29.

[45] M.S. Liang, W.K. Kang, K.C. Xie, J. Natural Gas Chem. 18 (2009) 110-113.

[46] H. Iida, K. Takayanagi, T. Nakanishi, T. Osaka, J. Colloid. Interface. Sci. 314 (2007) 274-280.

[47] H. Yan, J. Zhang, C. You, Z. Song, B. Yu, Y. Shen, Mater. Chem. Phys. 113 (2009) 46-52.

[48] M.A. Voinov, J.O. Sosa Pagán, E. Morrison, T.I. Smirnova, A.I. Smirnov, J. Am. Chem. Soc. 133 (2011) 35-41.

[49] S.-S. Lin, M. D. Gurol, Env. Sci. Technol. 32 (1998) 1417-1423.

[50] T.L.P. Dantas, V.P. Mendonça, H.J. José, A.E. Rodrigues R.F.P.M. Moreira, Chem. Eng. J. 118 (2006) 77-82.

[51] S. Song, Z.W. Liu, Z. He, A.L. Zhang, J.M. Chen, Environ. Sci. Technol. 44 (2010) 3913-3918.

[52] P.K. Stoimenov, V. Zaikovski, K.J. Klabunde, J. Am. Chem. Soc. 125 (2003) 12907-12913.

[53] J.H. Ramirez, C.A. Costa, L.M. Madeira, G. Mata, M.A. Vicente, M.L. Rojas-Cervantes, A.J. López-Peinado, R.M. Martín-Aranda, Appl. Catal. B: Environ. 71 (2007) 44-56.

Supporting Information for:

Shape-controlled nanostructured magnetite-type materials as highly efficient Fenton catalysts

Liwei Hou, Daniel Duprez, Hui Zhang, and Sébastien Royer

1. Materials

Synthesis 1-decyl-3-methyl imidazolium chloride (C_{10}mimCl): In a typical preparation procedure, 1-methylimidazole (0.5 mol) and 1-chlorodecane (0.7 mol) was mixed and stirred in a flask using a reflux unit. Then, the reaction mixture was stirred for an additional period of 48 h at 80 °C. For the purification, ethyl acetate was used in a rotary evaporator for several times.

Microcubes α-Fe_2O_3: An aqueous solution obtained by dissolving NaOH (8 mmol) in de-ionized water (36.7 mL) was added $FeCl_3 \cdot 6H_2O$ (2.67 mmol) under vigorous stirring. Subsequently, 8 mmol of the C_{10}mimCl was added into the homogeneous brown solution under continuous stirring. After 30 min, the solution was transferred into a stainless-steel autoclave with a capacity of 55 mL, sealed and heated at 140 ^oC for 15 h. When the reaction was completed, the autoclave was cooled to the ambient temperature. The red product was centrifuged at 10000 rpm for 10 min, washed repeatedly with de-ionized water and ethyl alcohol till neutrality, dried in the oven at 80 ^oC for overnight. The final product was labeled as Fe_2O_3-C.

Nanospheres α-Fe_2O_3: 2.67 mmol of $FeCl_3 \bullet 6H_2O$ and 12 mmol of CH_3COOK were put into 36.7 mL of de-ionized water under continuous stirring. Subsequently, 8 mmol of C_{10}mimCl was added into the obtained solution under stirring. The next steps of the synthesis are the same as Fe_2O_3-C, and the sample was denoted as Fe_2O_3-S in this work.

Porous nanorods α-Fe_2O_3: The α-Fe_2O_3 porous nanorods were synthesized in the NaOH aqueous solution. The first step was to prepare the α-FeOOH nanorods. Detailed synthesis procedures were the same as those for making Fe_2O_3-C, except the amount of NaOH changed to be 26.7 mmol. In the second step, the α-Fe_2O_3 porous nanorods were obtained by heating the as-prepared α-FeOOH nanorods in air at 300 °C for 3 h. The final product was labeled as Fe_2O_3-R.

2. X-ray photoelectron spectroscopy (XPS)

Compared to Fe_2O_3, no satellite peaks appear in the spectrum for Fe_3O_4 [1-3]. The absence of the satellite peak has been verified in our study. The peak positions of $Fe2p_{3/2}$ and $Fe2p_{1/2}$ are, respectively, 710.5 (S.D. = 0.05) and 724.1 ev (S.D. = 0.07) (Figure S1) and they are located at higher value obtained than for Fe_2O_3 [3]. Using the peak shape parameters and peak positions of Fe^{2+} and Fe^{3+} that are obtained for Fe_3O_4 reported in the literature [1], the Fe2p peak for Fe_3O_4 was deconvoluted into Fe^{2+} and Fe^{3+} component (example given in Figure S1). The calculated Fe^{2+}/Fe^{3+} ratio are presented in Table S1. It is obvious that the Fe^{2+}/Fe^{3+} ratio in rod-type material is much higher than in the commercial one. Furthermore, a change in Fe^{2+}/Fe^{3+} ratio was also observed in Table S1 before and after reaction. Due to the oxidation of the Fe_3O_4 in the reaction process, part of the Fe^{2+} was converted to Fe^{3+} after the reaction. As shown in Table S1, the ratio of Fe^{2+}/Fe^{3+} reduced to 41.0%, compared with the fresh catalyst (52.5%), but the value is still larger than for the commercial material.

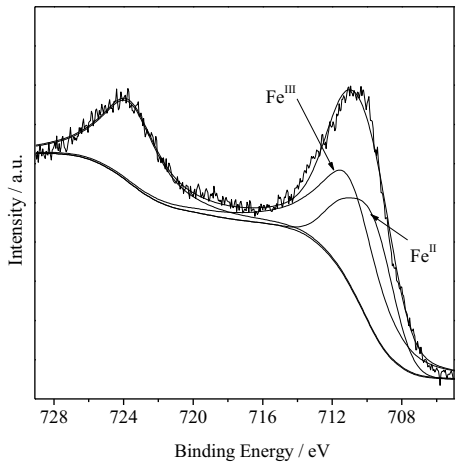


Figure S1 XPS details of the iron Fe $2p_{1/2}$ and Fe $2p_{3/2}$ peaks of the as-synthesized Fe_3O_4-R before reaction.

Table S1 Fe^{2+} and Fe^{3+} surface content on the materials.

Sample	Reaction time/ min	Surface atomic concentration/ %		Binding Energy/ ev	Fe^{2+}/Fe^{3+} / %	Percentage of Fe^{2+} reoxidation after reaction/ %
		Fe	O			
Fe_3O_4-Com	0	85.6	14.5	710.43	25.1	33.7
	90	86.4	13.6	710.40	16.6	
Fe_3O_4-R	0	80.8	19.2	710.44	52.5	38.8
	90	82.0	18.0	710.50	41.0	

3. Catalyst adsorption ability

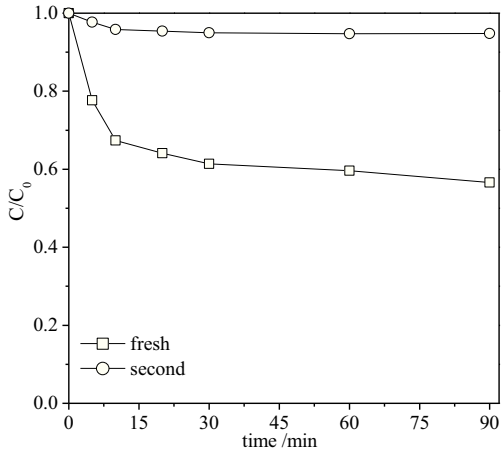


Figure S2 Adsorption of phenol on the surface of Fe_3O_4 (Reaction conditions: phenol 600 mg L^{-1}; Fe_3O_4-R: 0.25 g L^{-1}; pH: 4.0, T: 25 ^oC)

fresh: catalyst stays in contact 90 min with phenol solution; second: Fe_3O_4-R is recovered immediately after 90 min without washing, and then a new phenol solution is added to the recovered Fe_3O_4 for another 90 min reaction. While phenol is significantly adsorbed during the first cycle, the second cycle leads to a very limited phenol concentration decrease.

4. Influence of operational parameters on phenol removal

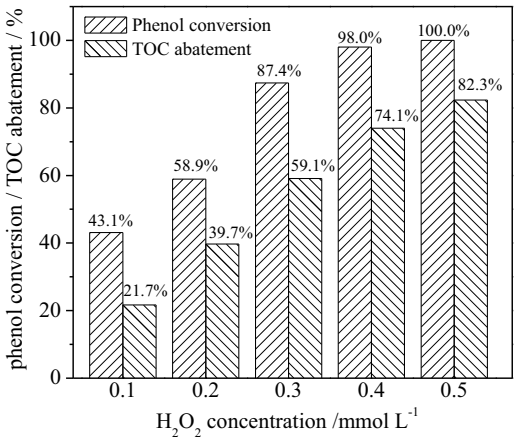


Figure S3 Effect of hydrogen peroxide concentration on phenol conversion and TOC abatement during the heterogeneous Fenton reaction. (Fe_3O_4-R: 0.25 g L^{-1}; phenol: 600 mg L^{-1}; pH: 4.0; T: 25 ^oC).

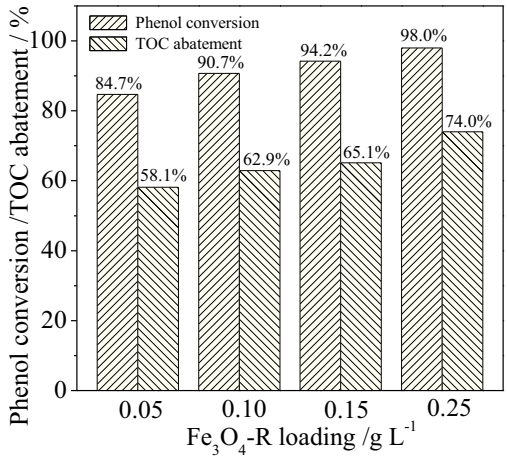


Figure S4 Effect of catalyst loading on phenol conversion and TOC abatement. (phenol 600 mg L^{-1}; H_2O_2 concentration: 40 mmol L^{-1}; pH: 4.0; T 25: ^oC).

5. Stability tests of Fe_3O_4-R

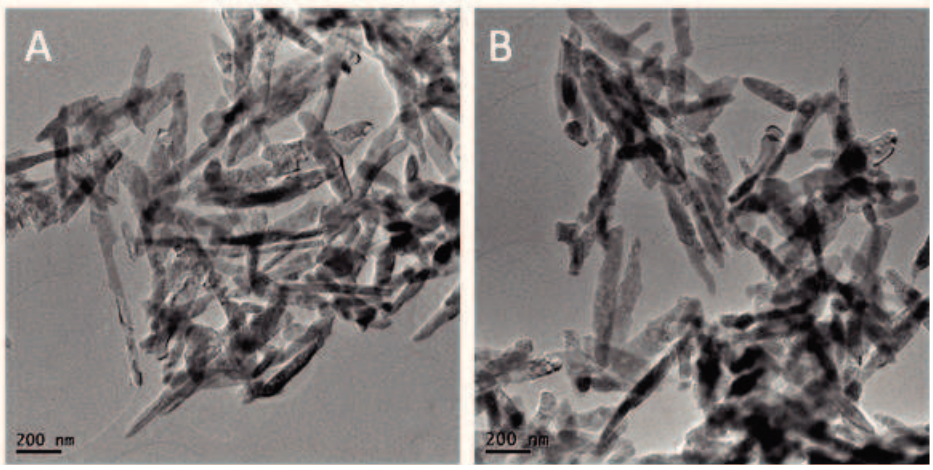


Figure S5 TEM of Fe_3O_4-R before (A) and after reaction (B).

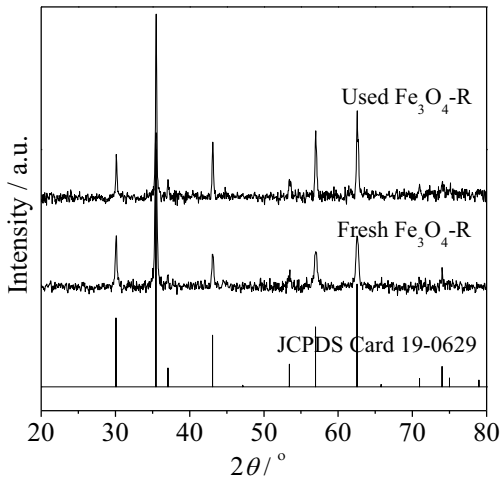


Figure S6 XRD patterns of Fe_3O_4-R before and after reaction.

6. Influence of the reduction temperature on the catalyst activity.

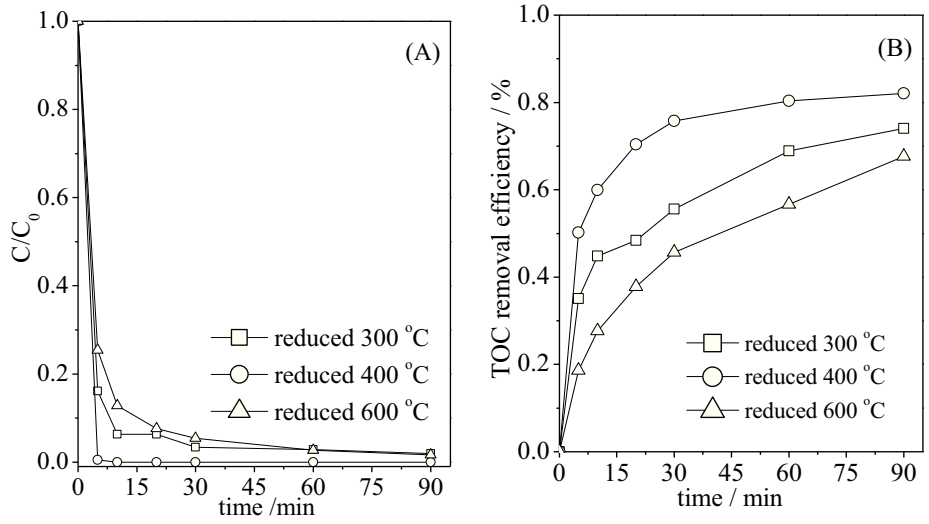


Figure S7. Degradation of phenol in the presence of Fe_2O_3-R reduced with H_2 at different temperatures (phenol: 600 mg L^{-1}; H_2O_2 concentration: 40 mmol L^{-1}; catalyst dosage: 0.25 g L^{-1}; pH: 4.0; T: 25 °C)

7. References

[1] D.D. Hawn, B.M. De Koven, Surf. Interface Anal. 10 (1987) 63-74.

[2] M. Muhler, R. Schlögl, G. Ertl, J. Catal. 138 (1992) 413-444.

[3] T. Yamashita, P. Hayes, Appl. Surf. Sci. 254 (2008) 2441-2449.

Chapter 8 Simple non-aqueous route to nano-perovskite mixed oxides

The successful synthesis of nanoscaled LaA_xO_3 (A = Co, Mn) through a novel non-aqueous benzyl alcohol route (BA) is reported. The obtained materials were characterised by X-ray diffraction, transmission electron microscopy and N_2 physisorption, while their oxygen mobilities were evaluated using oxygen isotopic exchange (OIE) experiment. These solids presented better properties in specific surface area (SSA), crystallite size (*D*), and redox ability, with comparison to the ones prepared by conventional citric acid method (CA). The OIE results showed that the oxygen mobility was strongly influenced by the physical properties (*D*, SSA), which was correlated well with their catalytic activities for phenol conversion and low temperature CO oxidation. Indeed, the BA route achieved much higher catalytic performances.

8.1. Introduction

Perovskite-based catalysts, of the general formula ABO_3, are important heterogeneous catalysts in industry due to their high potential, low cost and flexibility of composition, and they are especially useful in waste gas oxidation or combustion (NO_x, CO and methane) [1-3]. Indeed, some composites have been proposed as potential alternatives to the commercially used noble metals. Among perovskites, cobalt and manganese-based structures are found to be the most useful in the catalytic process due to their great versatility, excellent high-temperature thermal and hydrothermal stability, interesting activity, and low cost of the constituting elements [4-7]. More interestingly, in addition to their application in waste gas treatment, perovskites also act as efficient catalysts for wastewater treatment, due to the presence of transition metals with multiple valence states. $BiFeO_3$-type perovskites (BFO) are reported to be good catalysts for oxidative acetylation [8], photocatalysis [9] and catalytic activation of H_2O_2 [10]. A phase-pure layered perovskite, $LaNi_3O_{10}$, was employed as a catalyst for the removal of azo dyes [11].

Advanced oxidation technologies (AOPs) for wastewater treatment have appeared as a logical alternative to biodegradation due to the generation of hydroxyl

radicals ($^{\bullet}OH$) in these processes [10, 12-14]. The hydroxyl radicals react in a non-selective way with organic compounds, leading to harmless chemicals such as CO_2 and H_2O. This type of radical is easily generated using hydrogen peroxide and multivalent ions such as Fe, Co, and Mn. The generally accepted free radical mechanism for the classical homogeneous chain reaction involves the following steps, where A represents the transition metals, Fe, Co, and Mn, and n represents the valence state [15]:

$$H_2O_2 + A^n \rightarrow A^{n+1} + {}^{\bullet}OH + OH^- \quad (1)$$

$$H_2O_2 + A^{n+1} \rightarrow A^n + {}^{\bullet}HO_2 + H^+ \quad (2)$$

$$^{\bullet}OH + A^n \rightarrow Me^{n+1} + OH^- \quad (3)$$

$$A^{n+1} + {}^{\bullet}HO_2 \rightarrow A^n + O_2 + H^+ \quad (4)$$

$$A^n + {}^{\bullet}HO_2 + H^+ \rightarrow A^{n+1} + H_2O_2 \quad (5)$$

$$^{\bullet}HO_2 + {}^{\bullet}HO_2 \rightarrow H_2O_2 + O_2 \quad (6)$$

Although the classic homogenous catalyst system is highly efficient, it operates at strict pH levels to prevent the precipitation of metal ions, and extra metal ions are considered pollution after treatment, thus limiting widespread application. Unlike the traditional homogenous catalysts, heterogeneous catalysts, with hydrogen peroxide, can effectively oxidise organic compounds at a wide pH range. However, we found that the catalytic activity of pure metal oxides (Fe_3O_4, Fe_2O_3, MnO_2, etc.) was not effective in degrading organic compounds; organics were only slightly degraded at slow rate in H_2O_2/Fe_3O_4, H_2O_2/Fe_2O_3, and H_2O_2/MnO_2 systems. Due to weak catalytic activity, heterogeneous catalysts often require the aide of other advanced oxidation technologies, such as UV or ultrasound, to enhance the reaction rate. The need for extra equipment and energy consumption increases the cost of their use for wastewater treatment. In this sense, it is very important to develop more effective heterogeneous catalysts.

Considering that LaA_x-based (A = Co, Mn) nanoparticles simultaneously have a perovskite structure and multiple oxidation states, such as Mn^{2+}, Mn^{3+}, and Mn^{4+}, we anticipate these nanoparticles to be excellent candidates for CO oxidation and

catalytic activation of H_2O_2. It is known that the redox properties and catalytic performance of perovskites are critically dependent on their physical properties. Generally, conventional methods for perovskite preparation, such as calcination-milling [2] and citric acid routes, lead to large grain size (*D*), low specific surface area (*SSA*) and poor activity [16,17]. To overcome these limitations, improved synthetic approaches, such as the so-called sol-gel method [2], reactive grinding [18], nanocasting [19] and flame-spray pyrolysis [20], allow a higher surface area (30-50 m^2 g^{-1}) and smaller crystal size (< 20 nm). Although the formation of the tartrate complex keeps cations homogeneously dispersed, these catalysts achieve of greater catalytic performance over as-synthesised materials. Sintering is required due to the low calcination temperature. Reactive grinding is sufficient for LaA_xO_3 (Co, Mn) synthesis, but popularisation is largely restricted by the requirement for special equipment and a complex procedure [21]. Although a simple and efficient route for the preparation of supported nanocrystalline perovskites with sizes below 5 nm was developed by our group [22], it remains a challenge to directly synthesise size-limited and pure nanocrystalline perovskites.

In recent years, the so-called “benzyl alcohol route” has become a valuable pathway for nanoparticle preparation; this route offers excellent control over particle size, shape, crystallinity, order, purity, assembly behaviour, and isolability, while avoiding the use of any additional surfactants or templates [23,24]. This process may be defined as non-aqueous, and no water is generated in-situ during the different competitive reactions. Nanoparticles in powder form are highly desirable for many applications and industrial processing steps.

In this study, we aimed to extend the benzyl alcohol route to the preparation of pure LaA_xO_3 (A = Co, Mn) nanoparticles. Since we have shown that oxygen mobility, rather than redox capability, is well correlated to the oxidation performance of LaFe-based perovskites,[25] the oxygen isotopic exchange technique was utilised herein to investigate the oxygen mobility of the prepared samples and assess their catalytic activity. Considering that the study of LaA_xO_3 (A = Co, Mn) for wastewater

treatment is limited, phenol was selected as a model contaminant and was oxidised in the presence of catalysts and H_2O_2. The benzyl alcohol route (BA) for the preparation of LaA_xO_3 (A = Co, Mn) nanoparticles was shown to produce more active catalysts than the conventional citric-acid-route (CA).

8.2 Experimental Section

A series of La, Co, and Mn starting materials, as well as different solvothermal reaction conditions, were employed; pure $LaCoO_3$ and $LaMnO_3$ crystal phases were achieved, and the same material was prepared (see Supporting Information).

Characterisation of all the materials was performed by X-ray diffraction (XRD), N_2 physisorption, transmission electron microscopy (TEM), scanning electron microscopy coupled with energy dispersive X-ray spectroscopy (SEM-EDX), H_2-temperature-programmed reduction (H_2-TPR) and temperature-programmed oxygen isotopic exchange (TPOIE).

Activity measurement

CO oxidation reaction was performed in a tubular microreactor with 75 mg of catalyst. After activation at 300 °C of the catalyst under simulated air (30 mL min^{-1}), the reaction flow composed of 5 vol.% of CO - 20 vol.% O_2 - bal. N_2 at a total flow rate of 60 mL min^{-1} (given a GHSV of 22500 h^{-1}) was stabilized. The conversion was recorded under isothermal conditions each 20-30 °C (depending on the conversion). The concentration of CO and CO_2 in the effluent gas was on-line analyzed using a VARIAN (model CP-3800) gas chromatograph equipped with a TCD and a Porapak column for separation.

OIE (Oxygen Isotopic Exchange)

The exchange experiment was carried out in a recycling U-shaped microreactor. The recirculation volume (V = 60 cm^3; recirculation rate = 170 cm^3 s^{-1}) was coupled to a quadrupolar mass spectrometer (PFEIFFER VACUUM). The gas sampling was regulated by a thermo-valve adjusted to maintain a constant pressure of 1×10^{-6} mbar in the ionization chamber of the mass spectrometer. An equivalent of 20.0 mg of the

as-prepared sample is inserted in a microreactor, heat treated up to 300 °C under O_2 (ramp = 5 °C min^{-1}, total flow rate Q_{O2} = 20 mL min^{-1}) and cooled down to the test temperature. After temperature stabilization, the sample was evacuated under dynamic vacuum for 30 min. For the oxygen exchange experiments, around 65 mbar of pure $^{18}O_2$ was introduced into the recirculation volume. The temperature-programmed exchange experiments are performed from 100 °C to 600 °C (ramp = 2 °C min^{-1}), and partial pressure evolution of $^{18}O_2$ (mass 36), $^{16}O_2$ (mass 32), and $^{16}O^{18}O$ (mass 34) are recorded on the mass spectrometer allowing to quantify the ^{18}O fraction in the gas phase (α) and the number of oxygen atom exchanged (N_{ex}).

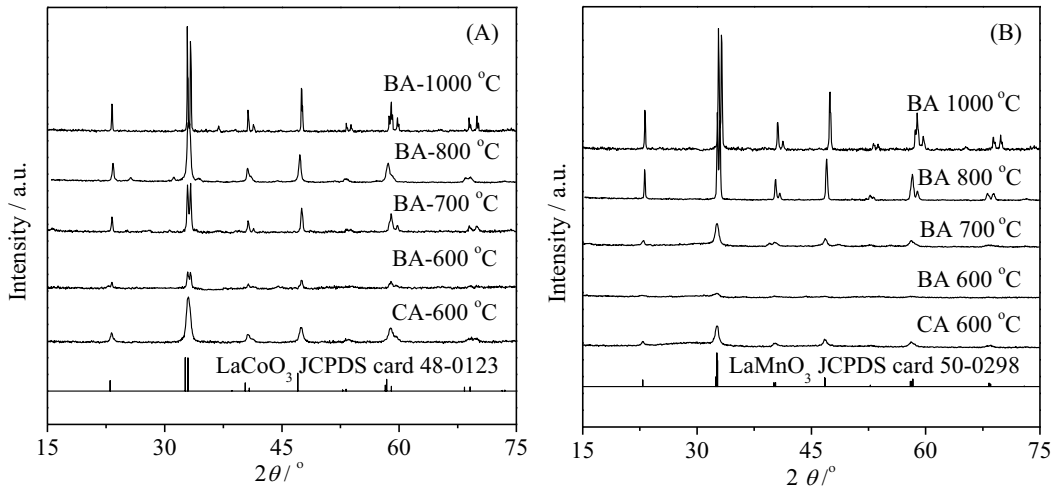


Figure 1. XRD results for $LaCoO_3$ and $LaMnO_3$ samples prepared by the BA and CA routes. (A) XRD results for LaCo-BA samples prepared at different calcination temperatures, including LaCo-CA-600; (B) XRD results for LaMn-BA samples prepared at different calcination temperatures, including LaMn-CA-600. Reference X-ray lines attributed to $LaCoO_3$ (JCPDS card 48-0123) and $LaMnO_3$ (JCPDS card 50-0298) are also shown.

8.3 Results and discussion

8.3.1 Physicochemical and structure properties

Samples prepared at different calcination temperatures (600 °C - 1000 °C), by the non-aqueous BA and citrate complexation routes, showed XRD reflections typical of the perovskitic phase. Figure 1 show that pure perovskite-type structures were obtained for the BA and CA samples, for both $LaCoO_3$ and $LaMnO_{3+\delta}$, compared to

the orthorhombic structure of $LaCoO_3$ (JCPDS card 48-0123) and $LaMnO_{3+\delta}$ (JCPDS card 50-0298). For $LaMnO_{3+\delta}$, it is often reported in the literature that samples are prepared in the air [26-29]. In this study, the oxygen content of the manganese-based perovskites was assumed to be 3.15, which is usually accepted in the literature. This corresponds to the fact that 30% of manganese is Mn(IV) in the oxidised perovskite structures.

Table 1 Physical properties of the BA and CA samples obtained at 600 °C.

Method	CA		BA	
Elemental composition	$LaCo_{0.98}O_3$	$LaMn_{0.97}O_{3.15}$	$LaCo_{0.96}O_3$	$LaMn_{0.96}O_{3.15}$
Crystal phases	P	P	P	P
S_{BET} (m^2 g^{-1})	21.7	26.3	8.9	17.5
D (nm)	14.8	18.4	21.8	28.0
S_{th} (m^2 g^{-1})	55.6	49.6	37.8	32.6
S_{th}/S_{BET}	2.6	1.9	4.2	2.6

P, $LaCoO_3$ and $LaMnO_3$ perovskite; D, particle size of $LaCoO_3$ and $LaMnO_3$ calculated from X-ray line broadening, using the Scherrer equation $D = K\lambda/(\beta\ cos\theta)$ after Warren's correction for instrumental broadening ($\beta^2 = B^2 - b^2$, where B is the FWHM and b is the instrumental broadening determined by the FWHM of the X-ray reflection of SiO_2, having particles larger than 150 nm, at $2\theta \approx 27^o$); S_{th}, theoretical specific surface area calculated assuming cubic particles of size D and a density of $LaCoO_3$ equal to 7.29 g cm^{-3} (S.Royer et al., 2005), and a density of $LaMnO_3$ equal to 6.57 g cm^{-3} (Van Roosmalen et al., 1994). S_{th}/S_{BET}, the ratio between the theoretical surface area and the BET surface area corresponds to a fraction of surface area lost by contact between crystal domains.

Normally, higher thermal treatment temperatures are used to ensure the complete crystallisation of the perovskite [30,31]. However, such high temperature treatments are accompanied by lower SSA, larger crystal size and, consequently, lower catalytic activity. A gradual decrease in FWHM of the XRD peaks with an increase in calcination temperature was observed, suggesting an increase in crystal size. This observation fits well with the corresponding values obtained from BET (SSA), as presented in Figure 2. Moreover, an important difference between the SSA, measured by N_2 adsorption, and the theoretical surface area, assuming a cubic-shaped crystal and calculated from D, (Table 1) was observed. It was determined that the S_{th}/S_{BET} ratio is of great importance for the properties of the solids, indicating that a fraction of

the surface is lost through contact between nanoparticles [32,33]. The larger the S_{th}/S_{BET} ratio, the more agglomerated the sample is. As shown in Fig. 2A-B, the ratio of S_{th}/S_{BET} increased for $LaCoO_3$ and $LaMnO_{3.15}$ (BA route) with increasing calcination temperatures. A high calcination temperature provoked a densification of the agglomerates, and a subsequent decrease in free surface between the elementary particles (S_{th}/S_{BET}) was observed.

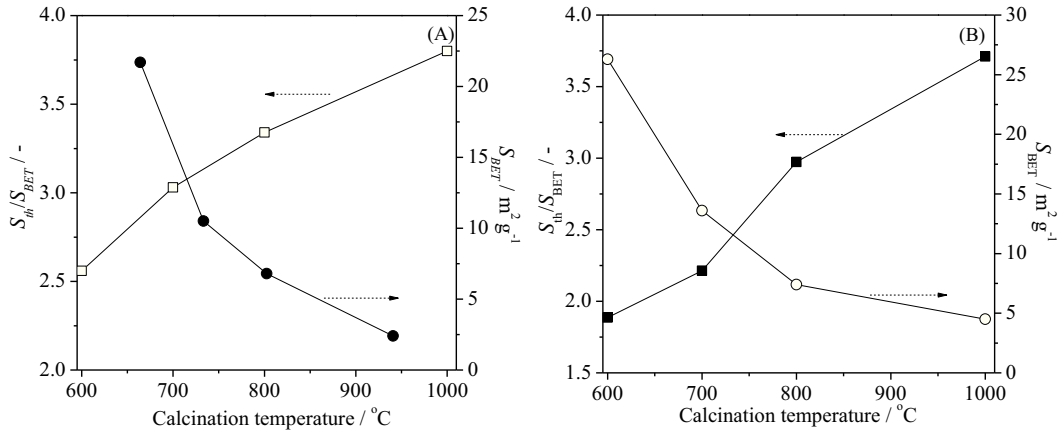


Figure 8-2. Plots of S_{th}/S_{BET} and SSA (obtained from BET treatment) of LaCo-BA-600 (A) and LaMn-BA-600 (B) samples at varying calcination temperatures.

It has been reported that moderate thermal treatment (600 °C) also produces a pure $LaCoO_3$ perovskite structure with more adequate physicochemical properties and, consequently, higher catalytic activity [32]. The CA samples calcined at higher temperatures (600, 700, 800 and 1000 °C) were analysed by XRD and showed pure perovskite structures (not shown). A larger surface area (21.7 m^2 g^{-1}) was achieved using the BA route after 600 °C calcination, which is much higher than the value for the $LaMnO_3$ sample obtained by the CA route (8.9 m^2 g^{-1}). Similarly, a higher surface area (26.3 m^2 g^{-1}) was observed for $LaMnO_3$ synthesised by the BA route, which is superior to that of $LaMnO_3$ synthesised by the CA route (17.5 m^2 g^{-1}) when both samples were calcined at the same temperature. Upon closer inspection, the differences between theoretical (S_{th}) and BET (S_{BET}) surface area ratios for the two routes (BA vs. CA) were found to be remarkable, becoming larger at higher temperature (Table 2); this result effectively confirms that the BA route prevented potential agglomeration of the perovskite.

Table 2. The ratio of theoretical S_{th} *or* S_{BET} surface area between BA and CA samples (BA: CA) obtained at each temperature.

Ratio of S_{th} or S_{BET} (BA:CA)	Samples	T / °C			
		600	700	800	1000
Ratio of S_{th} [a]	$LaCoO_3$	1.47	1.56	1.61	1.30
	$LaMnO_3$	1.52	1.39	1.36	1.28
Ratio of S_{BET} [b]	$LaCoO_3$	2.4	3.4	3.7	4.9
	$LaMnO_3$	1.5	3.1	3.5	4.4

[a] the theoretical surface areas were calculated from the surface area developed by a cubic unit volume of single crystal grain, assuming no agglomeration. [b] S_{BET} was obtained by N_2 adsorption measurement.

The morphology of the $LaCoO_3$ and $LaMnO_{3.15}$ samples, prepared by the BA and CA routes and calcined at 600 °C, was investigated by TEM, as shown in Figure 3. Based on images in Figure 3A and 3B, one can see that the $LaCoO_3$ samples synthesised via the BA route were composed of relatively isolated and spherical $LaCoO_3$ nanoparticles, with diameters ranging from 10 to 40 nm and without many large clusters or agglomerates (Figure 3B). However, large particles composed of closely packed nanoparticles, with diameters between 40-200 nm, were observed in samples prepared by the CA route (Figure 3C and 3D). These particles exhibited strong agglomeration and inhomogeneity in crystal size. This structure, with such poor uniformity and large crystal size, lead to a low SSA (8.9 $m^2 g^{-1}$, Table 1), which has an adverse effect on catalytic activity.

Morphological and structural features of the $LaMnO_3$ powders were also examined in detail by TEM. Figure 3E-3H displays that the different synthetic methodologies have a strong impact, not only on the crystal size but also on the ordered crystal morphology. Based on Fig. 3E and 3F, the shape of $LaMnO_3$ obtained by the BA route is regular quasi-spherical and the particles occur separately relative to those obtained by the CA route. As for crystal size, the samples prepared by the BA route are smaller than those of the CA route. The crystal size for samples prepared by the BA route was less than 40 nm, which is larger than the size calculated by XRD. However, the size of the BA samples was much smaller than that of the CA samples

(18.4 nm for BA *vs.* 28.0 nm for CA, presented in Table 1). The reason for this might be that benzyl alcohol is adsorbed on the surface of the precipitate, stopping the self-assembly process. It can be seen that the BA route is suitable for the formation of not only highly crystalline nanoparticles but also highly ordered organic-inorganic hybrid materials [34].

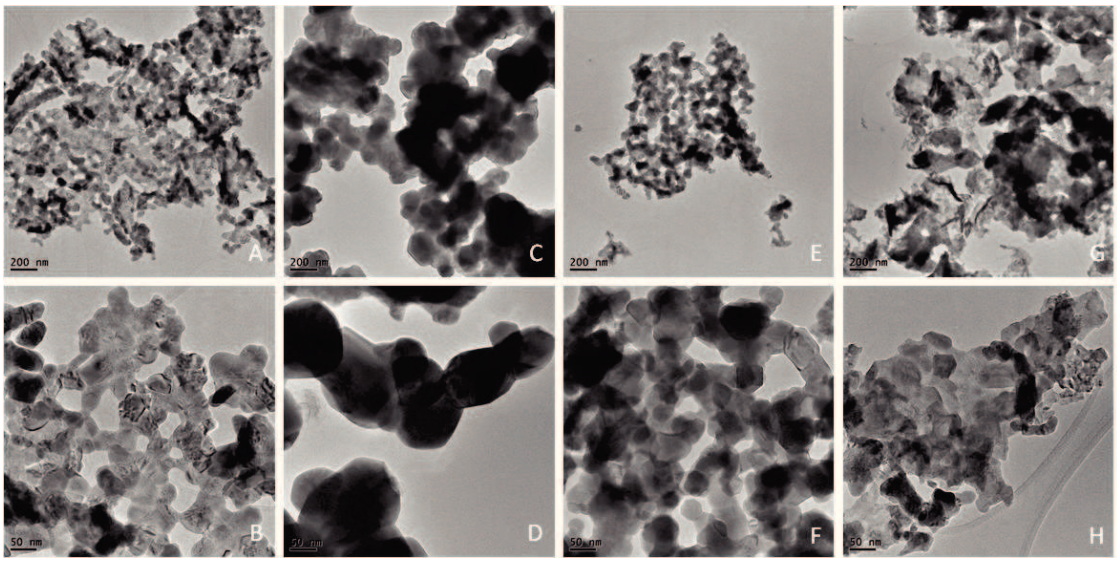


Figure 3. TEM images of LaCo-BA-600 °C (A-B); LaCo-CA-600 °C (C-D); LaMn-BA-600 °C (E-F); LaMn-CA-600 °C (G-H).

8.3.2 Redox properties as evaluated by H_2-TPR

The effect of morphology on the redox properties of the four catalysts was evaluated by H_2-TPR. The H_2 consumption profiles are presented in Fig. 4, while the calculated results are gathered in Table 3. Figure 4A and Table 3 showed the reduction process of $LaCoO_3$. In the case of LaCo-CA, the reduction started at 150 ^oC, and two separated reduction peaks centered at 393 ^oC and 650 ^oC were recorded. Based on the quantification of H_2 consumption, the first peak exactly resulted by the complete reduction of Co^{3+} to Co^{2+}, and the subsequent generation of Co^0 occurred after 475 ^oC. It is noted that almost all the Co^{3+} can be reduced to metallic Co^0 before 800 ^oC (~ 90%), showing its excellent redox property comparing to Fe^{3+} and Mn^{3+} in perovskite structure [11]. A quite different profile was obtained on BA sample, in which the

major reduction behaviour happened in the first peak before 475 °C (100% Co^{3+} to Co^{2+} with 53% Co^{2+} to Co^{0}). Additionally, the Co^{3+} reduction seemed to shift from 393 °C to 270 °C after the employ of BA route. Clearly, even though CA and BA $LaCoO_3$ presented close reduction proportions of Co^{3+} (both 100%) and Co^{2+} (90% for CA *vs.* 94% for BA) at the end of the TPR reaction, the redox abilities of the both ions enhanced strongly in BA sample. A half of Co^{2+} in LaCo-BA even showed the same redox capacity than Co^{3+} in LaCo-CA. The positive effect of the higher SSA and lower *D* of BA sample could contributed to such great enhancement.

As depicted in Figure 4B and Table 3, two separated reduction peaks were observed on both $LaMnO_3$ samples. Differing from $LaCoO_3$, Mn ion in $LaMnO_3$ could not be reduced to Mn^{0} until 900 °C in both CA and BA $LaMnO_3$, corresponding to our previous result [11]. In their first peaks below 600 °C, all the Mn^{4+} ions were totally reduced to Mn^{3+}, while Mn^{3+} to Mn^{2+} reaction were also partially occurred. Apparently, about 14% more of Mn^{3+} could be reduced in LaMn-BA comparing to LaMn-CA in the first peak (20% more until 900 °C), showing again the advantage of better physical properties of BA sample, as mentioned for $LaCoO_3$. Unfortunately, the effect to the redox property of Mn^{4+} could not be confirmed herein, since the two $LaMnO_3$ had the same reduction start temperature.

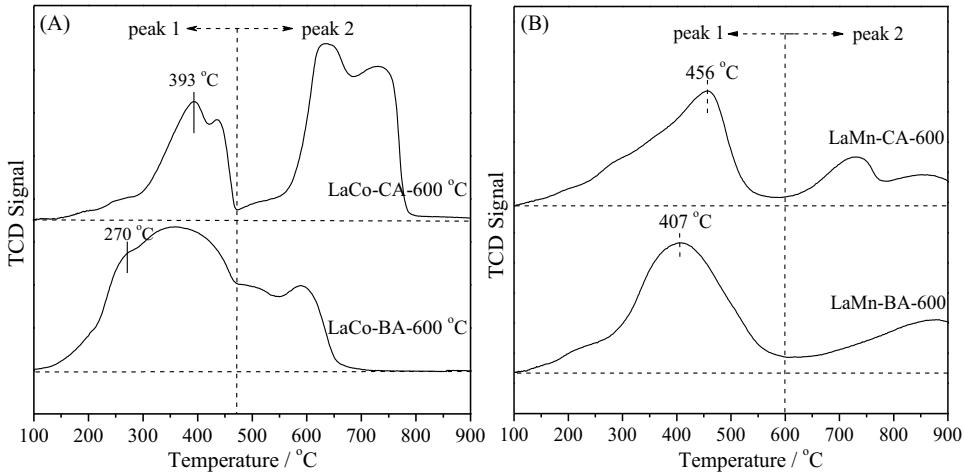


Figure 4. H_2-TPR profiles for (A) LaCo-BA-600 and LaCo-CA-600 ; (B) LaMn-BA-600 and LaMn-CA-600.

Table 3. H_2-TPR results for $LaCoO_3$ and $LaMnO_3$ samples

	Theoretical H_2 consumption[a] / mmol g^{-1}		Experimental H_2 consumption / mmol g^{-1}			Reduction proportion[c] %	
	$Mn^{4+} \rightarrow Mn^{3+}$	$Mn^{3+} \rightarrow Mn^{2+}$	total[b]	peak 1 (< 600 °C)	peak 2 (> 600 °C)	$Mn^{4+} \rightarrow Mn^{3+}$	$Mn^{3+} \rightarrow Mn^{2+}$
LaMn-BA	0.614	2.047	1.908	1.304	0.604	100 (peak 1)	63.19 (peak 1: 33.69; peak 2: 29.50)
LaMn-CA			1.496	1.028	0.468	100 (peak 1)	43.07 (peak 1: 20.21; peak 2: 22.86)
	$Co^{3+} \rightarrow Co^{2+}$	$Co^{2+} \rightarrow Co^{0}$	total	peak 1 (< 475 °C)	peak 2 (> 475 °C)	$Co^{3+} \rightarrow Co^{2+}$	$Co^{2+} \rightarrow Co^{0}$
LaCo-BA	2.034	4.068	5.844	4.191	1.653	100 (peak 1)	93.65 (peak 1: 53.02; peak 2: 40.63)
LaCo-CA			5.704	2.102	3.602	100 (peak 1)	90.21 (peak 1: 1.67; peak 2: 88.54)

[a], calculated values of H_2 to be consumed for the complete reduction of the different cations (reduction reactions depicted in the Table); [b], total molar of H_2 consumed for per gram of materials, issued from H_2-TPR experiment; [c], reduction proportion calculated by comparing each experimental H_2 consumptions with theoretical H_2 consumption.

8.3.3 Oxygen mobility capacity as evaluated by temperature-programmed oxygen isotopic exchange (TPOIE)

The OIE technique was developed by our group and successfully applied for the measurement of oxygen mobility in many metal oxide catalysts, including LaFe- and LaCo-based perovskites. OIE is much more effective and better suited for the study of oxidation behaviour of a catalyst compared to conventional O_2-TPD techniques [25,37]. Therefore, in order to generally compare the oxygen mobility capacity between CA and BA samples, TPOIE experiments were carried out. Figure 6 shows the cumulative number of oxygen atoms exchanged (N_e), the rate of exchange (R_e), and exchange temperature, as determined by TPOIE. Obviously, the total number of oxygen atoms exchanged at 600 ^oC was very close between BA and CA samples, implying that almost all the oxygen atoms were exchangeable below this temperature; this result is similar to that of LaFe-based perovskites [25]. In the case of $LaCoO_3$ (Figure 5A), oxygen atoms began to become activated at around 220 ^oC for both materials, corresponding to surface oxygen activation. Above 270 ^oC, an abundance of oxygen in BA-$LaCoO_3$ participated in the exchange reaction relative to the CA sample, and oxygen mobility capacity was largely improved for the BA sample. According to R_e plots, the exchange process can be separated into two steps, with different activation energies, for each sample. These processes occur at 220 ^oC - 400 ^oC and 400 ^oC - 600 ^oC for BA-$LaCoO_3$, while 350 ^oC can be the demarcation point for CA-$LaCoO_3$. Normally, taking into consideration the exchange temperature, the first step located in the low temperature zone is assigned to the oxygen exchange that occurs at the surface and subsurface of the sample grains. Bulk oxygen atoms start to exchange when temperature is increased, contributing to the second step. In the first step, 49.5% and 18.4% of oxygen in the solid was easily exchanged for the BA and CA $LaCoO_3$ samples, respectively. The large differences in SSA (21.7 $m^2\ g^{-1}$ for BA *vs.* 8.9 $m^2\ g^{-1}$ for CA) and *D* (14.8 nm for BA *vs.* 21.8 nm for CA) for the two samples clearly contributed to this difference; the higher SSA and lower *D* were, the larger the proportion of surface active sites. More than 80% of the oxygen atoms in the CA

sample were activated above 400 °C, exhibiting its poor oxygen mobility capacity. The highest exchange rate was achieved at 500 °C. A similar phenomenon was observed for the $LaMnO_3$ materials. The highest exchange rate of the four materials was detected for BA-$LaMnO_3$ at 360 °C where 57.6% of the oxygen took part in this exchange reaction in the first step. The separation of the two steps for the CA sample was not so apparent; the exchangeable oxygen in the first step only accounted for about 15%. According to the large proportion of exchanged oxygen in the first step, for the two BA perovskites, the activation of bulk oxygen atoms cannot be excluded as a possibility, in addition to an increase in surface/subsurface oxygen. In conclusion, the huge enhancements in oxygen mobility for the BA samples were attributed to their excellent physicochemical properties, comparing with the CA materials. More oxygen atoms (both from surface/subsurface and bulk) were available at medium temperatures, while higher temperatures are needed for the CA materials. Therefore, better oxidation activity can be reasonably expected for the BA samples.

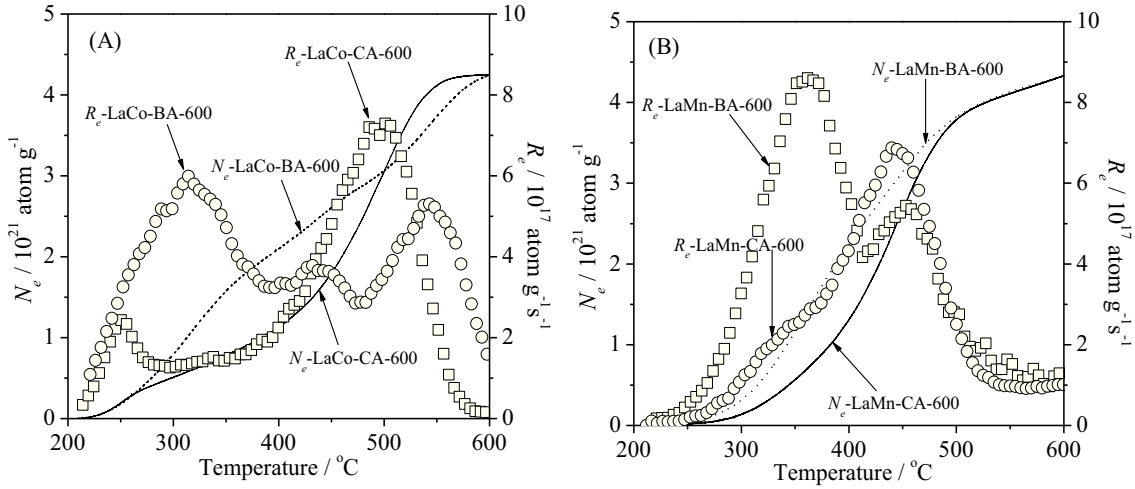


Figure 5. Plots of the number of exchanged oxygen atoms (N_e) and exchange rate (R_e) versus temperature of reaction for LaCo-BA-600, LaCo-CA-600 (A); LaMn-BA-600, and LaMn-CA-600 (B).

8.3.4 Catalytic acitivity evaluation

The CO oxidation activity results over the both $LaCoO_3$ and $LaMnO_3$ were presented in Figure 6 showing much higher oxidation performances obtained over BA samples than that of CA samples.

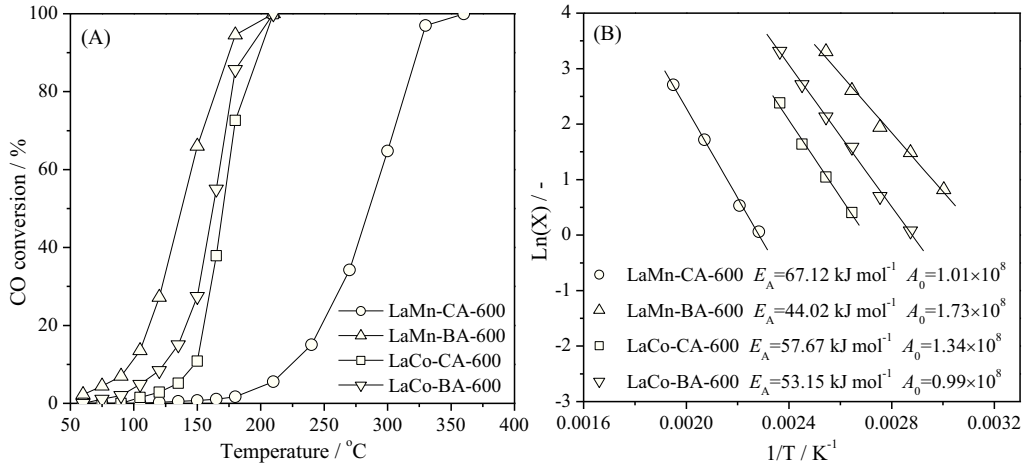


Figure 6 (A) CO conversion versus reaction temperature for LaCo-BA-600, LaCo-CA-600, LaMn-BA-600 and LaMn-CA-600. (B) Arrhenius plot obtained for CO oxidation reaction (conversions <30%); straight line, two parameters (E_A and A_0) linear regression; E_A and A_0, values of activation energy and pre-exponential factor calculated by linear regression on the Arrhenius plots.

It has been found that CO oxidation reaction over $LaCoO_3$ and $LaMnO_3$ perovskite proceeded through a redox surface oxidation mechanism in which surface oxygen from the solid will be consumed, rather than through a pure suprafacial mechanism. Thus, a higher mobility of oxygen on the surface or even subsurface as well as a better surface redox capacity are absolutely favorable to this reaction, which can be correlated to the activity improvement achieved over BA samples.

For phenol conversion, the catalytic aciticty tests were taken for $LaMnO_3$ samples, and the results were shown in Figure 7. Much higher activity was achieved by BA samples.

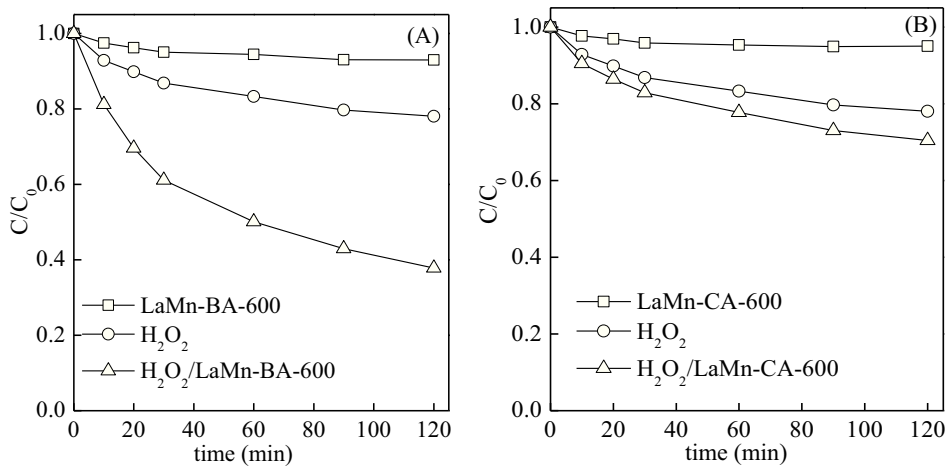


Figure 7. Comparison of the catalytic performance in the system of H_2O_2/LaMn-BA-600 (A) and H_2O_2/LaMn-CA-600 (B) in the presence of (1) H_2O_2 alone, (2) catalyst and (3) H_2O_2/catalyst. Experiment condition : phenol: 100 mg/L, catalyst : 1.0 g/L, H_2O_2: 50 mmol/L, pH: 4.0, T: 25 °C).

8.4 Conclusions

In conclusion, the successful extension of the benzyl alcohol route to the preparation of pure $LaCoO_3$ and $LaMnO_3$ nanoparticles was described. The BA $LaCoO_3$ and $LaMnO_3$ samples exhibited excellent physicochemical properties as well as enhanced redox capacity and oxygen mobility, leading to an increase in catalytic performance for CO oxidation or phenol conversion.

References:

[1] J.M.A. Van Roosmalen, E.H.P. Cordfunke, R.B. Helmholdt, H.W. Zandbergen. The defect chemistry of $LaMnO_{3\pm\delta}$: 2. structural aspects of $LaMnO_{3+\delta}$ [J]. J. Solid State Chem., 1994, 110 (1): 100-105.

[2] M. Kakihana, M. Yashima, M. Yoshimura, N. Ikeda, Y. Sugitani. Synthesis of high surface area $LaMnO_{3+d}$ by a polymerizable complex method [J]. J. Alloys Compd., 2009, 283 (1-2): 102-105.

[3] M. Popa, J. Frantti, M. Kakihana. Characterization of $LaMeO_3$ (Me: Mn, Co, Fe) perovskite powders obtained by polymerizable complex method, Solid State Ion., 2002, 154-155: 135-141.

[4] S. Royer, F. Bérubé, S. Kaliaguine, Effect of the synthesis conditions on the redox and catalytic properties in oxidation reactions of LaCo1-xFexO3, Appl. Catal. A: Gen. 282, 2005, 273-284.

[5] N. Pinna, The “benzyl alcohol route”: an elegant approach towards organic-inorganic hybrid nanomaterials, J. Mater. Chem. 17, 2007, 2769-2774.

[6] S. Royer, F. Berubé, H. Alamdari, R. Dacidson, S. Mcintyre, S. Kaliaguine, Appl. Catal. A 282, 2004, 273.

[7] J.P. Dacquin, C. Dujardin, P. Granger, J. Catal. 253, 2008, 37.

[8] L. Simono, F. Garin, G. Maire, Appl. Catal. 11, 1997, 167.

[9] J. P. Dacquin, C. Lancelot, C. Dujardin, P.D. Costa, G. Djega-Mariadassou, P. Beaunier, S. Kaliaguine, S. Vaudreuil, S. Royer, P. Granger, Influence of preparation methods of $LaCoO_3$ on the catalytic performances in the decomposition of N_2O, Appl. Catal. B: Environ. 91 (3-4), 2009, 596-604.

[10] J. A. Marcos, R.H. Buitrago, E.A. Lombardo, J. Catal. 105 (1987), 95.

[11] S. Royer et al. / Applied Catalysis B: Environmental 58 (2005) 273–288

[12] B.C. Tofield, W.R. Scott, J. Solid State Chem. 10 (1974) 183.

[13] J.M.A. Van Roosmalen, E.H.P. Cordfunke, R.B. Helmholdt, H.W. Zandbergen, J. Solid State Chem. 110 (1994) 320.

[14] P. Porta, S. De Rossi, M. Faticanti, G. Minelli, I. Pettiti, L. Lisi, M. Turco, J. Solid State Chem. 146 (1999) 291.

[15] S. Irusta, M.P. Pina, M. Menendez, J. Santamaria, J. Catal. 179 (1998) 400.

[16] L. Lisi, G. Bagnasco, P. Ciambelli, S. De Rossi, P. Porta, G. Russo, M. Turco, J. Solid State Chem. 146 (1999) 176.

[17] R. Zhang, A. Villanueva, H. Alamdari, S. Kaliaguine, Appl. Catal. A 307 (2006) 85–97.

[18] B. Levasseur, S. Kaliaguine, Appl. Catal. A 343 (2008) 29–38.

[19] L. G. Tejuca, J. L. G. Fierro (Eds.), Properties and Applications of Perovskite-Type Oxides, Marcel Dekker, New York, USA, 1992, pp. 271.

[20] E. Campagnoli, A. Tavares, L. Fabbrini, I. Rossetti, Y.A. Dubitsky, A. Zaopo, L. Forni, Effect of preparation method on activity and stability of LaMnO3 and LaCoO3 catalysts for the flameless combustion of methane. Appl. Catal. B: Environ. 55 (2005) 133-139.

[21] Y. Nishihata, J. Mizuki, T. Akao, H. Tanaka, M. Uenishi, M, Kimura, T. Okamoto, N. Hamada, *Nature* **2002**, *418*, 164-167.

[22] Farhadi, S.; Zaidi, M. Bismuth ferrite (BiFeO3) nanopowder prepared by sucrose-assisted combustion method: A novel and reusable heterogeneous catalyst for acetylation of amines, alcohols and phenols under solvent-free conditions. *J. Mol. Catal. A: Chem.* **2009**, *299*, 18–25.

[23] Gao, F.; Chen, X.; Yin, K.; Dong, S.; Ren, Z.; Yuan, F.; Yu, T.; Zou, Z.; Liu, J. Visible-light photocatalytic properties of weak magnetic BiFeO3 nanoparticles. Adv. Mater. 2007, 19, 2889–2892.

[24] W. Luo, L.H. Zhu, N. Wang, H.Q. Tang, M.J. Cao, Y.B. She, Efficient removal of organic pollutants with magnetic nanoscaled BiFeO3 as a reusable heterogeneous fenton-like catalyst, Enivron. Sci. Technol. 2010, 44, 1786-1791.

[25] M.A. Peňa, J.L. Fierro, Chem. Rev. 101 (2001) 1981.

[26] Yi N, Cao Y, Su Y, Dai WL, He HY, Fan KN. Nanocrystalline $LaCoO_3$ perovskite particles confined in SBA-15 silica as a new efficient catalyst for hydrocarbon oxidation. *Journal of Catalysis*. 2005; 230(1):249-253.

[27] Stephan K, Hackenberger M, Kiessling D, Wendt G. Total Oxidation of Methane and Chlorinated Hydrocarbons on Zirconia Supported $A_{1-x}Sr_xMnO_3$ Catalysts. *Chemical Engineering & Technology.* 2004; 27(6):687-693.

[28] Lee Y.N, Lago R.M, Fierro J.L.G, Cortes V, Sapina F, Martinez E. Surface properties and catalytic performance for ethane combustion on $La_{1-x}K_xMnO_{3+}\delta$ perovskites. *Applied Catalysis, A: General*. 2001; 207(1,2):17 24.

[29] S. Irusta, M.P. Pina, M. Menendez, J. Santamaria, J. Catal. 179 (1998) 400.

[30] M. Crespin, W. K. Hall, J. Catal. 1981, 69, 359-370.

[31] P. Ciambelli, S. Cimino, G. Lasorella, L. Lisi, S. De Rossi, M. Faticanti, G. Minelli, Appl. Catal. B 2002, 37, 231-241.

[32] S. Kaliaguine, A. Van Neste, V. Szabo, J. E. Gallot, M. Bassir, R. Muzychuk, Appl. Catal. A 2001, 209, 345-358.

[33] F. Kleitz, S. H. Choi and R. Ryoo, Chem. Commun. 2003, 2136-2137.

[34] G. L. Chiarello, I. Rossetti, L. Forni, J. Catal. 2005, 236, 251-261.

[35] M. Bonne, D. Sellam, J. -P. Dacquin, A. F. Lee, K. Wilson, L. Olivi, A. Cognigni, P. Marecot, S. Royer, D. Duprez, Chem. Commun. 2011, 47, 1509-1511.

[36] S. Kaliaguine, A.V. Neste, V. Szabo, J.E. Gallot, M. Bassir, R. Muzychuk, Perovskite-type oxides synthesized by reactive grinding part I. preparation and characterization, Appl. Catal. A: general 209 (2001), 345-358.

[37] M. Niederberger, G. Garnweitner, N. Pinna, M. Antonietti, J. Am. Chem. Soc. 2004, 126, 9120-9126;

Supporting Information for:

The general and simple non-aqueous route to prepare nano-perovskite mixed oxides with improved oxygen mobility and catalytic performances

Liwei Hou, Hui Zhang, Daniel Duprez, Sébastien Royer, Wei Yang, Runduo Zhang

Materials

Benzyl alcohol route:

$LaCoO_3$ (LaCo-BA-T)

$La(NO_3)_3 \cdot 6H_2O$ (2 mmol) was first dissolved in anhydrous benzyl alcohol (26.7 mL) (Sigma Aldrich) in a vial at room temperature. Cobalt (III) acetylacetonate (2 mmol) was dissolved in benzyl alcohol (40 mL) at room temperature. The reaction mixture was stirred for 30 min and transferred into an autoclave with a Teflon cap. The autoclave was heated to 200 °C for 24 h. The resulting brown suspension was centrifuged, followed by four washes with ethanol. After each washing step, the solvent was removed by centrifugation at 8000 rpm for 10 min. The collected material was left to dry in air at 80 °C overnight. Calcination was performed at elevated temperatures ranging from 600 ^{o}C to 1000 ^{o}C for 6 h. The prepared samples were labelled as LaCo-BA-T, where T refers to the calcination temperature.

$LaMnO_3$ (LaMn-BA-T)

$La(NO_3)_3 \cdot 6H_2O$ (2 mmol) was first dissolved with benzyl alcohol (26.7 mL) in a vial at room temperature. Subsequently, manganese (II) acetylacetonate (2 mmol) (Sigma Aldrich) was added to the solution. The procedure that followed was the same as for the LaCo-BA-*T* samples. These samples were labelled as LaMn-BA-T.

Characterisation of the materials was performed using X-ray diffraction (XRD), N_2 physisorption (for the surface area), transmission electron microscopy (TEM), scanning electron microscopy coupled with energy dispersive X-ray spectroscopy (SEM-EDX), H_2-temperature-programmed reduction (H_2-TPR) and temperature-programmed oxygen isotopic exchange (TPOIE). For a complete description of the methods and procedures, see SI file, Catalyst characterisations section.

Citric acid route:

$LaCoO_3$ (LaCo-CA-T)

Aqueous solutions of lanthanum (III) nitrate hexahydrate (20 mM) (≥ 99.0 %, Sigma-Aldrich) and cobalt (II) nitrate hexahydrate (20 mM) (97.7%, Alfa Aesar) were prepared with distilled water. Thereafter, an aqueous solution of citric acid (CA)(98 %, Prolabo, Paris), with a molar equivalence to La and Co (40 mM), was added drop-wise to the precursor solution under gentle stirring at 80 °C, resulting in the formation of a gel. The gel was dried in an oven at 110 °C overnight. Subsequently, the foam solid was crushed and calcined at 600 °C for 6 h (ramp rate = 5 ^{o}C min^{-1}). These samples were labelled as Co-CA-600.

$LaMnO_3$ (LaMn-CA-T)

Aqueous solutions of $La(NO_3)_3 \cdot 6H_2O$ (20 mM) and $Mn(NO_3)_2 \cdot 4H_2O$ (20 mM) (≥97.0 %, Sigma-Aldrich) were prepared with distilled water. Thereafter, 40 mM CA was added drop-wise to the precursor solution under gentle stirring at 80 °C, resulting in the formation of a gel. Afterwards, the procedure followed was the same as for $LaCoO_3$ samples. These samples were labelled as Mn-CA-T.

Characterisation

X-ray diffraction (XRD)

The catalyst structures were verified by X-ray diffraction using a D5005 diffractometer (Bruker), equipped with a CuKα radiation (λ=1.5406 Å). The signal was recorded every 3 s for *2θ* between 20° and 80° with a recording step of 0.05°. Phases were identified by comparison with the JCPDS database. Crystal size was determined using the Scherrer equation after applying Warren's correction for instrumental broadening.

N_2-physisorption

N_2 adsorption measurements were performed with a Micromeritics TRISTAR 3000 instrument and the surface areas of the catalysts were obtained by the Nrunauer-Emmett-Teller (BET) method.

Transmission electron microscopy (TEM)

Morphology and structure was evaluated by TEM coupled with Energy Dispersive X-ray Spectroscopy (EDXS). Micrographs were obtained on a JEOL 2100 instrument, operated at 200 kV with a LaB_6 source and equipped with a Gatan Ultra scan camera. EDX spectroscopy was carried out with a Hypernine (Premium) detector (active area: 30 mm^2) using the SM-JED 2300T software for data acquisition and treatment.

H_2-temperature-programmed reduction (H_2-TPR)

TPR experiments were performed with an AUTOCHEM instrument from Micromeritics. Approximately 90 mg of sample was introduced into the microreactor. The material was initially activated under simulated air (total flow rate = 30 mL min^{-1}) at calcination temperature for 1 h. After cooling down to room temperature, a reducing flow (1 vol.% of H_2 in Ar) was applied at a flow rate of 30 mL min^{-1}; the temperature of the reactor was increased from room temperature to 1000 °C with a ramp of 5 °C min^{-1}. Evolution of H_2 with temperature was recorded with an in-line TCD.

Temperature-programmed oxygen isotopic exchange (TPOIE).

The exchange experiment was carried out in a recycling U-shaped microreactor. The recirculation volume (V = 70 cm^3; recirculation rate = 170 cm^3 s^{-1}) was coupled to a quadrupolar mass spectrometer (MQG Blazers). Gas sampling was regulated by a thermo-value, adjusted to maintain a constant pressure of 1×10^{-6} mbar in the ionisation chamber of the mass spectrometer. The as-prepared samples (20.0 mg) were inserted into the microreactor, heat treated up to the calcination temperature under O_2 (ramp = 5 °C min^{-1}, total flow rate Q_{O2} = 20 mL min^{-1}), and cooled down to the test temperature. After temperature stabilisation, the sample was evacuated under dynamic vacuum for 30 min. For the oxygen exchange experiments, approximately 65 mbar of

pure $^{18}O_2$ was introduced into the recirculation volume. The temperature-programmed exchange experiments were performed from 100 °C to 600 °C (ramp = 2 °C min^{-1}), and partial pressure evolution of $^{18}O_2$ (mass 36), $^{16}O_2$ (mass 32), and $^{16}O^{18}O$ (mass 34) were recorded on a mass spectrometer that allows quantification of the ^{18}O fraction in the gas phase (α), the number of oxygen atom exchanged (N_{ex}), and the fraction of the solid exchanged at the end of the experiment (O_{ex}).

Chapter 9. General conclusion

Based on the results presented in Chapter 3 to Chapter 8, it was clearly demonstrated that multiples factors can affect the heterogeneous Fenton reaction. The first important point concerns the fraction of dissolved iron in the solution (unlike many published works), that first affects the catalytic activity. However, its contribution remains limited in regard of the global reaction rates. Activity also depended on the sorption capacity of the pollutant on the surface of the material, and its physico-chemical properties. The surface properties consequently play a very important role. The results obtained during the PhD then concern the role of the material and its properties, key parameters to control the heterogeneous Fenton reaction. In addition to classical H_2O_2 mediated processes, we demonstrated that persulfate ions can also be considered as a promissing oxidant for wastewater and soil treatment. Below are drawn achievements of the PhD work:

(1) Different morphologies of α-Fe_2O_3 have been synthesized using an ionic liquid-assisted hydrothermal method. Nanostructured Fe_3O_4 particles of defined morphologies were obtained through thermal reduction of α-Fe_2O_3 particles. All materials are pure phases.

(2) Reducibility experiments showed that α-Fe_2O_3 with various morphologies present comparable reduction properties. Reducibility is however strongly altered, with a first reduction process shifted to the low temperature, in the presence of noble metal on the surface.

(3) Oxygen mobility is favoured by the increase in surface area and decrease in crystal size, making the porous nanorod morphology the more active material for oxygen exchange.

(4) Owing to the favourable physical properties of the iron oxides obtained using the ionic liquid-assisted route, high activity for CO oxidation can be achieved. In addition, due to the high noble metal dispersion obtained over the porous nanorod morphology, Pd and Au containing materials showed extremely high activity.

(5) Magnetite catalysts in combination with H_2O_2 and ultrasound can efficiently convert TC. The catalyst exhibited good structural stability and a limited loss in performance upon reuse. The removal rate is affected by the initial TC, H_2O_2, and Fe_3O_4 concentrations; the temperature; and the ultrasonic power. The reaction is also affected by the initial pH.

(6) In this last process, the effluent toxicity, which was assessed using *D. magna*, decreased after it reached a maximum during the first period of the oxidation reaction. Then, noxious intermediates are produced during the first period of reaction.

(7) Experiments using different scavengers indicated that $^{\bullet}OH_{ads}$ plays a major role in the degradation process. More importantly, the TC oxidation mechanism proceeds through a TC intermediate adsorbed on the Fe_3O_4 surface.

(8) Mainly heterogeneous Fenton reaction happened for the degradation of TC and phenol, because Fe leaching from the oxide surface is negligible in our experiment conditions.

(9) Employing Fe_3O_4 in combination with $Na_2S_2O_8$ and ultrasound process can degrade tetracycline effectively. The degradation reaction mainly takes place on the surface of Fe_3O_4 and the leaching ion during the reaction remains very limited. The presence of $SO_4^{-\bullet}$, $^{\bullet}OH$ and $O_2^{-\bullet}$ scavengers would hinder the degradation reaction.

(10) The ultrasound can be used to accelerate the decomposition of $Na_2S_2O_8$ at room temperature. The maximum power efficiency is reached at 80 W and a further increase of power does not affect degradation rate of the reaction. Both the degradation rate and removal efficiency reach the highest level at the optimal initial pH of 3.7.

(11) A mechanism during sono-catalytic ozonation of tetracycline was proposed.

(12) Ultrasound enhanced the catalyst activity in the sono-catalytic ozonation process.

(13) Rod-type nanostructure exhibited exceptional activity toward phenol removal under mild conditions. Interestingly, the material activity is strongly affected

by the reduction degree, highlighting the beneficial effect of Fe^0/Fe_3O_4 mixed phase formation to achieve higher activity.

(14) The successful extension of the benzyl alcohol route to the preparation of pure $LaCoO_3$ and $LaMnO_3$ nanoparticles was described, and the samples exhibited excellent physicochemical properties as well as enhanced redox capacity and oxygen mobility, leading to increased catalytic performances.

Publications

[1] **Liwei Hou**, Hui Zhang*, Liguo Wang, Lu Chen. 2013, Ultrasound-enhanced magnetite catalytic ozonation of tetracycline in water. Chemical Engineering Journal. DOI 10.1016/j.cej.2013.06.013. (IF: 3.473; In Press)

[2] **Liwei Hou**, Hui Zhang*, Liguo Wang, Lu Chen, Yidong Xiong, Xiaofei Xue. 2013, Removal of sulfamethoxazole from aqueous solution by sono-ozonation in the presence of a magnetic catalyst. Separation and Purification Technology. DOI 10.1016/j.seppur.2013.05.014 (IF: 2.894; In Press).

[3] **Liwei Hou**, Qinghua Zhang, François Jérôme, Daniel Duprez, Fabien Can, Xavier Courtois, Hui Zhang*, Sébastien Royer*. 2013, Ionic liquid-mediated α-Fe_2O_3 shape controlled nanocrystal supported noble metals: highly active materials for CO oxidation. ChemCatChem 5 (7), 1978-1988. (IF: 5.181)

[4] Wei Yang, Runduo Zhang*, Biaohua Chen, Nicolas Bion, Daniel Duprez, **Liwei Hou**, Hui Zhang, Sébastien Royer*. 2013, Design of nanocrystalline mixed oxides with improved oxygen mobility: a simple non-aqueous route to nano-$LaFeO_3$ and the consequences on the catalytic oxidation performances. Chemical Communications, 49(43), 4923-4925. (IF: 6.378)

[5] **Liwei Hou**, Hui Zhang*, Xiaofei Xue. 2012, Degradation of tetracycline by ultrasound enhanced heterogeneous activation of peroxydisulfate by using magnetite as catalyst. Separation and Purification Technology, 84: 147-152. (IF: 2.894)

[6] Haigang Li, Yanwen Lin, Ping Yu*, Yunbai Luo, **Liwei Hou.** 2011, FTIR study of fattly acid fouling of reverse osmosis membranes: Effects of pH, Ionic strength, calcium, magnesium and temperature. Separation and Purification Technology. 77, 171-178. (IF: 2.921)

[7] Haigang Li, Yanwen Lin, Ping Yu*, Yunbai Luo, **Liwei Hou**. 2011, Relating organic fouling of reverse osmosis membranes to adsorption during the reclamation of secondary effluents containing methylene blue and rhodamine B. Journal of Hazardous Materials, 192 (2), 490-499. (IF: 4.172)

[8] Danna Zhou*, Jie Wang, **Liwei Hou**, Yan Zhao, 2012, Photochemistry of Fe(III)-tetracycline complex in aqueous solution under UV irradiation, Third International Conference on Digital Manufacturing and Automation, 608-611.

Under revision or to be submitted

[9] **Liwei Hou**, Daniel Duprez, Hui Zhang*, Sébastien Royer*, 2013, Shape-controlled nanostructured magnetite-type materials as highly efficient Fenton catalysts, Applied Catalysis B: Environmental, (major revision)

[10] **Liwei Hou**, Sébastien Royer*, Hui Zhang*, Liguo Wang. 2013, Design of a highly efficient AOP process using an ultrasound-assisted, heterogeneous Fenton-like reaction: example of tetracycline degradation over a commercial magnetite catalyst. Applied Catalysis B: Environmental, to submit.

[11] **Liwei Hou**, Sébastien Royer*, Daniel Duprez, Hui Zhang*, Wei Yang, Runduo Zhang. 2013, The benzyl route as a generic route to produce perovskite with improved oxygen transfert properties: to the design of highly active oxide catalysts, Nanoscale, to submit.